D 2022

U.PORTO
FEUP FACULDADE DE ENGENHARIA
UNIVERSIDADE DO PORTO

ENERGY STORAGE: DEVELOPMENT OF NON-AQUEOUS REDOX FLOW AND LIQUID METAL BATTERIES

KASHIF MUSHTAQ

DOCTORAL THESIS PRESENTED TO
FACULTY OF ENGINEERING OF THE UNIVERSITY OF PORTO IN
SUSTAINABLE ENERGY SYSTEMS (MIT PORTUGAL PROGRAM)

Massachusetts Institute of Technology

MIT Portugal

Blank Page

Energy storage: development of non-aqueous redox flow and liquid metal batteries

by

Kashif Mushtaq

Submitted to the Faculty of Engineering of the University of Porto in fulfillment of the requirements for the degree of

Doctor of Philosophy in Sustainable Energy Systems

May 2022

Author: _____

Kashif Mushtaq

Supervisor: _____

Dr. Adélio Mendes, Professor Catedrático,

Faculty of Engineering of the University of Porto (FEUP), Portugal.

Co-Supervisor: _____

Dr. Donald R. Sadoway, John F. Elliott Professor of Materials Chemistry,

Massachusetts Institute of Technology (MIT), USA

Ph.D. Thesis developed in the frame of the MIT Portugal Program

© 2022 Kashif Mushtaq, All rights reserved.

The Ph.D. thesis was developed at the following institutions.









Funding:







Acknowledgments

The work presented in the Ph.D. thesis results from the doctoral program in the sustainable energy system through the MIT Portugal Program which is an international collaboration between Portuguese Universities and the Massachusetts Institute of Technology (MIT). It is an honor to work under the supervision of two renowned and elite experts in the field, Prof. Dr. Adélio Mendes from the Laboratory for Process Engineering, Biotechnology, and Energy – LEPABE, Faculty of Engineering of the University of Porto, Portugal, and Prof. Dr. Donald R. Sadoway from Group Sadoway Laboratory, Department of Material Science and Engineering – DMSE, Massachusetts Institute of Technology – MIT, USA. MIT Portugal Program is acknowledged for providing the platform for this collaboration. Fundação para a Ciência e a Tecnologia – FCT, is acknowledged for their continous support to the scholar.

Many thanks to Professor Adélio Mendes for his guidance and encouragement not only in the professional but also in other walks of life. He is truly a mentor who understands his students and supports them at every step. He taught me not only to love science but also to strive to become an entrepreneur by transforming research into products.

My gratitude to Prof. Donald R. Sadoway for giving me this opportunity to work in his research group. His discussions in weekly meetings changed my thought process and teach me a new approach to handling the problems. I am truly thankful for his continuous encouragement and will always remember his words that if you want to develop something costing dirt-cheap then make it from dirt. He has taught me what it means to be a scholar and a scientist. I am thankful to all the members of Group Sadoway.

Thanks to my colleagues at Group Sadoway, MIT. Especially, Ji Zhao, and Norbert Weber, who teach me a lot, and will always acknowledge their support during my research work. I appreciate the numerous intriguing chats in which these fellows patiently explained the complexities of batteries.

This journey was influenced by numerous companions who contributed to my growth, broaden my horizons, and will remain an inspiration for the rest of my life. I would like to take this opportunity to appreciate all of them.

I am thankful to my lab colleagues who are no less than my friends. First of all, big thanks to Sofia Delgado and Márcia Santos, for the amazing teamwork to perform experiments and fruitful discussions for our articles. Thanks to João Azevedo, Tiago

Legarteira, André Monteiro, Elisabete, Daniela, Mafalda, Paula Dias, Tania Lopes, and D. Fátima Faustino. Special thanks to Catia Azenha and Carlos Almeida for bearing me as a neighboring colleague and to be very helpful in the lab. I would like to appreciate the work of Célia Couto, her continuous support for all the administrative tasks of this thesis, and her precious advice that assisted me with easy adaptability in Portugal.

To begin with family, a million thanks to my spouse, Aqsa Kashif. The success of this work is not possible without her love, patience, and encouragement. My son, Muhammad Musab Kashif, was just one year old at the start, and honestly speaking, my kid and thesis grew up together hand-in-hand. Later our family was blessed with my lovely daughter, Aima Kashif. She's the naughty one but always boosts me up after a long day at work.

Indeed, my parents have the most influence on my life and I will be eternally grateful to them for molding me into the person I am today. Thank you for nurturing my personality and keeping me motivated, Mushtaq Ahmed (Abu je) and Azra Mushtaq (Ammi jan).

My lifeline is the never-ending support from my beloved siblings Atif bhai, and Ayesha. The limitless support and love from my younger sibling Wasif Mushtaq, and our long discussions which always end up with big laughter have always kept me energized. A sister from another mother, Isma Irshad, deepest thanks for being there always, and our binge-watching sessions are unforgettable, especially during the difficult times of pandemic lockdowns.

Friendship is another word for love and understood this phrase from our gang of the MIT Portugal Program Dania, Daniela, Fatima, Shabnam, Marco, Lotfi, and Kamal. Every moment spent with friends is not less than a jewel. Cheers to my wonderful friends, Asif bhai, Zahid bhai, Mushtaq bhai, Qasim bhai, Niaz, and Mudassir. Asad Ali Zaidi, Ammar Qureshi, you guys have a special place in my heart. Last but not the least, special heartiest thanks to Karla and Behzad, who joined the journey lately but stayed there until the happy ending.

Sincere appreciation to the people of the European and American continent who supported me along this process, thanks for your hospitality!

Thank you all so much for being a part of this journey, and the chronicle of my life!

Preface

Kashif Mushtaq acknowledges MIT Portugal Program and FCT for the doctoral grant - PD/BD/128041/2016 and for extension to mitigate impacts of pandemic (Covid-19) - COVID/BD/151598/2020.

This work was financially supported by the research unit of Group Sadoway Laboratory, Department of Materials Science and Engineering, Massachusetts Institute of Technology, 77 Massachusetts Avenue, Cambridge, MA, 02139-4307, United States.

It was also financially supported by: i) LA/P/0045/2020 (ALiCE), UIDB/00511/2020 and UIDP/00511/2020 (LEPABE), funded by national funds through FCT/MCTES (PIDDAC); ii) projects POCI-01-0145-FEDER-016387 – "SunStorage" and POCI-01-0145-FEDER-030510 – "Sunflow" funded by FEDER funds through COMPETE2020 – Programa Operacional Competitividade e Internacionalização (POCI) and by national funds (PIDDAC) through FCT/MCTES; and iii) projects POCI-01-0145-FEDER-030223 – "Polysol", POCI-01-0247-FEDER-046109 – "Batteries 2030" and POCI- 01-0247-FEDER-046846 – "BluEnergy" co-funded by Operational Programme for Competitiveness and Internationalisation (COMPETE 2020), under the Portugal 2020 Partnership Agreement, through the European Regional Development Fund (ERDF).

Blank Page

Abstract

The transition toward a climate-neutral society requires fundamental changes in the way energy is being transformed, stored, and used. The implementation of renewable energy systems and electric battery vehicles encourages the development of energy storage systems, especially batteries. The motivation of this thesis is the development of non-aqueous electrochemical energy storage technologies offering high energy densities, such as liquid metal displacement battery (LDB) and non-aqueous redox flow battery (NAqRFB).

The evolution of an electricity-based society needs disruptive ideas that can enable the creation of sustainable batteries for the future. An innovative idea was reported about the discovery of a new type of battery named LDB, which is based on molten metal as the electrode and molten salt as the electrolyte. This cell uses a novel concept of a porous faradaic membrane instead of the traditional ion-selective ceramic membrane. Though a very promising new technology, it needs to address the self-discharge effect. This thesis studied the use of PbO as an additive to the electrolyte for reducing the diffusion coefficient of Pb ions. PbO acts as a supplementary barrier and complements the function of the faradaic membrane. The remedial actions allowed to increase the columbic efficiency of the cell from 92% to 97% without affecting the voltage efficiency.

The crossover of redox species through the membrane is problematic since it results in capacity loss and lower coulombic efficiency. It needs to be readily quantified before any commercial application of the NAqRFB. An *in-situ* electrochemical method, developed by the research group for redox flow batteries, was adapted for NAqRFB and validated through an *ex-situ* method and performance characterization. As a membrane diagnosis tool, this technique allows *in-situ* determination of crossover without the need for disassembling the devices.

The availability of an efficient membrane for the non-aqueous electrolytes is a challenging problem. Porous separators are currently being used but they display low selective transport for the ionic species and redox species of negolyte / posolyte get short-circuited. Thicker ion-exchange membranes are being used to avoid these disadvantages but at the cost of higher ohmic losses. Interestingly, these disadvantages can be overcome by incorporating a thin ion-exchange (IE) layer sandwiched between pair of microporous membrane separators. A composite membrane was developed and used for the rest of the study presented here as a proof-of-concept.

A meticulous study was carried out to understand the sudden capacity loss and noticeable degradation of non-aqueous vanadium flow batteries. The presence of moisture and/or oxygen on both the electrolyte and carbon felts was confirmed to trigger a parasitic reaction that favors the formation of irreversible $VO(acac)_2$, which in turn hinders the performance of NAqRFBs. The main sources for this parasitic reaction were studied and it was found that one of the culprits refers to the use of oxygen-rich electrodes. An innovative technique was deployed to fix this degradation mechanism and thus increase the lifetime of the battery, which consists of using a tailored and microstructural carbon felt surface modification based on a hydrogen reduction treatment.

Pristine carbon felt electrodes, available commercially, often display high overpotentials when running the electrochemical reactions in a non-aqueous medium. Hence, it is crucial to develop stable high-performance electrodes, offeringg low activation overpotentials, low ohmic losses, and high porosity for a uniform distribution of the electrolyte. This study acknowledges the influence of using attached carbon-based nanoparticles to the fibers of the supporting carbon felt electrodes. Post-mortem analysis revealed that the nanoparticles remained attached to the fibers even after intense charge-discharge cycling.

The market leader Li-ion battery (LIB) technology demands the use of critical raw materials. In contrast, Redox Flow Battery (RFB) can use different electrolyte chemistries with minimal adaptations, making them suitable to take advantage of locally available raw materials. An aluminum-ion-based NAqRFB is introduced for the first time, which is a widely accessible raw material.

Present commercial RFB technology is based on the redox reactions of electroactive metals, which are constrained by material abundance, cost, and environmental issues. These issues are prompting scientists to look into organic-based technologies as potential metal-free battery alternatives. NAqRFB opens the window of using redox species outside the electrochemical stability range of aqueous electrolytes. The use of 1,4 Naphtoquinone ions for redox flow batteries was rarely addressed. The novel NQ-ion-based non-aqueous redox flow battery was introduced in this study as a proof-of-concept.

Resumo

A transição para uma sociedade com pegada carbónica reduzida requer mudanças fundamentais no processo de transformação, armazenamento e utilização de energia. A implementação de sistemas de energia renovável e veículos elétricos incentivam o desenvolvimento de sistemas para o armazenamento de energia, especialmente baterias. O principal objetivo desta dissertação é desenvolver tecnologias para o armazenamento de energia eletroquímica, não aquosa, que oferecem altas densidades de energia, como bateria de deslocamento de metal líquido (LDB) e bateria de fluxo redox não aquosa.

A evolução para uma sociedade mais dependente da eletricidade precisa de ideias disruptivas que possam permitir a criação de baterias sustentáveis para o futuro. Uma ideia inovadora na área das baterias são as LDB's. O funcionamento desta é baseado num metal fundido como elétrodo e sal-fundido como eletrólito. Esta célula utiliza um novo conceito, uma membrana faradaica porosa em vez da tradicional membrana cerâmica íon-seletiva. Embora seja uma nova tecnologia bastante promissora, esta precisa de se focar no efeito de auto-descarga. Esta tese estuda a utilização de PbO como um aditivo para o eletrólito para reduzir o coeficiente de difusão dos íons de Pb. O PbO atua como barreira suplementar e complementa a função da membrana faradaica. As ações corretivas permitiram aumentar a eficiência coulombica da célula de 92% para 97%, sem afetar a eficiência da tensão.

O cruzamento de espécies redox através da membrana é problemático, pois leva à perda de capacidade e menor eficiência coulombica. O cruzamento precisa ser quantificado antes de qualquer aplicação comercial da bateria de fluxo redox não aquosa (NAqRFB). Um método eletroquímico *in-situ*, que foi desenvolvido pelo grupo de pesquisa para baterias de fluxo redox, foi adaptado para NAqRFB e validado através de um método *ex-situ*, assim como a caracterização do seu desempenho. Como ferramenta de diagnóstico de membrana, esta técnica permitiu a determinação *in-situ* do cruzamento sem a necessidade de desmontar os dispositivos.

A disponibilidade de uma membrana eficiente para os eletrólitos não aquosos é um problema desafiador. Os separadores porosos são utilizados atualmente, no entanto exibem um transporte seletivo de espécies iônicas muito baixoe espécies redox de negolito / posólito, entram em curto-circuito. Membranas de troca iônica mais espessas estão a ser utilizadas para evitar esses problemas, mas com elevado custo de perdas ôhmicas. Curiosamente, essas desvantagens podem ser superadas pela incorporação de

uma fina camada de troca iônica (IE) ensanduichada entre um par de separadores de membrana microporosa. A membrana composta foi desenvolvida e utilizada no restante trabalho como uma prova de conceito.

Um estudo meticuloso foi realizado para entender a perda repentina de capacidadee a degradação percetível de baterias de fluxo de vanádio não aquosas. A presença de humidade e/ou oxigênio, tanto no eletrólito quanto nos feltros de carbono, desencadeia uma reação parasitária. Esta favorece a formação de $VO(acac)_2$ irreversível que por sua vez dificulta o desempenho das NAqRFBs. As principais fontes dessa reação parasitária foram estudadas e constatou-se que um dos principais causadores são os elétrodos ricos em oxigênio. Uma técnica inovadora foi implementada para corrigir esse mecanismo de degradação e, assim, aumentar a vida útil da bateria. Esta técnica consiste na utilização de uma modificação de superfície de feltro de carbono personalizada e microestrutural, com base num tratamento térmico de redução de hidrogênio.

Os elétrodos de feltro de carbono puro, disponíveis comercialmente, geralmente exibem altos sobrepotenciais ao executar as reações eletroquímicas em meio não aquoso. Portanto, é crucial desenvolver elétrodos estáveis de alto desempenho, apresentando baixos sobrepotenciais de ativação, baixas perdas ôhmicas e elevada porosidade, para uma distribuição uniforme do eletrólito. Este estudo reconhece a influência do uso de nanopartículas à base de carbono, aderidas às fibras dos elétrodos de feltro de carbono de suporte. A análise *post-mortem* revelou que as nanopartículas continuaram juntas às fibras mesmo após intensos ciclos de carga e descarga.

A tecnologia de bateria líder de mercado (bateria Li-ion) exige a utilização de matérias-primas críticas. Por outro lado, uma bateria de fluxo redox (RFB) usa diferentes químicos eletrolíticos com adaptações mínimas, tornando-as adequadas para aproveitar as matérias-primas disponíveis localmente. Uma NAqRFB com base em íons de alumínio é introduzida pela primeira vez, o que se trata de uma matéria prima de fácil acesso.

A tecnologia RFB comercial atual é baseada nas reações redox de metais eletroativos, que são limitados pela abundância de material, custo e questões ambientais. Estes problemas, conduzem os cientistas para tecnologias com base orgânica como possível alternativa para bateria sem metal. A NAqRFB abre a janela para a utilização de espécies redox fora da faixa de estabilidade eletroquímica de eletrólitos aquosos. Uma solução raramente estudada é a utilização de íons 1,4 Naftoquinona para baterias, que foi introduzida neste estudo como uma prova de conceito.

Version for indexing in ProQuest

Energy storage: development of non-aqueous redox flow and liquid metal batteries

by

Kashif Mushtaq

Submitted to the Faculty of Engineering of the University of Porto
on May 26th, 2022 in partial fulfillment of the requirements for the degree of
Doctor of Philosophy in Sustainable Energy Systems

ABSTRACT

The experimental study was performed by targeting high energy density storage systems, such as liquid metal displacement batteries (LDB) and non-aqueous redox flow batteries (NAqRFB). The literature review highlighted key challenges to be targeted in these domains. (i) LDB is a promising technology but needs mitigation of the self-discharge effect. It was addressed by complementing the faradaic function of the membrane through reversible side reactions by the addition of PbO, which enabled it to achieve the highest reported columbic efficiency of 97 %. The remaining challenges are related to NAqRFB: (ii) Lack of facile technique to quantify crossover through membranes and an *in-situ* diagnostic tool was developed in this study. (iii) Composite membrane having layers of the microporous separator and ion-exchange layer was developed to address the lack of highly conductive and selective membranes for non-aqueous electrolytes. (iv) Presence of abundant oxygen condemns the performance of NAqRFB and parasitic reactions adversely affect the stability of the battery and leads to high capacity fade. The hydrogen reduction thermal treatment was implemented to develop oxygen-less electrodes. (v) Carbon felt electrodes have good mechanical strength and compressibility but they offer poor kinetics and low electrochemical surface area. Coating of nano-particles was performed using a robust drop-casting method, which improved the performance of the NAqRFB. (vi) Higher electrochemical window for operation of non-aqueous electrolytes allowed to broaden the search toward finding low-cost and abundant redox species for NAqRFBs. Novel batteries having aluminum (Al^{3+}/Al) as negolyte and coupled with posolyte of $M(acac)_3$, M = Cr, Mn, V, Fe, and Fc were introduced as a proof-of-concept. (vii) Similarly, novel batteries having bio-inspired metal-free negolyte based on Naphthoquinone and coupled with other posolytes of $M(acac)_3$, M = Cr, Mn, Fe were developed as a proof-of-concept.

Supervisor: Dr. Adélio Mendes, Professor Catedrático, FEUP, Portugal
Co-supervisor: Dr. Donald R. Sadoway, Professor, MIT, USA

Blank Page

Table of Contents

Acknowledgments v
Preface vii
Abstract ix
Resumo xi
Table of Contents xv
List of Figures xx
List of Tables xxvi
List of Acronyms xxviii
List of Symbols xxix
List of Publications xxxi
1. Introduction 2
1.1 Energy Storage – A necessity rather than a privilege 4
1.2 Bibliometricic Analysis 6
1.2.1 Research streamline of Redox Flow Batteries 6
1.2.2 Research trends 7
1.2.3 Countries leading the RFB research 7
1.3 Electrochemistry of Redox flow battery 10
1.4 Electrochemical Cells 11
1.4.1 Transition to the non-aqueous electrochemical system 12
1.5 Redox Species 15
1.5.1 Metal-based Redox Species 17
1.5.2 Metal-free Redox Species 21
1.6 Solvents 22
1.6.1 Operational Temperature Range 23
1.6.2 Electrochemical Window 23
1.6.3 Solubility 23
1.6.4 Viscosity 25
1.7 Supporting Electrolytes 26
1.8 Membranes 27
1.8.1 Anion and Cation Exchange Membranes (AEMs and CEMs) 28
1.8.2 Size Exclusion Membranes (Porous membranes) 30
1.9 Electrodes 30

1.10 Research Strategy for Thesis 33
Part I 35
2. Self-discharge mitigation of liquid metal displacement battery 36
2.1 Introduction 38
2.2 Materials and Experimental Methods 41
2.2.1 Chemicals 41
2.2.2 Preparation of Membrane 41
2.2.3 Assembly and assessment of the liquid displacement cell 41
2.3 Results and discussion 42
2.3.1 Mitigation of self-discharge 42
2.3.2 Impact of mitigation on the impedance of the cell 47
2.3.3 Impact of mitigation on the polarization of the cell 48
2.4 Conclusion 51
Part II 53
3. *In-situ* crossover diagnostics to assess membrane efficacy 54
3.1 Introduction 56
3.2 Experimental Methods 60
3.2.1 Electrolytes 60
3.2.2 Membranes 61
3.2.3 Treatment of electrodes 61
3.2.4 Cyclic Voltammetry of redox species 62
3.2.5 *In-situ* and *Ex-situ* measurements for the crossover of probing species 62
3.2.6 NAqRFB assembly and assessment 63
3.3 Results and Discussions 63
3.3.1 Feasibility of Ferrocene as probing species 63
3.3.2 Crossover of probing species by different membranes 64
3.3.3 *Ex-situ* validation for the crossover of probing species 68
3.3.4 Characterization of $V(acac)_3$ as redox species 69
3.3.5 Impact of crossover on the performance of a flow-cell 71
3.4 Conclusion 75
4. Composite membranes 78
4.1 Introduction 80
4.2 Experimental 81
4.2.1 Electrolytes 81

4.2.2 Electrodes 82
4.2.3 Membranes 82
4.2.4 Cyclic Voltammetry of redox species 83
4.2.5 *In-situ* crossover measurement of redox species 83
4.2.6 NAqRFB assembly and assessment 84
4.3 Results and Discussions 84
4.3.1 Battery electrolyte characterization 84
4.3.2 Ionic conductivity of membranes 86
4.3.3 Membrane conductivity, crossover of redox species, and selectivity 87
4.3.4 Impact of composite membrane on the performance of redox flow cell 90
4.3.5 Impedance and polarization analysis 92
4.3.6 Linking selectivity of membrane and flow cell efficiency 96
4.4 Conclusion 97
5. Parasitic reaction free electrodes 100
5.1 Introduction 102
5.2 Experimental Methods 103
5.2.1 Materials 103
5.2.2 Preparation of the electrodes 104
5.2.3 Morphology characterization 104
5.2.4 Electrochemical characterization 104
5.3 Results and discussions 105
5.3.1 Environmental moisture and oxygen effect on the stability of redox species 105
5.3.2 Electrochemical Surface Area of modified electrodes 107
5.3.3 Impact of surface modifications on the redox reaction reversibility 110
5.3.4 Electrode stability on the presence of oxygen-rich/free surface 110
5.3.5 Morphology characterization applied to prepared electrodes 112
5.3.6 Performance of the redox flow cell 114
5.4 Conclusion 118
6. Carbon felt electrodes augmented with nanoparticles 122
6.1 Introduction 124
6.2 Experimental Methods 126
6.2.1 Materials 126
6.2.2 Preparation of Electrodes 126
6.2.3 Cyclic Voltammetry 127

6.2.4 Physicochemical characterization 127
6.2.5 Redox flow-cell assembly and electrochemical assessment 127
6.3 Results and discussions 128
6.3.1 Characterization of electrolyte 128
6.3.2 Characterization of augmented electrodes 129
6.3.3 Performance of electrodes in the redox flow cell 133
6.3.4 Optimization of Nafion ionomer concentration in the CNT-electrodes 137
6.3.5 Application of noble metals as catalyst 138
6.3.6 Storage capacity fade 141
6.4 Conclusion 141
7. Aluminum ion based NAqRFB 146
7.1 Introduction 148
7.2 Experimental Methods 150
7.2.1 Materials 150
7.2.2 Cyclic Voltammetry 150
7.2.3 Redox flow-cell assembly and assessment 151
7.3 Results and discussions 151
7.3.1 Electrochemical characterization of electrolyte 151
7.3.2 Battery cycling performance 154
7.3.3 Storage capacity fade 155
7.4 Conclusion 160
8. Bio-inspired eco-friendly negolyte 164
8.1 Introduction 166
8.2 Experimental Methods 168
8.2.1 Materials 168
8.2.2 Cyclic Voltammetry 168
8.2.3 Redox flow-cell assembly and assessment 168
8.3 Results and discussions 169
8.3.1 Electrochemical characterization of electrolyte 169
8.3.2 Battery cycling performance 172
8.3.3 Storage capacity fade 174
8.4 Conclusion 178
9. Retrospectives, Conclusions, and Perspectives 180
9.1 Retrospectives 180

9.2 Conclusions 181
9.3 Perspectives 183
10. References 185
11. Supplementary Information I
11.1 Supplementary Information for Chapter 2 I
11.2 Supplementary Information for Chapter 3 III
11.3 Supplementary Information for Chapter 4 IV
11.4 Supplementary Information for Chapter 5 V
11.5 Supplementary Information for Chapter 6 IX
11.6 Supplementary Information for Chapter 7 XVIII
11.7 Supplementary Information for Chapter 8 XXIV

List of Figures

Figure 1.1 Balance between electricity supply and demand ([10]). 5

Figure 1.2: Classification of electricity storage technologies (Source: [11]) 5

Figure 1.3: The increasing number of publications in the field of redox flow batteries (Source: Web of Science). 8

Figure 1.4: Research streamline of redox flow batteries 8

Figure 1.5 Leading countries in redox flow batteries research. 10

Figure 1.6 Schematic of a redox flow battery in a generalized form having dummy redox species of $A^{3+/2+}$and $C^{5+/4+}$. 14

Figure 1.7 Three electrode cell configuration for cyclic voltammetry. (a) 50 ml cell connected to the Autolab potentiostat (b) Cell is assembled with WE = glassy carbon electrode from Metrohm having diameter of 3 mm (c) Cell is assembled with WE = carbon felt electrode as sample-to-study. Acronyms: WE = Working electrode, RE = Reference electrode, CE = Counter electrode. 14

Figure 1.8 3D Model of the in-house made redox flow cell used for all the experiments. Half-cells are symmetric up to the membrane and the figure is showing exploded view of only the half side. 15

Figure 1.9 The experimental setup of a single cell of the redox flow battery. Posolyte and negolyte is supplied from the reservoir beside the cell and circulated using the peristaltic pump at the same flow rate. (a) Reservoir size is 100 ml (b) Reservoir size is 25 ml. Acronyms: WE = Working electrode, CE = Counter electrode. 15

Figure 1.10 Redox flow battery (RFB) classification based on solvent and redox species. Acronyms: ILs = Ionic liquids, DES = Deep eutectic solvents. The scope of this thesis is limited to green-coloured branches of the RFB classification. 16

Figure 1.11 Metal-based redox species with different ligands: (a) acetylacetonate complexes, (b) 2,2-bipyridine complexes, (c) metallocene, (d) dithiolate vanadium complex, (e) tetradentate nickel complex, and (f) ACN–copper complex. (Source: [12]) 22

Figure 1.12 Structures and redox reactions of (a) AQ, (b) PTIO, (c) TEMPO, and (d) N-methylphthalimide during oxidation and reduction. (Source: [12]) 24

Figure 1.13 The supporting electrolyte, solvent, and nature of the electrode influence the electrochemical window which is measured in this document using cyclic voltammetry. Acronyms: Sodium perchlorate ($NaClO_4$), Tetraethylammonium tetrafluoroborate ($TEABF_4$), Tetramethylammonium hexafluorophosphate ($TEAPF_6$), Tetrabutylammonium perchlorate (TBAP), N,N-Dimethylacetamide (DMA), Propylene carbonate (PC), Acetonitrile (ACN). 24

Figure 2.1 Schematic of a Liquid Displacement Battery. The detailed view shows the ion transport and faradaic reaction across a porous electronically conductive membrane. 40

Figure 2.2 LiCl - KCl pseudo-binary phase diagram. Liquid metal displacement battery used molten salt electrolyte in eutectic mole composition of LiCl : KCl = 40.8 % : 59.2 %. Adapted from [111]. 40

Figure 2.3 Assembly of the liquid displacement battery having the faradaic membrane. 43

Figure 2.4 Charge-discharge cycling for activation phase in three steps. Step 1: Capacity of 25 mAh at a constant current of 50 mA for 0.5 h. Step 2: Capacity of 250 mAh at a constant current of 100 mA for 2.5 h. Step 3: Capacity of 500 mAh at a constant current of 200 mA for 2.5 h (Inset shows η_{CE}, η_{VE}, η_{EE}, and capacity for the cycles respectively). 45

Figure 2.5 The result of the self-discharge test without the addition of lead oxide and after the addition of 2 molar percentage of PbO into the composition of the electrolyte. 46

Figure 2.6 Charge discharge cycling of the liquid displacement cell having a capacity of 500 mAh at a current of 200 mA: (a) Control experiment without the addition of PbO. (b) After the addition of 2 molar percentage of PbO into the electrolyte. (c) Efficiencies of both experiments. (d) Comparison of capacity vs. the potential for the best performing charge-discharge cycle. 46

Figure 2.7 Impedance curve obtained by electrochemical impedance spectroscopy in the frequency range from 2.5 kHz to 1 Hz having an amplitude of 10 mV. The inset shows the equivalent circuit model used for curve fitting. 49

Figure 2.8 Polarization curves while charging the cell from 0.4 V to 2.2 V. The solid lines represent voltage as a function of current density and the dotted lines represent power as a function of current density ($mA \cdot cm^{-2}$). The active area of the cell is 2 cm^2. 50

Figure 2.9 Polarization curves while discharging the cell from 1.8 V to 0.3 V at a scan rate of 10 $mV \cdot s^{-1}$. The solid lines represent voltage as a function of current density and the dotted lines represent iR-free curves. 50

Figure 3.1 Schematic for the principles of crossover measurements in non-aqueous redox flow battery having ferrocene as probing species, $TEABF_4$ as supporting electrolyte, and acetonitrile as solvent. 59

Figure 3.2 (a) Cyclic voltammogram of Ferrocene as probing species in a three-electrode setup having glassy carbon as the working electrode, platinum wire as the counter electrode, and Ag/Ag^+ as the non-aqueous reference electrode. (b) Voltammogram displayed a nearly negligible constant current of having an average of ca. 0.00787 $mA \cdot cm^{-2}$. 65

Figure 3.3 Crossover molar flux rate of ferrocene as probing species. LSV voltammograms were performed at 100 $\mu V \cdot s^{-1}$ from cells assembled with each of the membranes. 66

Figure 3.4 Crossover molar flux of $V^{4+/3+}$ as probing species. LSV voltammograms were performed at 50 $\mu V \cdot s^{-1}$ from cells assembled with each of the membranes. This gives crossover molar flux of 8.82 $\mu mol \cdot h^{-1} \cdot cm^{-2}$ and 4.65 $\mu mol \cdot h^{-1} \cdot cm^{-2}$ for Nafion 115 and Nafion 117 respectively. The trend is similar and almost twice the molar flux difference between Nafion 117 and Nafion 115, like the measurement taken using the ferrocene as probing species. 68

Figure 3.5 (a) UV-vis spectrum for samples collected after each LSV measurement. Inset shows the analysis of data from calibration curves leading to the determination of the molar absorption coefficient ($\varepsilon = 89.747\ M^{-1} \cdot cm^{-1}$). (b) UV-vis spectrum is used as calibration curves to follow the Beer-Lambert equation and to determine the value of epsilon. 70

Figure 3.6 Comparison between the permeance to ferrocene and the electrochemical crossover for the selected cation and anion membranes. Lines were added for guiding the eyes. 71

Figure 3.7 (a) Cyclic voltammogram as a function of scan-rate in the range of 20 $mV \cdot s^{-1}$ to 100 $mV \cdot s^{-1}$ of V^{2+}/V^{3+} and V^{3+}/V^{4+} (b) Peak potentials and redox potential for the V^{2+}/V^{3+} and V^{3+}/V^{4+}

redox couple, (c) Peak currents and their current ratios (I_c/I_a), (d) Randles-Sevcik analysis for $V(acac)_3$ oxidation and reduction. 72

Figure 3.8 Charge-discharge curves at 2 $mA \cdot cm^2$ at flowrate of 20 $cm^3 \cdot min^{-1}$ having nonaqueous electrolyte (Acetonitrile + 0.05 M $V(acac)_3$ + 0.1 M $TEABF_4$) (a) and (b) Three hour expcerpt of charge-discharge cycles of cell having Nafion 117 and Nafion 115 (c) Coulombic, potential and energy efficiency for each cycle (d) Capacity for each cycle during charging and discharging and indicating capacity loss of 34% and 55% in the cell having Nafion 117 and Nafion 115 respectively. 74

Figure 3.9 (a) Electrochemical impedance curve (-Nyquist Plot) for the cells having Nafion 117 and Nafion 115 (b) Polarization curve analysis at a scan rate of 20 $mV \cdot s^{-1}$ for the cells having Nafion 117 and Nafion 115. 75

Figure 4.1 Sketch of a non-aqueous redox flow using the described composite membrane. 81

Figure 4.2 (a) Cyclic voltammogram as a function of scan-rate in the range of 20 $mV \cdot s^{-1}$ to 100 $mV \cdot s^{-1}$ of V^{2+}/V^{3+} and V^{3+}/V^{4+} (b) Peak potentials and redox potential for the V^{2+}/V^{3+} and V^{3+}/V^{4+}redox couple. (c) Peak currents and their current ratios (I_c/I_a). (d) Randles-Sevcik analysis for $V(acac)_3$ oxidation and reduction. 85

Figure 4.3 Conductivity of the membranes. Composite membranes are designated as C45-HP-C45 and C25-HP-C25. 86

Figure 4.4 Crossover measured current density at the scan rate of 50 $\mu V \cdot s^{-1}$ and flow rate of 3 $ml \cdot min^{-1}$. Working electrode having blank electrolyte consisting of 0.1 M $TEABF_4$ + Acetonitrile and counter electrode having electrolyte with active species of 0.02 M $V(acac)_3$ + 0.1 M $TEABF_4$ + Acetonitrile. 89

Figure 4.5 The conductivity of membranes as a function of the permeation diffusivity (D_A) of vanadium ions. The conductivity values are obtained from Figure 4.3 and D_A numbers are derived from Figure 4.4. 90

Figure 4.6 Charge-discharge cycling of redox flow cell having vanadium based non-aqueous electrolyte - 0.02 M $V(acac)_3$ + 0.1 M $TEABF_4$ + Acetonitrile - flowing at 30 $ml \cdot min^{-1}$ operating at C_{rate} = 0.84C (a) coulombic efficiency (b) voltage efficiency (c) energy efficiency (d) Excerpt from the 50 cycles performed on composite membrane C45-HP-C45 (e) Excerpt from the 50 cycles performed on composite membrane C25-HP-C25 (f) Excerpt from the 50 cycles performed on nafion membrane N115. 93

Figure 4.7 Impedance spectroscopy performed after charge-discharge cycling at SOC = 50 % (OCP = 1.5 V), electrolyte flowing at 30 $ml \cdot min^{-1}$, and having an active area of 7.29 cm^2. The -Nyquist plotted as scatter plot and lines represent the corresponding equivalent circuit fitting on each curve. 94

Figure 4.8 Polarization curves for the NAqRFB while sweeping in the range of 0.1 V to 2.5 V at the scan rate of 20 $mV \cdot s^{-1}$ and electrolyte flowing at 30 $ml \cdot min^{-1}$. 95

Figure 4.9 Ideal trend of round trip energy efficiency as a function of membrane selectivity. 96

Figure 5.1 Voltammogram using 3-electrode cell configuration (a) for the non-aqueous electrolyte having redox species $V(acac)_3$ without any contamination (b) highlighting the effect of gradually adding moisture (water) on the redox couples a) V^{+2}/V^{+3} and V^{3+}/V^{4+} depicting the parasitic product $VO(acac)_2$ (c) V^{3+}/V^{4+} at different moisture concentrations (100 ppm – 50k ppm) (d)

Degradation test was performed from inert nitrogen (N_2) environment to oxygen (O_2) saturation for 20 minutes and then repeated with saturation for 4 hours, first with O_2 and then recovered by N_2. 107

Figure 5.2 Cyclic voltammograms for screening the effect a) of the heat treatment environment in Pristine (P), Pristine + Hydrogen treated @ 400 °C (PH), Pristine + Oxygentreated @ 400 °C (PO), Pristine + Oxygen + Hydrogen treated @ 400 °C (POH) carbon felts at 10 $mV \cdot s^{-1}$; b) the effect of increasing the temperature from 400 °C in PH and POH to 700 °C in PH2 and POH2 at 10 $mV \cdot s^{-1}$. 108

Figure 5.3 Comparison of electrochemical surface areas obtained by CV analysis from Randles-Sevick study for P, PH, PH2, PO, POH, and POH2 carbon felts. 109

Figure 5.4 Loss of reversibility (I_{pa} / I_{pc}) ratio after AST/degradation test for PO and POH2. ... 111

Figure 5.5 FTIR performed on samples of carbon felt. Legend: Pristine (P), Pristine + Oxygen treatment (PO), Pristine + Hydrogen treatment at 400 °C (PH), Pristine + Hydrogen treatment at 700 °C (PH2), PO + Hydrogen treatment at 400 °C (POH), and PO + Hydrogen treatment at 700 °C (POH2). 112

Figure 5.6 SEM images of carbon felts at 12500 X; a) pristine (P), b) Pristine + Hydrogen treatment at 400 °C (PH), c)), Pristine + Hydrogen treatment at 700 °C (PH2), d) Pristine + Oxygen treatment (PO) d), PO + Hydrogen treatment at 400 °C (POH), and f) PO + Hydrogen treatment at 700 °C (POH2). 113

Figure 5.7 Performance of V-NAqRFB assembled with prepared electrodes operating at the flow-rate of 30 ml min^{-1} at the C-rate of 1.35C i.e. 6.2 mA cm^{-2} (a) Coulombic Efficiency (η_{CE}) (b) Voltage efficiency (η_{VE}) (c) Energy Efficiency (η_{EE}) (d) Capacity for each cycle. 117

Figure 5.8 Impedance curves obtained through electrochemical impedance spectroscopy performed at E_{OCP} = 1.5 V from 250 kHz to 100 mHz with an amplitude of 10 mV. (a) Performed before charge-discharge cycling (b) Performed after charge-discharge cycling. 118

Figure 5.9 Polarization curves obtained while linear sweeping in the range of 0.1 V to 2.5 V at the scan rate of 20 mV s^{-1} and electrolyte flowing at 30 ml min^{-1} 118

Figure 6.1 Cyclic voltammogram in a 3-electrode configuration cell, using platinum wire as a counter electrode, and Ag/Ag^+ as a reference electrode. The electrolyte was 0.1 M $TEABF_4$ + 0.02 M $V(acac)_3$ + Acetonitrile for V^{2+}/V^{3+} reaction i.e. for negolyte. (a) Measurements at various scan rates for the same sample of CNT 30 (b) Measurements at 20 $mV \cdot s^{-1}$ for each sample. 130

Figure 6.2 Surface morphology of carbon fibers of carbon felts with rGO nanoparticles at (a) 340 x (b) 2500 x and (c) 7600 x magnification; graphene nanoparticles at (c) 340 x (d) 2500 x and (e) 7600 x magnification and Ketjen at (f) 340 x (g) 2500 x and (h) 7600 x magnification. The loading of the modified carbon felts with nanoparticles was maintained at 11 % of the total weight with an I/C of 30 wt. %. 132

Figure 6.3. Surface morphology of carbon fibers of carbon felts with CNT nanoparticles at (a) 340 x (b) 2500 x and (c) 7600 x magnification; Vulcan XC7 nanoparticles at (c) 340 x (d) 2500 x and (e) 7600 x magnification and the pristine carbon felt at (f) 340 x (g) 2500 x and (g) 7600 x magnification. The loading of coated nanoparticles was maintained at 11 % of the total weight with an I/C of 30 wt. %. 133

Figure 6.4 Charge discharge cycling of the NAqRFB-cell assembled with each sample of electrodes coated with nanoparticles of Vulcan Carbon Black - V, Ketjen Carbon Black - K,

Carbon Nanotubes - CNT, Graphene Oxide - rGO and Graphene - G. Results are compared with Pristine electrodes - P. (a) Coulombic Efficiency, (b) Voltage Efficiency, (c) Energy Efficiency, (d) Recorded potential of 2nd cycle as a function of capacity. 136

Figure 6.5 Impedance curves measured after CDC through electrochemical impedance spectroscopy (EIS) in the range of 100 mHz to 250 kHz at an amplitude of 10 mV while the cell was maintained at E_{OCP} = 1.5 V. 137

Figure 6.6 iV-curves of the NAqRFB-cell (a) Polarization in charging mode was performed before CDC through scanning at 10 $mV \cdot s^{-1}$ from 0.1 V to 2.5 V; (b) Polarization in discharging mode was performed after CDC by scanning at 10 $mV \cdot s^{-1}$ from 2.5 V to 0.1 V. 137

Figure 6.7 Charge discharge cycling for the CNT-electrode samples. Electrodes were prepared using ink having 5 wt. %, 15 wt. %, and 30 wt. % concentration of Nafion ionomer. (a) Coulombic efficiency, (b) Voltage efficiency, (c) Energy Efficiency, (d) Charge-discharge curve for the second cycle. 139

Figure 6.8 NAqRFB equipped with MWCNT based electrode. Sample electrodes were prepared at 5 wt. %, 15 wt. %, and 30 wt. % addition of Nafion ionomer as binding solution. The impedance curves were retrieved after CDC at 1.5 V from 250 kHz to 100 mHz at 10 mV AC amplitude. (a) & (b) Polarization curves in charge/discharge modes. (c) Impedance curves and the inset show the values of ohmic resistance R_O and charge transfer resistances R_{CT} (Lines are added in the inset). 140

Figure 6.9 NAqRFB-cell equipped with the electrodes coated with rGO and Platinum as a catalyst, Pt-rGO electrode. (a) Coulombic efficiency (b) Voltage efficiency (c) Energy efficiency (d) Impedance curve (e) Polarization in discharging mode (f) Polarization in charging mode. 143

Figure 6.10 NAqRFB-cell assembled with each sample of electrodes operated at C-rate = C/2, i.e., 4.6 $mA \cdot cm^{-2}$ at the flow rate of 30 $ml \cdot min^{-1}$ (a) Capacity (b) Energy density 144

Figure 7.1 Materials in Q1 are categorized by European Union as Critical Raw Materials for the year 2020. Materials from Q2 should be targeted for future technologies [186]. 149

Figure 7.2 Cyclic voltammetric analysis of redox species having respective cell potentials. 153

Figure 7.3 Cyclic voltammetry analysis of $Al(acac)_3$ (a) Voltammograms (b) Randles-sevcik plots (iP vs. $v^{1/2}$) showing reversibility condition. 153

Figure 7.4 Charge-discharge cycling of cells each having negolyte as $Al(acac)_3$ and posolyte of $Cr(acac)_3$, $Fe(acac)_3$, $Mn(acac)_3$, $V(acac)_3$, and Ferrocene. (a) Coulombic efficiency (b) Voltage efficiency (c) Energy efficiency. 156

Figure 7.5 Electrochemical impedance spectroscopy measured in the range of 100 mHz to 250 kHz at AC amplitude of 20 mV. (a) Impedance curves (b) Equivalent circuit used for impedance curve fitting. 158

Figure 7.6 NAqRFB-cells having mentioned electrolytes. (a) Capacity and (b) Energy density are calculated using the mass of redox species used for negolyte. 159

Figure 7.7 Voltammograms taken after charge/discharge cycling for the NAqRFB-cells having mentioned negolytes and posolytes. (a) Al || Cr (b) Al || V (c) Al || Mn (d) Al || Fc (e) Al|| Fe. 160

Figure 8.1 Cyclic voltammograms of the redox species having respective cell potentials. 171

Figure 8.2 Cyclic voltammetry analysis of 1,4-Naphthoquinone (a) Voltammograms (b) Randles-sevcik plots (iP vs. $v^{1/2}$) showing the linear relationship for the condition of kinetic reversibility. 171

Figure 8.3 Cyclic voltammetry analysis of Chromium acetylacetonate. (a) Voltammograms (b) Randles-sevcik plots (iP vs. $v^{1/2}$) showing the linear relationship for the condition of kinetic reversibility. 171

Figure 8.4 Cyclic voltammetry analysis of Vanadium acetylacetonate. (a) Voltammograms (b) Randles-sevcik plots (iP vs. $v^{1/2}$) showing the linear relationship for the condition of kinetic reversibility. 172

Figure 8.5 Cyclic voltammetry analysis of Manganese acetylacetonate. (a) Voltammograms (b) Randles-sevcik plots (iP vs. $v^{1/2}$) showing the linear relationship for the condition of kinetic reversibility. 172

Figure 8.6 Charge-discharge cycling of cells each having negolyte as NQ and posolyte of $Cr(acac)_3$, $Mn(acac)_3$, and $V(acac)_3$. (a) Coulombic efficiency, (b) Voltage efficiency, (c) Energy efficiency, (d) Capacity, (e) Energy density were calculated using the mass of redox species used for negolyte i.e. NQ, and (f) Polarization response indicating limiting current density of the cells having 0.06 M concentration and flow rate of 30 $ml \cdot min^{-1}$. 176

Figure 8.7 Electrochemical impedance spectroscopy measured in the range of 100 mHz to 250 kHz at AC amplitude of 20 mV. (a) Impedance curves, (b) Equivalent circuit used for impedance curve fitting. 177

Figure 8.8 Voltammograms taken after charge/discharge cycling for the NAqRFB-cells having mentioned negolyte and posolyte. (a) NQ || V (b) NQ || Mn. 177

List of Tables

Table 1.1 Advantages and disadvantages of renowned energy storage technologies (Source: [12]) 6

Table 1.2 Top 15 frequent keywords used by researchers to search the database of Redox flow battery..... 9

Table 1.3 Top 10 research hubs for redox flow batteries..... 9

Table 1.4 Basic differences between aqueous and non-aqueous RFBs..... 13

Table 1.5 Conductivity of supporting electrolytes in various battery applications. 27

Table 1.6 Commercial membranes used for non-aqueous RFBs. 29

Table 1.7 Structure of Ph.D. thesis highlighting the contributions 34

Table 2.1 Fitting parameters and RC circuit impedance analysis of the equivalent circuit for the impedance curves shown in Figure 2.7. 49

Table 3.1 Characteristics of the selected commercial membranes. 61

Table 3.2 Crossover molar flux rates for ferrocene as probing species 66

Table 4.1 Properties of the used membranes. 83

Table 4.2 Fitting parameters and RC circuit impedance analysis of the equivalent circuit for the impedance curves shown in Figure 4.7. 94

Table 5.1. Treatments applied to as-received electrodes..... 104

Table 5.2 Summary of electrochemical parameters determined by CV for P, PH, PH2, PO, POH and POH2 CFs for V^{2+}/V^{3+} redox couple in 0.1 M $TEABF_4$ + 0.02 M $V(acac)_3$ + Acetonitrile electrolyte at the scan rate of 10 mV s^{-1}. 110

Table 5.3 Summary of electrochemical parameters determined by CV for PO and POH2 CFs for V^{3+}/V^{2+} redox couple in 0.1 M $TEABF_4$ + 0.02 M $V(acac)_3$ + Acetonitrile electrolyte at the scan rate of 10 mV·s^{-1} at the beginning of life (BoL) and upon the AST/stability test. 111

Table 6.1 Peak to peak potential separation, peak current ratios, recorded at 20 mV·s^{-1} and fitting result for the reaction rate constants of oxidation V^{2+}/V^{3+} (negolyte) and reduction, V^{3+}/V^{4+} (posolyte) processes on different electrodes obtained using Equation (9). 131

Table 6.2 Ohmic and charge transfer resistances from the first semi-circle of impedance curves taken before and after charge-discharge cycling of cell equipped with each sample electrodes. 135

Table 6.3 Summary of the results of the NAqRFB-cell equipped with each of the coated electrodes and optimization of the electrodes containing varying ink composition having Nafion ionomer binding solution. 144

Table 7.1 Diffusion coefficients of redox couples 154

Table 7.2 Parameters of the equivalent circuit fitted on the impedance curves for each cell. .. 158

Table 7.3 Summary of the 20 charge-discharge cycles for each battery type having mentioned posolyte and negolyte. 159

Table 8.1 Diffusion coefficients of redox couples 170

Table 8.2 Polarisation analysis for each cell indicating current density at the flow-limiting condition and ohmic losses at 1.4 $mA \cdot cm^{-2}$ 174

Table 8.3 Parameters of the equivalent circuit from Figure 8.7 (b) fitted on the impedance curves of Figure 8.7 (a) for each type of NAqRFB-cell. 174

Table 8.4 Summary of the 26 charge-discharge cycles for each type having mentioned posolyte and negolyte. 178

List of Acronyms

SDG	Sustainable Development Goals
RFB	Redox Flow Batteries
WoS	Web of Science
CE	Counter Electrode
RE	Reference Electrode
NAqRFB	Non-Aqueous Redox Flow Battery
CAN	Acetonitrile
PC	Propylene Carbonate
DMF	Dimethylformamide
DMSO	Dimethyl Sulfoxide
UV-Vis	Ultraviolet–Visible Spectroscopy
RH	Relative Humidity
NPs	Nanoparticles
CNT	Multi-Walled Carbon Nanotubes
ESS	Electricity Storage System
LSV	Linear Sweep Voltammetry
CV	Cyclic Voltammetry
WE	Working Electrode
SOC	State Of Charge
DES	Deep Eutectic Solvents
AEM	Anion Exchange Membranes
CEM	Cation Exchange Membranes
LDB	Liquid Displacement Battery
E_{OCP}	Open Circuit Potential
CDC	Charge-Discharge Cycling
EIS	Electrochemical Impedance Spectroscopy
PEMFC	Polymer Electrolyte Fuel Cell
PFSA	Perfluorosulfonic Acid
IEM	Ion-Exchange Membrane
SEM	Scanning Electron Microscope
FT-IR	Fourier-Transform Infrared Spectroscopy
DI	Deionized
ECSA	Electrochemical Surface Area
rGO	Reduced Graphene Oxide
EDX	Energy-Dispersive X-Ray Spectroscopy

List of Symbols

U_{MAX}	Maximum energy density (Wh·L^{-1})
E_{OCP}	Open circuit potential (V)
C_A	Maximum concentration / solubility (M)
F	Faraday's constant
q_E	elementary charge
ε_0	permittivity in a vacuum
ε_r	relative permittivity
k_B	Boltzmann constant
Λ_m	limiting molar conductivity
μ	Viscosity
N_A	Avogadro's number
k	Stoke's constant
μ	Dynamic viscosity
η_{CE}	Coulombic Efficiency (%)
η_{VE}	Voltage Efficiency (%)
η_{EE}	Energy Efficiency (%)
$Z_{RC,a}$	Impedance of RC circuit (Ω)
$Z_{RC,c}$	Impedance of RC circuit (Ω)
Z_{CELL}	Cell imopedance (Ω)
J_i	Crossover molar flux
D_i	Diffusion coefficient
$\frac{\partial C_i}{\partial x}$	Concentration gradient
n or n_i	Participating number of electrons
$i_{diffusion}$	Current density due to concentration gradient
i_{lim}	Transport limiting current density (mA·cm^{-2})
$i^p_{ox/red}$	Peak current density for CV (mA·cm^{-2})
A	Area of the working electrode (cm^2)
C^O	Bulk concentration of electrolyte
κ_m	Conductivity of the membrane (S·cm^{-1})
ℓ	Thickness of membrane
R_1	Cell resistance without membrane
R_2	Cell resistance with membrane

R_{A}	Area-specific ohmic resistance of membrane to the cation permeation of the redox species
R_{m}	Area-specific ohmic resistance of the membrane to the ionic permeation of the balancing cation
R_{Ω}	Ohmic resistance (**Ω**)
i_{A}	Crossover current of the redox species
α	Ideal selectivity of membrane
$\eta_{\mathrm{EE,max}}$	Maximum efficiency of a flow battery (%)
τ	Ratio between charge to discharge times
ϕ	Proportionality Constant
E_0	Equilibrium potential (V)
E_{PA}	Anodic peak potential (V)
E_{PC}	Cathodic peak potential (V)
E_{A}	Anodic redox potential (V)
E_{C}	Cathodic redox potential (V)
m	total number of peaks
I_{P}	Peak current
K^O	Reaction rate constant
R	Gas constant
v	Scan rate
η_{o}	Ohmic Losses (V)
η_{m}	Mass transport overpotentials (V)
η_{a}	Activation Overpotential (V)

List of Publications

Journals

1. *K. Mushtaq, J. Zhao, N. Weber, A. Mendes, D.R. Sadoway, Self-discharge mitigation in a liquid metal displacement battery, J. Energy Chem. 66 (2022) 390–396.* https://doi.org/10.1016/j.jechem.2021.08.015

2. *K. Mushtaq, T. Lagarteira, A.A. Zaidi, A. Mendes, "In-situ crossover diagnostics to assess membrane efficacy for non-aqueous redox flow battery", J. Energy Storage. 40 (2021) 102713.* https://doi.org/10.1016/j.est.2021.102713

Peer-reviewed Conferences

3. *K. Mushtaq, Ji Zhao, N. Weber, D. Sadoway, "Performance enhancement and characterization of liquid displacement battery having faradaic membrane", 14th Workshop on Reactive Metal Processing RMW14, (March 2019), Massachusetts Institute of Technology, Cambridge, US.* http://www.okabe.iis.u-tokyo.ac.jp/core-to-core/rmw/RMW14_index.html

4. *K. Mushtaq, A. Mendes, "In-situ crossover measurements for vanadium-based non-aqueous redox flow battery", 239th ECS Meeting (June 2021), Chicago, USA.*
URL: https://ecs.confex.com/ecs/239/meetingapp.cgi/Paper/147222

5. *K. Mushtaq, A. Mendes, "Hybrid Membrane Leading to Improved Ionic Selectivity for Non-Aqueous Redox Flow Battery", 239th ECS Meeting (June 2021), Chicago, USA.*
Link: https://ecs.confex.com/ecs/239/meetingapp.cgi/Paper/147379

6. *K. Mushtaq, S. Delgado, A. Mendes, "Thermal Hydrogen Treatment of Electrodes for Performance and Stability Enhancement of Non-Aqueous Redox Flow Batteries", 239th ECS Meeting (June 2021), Chicago, USA.*
Link: https://iopscience.iop.org/article/10.1149/MA2021-013232mtgabs

7. *K. Mushtaq, S. Delgado, A. Mendes, "Nanoparticles Coated Electrodes for Vanadium-Based Non-Aqueous Redox Flow Battery", 240th ECS Meeting (October 10 – 14, 2021), USA.*
Link: https://iopscience.iop.org/article/10.1149/MA2021-0251924mtgabs/meta

8. *K. Mushtaq, S. Delgado, A. Mendes, "Novel Aluminum-Ion Based Non-Aqueous Redox Flow Battery", 240th ECS Meeting (October 10-14, 2021), Digital Meeting, USA.*
Link: https://iopscience.iop.org/article/10.1149/MA2021-0251925mtgabs

9. *K. Mushtaq, A. Mendes, "Step toward eco-friendly green source of non-aqueous electrolytes for redox flow battery", 240th ECS Meeting (October 10-14, 2021), Digital Meeting, USA. Link: https://ecs.confex.com/ecs/240/meetingapp.cgi/Paper/153625*

10. *K. Mushtaq, R. Monteiro, Asad A. Zaidi, N. Delgado, A. Mendes, "Current density improvement for vanadium redox flow cell having interdigitated flow-field", ECS Meet. Abstr. MA2018-02 (2018) 28.* https://doi.org/10.1149/ma2018-02/1/28.

11. *K. Mushtaq, R. Monteiro, A. Mendes, "Impact of varying bipolar plates having flow-fields on the performance of redox flow battery at high current density", ECS Meet. Abstr. MA2020-02 (2020) 303–303.* https://doi.org/10.1149/ma2020-022303mtgabs.

Articles under submission

- *K. Mushtaq, A. Mendes, "Composite membrane for non-aqueous redox flow battery", Electrochimica Acta.*
- *K. Mushtaq, S. Delgado, A. Mendes, "Oxygen-less electrodes for high stability in non-aqueous redox flow batteries", Journal of Energy Storage.*
- *K. Mushtaq, S. Delgado, A. Mendes, "Carbon felt electrodes augmented with nanoparticles for non-aqueous redox flow battery", Journal of Energy Storage, Elsevier*
- *K. Mushtaq, A. Mendes, "Aluminium redox ion-based non-aqueous redox flow battery", ACS Energy Letters.*
- *K. Mushtaq, A. Mendes, "Naphthaquinone redox ion-based non-aqueous redox flow battery", ACS Energy Letters.*

Chapter 1

Introduction

1. Introduction

Adapted from the following articles:

Márcia S. Santos, Luciana Peixoto, K. Mushtaq, et. al., "Bioelectrochemical energy storage in a Microbial Redox Flow Cell", Journal of Energy Storage, Volume 39, July 2021, 102610, Elsevier. https://www.sciencedirect.com/science/article/pii/S2352152X21003522.

K. Mushtaq, R. Monteiro, Asad A. Zaidi, N. Delgado, A. Mendes, "Current density improvement for vanadium redox flow cell having interdigitated flow-field", ECS Meet. Abstr. MA2018-02 (2018) 28. https://doi.org/10.1149/ma2018-02/1/28.

K. Mushtaq, R. Monteiro, A. Mendes, "Impact of varying bipolar plates having flow-fields on the performance of redox flow battery at high current density", ECS Meet. Abstr. MA2020-02 (2020) 303–303. https://doi.org/10.1149/ma2020-022303mtgabs.

"Research is to see what everybody else has seen, and to think what nobody else has thought." – Albert Szent-Györgyi

History is marked by the fact that the development of energy technology has transformed human life. A sharp eye on the timeline of energy use revealed that it has experienced four industrial revolutions. The use of coal and its mass extraction in 1765 was marked as the first revolution [1]. This led to the invention of the steam engine and metal forging, which revolutionized the manufacturing process. With coal-powered equipment, fabric could be spun and woven on spinning machines and looms. The second revolution began in 1870 and lasted until 1880. The discovery of electricity, gas, and oil was key to this. The combustion engine was invented later, and the concept of mass production accelerated the industry. The third industrial revolution was witnessed in 1957 when the first commercial electricity-generating plant powered by nuclear energy was installed [2]. The first oil crisis in 1973 indicated that the oil age would end [3], and depletion of fossil fuels was expected along with the effects of climate change. As we continue moving into the fourth industrial revolution, the momentum comes from renewable energy sources and the acceleration of digital technology [4]. This revolution is marked by disruptive moments such as the Kyoto Protocol [5] and the Paris Agreement [6], where countries settle on common and individual goals to improve the present and future environmental situation. The purpose of this shift toward renewable energy sources such as solar, wind, geothermal, and biomass is to ensure the sustainable development of humanity. There are 17 sustainable development goals (SDGs) [7] adopted by all United Nations member states in 2015 and stated in the 2030 agenda for sustainable development. The research presented in this thesis targets the (SDG No. 7) affordable and Clean Energy, (SDG No. 11) Sustainable cities and communities, and (SDG No. 13) Climate action.

1.1 Energy Storage – A necessity rather than a privilege

If Alexander Graham Bell was somehow teleported to the 21st century, he would have no idea what modern telephony entails, yet Nicola Tesla, a key early inventor of the grids, would be well acquainted with the grid. He would be familiar because it has been utilized in most parts of the world in a similar fashion since the last century.

Climate change is one of the most pressing issues of our day. By 2050, Europe intends to achieve its vision of a climate-neutral society [8]. This transition encourages people to come up with new ways to mitigate the negative impacts of energy consumption and conversion. This also influences the production, consumption, and storage of electrical energy. Large-centralized power plants are being complemented by distributed generation and this requires changes in the technology used for the management of the transmission and distribution services. The large-scale integration of renewable energy into a grid causes instabilities, which can be mitigated by the use of effective energy storage technologies. It helps to maximize the utilization of renewable energy and also assists in load leveling. Integration of power produced through renewable energy sources keeps on increasing and is forecasted to reach a 100 % level by 2050.

The dispatching center of the electricity transmission network needs to ensure the reliability of the power supply. The scenario of complete switching without any backup from a conventional power plant will cause reliability issues because of the intermittent nature of renewable energy supply. The large-scale electricity storage system can help to increase the reliability of the system and convert the renewable energy power plant to behave like a conventional power plant by charging during excess energy supply and discharging during low energy supply. It is necessary for the present electric power systems that electric supply (production) remains always equal to electric demand (load). The imbalance between supply and demand affects the power quality. This causes deviation from the standard frequency of 60 Hz or 50 Hz which is highly undesirable for the electric network. Large scale electricity storage system (ESS) can mitigate this effect by acting as buffer storage to increase supply for a short time to meet the demand. The schematic is shown in Figure 1.1 for further elaboration.

Electricity storage technologies include a large set of centralized and distributed designs that can supply an array of services to the energy system. Different systems for the storage of electricity have been developed for many years. There are different ways of classifying the storage technologies and one of the possible classifications is shown in

Figure 1.2, which is based on the method in which energy is stored. The comparison of the renowned technologies is given in Table 1.1. Electric car adoption is also a critical step in the fight against CO_2 emissions. The actual facilitators for this ambition are batteries, but they must be made safer, better performing, more sustainable, and inexpensive. Batteries should function well above their present-day performance. Furthermore, reliable batteries can improve the present grid's robustness while cutting emissions [9]. The most promising commercial battery technologies are lithium-ion, lead-acid, redox-flow, and high-temperature batteries such as sodium-sulfur and liquid metal batteries [10]. Especially, the technological options of redox flow and high-temperature batteries promise low specific cost and easy upscaling. This makes them very attractive for stationary storage applications.

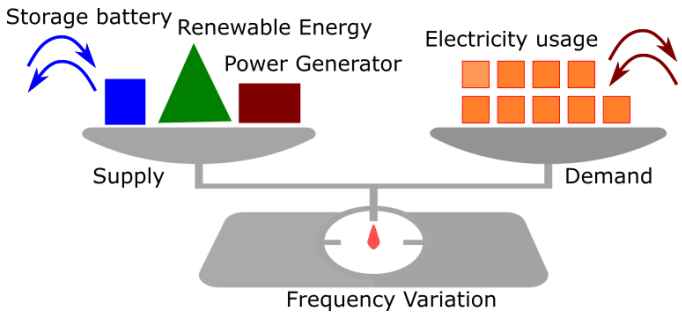


Figure 1.1 Balance between electricity supply and demand ([11]*).*

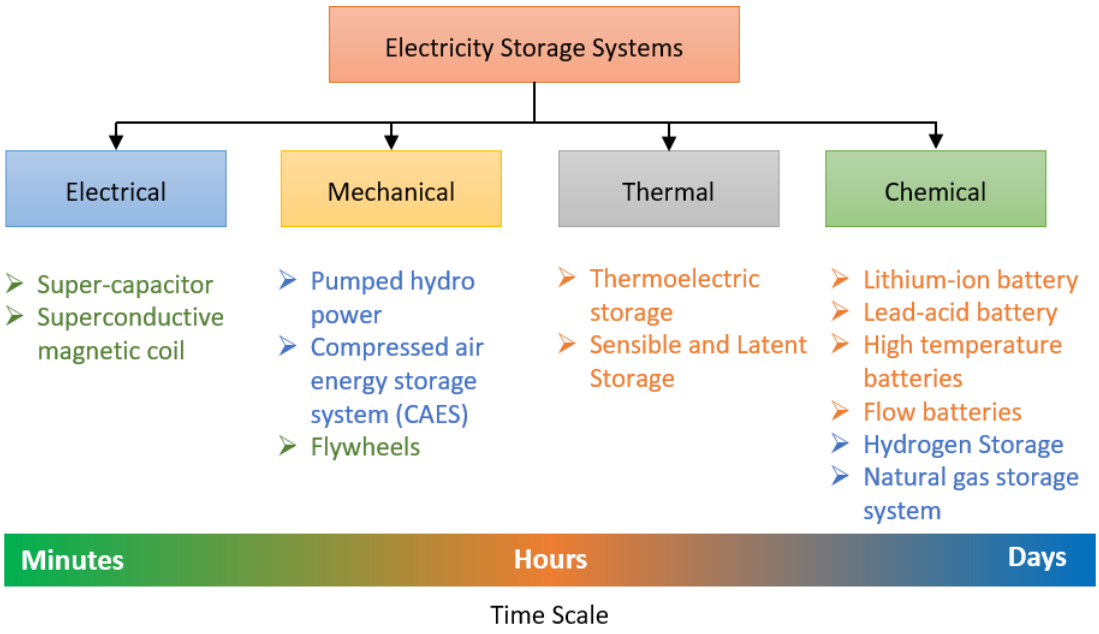


Figure 1.2: Classification of electricity storage technologies (Source: [12]*)*

Table 1.1 Advantages and disadvantages of renowned energy storage technologies (Source: [13]*)*

Energy Storage Technologies	Advantages	Disadvantages
Sodium-sulfur battery	High energy and power density	High operating temperature and poor safety
Lithium-ion battery	High coulombic efficiency, energy, and power density	Poor safety and short cycle life
Lead-acid battery	Mature technology and lowcost	Short cycle life and environmental pollution by lead
Supercapacitor	High power density and long cycle life	High cost and low energy density
Pumped storage	High capacity and mature technology	Need appropriate geographical environment
Compressed air energy storage	High capacity	Need appropriate geographical environment
Flywheel energy storage	High power density	Need vacuum and high requirements for flywheel material
Superconducting magnetic energy storage	High power density	Low-temperature operation and high cost
Flow battery	Flexible design and safety	Low energy density

1.2 Bibliometricic Analysis

1.2.1 Research streamline of Redox Flow Batteries

Redox flow batteries (RFB) have been a pivot to the research community as evident by the increasing number of publications over time, Figure 1.3. The very first publication on the topic is spotted in 1984 and followed by 1988 on the topic of all-vanadium redox flow battery [14]. For the next two decades, the topic couldn't get much attention until 2002 when the concept of chromium and cerium redox couples was introduced. Later on, these concepts became the mainstream of the research as evidenced by the highest number of citations on these topics and especially for these two highly cited references [15,16]. Afterward, redox flow batteries became the center of attention

for the community, and the amount of publications on the topic is being increased. The last four decades 1981-90, 1991-00, 2001-10 and 2011-20 contributed an increment of 0.6 %, 1.53 %, 5.13 % and 93.73 %, respectively.

1.2.2 Research trends

Data from Web of Science (WoS) spanning over the last 50 years was spotted out for research streamline of redox flow batteries. There are 3333 articles indexed in WoS in relevance to this topic out of which 83.64 % are research articles and are selected for content analysis. Content analysis is a data mining technique that analyses the contents of the article and highlights the most frequent words. For the present case, 7190 keywords were extracted from the literature. To highlight the most frequent keywords, the words with a minimum occurrence of 50 were highlighted and only 91 meet the threshold as displayed in Figure 1.4. The size of the circle denotes the frequency of occurrence, lines denote the co-occurrence of keywords and color is mapped to the particular year. The top 15 frequently used keywords by researchers are highlighted in Table 1.2.

1.2.3 Countries leading the RFB research

There are about 63 countries currently active in this research field. A filter was applied to sort out the top contributing countries. The threshold was set to a minimum 10 number of publications and 100 citations. As a result, the top 28 contributing countries were filtered out as depicted in Figure 1.5. China is the top contributing country for the number of articles published, it alone contributes 33.85 % to the total number of publications available on the web of science (WoS) on this topic. China is followed by the USA, South Korea, and Germany contributing 22.16 %, 10.9 %, and 8.42 % in the category of the number of publications. In terms of the number of citations, the USA is leading the list with 10.7 % more citations than China, which is then followed by Australia, England, and Germany. A list of the top 10 countries along with their contributions is provided in Table 1.3.

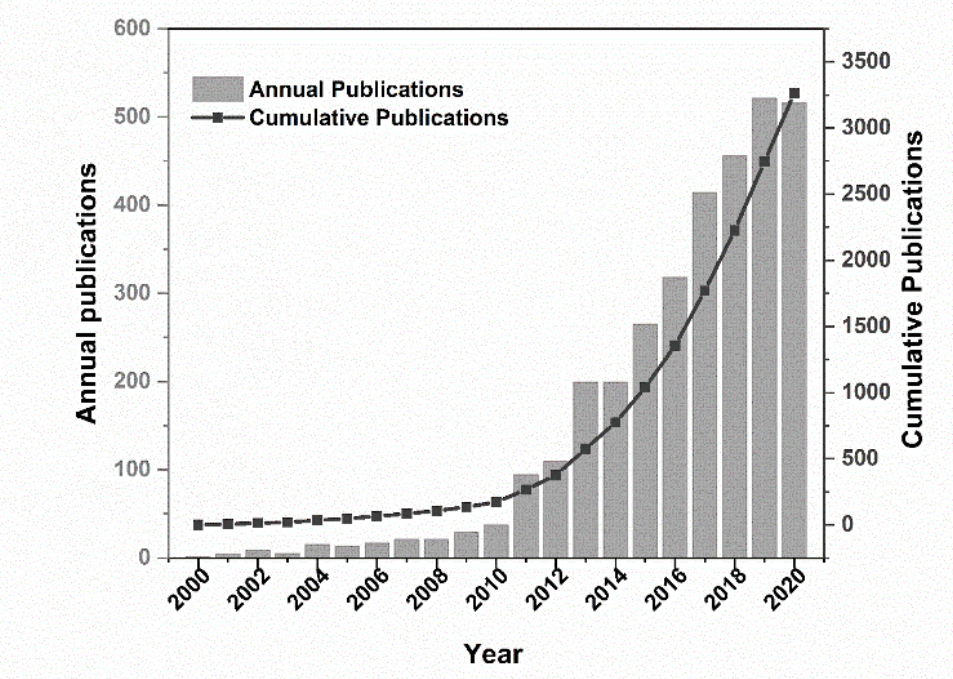


Figure 1.3: The increasing number of publications in the field of redox flow batteries (Source: Web of Science).

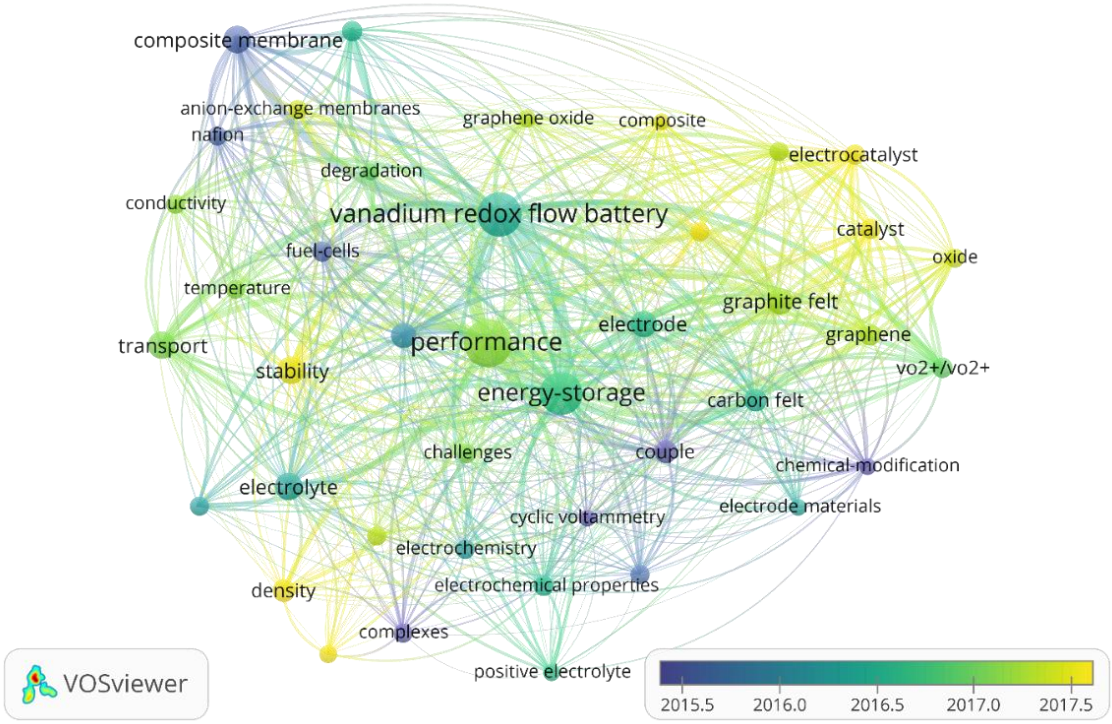


Figure 1.4: Research streamline of redox flow batteries

Table 1.2 Top 15 frequent keywords used by researchers to search the database of Redox flow battery

Keywords	**% Occurrence**
Performance	12.94
Vanadium redox flow battery	11.08
Energy-storage	9.82
Transport	3.37
Electrolyte	3.35
Stability	3.35
Composite membrane	3.26
Graphite felt	3.14
Electrode	3.10
Membrane	2.67
Carbon felt	2.16
Density	2.02
Couple	1.98
Graphene	1.91
VO^{2+}	1.68

Table 1.3 Top 10 research hubs for redox flow batteries

Country	**Percentage of contribution in documents (%)**	**Percentage of contribution in citations (%)**
China	33.9	27.1
USA	22.2	30.4
South Korea	10.9	5.4
Germany	8.4	5.4
England	4.5	5.4
India	4.0	1.3
Australia	3.7	5.6
Japan	3.7	3.1
Singapore	3.6	3.1
Spain	2.7	1.8
Others	2.6	11.4

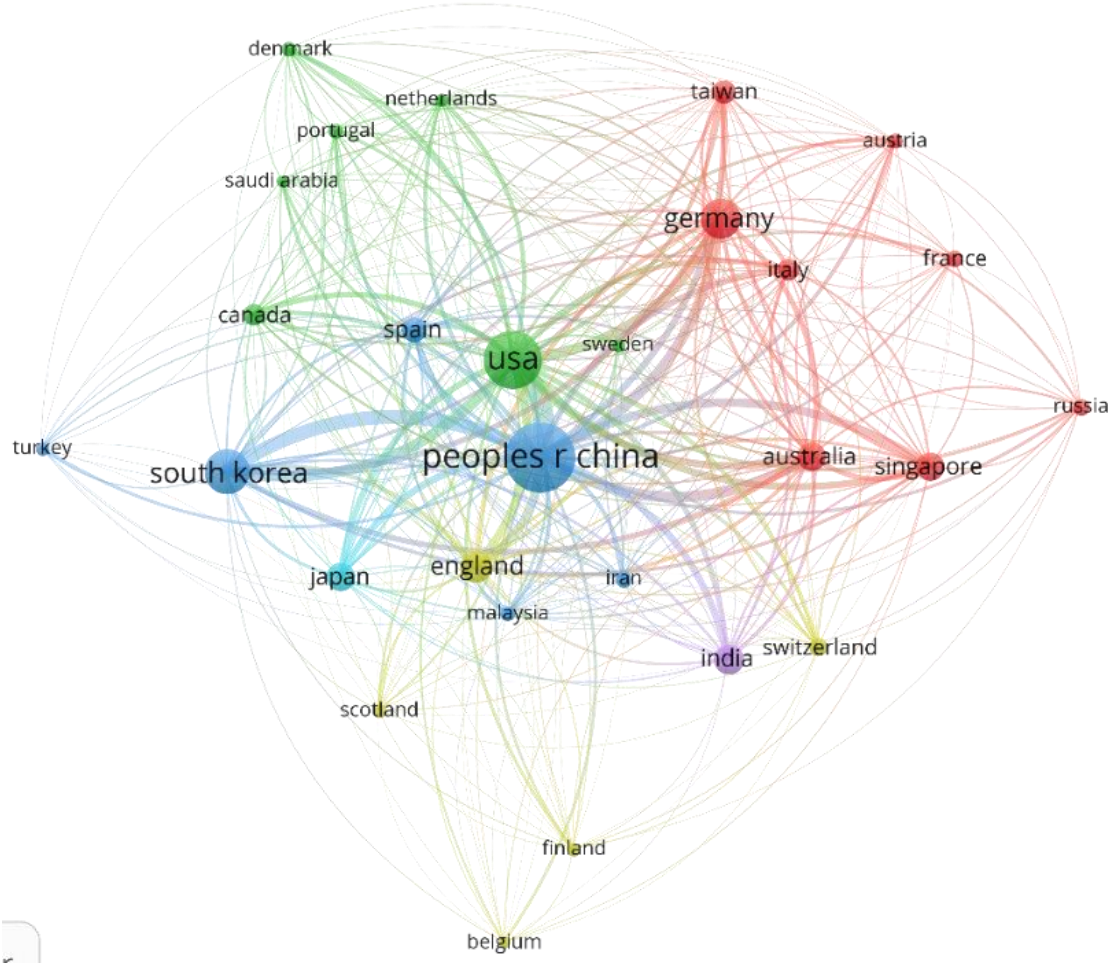


Figure 1.5 Leading countries in redox flow batteries research.

1.3 Electrochemistry of Redox flow battery

A redox flow battery is an electrochemical device that stores energy in a liquid electrolyte. The liquid electrolyte consists of three main ingredients. “Redox species” undergoes the electrochemical redox reaction to store energy, “supporting electrolyte” is responsible for increasing the electrolyte’s conductivity, and “Solvent” provides high solubility of redox species. This electrolyte is stored in two separate reservoirs and continuously pumped into flow cell. An ion exchange membrane separates electrolytes on the positive side (referred to as posolyte) and negative (referred to as negolyte). The membrane is responsible for preventing cross-contamination of redox species while allowing the transport of balancing ions to complete the system's circuit. The energy is stored or delivered from redox species through redox reactions happening at the surface of the electrodes [13]. The energy conversion is based on the reversible redox reactions of two redox couples (*e.g.* A^{3+}/A^{2+} and C^{5+}/C^{4+}), as shown in the following

equations (1.1) to (1.3) [17]. Each of the redox couples A and C are in separate reservoirs, as shown in Figure 1.6. The electrolytes having redox couples of A^{3+}/A^{2+} and C^{5+}/C^{4+} circulate in both half cells at a certain flow rate and reactions in discharging direction are given below.

At Positive Electrode:

$$C^{5+} + e^{-} \rightleftharpoons C^{4+}, \qquad E_C \tag{1.1}$$

At Negative Electrode:

$$A^{3+} + e^{-} \rightleftharpoons A^{2+}, \; E_A \tag{1.2}$$

Cell Reaction (discharge):

$$A^{2+} + C^{5+} \rightleftharpoons A^{3+} + C^{4+}, \quad \Delta E_{\mathrm{CELL}} = E_C - E_A \tag{1.3}$$

RFB can be designed using symmetric redox couples having multiple oxidation states such as Vanadium [18] or can also be operated using the electrolyte having asymmetric redox couples such as Iron-Chromium chemistry [19]. The characteristics of the battery are highly dependent on the selection of redox species. For the case of an aqueous-based vanadium redox flow battery, the redox species are selected to be A = V^{3+}/V^{2+} and C = V^{5+}/V^{4+}. Similarly for Iron-Chromium aqueous electrochemistry, the redox couples are selected to be A = Cr^{3+}/Cr^{2+} and C = Fe^{3+}/Fe^{2+}.

1.4 Electrochemical Cells

The voltammetry analysis is the starting point to assess the performance of an electrochemical system. The techniques of linear sweep voltammetry (LSV) and cyclic voltammetry (CV) were used throughout this thesis. These were performed using static cells having a 3-electrode configuration. It was comprised of Glassy carbon or the "Sample-to-study" as the working electrode (WE), Platinum wire served as a counter electrode (CE), and electrode Biologic RE-7, filled with 0.01 M $AgNO_3$ + 0.1 M TBAP + Acetonitrile, was used as a reference electrode. The experimental setup is shown in Figure 1.7.

The performance of the battery was assessed using a single flow cell in a two-electrode configuration. The fuel cell technology inspires the architecture of a flow cell. The operational requirements of both technologies are different, and the design should be optimized considering the flow of the liquid electrolytes across the thicker and porous electrodes. The in-house made redox flow cell was designed with inspiration from the

commercial fuel cell unit from Pragma Industry. The 3-D model is shown in Figure 1.8, it is comprised of inlet/outlet ports using Swagelok stainless steel connectors; stainless steel end plates; plastic insulators; current collectors made of gold-coated copper; bipolar plates made of highly conductive graphite; Teflon O-rings; gasket 1, spacer, gasket 2 to keep the compression up to 34 %. The carbon felt electrodes and membranes were chosen as per the requirement of the study. The main modification includes replacing the bipolar plates having broader channels to ease the electrolyte flow, the material of components used to seal the cell to ensure compatibility, and inlet/outlet ports of the cell to a larger size to reduce back pressure on the peristaltic pump. The experimental setup of the flow cell being used throughout the thesis is shown in Figure 1.9.

1.4.1 Transition to the non-aqueous electrochemical system

The most commercialized redox flow battery technology now available is an aqueous all-vanadium RFB (VRFB), which employs water-soluble vanadium ions in various oxidation states as redox species. This technique, which was first conceived in 1986 [20] and can be classified as Figure 1.10, continues to stimulate the curiosity of researchers. One of the significant shortcomings of VRFB is their inherently low energy density compared to battery technologies where energy is stored in solid electrodes such as Li-ion, Ni-metal hydride, and Ni-Cd batteries. The mentioned technologies have volumetric energy densities higher than 100 $Wh{\cdot}L^{-1}$, whereas the highest reported energy density for aqueous VRFB was *ca.* 52 $Wh{\cdot}L^{-1}$, which was also only achieved using 3 M vanadium solutions [21]. Most commercial VRFBs have an energy density of around 25 to 30 $Wh{\cdot}L^{-1}$ [22]. The upper bound in the energy density (U_{MAX}, $Wh{\cdot}L^{-1}$) for an RFB can be estimated by equation (1.4) [23].

$$U_{\mathrm{MAX}} = \frac{1}{2} E_{\mathrm{OCP}} n F C_{\mathrm{A}} \qquad (1.4)$$

where n is the number of electrons transferred per molecule of redox species during the redox reaction, E_{OCP} is the open circuit potential (V), C_A is the maximum concentration/solubility of the redox species ($mol{\cdot}L^{-1}$), and F is Faraday's constant ($26.8\ Ah{\cdot}mol^{-1}$).

Equation (1.4) shows that energy density can be enhanced by increasing the concentration of redox species, cell potential or increasing the number of involved electrons in the reaction. The option of increasing the concentration of vanadium in aqueous electrolytes has already reached the limit. Polyoxometalate-based RFBs are

being investigated to increase the number of electrons transferred per reacting molecule [24]. The water-splitting reaction occurs at *ca.* 1.6 V, which limits a further increase in the potential of the aqueous-based battery technologies. Using non-aqueous electrolytes of either ionic liquids, deep eutectic solvents, or molecular organic solvents opens the doors to redox potentials [25]. Additionally, non-aqueous electrolytes allow the use of new redox species incompatible with aqueous electrolytes due to low solubility, chemical reactivity, or redox potentials outside the electrochemical window of water. Moreover, a range of supporting electrolytes and solvents can be used for this application, enabling higher solubility of the redox species. Summing up altogether, these benefits can lead to higher energy density and lower energy storage costs [26]. Non-aqueous redox flow battery (NAqRFB) is a candidate among the next generation of batteries.

The basic principles of aqueous and non-aqueous RFB are similar except for the change in the solvent and balancing ion from supporting electrolyte. Since the behavior of the redox species depends on the solvent, components such as electrodes, membranes, and bipolar plates need to be adjusted accordingly. These adjustments reveal new opportunities as well as new challenges. For understanding perspective, the basic differences between aqueous RFB and nonaqueous RFBs are given in Table 1.4.

Table 1.4 Basic differences between aqueous and non-aqueous RFBs

Key Components	Aqueous RFBs	Nonaqueous RFBs
Redox Species	Metal ions *e.g.*, V^{3+}/V^{2+}, VO^{2+}/VO_2^{+}, Fe^{3+}/Fe^{2+}, Cr^{3+}/Cr^{2+}, among others and non-metal ions *e.g.*, S_2^{2-}/S^{2-}	Metal ligand complexes *e.g.* complexes of V, Ru, Cr, Mn, U, and Co with varying ligands and organic compounds *e.g.* TEMPO
Solvent	H_2O	Acetonitrile, Propylene carbonate (PC), Dimethylacetamide (DMA), *etc.*
Supporting Electrolyte	H_2SO_4, HCl, salt, among others	$TEABF_4$, $TEAPF_6$, $TBAClO_4$
Balancing ion	H^+, Cl^-, among others	BF_4^-, BF_6^-, Li^+, TEA^+
Electrode	Graphite, other carbon-based materials,	Graphite, Ni, Mo, among others
Membrane	AEM, CEM, and porous membrane	AEM, CEM, and porous membrane

Acronyms: AEM = Anion exchange membrane, CEM = Cation exchange membrane

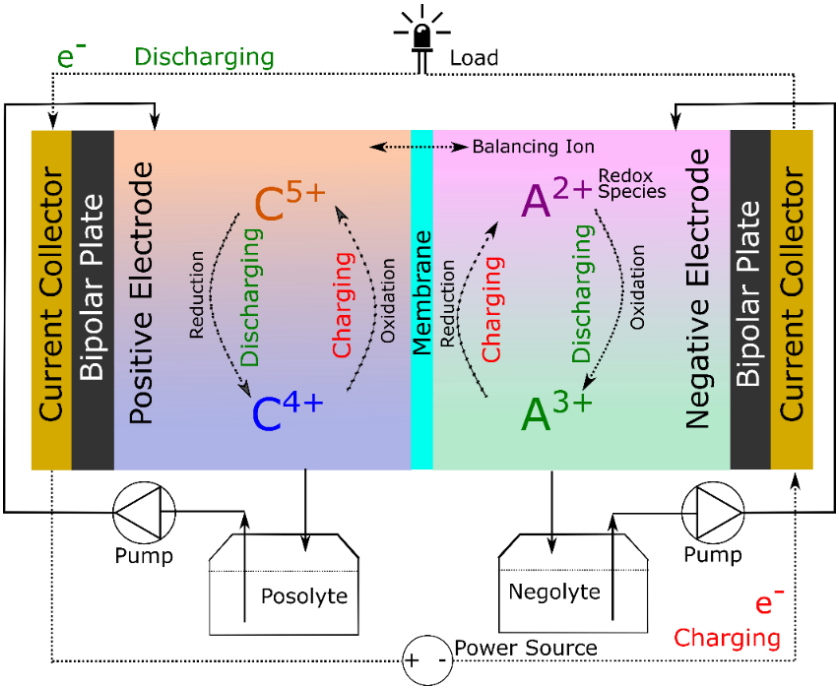


Figure 1.6 Schematic of a redox flow battery in a generalized form having dummy redox species of $A^{3+/2+}$ *and* $C^{5+/4+}$.

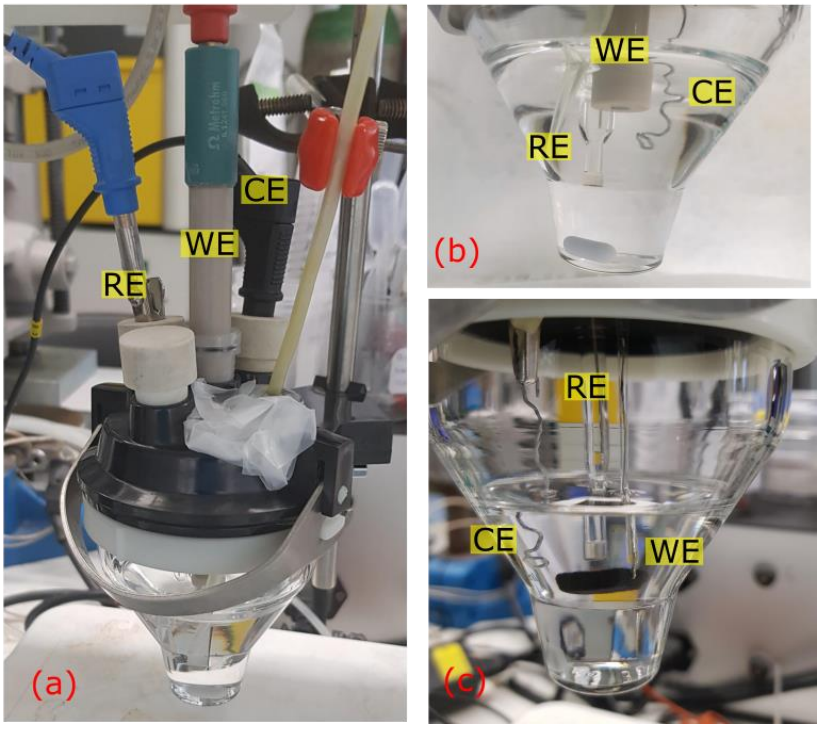


Figure 1.7 Three electrode cell configuration for cyclic voltammetry. (a) 50 ml cell connected to the Autolab potentiostat (b) Cell is assembled with WE = glassy carbon electrode from Metrohm having diameter of 3 mm (c) Cell is assembled with WE = carbon felt electrode as sample-to-study. Acronyms: WE = Working electrode, RE = Reference electrode, CE = Counter electrode.

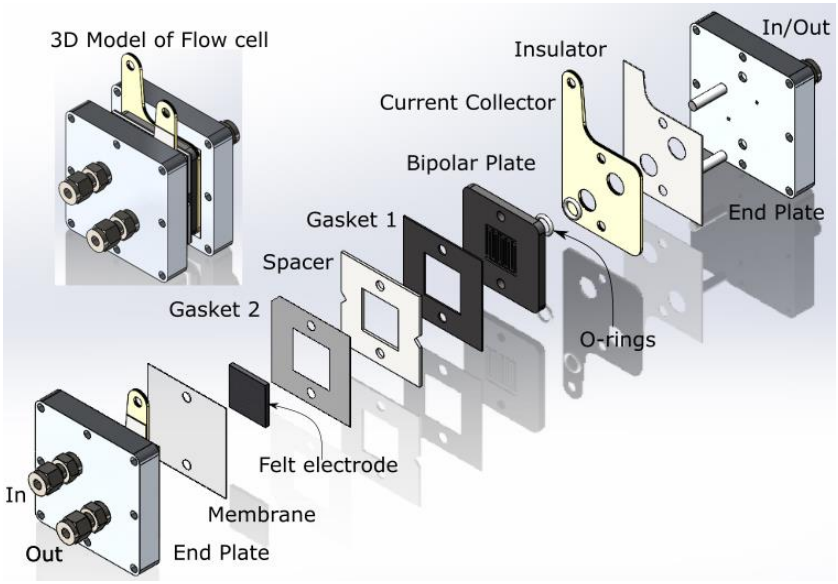


Figure 1.8 3D Model of the in-house made redox flow cell used for all the experiments. Half-cells are symmetric up to the membrane and the figure is showing exploded view of only the half side.

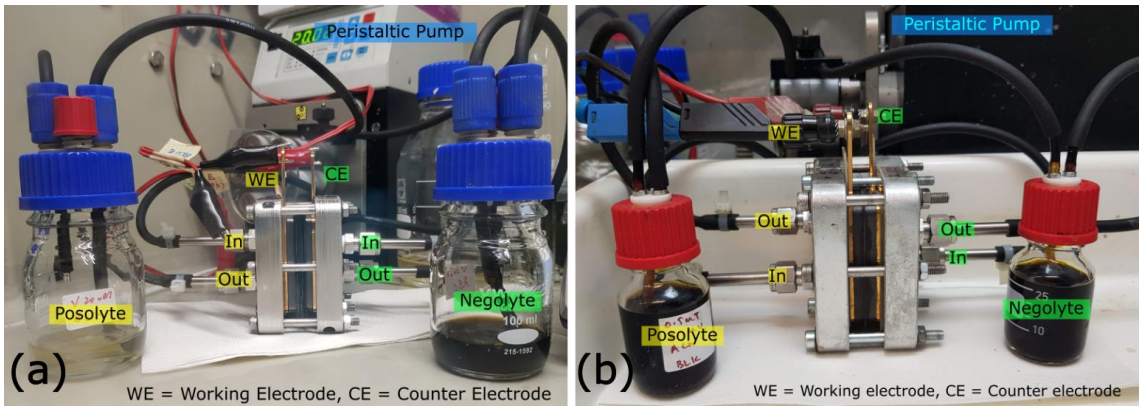


Figure 1.9 The experimental setup of a single cell of the redox flow battery. Posolyte and negolyte is supplied from the reservoir beside the cell and circulated using the peristaltic pump at the same flow rate. (a) Reservoir size is 100 ml (b) Reservoir size is 25 ml. Acronyms: WE = Working electrode, CE = Counter electrode.

1.5 Redox Species

The operation of the RFB needs circulation of posolyte and negolyte from the positive and negative electrodes, respectively. The redox reaction happening at the electrode's surface is responsible for storing energy into the electrolyte, as shown in Figure 1.6. The electrochemical oxidation occurs at the positive half-cell while charging the cell, and electrochemical reduction occurs at the negative half-cell. Continuous charging keeps on changing the redox species valency state unless it consumes all of the

redox species. While charging, the State of Charge (SOC) increases from 0 % to 100 %. The recommended procedure is to operate the battery from SOC = 25 % to SOC = 75 %, and it is to avoid the conditions of overcharging or deep discharging.

The selection of redox species is the starting point for designing a new RFB because the cell potential depends on the redox potential produced by redox species. The electrochemical series [27] can be used to choose the pairs of the redox species having a potential difference between their redox potentials. Later, this selection needs to be confirmed using cyclic voltammetry to get the exact values of redox potentials *vs.* reference electrode (usually Ag^{+}/Ag or ferrocene is used as a reference for non-aqueous electrochemistry). The cell potential is calculated from the difference in the redox potentials. The flexibility of choosing the redox species to get the desired cell potential is the most attractive benefit of the RFB. But this benefit cannot be exploited only by using the aqueous-based electrolyte because the water-splitting reaction put a barrier of 1.6 V. The concept of using a non-aqueous solvent enable the choice of redox species having potential beyond the electrochemical window of the water. Latter is one of the main motivations of this study. The redox species can be classified into metal-based redox species and metal-free redox species.

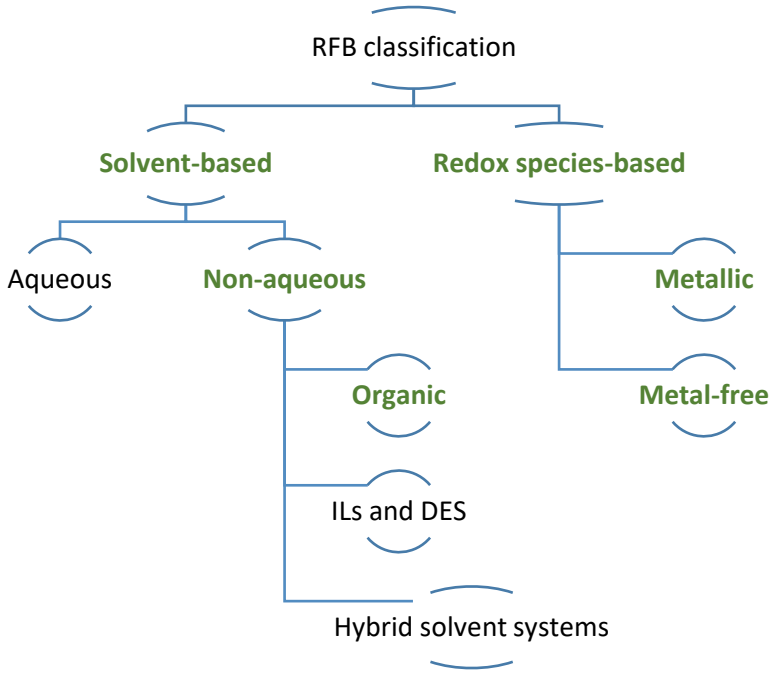


Figure 1.10 Redox flow battery (RFB) classification based on solvent and redox species. Acronyms: ILs = Ionic liquids, DES = Deep eutectic solvents. The scope of thesis is limited to green-coloured branches of the RFB classification.

1.5.1 Metal-based Redox Species

Metal-based refers to the redox species having transition metal centers that offer several oxidation states. The combination of different metal-centers enables higher cell potential, but only the redox species providing reversible reaction can be chosen for RFB. The low solubility of the metal ion can be overcome by using ligands that provide reasonable solubility in non-aqueous solvents. The ligands can be further tailored to increase solubility. Milestone examples for non-aqueous RFBs constructed with metal-based redox systems include Ruthenium by Matsuda *et al.* in 1988 [28], Uranium by Yamamura *et al.* in 2002 [29], Vanadium by Thompson *et al.* in 2009 [30], Manganese in 2011 [31], Chromium by Sleightholme et al. in 2010 [32], Nickel by K. J. Kim and Y. J. Kim et al. in 2011 [33], Cobalt by Li et al. in 2012 [34], and polyoxometalate by Anderson et al. in 2013 [35].

Interestingly, Vanadium is currently the most investigated candidate for NAqRFB, similar to aqueous RFB. Vanadium is being used as model redox species to study vanadium-based non-aqueous redox flow batteries (V-NAqRFB) [23]. The ability of this electrolyte to start the battery from the same valency state (V^{3+}) for both half cells makes it more appealing. It dissolves readily in most organic solvents and is commercially available at fair prices, making it a promising candidate for future commercial versions of non-aqueous redox flow batteries. Ruthenium shows good reversibility but being less abundant makes it expensive. Chromium is highly toxic in the oxidation state of Cr^{4+}, and in contrast, Ni^{2+} and Co^{2+} are less toxic. However, these metals offer reduced electrolyte cost but often show less redox reversibility and reduced solubility. The lower solubility of redox species into non-aqueous solvents is a significant concern but can be solved using different ligands.

Metal-centers having ligands are employed to increase the solubility of redox species. Another intriguing effect is the change in the redox potential by using the ligands. The governing idea is to tailor the ligands of a metal center for the desired redox potential and increased solubility [36]. The most commonly employed redox species are discussed in the following sections, and their molecular structure is shown in Figure 1.11.

Acetylacetonate Ligands

The most attractive point for using acetylacetonate is its commercial availability with several metal ligands such as V, Cr, Mn, Al, Ru, U, and Fe. Yamamura in 2002 [36] used uranium β-diketonates for an all-uranium redox flow battery. The redox pairs of

U^{6+}/U^{5+} were used as posolyte and U^{4+}/U^{3+} as negolyte. The cell potential for this combination was reported to be 1 V. The solubilities of the uranium β-diketonates were measured in four polar aprotic solvents of Acetonitrile (ACN), Propylene Carbonate (PC), Dimethylformamide (DMF), and Dimethyl sulfoxide (DMSO). It was found to be *ca.* 0.8 M for U^{6+} and *ca.* 0.4 M for U^{4+} complexes for all the solvents. Chakrarbati [37] proposed Ruthenium acetylacetonates redox species for RFB applications using tetraethylammonium tetrafluoroborate (as supporting electrolyte and acetonitrile as solvent *i.e.* 0.1 M $Ru(acac)_3$ + 0.5 M $TEABF_4$ + ACN. The cell potential was 1.75 V, charged to the maximum current density of 58 $mA{\cdot}cm^{-2,}$ and discharged at 10 $mA{\cdot}cm^{-2}$. The voltage efficiency achieved up to η_{VE} = 55 % and output power up to 0.18 W.

Later studies were reported for the acetylacetonate having other metal-centers such as $V(acac)_3$ [38], $Cr(acac)_3$ [32], and $Mn(acac)_3$ [39] were used by the researchers having similar supporting electrolytes and solvent. The ligand of acetylacetonate in Acetonitrile offers solubilities of these *ca.* 1 M, 0.4 M, and 0.6 M at room temperature, respectively. These RFB use of symmetric electrolyte referring to the similar electrolyte is used in both half cells and during the first cycle, it is separated into different redox couples. The redox couple of Cr^{2+}/Cr^{3+} and Cr^{3+}/ Cr^{4+} offered the highest cell potential up to 3.4 V, followed by the redox couple of V^{2+}/V^{3+} and V^{3+}/ V^{4+} offering up to 2.2 V, and finally by the redox couple of Mn^{2+}/Mn^{3+} and Mn^{3+}/ Mn^{4+} offering up to 1.1 V. The higher potential offered by the chromium electrochemistry seems attractive. Still, the quasi-reversibility hinders the battery cycling performance. However, having a higher positive potential Cr^{3+}/ Cr^{4+} makes it a suitable option to be the posolyte. Symmetric RFB based on Manganese (Mn) is offering cell potential within the range similar to the aqueous RFB but it offers higher positive redox potential which make it appealing as non-aqueous posolyte. The electrochemistry of $V(acac)_3$ [40] enjoyed considerable interest in literature because of the reversible reactions, having good solubility in ACN, and offering cell potential 37.5 % higher cell than aqueous Vanadium based RFB (*i.e.* having E_{CELL} = 1.6 V). It is being used as a commercially available model reagent to study the performance of NAqRFB-cell. The battery reactions of the vanadium-based non-aqueous electrochemistry are given in the discharging direction by equations (1.5) and (1.6) [40]:

$$[V(IV)(acac)_3]^+ + e^- \rightleftharpoons V(III)(acac)_3, E_C = 0.45\ V\ vs.\ Ag^+/Ag \qquad (1.5)$$

$$V(III)(acac)_3 + e^- \leftrightharpoons [V(II)(acac)_3]^-, E_A = -1.75\ V\ vs.\ Ag^+/Ag \qquad (1.6)$$

Cobalt(II) complexes based on bis(acetylacetone)ethylenediamine ligands [41] were used by Zhang. The cell potential offered by the symmetric electrolyte was 2.2 V and the system was found to be sensitive to oxygen and water. Columbic efficiency of 90 % was achieved using the H-cell. The voltammograms highlighted that the redox couples are quasi-reversible, and there was one electrode disproportionation.

The limitation of lower solubility of metal-center redox species can be altered by tailoring the structures of the ligands. A series of phenyl-substituted chromium(III) acetylacetonate complexes and ester-functionalized chromium(III) and vanadium(III) acetylacetonate complexes were designed by Suttil *et al.* [39]. The solubility was improved up to 1.8 M and 1.32 M for the chromium and vanadium complexes with 2 - methoxyethyl-substituted esters. Static H-cell having 0.5 M $TEABF_4$ and ACN was used for battery cycling. The cell potential was 2.11 V, and the columbic efficiency was 92 % at a current density of 10 $mA \cdot cm^{-2}$.

Bpy Ligands

Bipyridine ligands are available for several metal centers, such as Ru, Fe, Ni, Co, and Cr. The literature [28,38,42] reported the use of Ruthenium-based non-aqueous system having tris(2,2-bipyridine) ruthenium(II) tetrafluoroborate $[Ru(bpy)_3(BF_4)_2]$ complexes. The solubility of this redox couple was poor in organic solvents such as acetonitrile. Jae-Hun Kim [43] designed asymmetric NAqRFB using Fe and Ni redox couples which exhibits the cell potential of 1.9 V. Tri(2,2-bipyridine) iron(II) tetrafluoroborate; $Fe(bpy)_3(BF_4)_2$ and tri(2,2- bipyridine) nickel(II) tetrafluoroborate; $Ni(bpy)_3(BF_4)_2$ was used as posolyte and negolyte, respectively. Interestingly, it was observed that the reactivity and kinetics of the electrochemical reactions of the metal-centers depend on the type of metal electrodes. This gives a possibility to use metal electrodes other than widely used carbon electrodes.

All-Cobalt [44] and Co-Fe [45] based NAqRFB using 1,10-phenanthroline (phen) ligands was developed by Xing *et al.* and by using the electrolyte of ACN + tetraethylammonium hexafluorophosphate ($TEAPF_6$). The symmetric electrolyte of Cobalt exhibits redox couples of Co^{+}/Co^{2+} and Co^{2+}/Co^{3+}, which offer a cell potential of 1.45 V. The voltammograms highlighted that half-cell reactions are quasi-reversible resulting in a η_{CE} = 52 % at SOC = 50 % for an electrolyte having 0.01 M $[Co(phen)_3]_2$ + 0.5 M $TEAPF_6$ + ACN. The cell potential was increased to 2.1 V for the asymmetric

combination of $[Fe(phen)_3]_2$ with $[Co(phen)_3]$. The battery performance reached up to η_{CE} = 80 %, η_{VE} = 48 %, and η_{EE} = 39 %, averaged for the 25 cycles.

Bis(cyclopentadienyl) Ligands

Ferrocene-containing compounds have been used as a standard reference for non-aqueous electrochemistry because of their high reversibility and stable redox reactions. This makes it attractive for the application of RFB but these compounds have limited solubility. Interestingly, ionic modification to bis(trifluoromethanesulfonyl)imide (Tf_2N) ligand of redox species [45] enabled the increase in solubility of Ferrocene up to 8.5 times from pristine in a mixture of ethylene carbonate (EC), PC, and ethyl methyl carbonate (EMC). A semi-flow cell having a Li-metal anode was cycled up to 100 times without significant capacity loss. The bis(cyclopentadienyl) ligand with iron and cobalt modified by Hwang *et al.* [45] didn't improve solubility, but higher redox potential was achieved *ca.* 1.9 ~ 2.2 V.

Redox species with other ligands

Deep eutectic solvents (DES) are now classified as a new class of ionic liquids, and these were also researched to be used for NAqRFBs. Different complexes comprising Cu, Fe, and Zn were formed using DES of choline chloride and ethylene glycol [46–50]. This system has metals in very high concentrations but possesses low electrolyte conductivity and sluggish mass transport.

The cell potential for all-Copper and all-Iron is 0.75 V and 1.1 V; which loses the interest of researchers being almost equal to aqueous RFB. The Zn-Fe system achieved the η_{EE} = 78 % at a current density of 0.5 $mA \cdot cm^{-2}$. The nickel(II)–1,4,8,11-tetra-azacyclo-tetra-decane (cyclam) redox species was also used for NAqRFB [46]. The voltammograms highlighted that nickel (II) complex have redox couples Ni^{3+}/ Ni^{2+}, 1.81 V *vs.* Fc^{+}/Fc and Ni^{2+}/Ni^{+}, 0.74 V *vs.* Fc^{+}/Fc. The system used EC and PC mixture and 1.0 M $TEABF_4$ as supporting electrolytes.

Liquid metal salts are the new type of ionic liquid that functions as solvent and electrolyte. The proof-of-concept all-copper [51,52] having $[Cu(MeCN)_4]$[Tf2N] was presented. The main advantage is the higher copper concentration, resulting in a higher energy density of 75 $Wh \cdot L^{-1}$ and η_{CE} = 85 %.

1.5.2 Metal-free Redox Species

The metal-free redox species are relevantly recent, and there are fewer examples as compared to the latter mentioned redox species. The primary motivation to use these is the inherent high solubility in organic solvents while providing different redox potentials than metal-based redox species. The desired characteristic of being easily reduced and oxidized remains the same. The most reported redox species are discussed below.

Quinone

Anthraquinone and camphorquinone are widely used in RFBs [53–57]. Among quinones, anthraquinones derivatives have been studied most, and their redox mechanism is well understood. However, anthraquinone exhibits low solubility in most electrolytes, especially acetonitrile-based. To overcome this, 1,5-bis(2-(2-(2-methoxy ethoxy) ethoxy) ethoxy) anthracene-9,10-dione has been prepared by simple modification of the corresponding 1,5-dichloroanthraquinone. It has four reversible redox reactions in ACN and can be used as both posolyte or negolyte. The cell potential is *ca.* 1.76 V for single electron transfer and *ca*. 2.72 V for 2-electron transfer. The H-type cell cycling performance was averaged to η_{CE} = 80 % and η_{EE} = 50 % at a current of 5 mA. The low solubility of diaminoanthraquinone is still the main challenge (*e.g.* 0.02 M in ACN).

PTIO

This redox species (2-phenyl-4,4,5,5tetramethylimidazoline-1-oxyl-3-oxide, PTIO) can be used as posolyte and negolyte, which helps to counteract the severity of the cross-mixing. It has high solubility of 2.6 M in ACN, and the battery exhibit a cell potential of 1.7 V [53]. As shown in Figure 1.11, the redox-active part is nitro-oxide radical, which can undergo reduction to form an aminoxyl anion and oxidation to get oxoammonium anion. Similar to AQ, the aromatic ring is responsible for stabilization.

TEMPO

The all-organic redox cell was reported using 4-Oxo 2,2,6,6-tetramethyl-1-piperidinyloxy (4-Oxo TEMPO) as a posolyte and (1S)-(+)-Camphorquinone as a negolyte [53,58]. TEMPO is stabilized by the methyl groups neighboring the N-O moiety, as shown in Figure 1.11 (c). It has only one redox pair and is usually used as a posolyte. The NAqRFB with these redox species yields a cell potential of 2.12 V at a SOC = 50 %. The battery cycling performance was averaged to η_{CE} = 80.3 % and η_{EE} = 71.3 %.

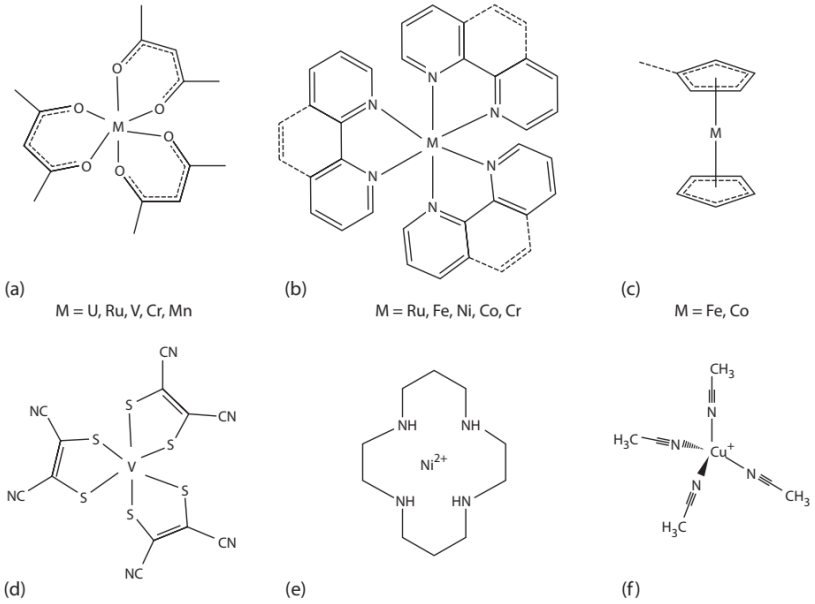


Figure 1.11 Metal-based redox species with different ligands: (a) acetylacetonate complexes, (b) 2,2-bipyridine complexes, (c) metallocene, (d) dithiolate vanadium complex, (e) tetradentate nickel complex, and (f) ACN–copper complex. (Source: [13]*)*

N-methylphthalimide

The voltammograms of the redox species highlighted the quasi-reversible but stable redox reactions, and the redox potential was measured to be -1.3 V *vs.* Ag/Ag^+ [59]. TEMPO was employed as posolyte and N-methylphthalimide as negolyte. The battery cycling performance was averaged to η_{CE} = 90 % for the first 20 cycles.

1.6 Solvents

The solubility of redox species and supporting electrolytes is directly dependent on the polarity of solvents. Since organic solvents have less polarity and this hinders them from offering higher solubility. Mixing different solvents has proved beneficial to fine-tune the properties for the applications to the RFB field [60]. The volatility of the organic solvents is also a safety concern and should be handled with proper precautions. The application of deep eutectic solvents (DES) is becoming favorable because of its economical aspects and can be prepared conveniently [47,48,61,62].

An ideal solvent should have the following characteristics [61].

- It is liquid at experimental temperatures.
- It dissolves high concentrations of the redox species and supporting electrolytes.
- It is stable toward the redox reactions within the potential range of the experiment.
- It does not lead to parasitic reactions with the other components.

1.6.1 Operational Temperature Range

The aqueous-based electrolyte cannot be operated at sub-zero temperatures, which adds the benefit of using non-aqueous electrolytes. Shallow temperatures are possible using solvents such as tetrahydrofuran THF or Acetonitrile ACN, which have freezing points of - 108 °C and - 44 °C, respectively. There are also solvents with significantly higher boiling points than water, such as N-methyl-2-pyrrolidone or Propylene carbonate (204°C and 242°C, respectively [63]). For the cases of high operating temperatures, DES can also be used instead of organic solvents.

1.6.2 Electrochemical Window

It is subjected to the interaction of solvent with supporting electrolyte and material of the working electrode. The water-splitting reaction occurs at *ca.* 1.6 V, which limits a further increase in the potential of the aqueous-based battery technologies. The non-aqueous electrolyte should remain stable within this electrochemical window while also providing flexibility to choose redox species having a significant potential difference between the redox pairs. The electrochemical window for the electrochemical systems studied in this document is shown in Figure 1.13, which highlights the effect of variation in each factor. Cyclic voltammetry can be performed on the blank electrolyte (without any redox species) to measure the electrochemical window for any particular combination.

1.6.3 Solubility

The energy capacity of the cell is directly dependent on the concentration of the redox species in the electrolyte. Therefore, solubility offered by the solvent is another essential selection criterion while designing the NAqRFB. Solvents are usually classified into polar protic, dipolar aprotic, and non-polar. Polar protic solvents are compounds that the generalized formula of ROH can represent. Solvents in the class of dipolar aprotic contain a bond that has a significant bond dipole. Typically this bond is multiple bonds between carbon and either oxygen or nitrogen. Non-polar solvents have low dielectric constants and are not miscible with water. The solubility is dependent on the polar interactions, Van der Waals forces, or hydrogen bonding. Ions mostly need strong dipolar interactions to reach high solubility. For this reason, researchers often choose dipolar aprotic solvents such as Acetonitrile (ACN) and propylene carbonate (PC).

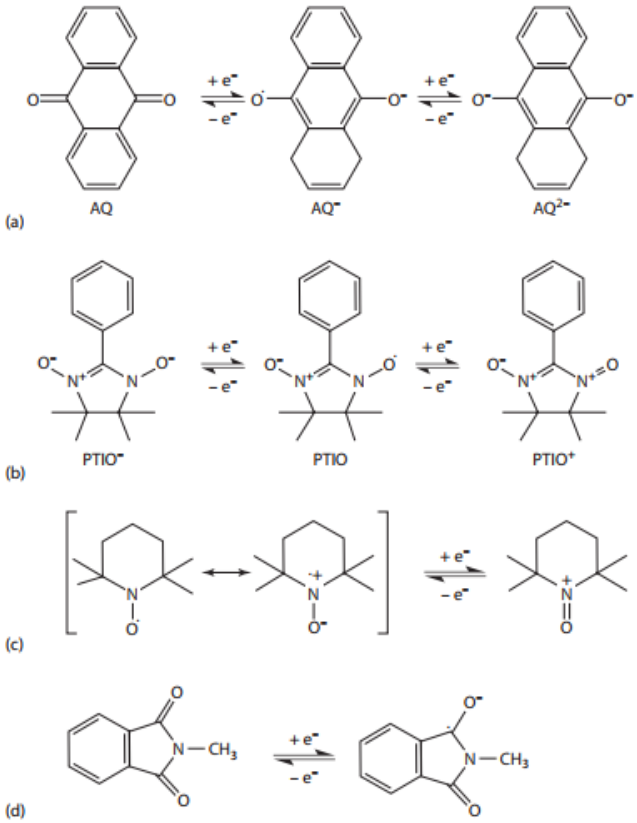


Figure 1.12 Structures and redox reactions of (a) AQ, (b) PTIO, (c) TEMPO, and (d) N-methylphthalimide during oxidation and reduction. (Source: [13]*)*

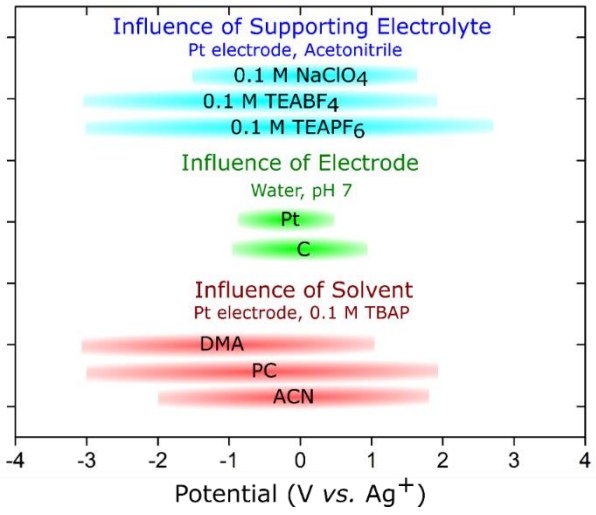


Figure 1.13 The supporting electrolyte, solvent, and nature of the electrode influence the electrochemical window which is measured in this document using cyclic voltammetry. Acronyms: Sodium perchlorate ($NaClO_4$), Tetraethylammonium tetrafluoroborate ($TEABF_4$), Tetramethylammonium hexafluorophosphate ($TEAPF_6$), Tetrabutylammonium perchlorate (TBAP), N,N-Dimethylacetamide (DMA), Propylene carbonate (PC), Acetonitrile (ACN).

However, reaching a higher concentration of redox species in the electrolyte solution is essential, and the oxidation state of the redox species and supporting electrolyte. The latter should be dissociated into the ions to enable high reversibility and ionic conductivity. The Denison Ramsey model - Equation (1.7) - provides a correlation between the dissociation constant (K_d) of an ion pair and the relative permittivity of a solvent.

$$-\ln(K_\mathrm{d}) = \frac{{q_\mathrm{E}}^2}{\varepsilon_0 \cdot \varepsilon_\mathrm{r} \cdot L \cdot k_\mathrm{B} \cdot T} \tag{1.7}$$

where q_E is the elementary charge, ε_0 and ε_r are the permittivity in a vacuum and the relative permittivity, L is the distance of the closest approach of the two ions of a dissolving species, k_B is the Boltzmann constant, T is the temperature. This equation (1.7) highlights that a more significant fraction of ions is in a dissociated state if a more polar solvent is used. Polar and dipolar solvents are a good choice to ensure high redox solubility and a high amount of dissociated ions.

1.6.4 Viscosity

Redox flow battery store / retrieve the energy into the electrolyte and the pump is used for circulation. Choosing a low viscous solvent allows for lower pumping requirements resulting in higher overall efficiency of the system. It is not only crucial from the design point of view but also the diffusion of ions is also dependent on the viscosity. Stoke's law explains the relationship between the limiting molar conductivity (Λ_m) and viscosity (μ) as given below.

$$\Lambda_\mathrm{m} = \left(z^2 \cdot \frac{F^2}{\pi \cdot N_\mathrm{A}}\right) \times \frac{1}{(k \cdot \mu \cdot r)} \tag{1.8}$$

where z is the charge number; F is the Faraday's constant; N_A is the Avogadro's number; k is the Stoke's constant; μ is the dynamic viscosity; r is the ionic radius. Equation (1.8) highlights the inverse relationship between conductivity and viscosity. It is critical for redox flow battery operation that the all the reagents (such as redox species and salt for supporting electrolytes) dissolve into solvent while allowing dissociation into the ionic form necessary for redox reaction. The intelligent selection is to choose a solvent having low viscosity, high conductivity, and good dissociation of ions. The latter reasons encourage researchers to choose Acetonitrile because it offers high polarity with low viscosity and is also readily available for industrial applications.

1.7 Supporting Electrolytes

Organic solvents have a limited electric conductivity, which compels the inclusion of supporting electrolytes. Protons and hydroxyl ions are frequently used in aqueous RFBs. The low polarity of organic solvents, compared to water, hampers the dissociation of those small ions. As a result, alternative larger ions must be chosen to boost conductivity. Both the supporting cation and anion have specific properties that contribute to the ionic conductivity of the electrolyte through the membrane. When comparing different supporting ions, the limiting molar conductivity is a reasonable metric to use. Table 1.5 displays conductivity examples of supporting electrolytes for various electrochemical applications. The supporting electrolytes in nonaqueous RFBs have substantially lower conductivities than those in aqueous RFBs.

The supporting electrolyte in aqueous RFBs is usually H^+ or OH^-, which have outstanding molar conductivity (Λ_m = 349.81 $S \cdot cm^2 \cdot mol^{-1}$ and 198.0 $S \cdot cm^2 \cdot mol^{-1}$, respectively). The supporting anions BF_4^- [64], ClO_4^-, and PF_6^- [34,65] are the smallest ions used for non-aqueous RFBs having the ionic radii of 2.29 Å, 2.37 Å, and 2.54 Å, corresponding to the limiting molar conductivities of 108.5 $S \cdot cm^2 \cdot mol^{-1}$ [66], 103.6 $S \cdot cm^2 \cdot mol^{-1}$ [66], and 102.8 $S \cdot cm^2 \cdot mol^{-1}$ [67] in Acetonitrile, respectively. Because of its low viscosity, Acetonitrile offers the highest conductivity compared to other solvents with supporting electrolytes. These supporting anions have similar degradation potentials to several common organic solvents (*e.g.*, 3.1 - 3.8 V in PC *vs.* SHE at 25°C); therefore, they can be utilized without restricting the electrochemical window (ECW).

Tetraalkylammonium ions are the most prevalent nonaqueous RFB supporting cations, with tetraethylammonium (TEA^+) [64] and tetrabutylammonium (TBA^+) [34,65] being the most common. In the instance of the supporting cations, the smaller TEA^+ has a higher limiting molar conductivity of 85.19 $S \cdot cm^2 \cdot mol^{-1}$ (in ACN *vs.* SHE at 25 °C), compared to 61.63 $S \cdot cm^2 \cdot mol^{-1}$ for TBA^+ [68]. Since these tetraalkylammonium molecules are larger than the previously described supporting anions, their limiting conductivities are lower. The limiting molar conductivity of the supporting anion and cation is identical when their molecular sizes are similar. Other supporting cations exist in addition to tetraalkylammoniums, with Li^+ being a prominent example. Lithium has one of the lowest ionic radii, *ca.* 0.76 Å. Despite this, it exhibits a limiting molar conductance of 69.97 $S \cdot cm^2 \cdot mol^{-1}$ in Acetonitrile [63], which lies between the conductivities of cations TEA^+ and TBA^+.

For nonaqueous RFBs, the solubility of the supporting ions is critical, just as it is for other components. In the case of tetraalkylammonium ions, solubility rises with chain length as van der Waals interactions with the solvent increase. However, the inherent solubility of the ions should be taken into account, along with the solubility of other ions. For example, higher concentrations of Vanadium acetylacetonate - $V(acac)_3$ - can considerably reduce the solubility of $TEABF_4$. As a result, the supporting electrolyte concentration should be carefully selected, as the conductivity of the electrolyte should be balanced with the concentration of redox-active species. Furthermore, using high concentrations of supporting ions lowers molar conductivities because those highly concentrated samples also contain a large fraction of associated ions that are not active for ion transport. Increasing the amount of supporting ions, on the other hand, increases the number of ion concentrations. Since the two trends are at odds, a critical concentration should be identified to improve the tradeoff.

Table 1.5 Conductivity of supporting electrolytes in various battery applications.

Supporting Electrolyte	Solvent	Conductivity ($mS \cdot cm^{-1}$)	Application	Ref.
H_2SO_4 ($3.0\ mol \cdot L^{-1}$)	H_2O	790	Aqueous Vanadium RFBs	
KOH (29.4 wt %)	H_2O	540	Aqueous alkaline batteries	[69]
$TEABF_4$ ($1.0\ mol \cdot L^{-1}$)	Acetonitrile	60	Nonaqueous RFBs	[69]
$LiPF_6$ ($1.0\ mol \cdot L^{-1}$)	EC + DMC	10.7	Lithium based batteries	[70,71]

Acronyms: EC = Ethylene carbonate, DMC = Dimethyl carbonate

1.8 Membranes

The membrane is an essential component of nonaqueous RFBs because it prevents self-discharge by avoiding cross-contamination of redox species in the posolyte and negolyte, which are segregated into two compartments. The membrane must also selectively transport balancing-ions with a low area resistivity during cell operation to complete the electric circuit [72–74]. An ideal membrane for a nonaqueous RFB should comply with the following criteria.

a) *High ionic conductivity of balancing-ions:* The membrane must allow for electroneutrality, permitting balancing-ions to diffuse from the posolyte to the negolyte and vice versa. The high ionic conductivity is essential to maximize cell performance while minimizing voltage efficiency loss.

b) *High ionic selectivity of redox species:* Even though the balancing ions need high permeability, the redox species must be isolated. The redox species can permeate during the operation of a nonaqueous RFB, resulting in the crossover. As a result, the reactive species react directly instead of passing through the electric circuit to provide useful work, causing capacity loss and degradation in the cell's efficiency.

c) *Chemical and mechanical stability:* Unlike aqueous RFBs, membranes in nonaqueous RFBs are exposed to organic solvents such as Acetonitrile (ACN) or Propylene Carbonate (PC) during the oxidation and reduction of redox species. The membrane must maintain its physical form for hundreds or thousands of battery cycles. Good chemical and mechanical stability are essential to ensure a long lifetime of RFB.

Since non-aqueous RFB is still a nascent and rapidly developing technology, no commercial membranes meet the earlier mentioned criteria. As a result, appropriate membranes must be developed before any pilot or commercial deployment of nonaqueous RFBs. Membrane separation in flow batteries is generally based on a combination of the Donnan effect and size exclusion. The problem of species separation, on the other hand, is quite complicated. Since the redox species are positively charged on both sides of the cell in the Fe-Ni system, the anion exchange membranes (AEMs) should have a low permeability for the redox species, whereas all-vanadium systems have redox species with the opposite bias. In this circumstance, selecting an effective ion-exchange membrane to maximize battery performance is challenging.

The redox species in nonaqueous flow batteries are substantially larger than the balancing-ions. In this instance, it is feasible to utilize nano-porous membranes, allowing only the transport of tiny, charge-balancing ions and not redox species. As a result, composite porous charged membranes may be the best option.

1.8.1 Anion and Cation Exchange Membranes (AEMs and CEMs)

Commercial AEMs and CEMs have been developed for the desalination of the sea or brackish water and treat industrial effluents [75]. Because such membranes were not designed for organic electrolytes, they lack sufficient chemical and mechanical stability

needed for use in nonaqueous RFBs [76]. Nonetheless, they have been used in various nonaqueous RFBs to some extent, demonstrating their general applicability - Table 1.6.

The Nafion series membranes are the most often utilized CEMs in nonaqueous RFBs. The type of counterion in the membrane substantially affects the conductivity, according to the research on the ion-exchange behavior of Nafion 1035 membranes in nonaqueous vanadium acetylacetonate RFBs employing $TEABF_4$ as the supporting electrolyte. In ACN, the membrane's conductivity was 0.7 $mS \cdot cm^{-1}$. Weakening the anionic site contact by introducing the tetrabutylammonium and tetraethylammonium ions helped improve the conductivity by a factor of 7 and 14, respectively [77].

Small, positively charged balancing ions, such as Li^+, have also been reported in nonaqueous RFBs that employ 2,5-di-tert-butyl-1,4-bis(2-methoxyethoxy) benzene quinoxaline-derivative redox-active materials [78]. Using a commercial Nafion 117 membrane in this context could reduce redox species' permeability while maintaining good Li^+ conductivity.

Table 1.6 Commercial membranes used for non-aqueous RFBs.

Types	Name	Area resistance ($\Omega \cdot cm^2$)	Electrolyte	Cell type	Charge-Discharge density ($mA \cdot cm^{-2}$)	Efficiency (%)	Ref.
AEM	Neosepta AHA	36.2	0.05 M $V(acac)_3$ + 1 M $TEABF_4$ + ACN	Flow-cell	0.3 / 0.3	EE 90	[79]
	AMI-7001		0.01 M $V(acac)_3$ + 0.5 M $TEABF_4$ + ACN	H-type cell	2.2 / 0.2	CE 47	[80]
	Fumasep FAP-PK	48.8	0.4 M $Fe(bpy)_3$ / 0.2 M $Ni(bpy)_3$ + 0.5 M $TEABF_4$ + PC	Flow-cell	2.0 / 2.0	CE 94, VE 82	[81]
CEM	Nafion 1035	1.0	0.1 M $V(acac)_3$ + 0.5 M $TEABF_4$ + ACN	Flow-cell	10.0 / 10.0	CE 91, EE 80	[77]
Porous Membrane	Celgard 2400	4.5	0.01 M $V(acac)_3$ + 0.1 M $TEABF_4$ + ACN	Flow-cell	1.39 / 1.39	CE 49, EE 32	[82]
	Daramic	1.5	0.1 M $V(acac)_3$ + 0.5 M $TEABF_4$ + ACN	Flow-cell	10.0 / 10.0	CE 74, EE 68	[77]

Acronyms: EE = Energy efficiency, CE = Coulombic efficiency, VE = Voltage efficiency

1.8.2 Size Exclusion Membranes (Porous membranes)

As previously indicated, redox couples can be made up of ligated metal complexes and massive organic molecules. Porous membranes or size exclusion membranes are an interesting technique for separating redox species and charge balancing-ions. Since balancing-ions are often significantly smaller [83], the porous membrane allows for high balancing-ion conductivity and offers low ohmic resistance, enabling the nonaqueous RFBs to operate at high current densities [79]. Porous membranes are available in a variety of shapes and sizes. As an example, the commercial Daramic porous separator was utilized in a PTIO-based RFB [65]. The approach's generality has also been demonstrated using commercially available porous polypropylene [84] and a porous polyethylene separator [85].

A rigorous examination of through-plane conductivities comparing numerous commercial ion-exchange membranes and the commercial microporous Celgard 2500 membrane highlights that microporous membranes had significantly lower conductivity than the tested ion-exchange membranes while using ionic-liquids as solvents [81]. Because of the lower thickness of the membrane, the conductivity was comparable to that of the best AEMs. The Celgard 2500 membrane's conductivity exceeded the other membranes evaluated when ACN was utilized as the solvent and $TEABF_4$ as the supporting electrolyte [81].

1.9 Electrodes

The cell potential (V_{CELL}) during discharging of NAqRFB systems is lower than the open circuit potential (E_{OCP}) at any instant. The battery researchers are striving to reduce this difference to achieve higher performance of this technology. This difference (voltage loss) is comprised of activation polarization, ohmic losses, and concentration polarization [86]. At any instance throughout the cell's operation, the cell potential can be stated as follows:

$$V_{CELL} = E_C - E_A - \eta_A - \eta_C - I \times R_\Omega \qquad (1.9)$$

where V_{CELL} is the discharge potential at any point while discharging the cell at current I; the difference between E_C and E_A represents open-circuit voltage (E_{OCP}); η_A and η_C are overall activation and concentration overpotentials for both anodic and cathodic reactions during the discharging process; and R_Ω is the ohmic resistance. The overall internal resistance during the discharging process is given as:

$$R_{\mathrm{CELL}} = \frac{\eta_{\mathrm{A}}}{I} - \frac{\eta_{\mathrm{C}}}{I} - R_{\Omega} \qquad (1.10)$$

The performance of the cell can be improved by lowering the overall internal resistance of the cell. The activation polarization resistance (η_{A}/I), also known as the electron transfer resistance or charge transfer resistance (R_{CT}), is closely linked to the electrocatalytic activity of the electrodes [87]. The physical resistance of the battery's essential components, such as electrodes, ion exchange membrane, electrolyte, and bipolar plates, as well as the contact resistance between electrodes and bipolar plates, contribute to making up ohmic resistance (R_{Ω}). Any improvements in the conductivity of these components can decrease the ohmic resistance. The surface condition of the bipolar plates and/or the clamping conditions could reduce the corresponding contact resistance leading to lower ohmic resistance.

The concentration polarization resistance (η_{C}/I) or mass transport overpotential is proportional to the flowing condition of the electrolyte. By increasing the flow rate, the thickness of the electrolyte diffusion layer will be reduced to some extent and vice versa. The introduction of a flow field can assist but there is no universal single solution for this optimization. It is recommended to consider the individual unique design of each flow cell to develop strategies to lower mass transport effects. Another approach is the uniform distribution of electrolytes through flow channel modification such as optimizing channel width and length.

Electrolytes are the energy storage medium for RFBs, and electric charges can be stored or released via reduction/oxidation reactions of redox species by acquiring different valence states. The electrodes used in any RFB only provide an active surface to perform electrochemical reactions instead of participating in the redox reaction like other types of batteries such as Li-ion, lead-acid, Ni-MH, *etc*.

Electrodes can play a vital role in lowering the activation and ohmic resistance [88], which are two main parts of the equation (1.10). The aforementioned reasons highlight that the requirement of electrodes for any redox flow battery is different from other types of batteries, where electrodes participate in the battery reactions such as Li-ion, lead-acid, Ni-MH, *etc*. In addition to providing a platform for the reactions, electrodes are also responsible to assist in the dispersion of electrolytes from bipolar plates to the ion-exchange membranes. Targeting the scope of this document, the prerequisite of the electrodes for the non-aqueous redox flow batteries can be summarized as [86,89–91]:

a) Favorable electro-catalytic activity: Carbon felt electrodes are cost-competitive, but they offer lower surface area and slow kinetics [92]. Various treatments [93–95] are reported to get oxygen functional groups to enhance the performance of V-RFBs. Since non-aqueous electrolytes are sensitive to the presence of oxygen and treated electrodes can become an additional source of oxygen, resulting in the adverse performance of NAqRFBs [96,97]. The presence of oxygen functional groups at the surface of the carbon-felt electrodes leads to parasitic reactions and severe capacity fade is observed [40,77]. Therefore, oxygen-free electrodes or electrodes having inert functional groups are recommended to be used for non-aqueous electrolytes.

b) It is recommended to use a three-dimensional structure having high porosity, shape retention during compression, and good mechanical strength and toughness. Conventional electrode materials, such as carbon felt [73], graphite felt [98], carbon paper [99], and carbon cloth [100] rely on beneficial porous structures with fair electrical conductivity and offer good chemical stability, and good corrosion resistance [101].

c) A larger electrochemical surface area is highly beneficial to improving voltage efficiency and limiting current density. It can be performed using the coating of various nanoparticles such as carbon nanotubes, graphene, reduced graphene oxide, and carbon black. There are numerous studies reported for aqueous RFBs [102,103] but a research gap exists in studying the impact of adding different nanoparticles to the electrodes for NAqRFBs. As reported elsewhere [104], carbon nanotubes for posolyte and graphene for negolyte is a good combination.

d) Higher electrical conductivity can be achieved by using the augmentation of highly conductive noble metals [105]. The nonaqueous electrolytes are not acidic, so this enabled use of metal foams as electrodes [86] providing higher electrical conductivity.

e) Workable in the wide electrochemical window of non-aqueous electrolytes. The purpose of the electrodes is to provide electrocatalytic activity, so these should not exhibit redox behavior within the chosen electrochemical window [106]. The electrodes should also offer good chemical stability and compatibility.

1.10 Research Strategy for Thesis

The thesis is focused on the research studies about non-aqueous redox flow battery (NAqRFB) under the supervision of Prof. Adélio Mendes at the Faculty of Engineering, University of Porto (FEUP), Portugal, and worked on the liquid displacement battery under the co-supervision of Prof. Donald R. Sadoway during the stay at Massachusetts Institute of Technology (MIT), Cambridge, US.

The structure of the Ph.D. thesis highlights the contributions of this work as mentioned in Table 1.7 and it is divided into the parts: (Part I) Liquid Displacement Battery (LDB), (Part II) Non-aqueous Redox Flow Battery (NAqRFB).

Liquid Displacement Batteries (LDB) are promising but need mitigation for the self-discharge effect. Reducing the diffusion coefficient of lead ions can be a way forward. Part I is having Chapter 2, which is targeted at mitigating of self-discharge defect of LDBs.

Although non-aqueous battery development has sparked worldwide attention, there are still some significant challenges to overcome before large-scale or pilot-scale implementation may be achieved. The state-of-the-art highlighted following research questions which are addressed in this thesis to overcome these challenges:

(a) High crossover through membranes
(b) High internal resistance
(c) Parasitic reactions affect the stability of electrolytes and capacity retention
(d) Electrodes have a lower surface area and slow kinetics.
(e) Global availability and higher cost of redox species for NAqRFB
(f) Eco-friendly alternatives while offering high solubility

Part II is having Chapter 3 targets challenge no. (a) whereas, Chapter 4 targets challenge no. (b). Electrodes improvements were performed in Chapters 5 and 6 addressing challenge no. (c) and (d). Novel electrolytes are presented as proof-of-concept NAqRFB-cells in Chapters 7 and 8 addressing challenges no. (e) and (f). The last chapter summarized all the contributions of the Ph.D. thesis in the concluding words and future recommendations.

Table 1.7 Structure of Ph.D. thesis highlighting the contributions

Thesis	About NAqRFB and LDB		Chapter 1	Introduction to NAqRFB
	Part 1	Research on LDB	Chapter 2	Self-discharge mitigation of LDB
	Part 2	Research on NAqRFB	Chapter 3	*In-situ* crossover diagnostics
			Chapter 4	Composite membrane
			Chapter 5	Parasitic reaction free electrodes
			Chapter 6	Nanoparticles coated electrodes
			Chapter 7	Novel Aluminium-ion based NAqRFB
			Chapter 8	Bio-inspired eco-friendly negolyte
	About NAqRFB and LDB		Chapter 9	Retrospectives, Conclusions, and Perspectives

Part I

Chapter 2

Self-discharge mitigation of liquid metal displacement battery

2. Self-discharge mitigation of liquid metal displacement battery

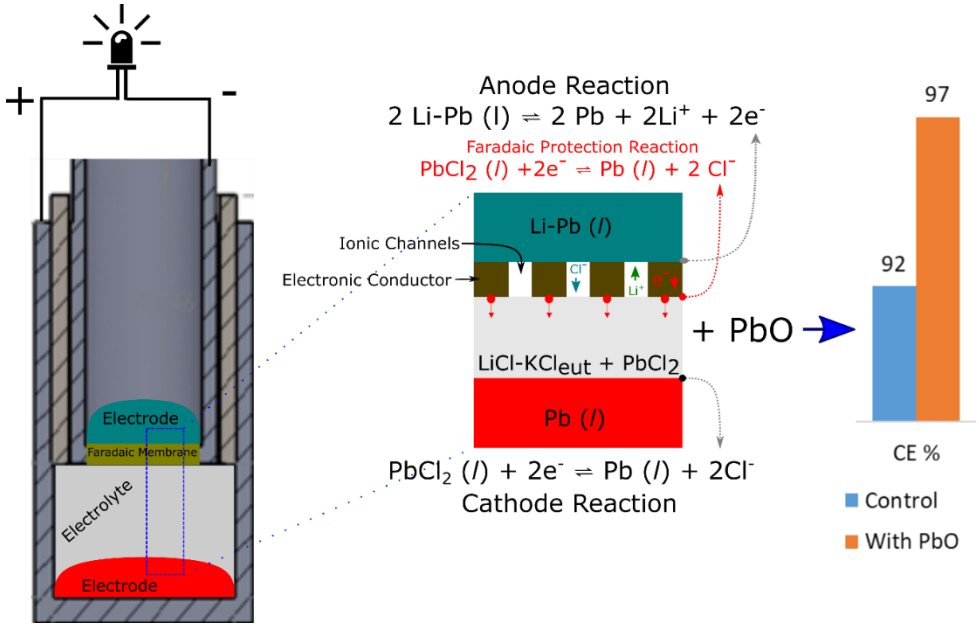
Adapted from the following articles:

K. Mushtaq, Ji Zhao, N. Weber, D. Sadoway, "Performance enhancement and characterization of liquid displacement battery having faradaic membrane", 14th Workshop on Reactive Metal Processing RMW14, (March 2019), Massachusetts Institute of Technology, Cambridge, US.
URL: http://www.okabe.iis.u-tokyo.ac.jp/core-to-core/rmw/RMW14_index.html

K. Mushtaq, Ji Zhao, N. Weber, A. Mendes, D. Sadoway, "Self-discharge mitigation of liquid metal displacement battery", Journal of Energy Chemistry, Elsevier.
URL: https://doi.org/10.1016/j.jechem.2021.08.015

Recently, a disruptive idea was reported about the discovery of a new type of battery named Liquid Displacement Battery which is based on molten metal as the electrode and molten salt as electrolyte. This cell was using a novel concept of a porous faradaic membrane instead of the traditional ion-selective ceramic membrane. LDBs are promising but need mitigation for the self-discharge effect. Reducing the diffusion coefficient of lead ions can be a way forward and a solution can be the addition of PbO into the electrolyte. The latter acts as a supplementary barrier and complements the function of the faradaic membrane. The remedial actions allowed to increase the cell's columbic efficiency from 92% to 97% without affecting the voltage efficiency. The impact of adding PbO on the impedance and polarization of the cell was studied. The limiting current density also increased from 575 $mA \cdot cm^{-2}$ to 831 $mA \cdot cm^{-2}$ for a 500 mAh cell and the limiting power from 2.53 W to 3.66 W.

Graphical Abstract



The addition of PbO acts as a mitigator to suppress self-discharge and enhance the performance of the liquid metal displacement battery.

2.1 Introduction

Climate change is one of the biggest challenges of the current era. Europe is committed to achieving the vision of a climate-neutral society by 2050 [8]. This transition motivates us to find innovative solutions for the mitigation of the adverse effects of energy consumption and conversion. This also drives how electrical energy is produced, consumed, and stored. Implementation of electric vehicles is also a key step toward battling CO_2 emissions. Batteries are the true enablers for this vision, but these need to be made safer, better performing, more sustainable, and affordable. Batteries should exhibit high performance beyond their capabilities today. Furthermore, reliable batteries can provide greater resiliency to the existing grid while also lowering emissions [9]. The most promising commercial battery technologies are lithium-ion, lead-acid, redox-flow, and high-temperature batteries such as sodium-sulfur and liquid metal batteries [10]. Especially, the technological options of redox flow and high-temperature batteries promise low specific cost and easy upscaling. This makes them very attractive for stationary storage applications.

The transition to a more electricity-based society needs disruptive ideas that can enable the creation of sustainable batteries for the future. In the continuation of these efforts, recently a ground-breaking idea was reported by Group Sadoway laboratory, MIT, USA by discovering a new type of battery named Liquid Displacement Battery (LDB) [9]. The latter combines the benefits of the liquid metal battery with those of membrane-based cells, *e.g.*, the sodium-sulfur battery, which relies on a β”-Al_2O_3 Na-ion conducting membrane. The fragility and brittleness of the β”-Al_2O_3 ceramic set severe design constraints and limit its performance. Also, its vulnerability to attack by transition-metal ions in chloroaluminate melt is a concern. LDB has a new concept of a porous electronically conductive membrane instead of an ion-selective ceramic conductor. This membrane removes the barrier for researchers to choose only liquid Na for negative electrodes and solid halides for positive electrodes [9].

The schematic of a liquid displacement battery based on the electrochemistry of Li-Pb || $PbCl_2$ is shown in Figure 2.1. The negative electrode is comprised of molten Li - Pb, where Li is the active species and Pb serves as the host metal. The eutectic composition of LiCl - KCl is used as a molten-salt electrolyte. Molten Pb is serving as the positive electrode and $PbCl_2$ exists in the electrolyte in a dissolved state. The

electrochemistry of Pb/Pb^{2+} displacement reactions in molten LiCl-KCl is explained by Huayi Yin [9] as given below.

$$2\,Li\left(Pb_{(l)}\right) + 2\,Cl^{-}_{(LiCl-KCl(l))} \rightleftharpoons 2\,LiCl_{(LiCl-KCl(l))} + 2\,e^{-} \quad (2.1)$$

$$PbCl_{2(LiCl-KCl(l))} + 2\,e^{-} \rightleftharpoons Pb_{(l)} + 2\,Cl^{-}_{(LiCl-KCl(l))} \quad (2.2)$$

This leads to the cell displacement reaction

$$2\,Li\left(Pb_{(l)}\right) + PbCl_{2(LiCl-KCl(l))} \leftrightarrow Pb_{(l)} + 2\,LiCl_{(LiCl-KCl(l))} \quad (2.3)$$

The use of membranes is a widely accepted concept in the field of batteries and fuel cells. Mostly, ion exchange membranes are used as an electrolyte barrier between the half-cells. The membranes fabricated for this study enable ion exchange because of their porous nature and are also electronically conductive to allow for a "faradaic protection" reaction. When Pb^{2+} ions reach the lower surface of the membrane, they will be reduced faradaically into Pb metal. The lead droplets, formed at the surface of the membrane, sink back into the pool of Pb (*l*). This self-discharge reaction, which is caused by the diffusion of lead ions from the bottom of the electrolyte towards the membrane, is of course detrimental. The membrane acts here simply as a lead barrier preventing irreversible lead transfer from the positive to the negative electrode. LDBs built in the past exhibited a columbic efficiency of 92 % and an energy efficiency of 71 % while operating at a current density of 150 $mA \cdot cm^{-2}$ at a temperature of 410 °C. The limited columbic efficiency is not caused by irreversible side reactions, but simply by the self-discharge reaction, explained above [9]. LDBs are promising but require further mitigation strategies to reduce self-discharge. The latter is the scope of this study.

The reported battery is relatively recent, but the electrochemical reactions explained above are well established and are being used for lead deposition from molten chlorides. The characteristics of the mixtures of molten salts and metals are reported elsewhere [107]. The diffusion coefficient of lead ions in molten chloride mixtures has been reported to be 2×10^{-5} $cm^2 \cdot s^{-1}$; the cathodic deposition of lead was found to be diffusion controlled [108–111] for the diluted solution of $PbCl_2$ in molten KCl-LiCl at 400 °C - Figure 2.2. A formulation based on applying Faraday's law and species transport equations leads to a relationship highlighting the direct proportionality of the self-discharge current density and the diffusion coefficient. The mathematical formulation is given in the supplementary information (*c.f.* 11.1).

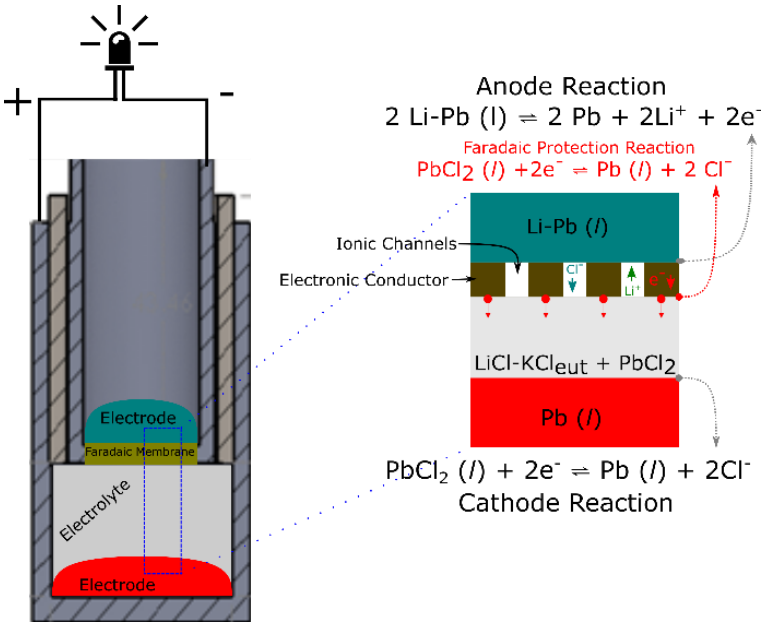


Figure 2.1 Schematic of a Liquid Displacement Battery. The detailed view shows the ion transport and faradaic reaction across a porous electronically conductive membrane.

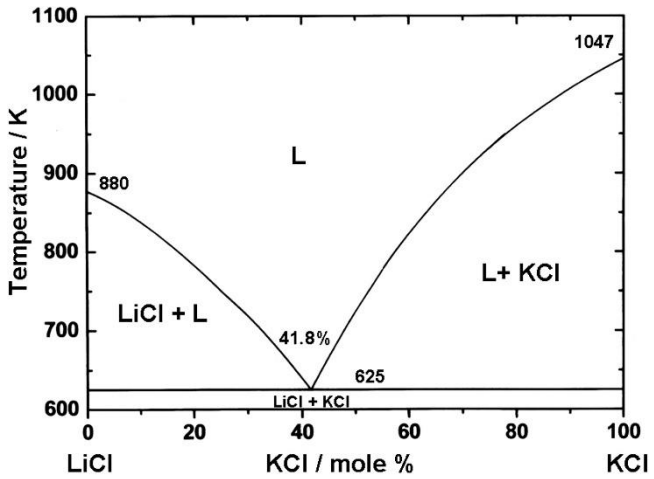


Figure 2.2 LiCl - KCl pseudo-binary phase diagram. Liquid metal displacement battery used molten salt electrolyte in eutectic mole composition of LiCl : KCl = 40.8 % : 59.2 %. Adapted from [112].

Different remedies can be used to reduce self-discharge such as increasing the thickness of the electrolyte (salt) layer, reducing the solubility of $PbCl_2$ in the electrolyte, lowering the operating temperature, freezing the electrolyte during standstill, binding $PbCl_2$ to some other structure inside the Pb [113], or by using an electrolyte featuring a miscibility gap. The idea of this study is to convert $PbCl_2$ into another complex compound leading to a reduction of the diffusion of the Pb-ions.

2.2 Materials and Experimental Methods

2.2.1 Chemicals

Lead (99.99%, anhydrous, Sigma Aldrich) was used as electrodes. The electrolyte was prepared using the eutectic composition for a mixture of lithium chloride (LiCl, 99.9 % anhydrous supplied by Alfa Aesar) and potassium chloride (KCl, 99.9% anhydrous supplied by Alfa Aesar). Membranes were prepared using titanium nitride (TiN) powder (Alfa Aesar, 99.7%, <10 μm) and Magnesia (MgO) nano-powder (Inframat Advanced Materials). Lead-oxide was also obtained from Alfa Aesar.

2.2.2 Preparation of Membrane

The porous TiN membrane referred to as the faradaic membrane was prepared using the method reported by [114]. The mixture having 5.4 g TiN powder and 0.6 g MgO nano-powder was mixed thoroughly by a pestle. It was then transferred into the graphite crucible (outer diameter: 2.54 cm, inner diameter: 2.3 cm, height: 4.4 cm) with an opening at the bottom having a diameter of 2 cm. This graphite crucible is acting as a current collector for the negative electrode as shown in Figure 2.3. The powder inside the crucible was hydraulically pressed by inserting a graphite rod. This gives mechanical strength to the powder and helps in attaching it to the crucible surface. This helps to avoid any leakage of the molten negative electrode during battery operation. The assembly was then transferred to the tube furnace which was purged three times with ultrapure Ar (99.99 %). Finally, it was blanketed with argon gas and heated to 1100 ^{O}C at a ramping rate of 6 ^{o}C·min^{-1}. The prepared assembly of the negative current collector carrying the mounted membrane was taken out of the furnace and allowed to cool to room temperature.

2.2.3 Assembly and assessment of the liquid displacement cell

The assembly of the liquid displacement cell is shown in Figure 2.3. Graphite crucibles were used to contain the molten electrode and molten salts. The positive electrode was connected to a metal rod serving as the current collector. The crucibles were insulated by using a ceramic sleeve. In the beginning, positive electrodes were loaded with layers of lead granules followed by a mixture of LiCl and KCl as molten salt electrolytes having a eutectic composition [115]. The negative electrode consisting of lead granules was placed on top of the solid electrolyte. This assembly was placed inside the furnace maintained at 415 ^{o}C to obtain molten layers of all the added reagents. It was ensured that the bottom part of the negative electrode with its membrane was in good

contact with the molten salt electrolyte before the start of measurements. Data obtained from charge/discharge cycling enabled the calculation of coulombic, voltage, and energy efficiencies (η_{CE}, η_{VE}, and η_{EE}, respectively) for each cycle as given below.

$$\eta_{\mathrm{CE}_i} = \frac{\int_{t_{\mathrm{d},0}}^{t_{\mathrm{d},f}} I_{\mathrm{d}}\, dt}{\int_{t_{\mathrm{c},0}}^{t_{\mathrm{c},f}} I_{\mathrm{c}}\, dt} \tag{2.4}$$

$$\eta_{\mathrm{VE}_i} = \frac{\int_{t_{\mathrm{d},0}}^{t_{\mathrm{d},f}} E_{\mathrm{d}}(t)dt}{\int_{t_{\mathrm{c},0}}^{t_{\mathrm{c},f}} E_{\mathrm{c}}(t)dt} \times \frac{(t_{\mathrm{c},f} - t_{\mathrm{c},0})}{(t_{\mathrm{d},f} - t_{\mathrm{d},0})} \tag{2.5}$$

$$\eta_{\mathrm{EE}_i} = \eta_{\mathrm{CE}_i} \times \eta_{\mathrm{VE}_i} \tag{2.6}$$

where I is current, E is the cell potential difference, t is time, subscript i stands for the cycle number, subscript c for the charge, subscript d for discharge, subscript 0 for initial, and subscript f for final.

Activation of the cell was performed before conducting any measurements. Self-discharge measurements were performed by charging the cell up to the capacity of 500 mAh and then recording the open circuit potential (E_{OCP}) at the no-load condition for up to 48 h. This technique helps to isolate the impact of self-discharge on the performance of the cell. Impedance measurements were recorded at 10 mV amplitude and across the frequency range of 2.5 kHz to 1 Hz using the Autolab workstation. Potentiostatic measurements were performed to acquire polarization data from 0.4 V to 2.2 V at a scan rate of 10 $\mathrm{mV \cdot s^{-1}}$. The ohmic resistance contribution from the wires – 0.02 Ω – was subtracted from all polarization and impedance measurements.

2.3 Results and discussion

2.3.1 Mitigation of self-discharge

The activation of the molten electrodes and the molten electrolyte was performed through charge-discharge cycling (CDC) until the cell reached the operating capacity of 500 mAh. The cycling was done step-wise by operating the cell at the capacities of 25 mAh, 250 mAh, and 500 mAh as shown in Figure 2.4 (*i.e.* CDC at 50 mA, 100 mA, and 200 mA for charging times of 0.5 h, 2.5 h, and 2.5 h respectively). During the activation phase, the columbic efficiency at 25 mAh capacity increased from 25.5 % to 90.1 % in 5 cycles, which indicates that there was no short-circuiting through the membrane. The response of the cell recorded at 250 mAh and 500 mAh have shown similar values of

efficiency. The maximum value of the columbic efficiency achieved at 500 mAh was 91.3 % and of the voltage efficiency 74.98 %, which served together with the state-of-the-art value [114] and also used as a comparative benchmark in this study.

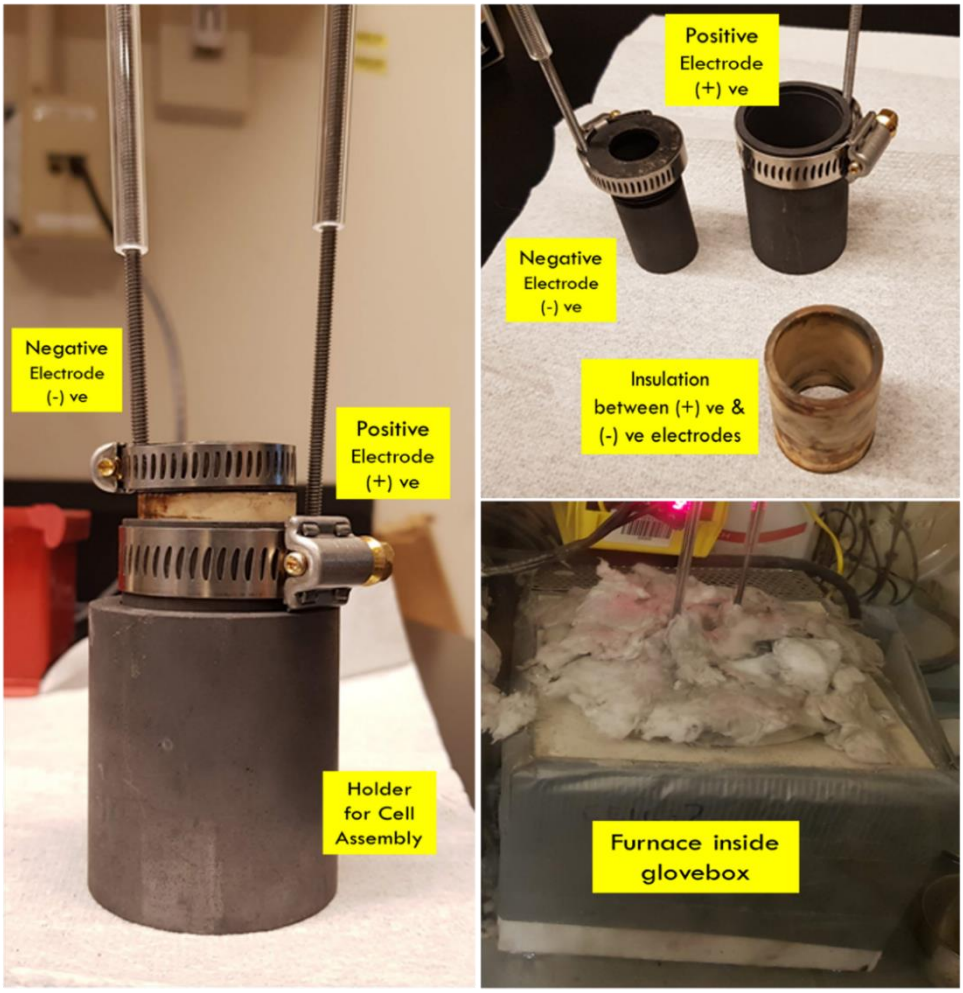


Figure 2.3 Assembly of the liquid displacement battery having the faradaic membrane.

The presented study is a continuation of a previous article [114]. The latter can be consulted for the detailed chemical and electrochemical characterizations of the lower surface of the membrane including SEM images and EDS mapping, which was performed before and after 100 cycles. The permeation rate of Pb^{2+} was measured by direct-current plasma chemical analysis. It was also evident that the performance of the cell is stable until 400 cycles. Nevertheless, it was observed that the battery exhibited a certain self-discharge at open-circuit conditions. Therefore, retention of the stored energy becomes the primary concern, and repetition of other results was avoided to remain focused solely on the mitigation of self-discharge.

There was an interesting study reported by Pershin et al. [108] for the electrodeposition of Pb. They reported the formation of a Pb_2OCl_2 compound when

adding PbO into a lead-contained melt. Hence, the addition of PbO to LiCl-KCl-$PbCl_2$ melt results in the reaction.

$$PbCl_2 + PbO \rightleftharpoons Pb_2OCl_2 \qquad (2.7)$$

The presence of PbO in the electrolyte complements the function of the faradaic membrane by providing additional steps for the electrochemical conversion of Pb^{2+}. It serves as an additional barrier to the diffusion of Pb^{2+}. This leads to the modification in the positive electrode half-cell reaction and can be described as below.

$$Pb_2O^{2+} + 2e^- \rightleftharpoons PbO + Pb^0 \qquad (2.8)$$

The diffusion-controlled process of self-discharge can be decreased because of the reduced concentration of free Pb^{2+} ions resulting from the formation of the Pb_2O^{2+} ions in the electrolyte. These two additional side reactions complement the functioning of the faradaic membrane. Pershin et al. [108] also optimized the effect of PbO in the lead-contained melt using various molar percentages of 0.54 %, 1.20 %, 1.78 %, and 2 %. The best results were observed for the 2 molar percentage and therefore chosen for further testing in the liquid metal displacement battery.

Self-discharge was examined by charging the cell up to the capacity of 500 mAh and then measuring the open circuit potential (E_{OCP}) for up to 48 hours without any applied current. During this resting phase, the cell was maintained at constant temperature and other ambient conditions, therefore any change in the value of E_{OCP} can be assigned to the self-discharge of the cell.

The result of the self-discharge test as a function of E_{OCP} is shown in Figure 2.5. It was observed that the cell potential kept on decreasing over time and there is a rapid drop for the control experiment after 24 hours of resting phase. However, a significant improvement was observed after the addition of 2 molar percent of PbO into the electrolyte of the cell. Then, the cell voltage remains stable even after 24 hours, and only a slight decrease was observed until 48 hours of the resting phase. The addition of PbO into the electrolyte results in a complex compound Pb_2OCl_2 and works as an additional filter to stop the crossover of Pb^{2+} ions which are responsible for the self-discharge. Interestingly, the two curves overlay each other for the region of up to 24 hours and the rate of self-discharge did not get prominent until E_{OCP} = 1.5 V.

During discharging of the cell, the reduction of Pb^{2+} is supported by oxidation of Li from the Li-Pb pool at the negative electrode. The pores of the membrane act as ionic

channels and assist the passing of Li^+ into the electrolyte. Moreover, there are two pathways for the electrons and the value of the columbic efficiency (η_{CE} = 91 %) as shown in Figure 2.6 suggests that the dominant pathway is the external circuit taking most of the total output of current. The electronically conductive membrane is providing the second pathway. It facilitates the reaction of Pb^{2+} at the lower surface of the membrane, blocking the transport of Pb^{2+} to the negative electrode (having a Li-Pb pool above). This confines the liquid Pb back to the positive electrode (having a Pb pool below). Since the addition of PbO provides additional reversible reactions, the need for electrons to be supplied through the second pathway is reduced. This in return increased the current flowing from the dominant pathway *i.e.* external circuit resulting in an increase in coulombic efficiency up to 97 % without affecting the voltage efficiency as shown in Figure 2.6 (c).

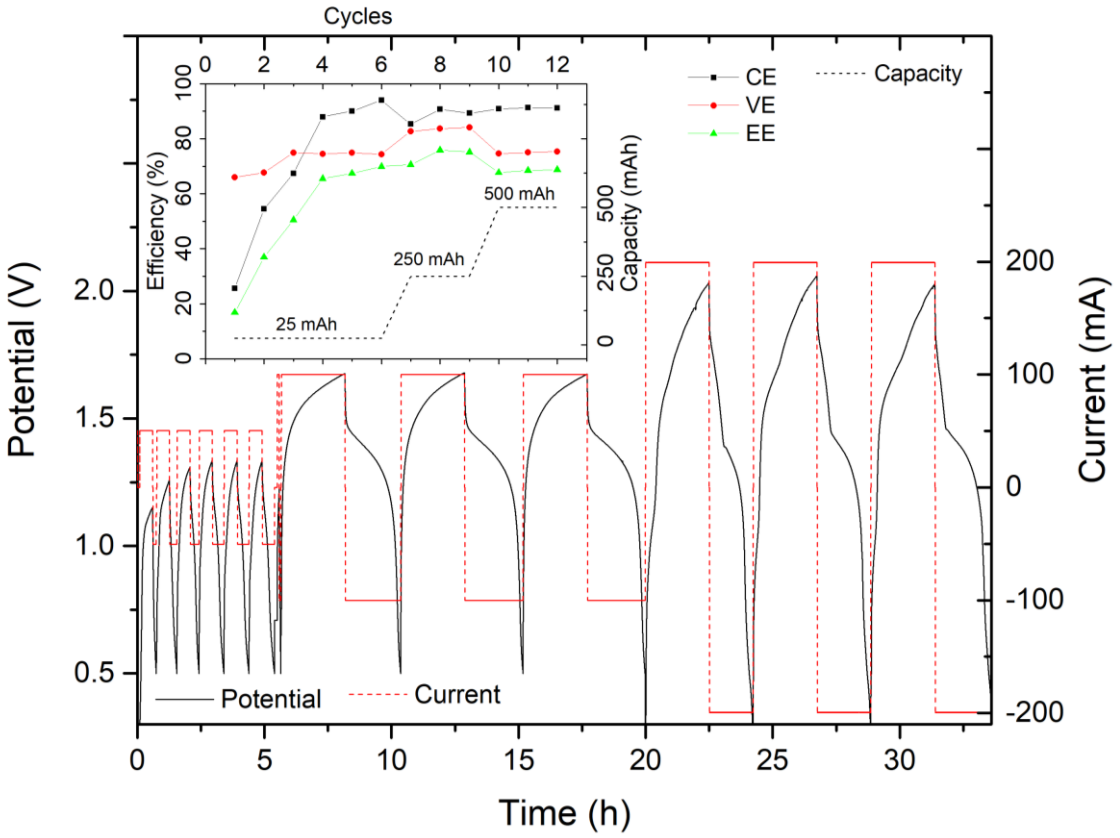


Figure 2.4 Charge-discharge cycling for activation phase in three steps. Step 1: Capacity of 25 mAh at a constant current of 50 mA for 0.5 h. Step 2: Capacity of 250 mAh at a constant current of 100 mA for 2.5 h. Step 3: Capacity of 500 mAh at a constant current of 200 mA for 2.5 h (Inset shows η_{CE}, η_{VE}, η_{EE}, and capacity for the cycles respectively).

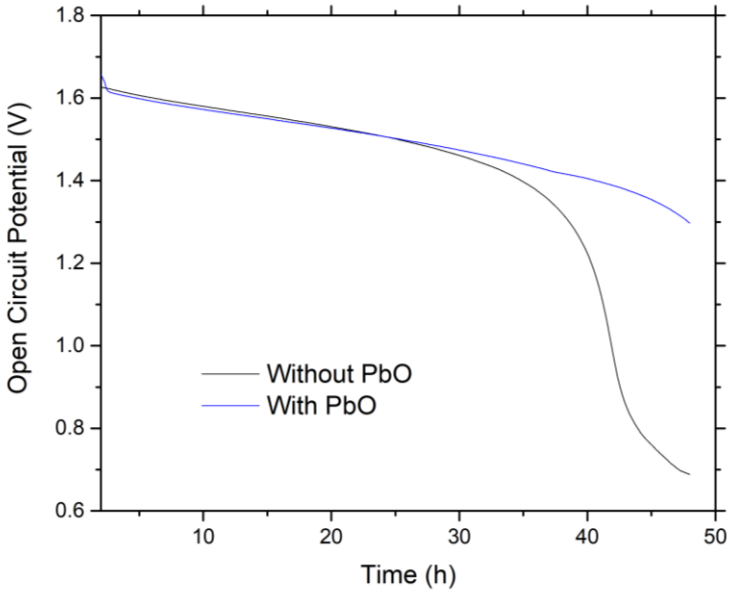


Figure 2.5 The result of the self-discharge test without the addition of lead oxide and after the addition of 2 molar percentage of PbO into the composition of the electrolyte.

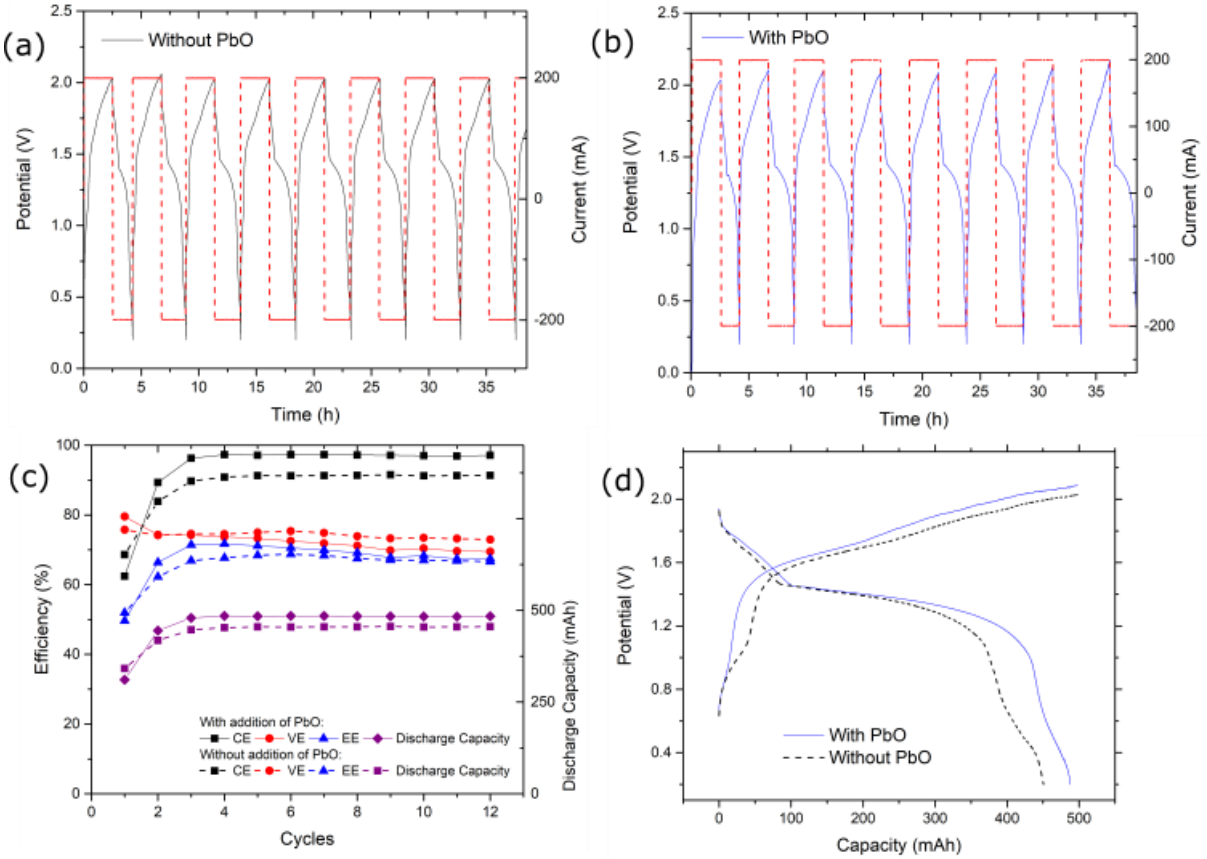


Figure 2.6 Charge discharge cycling of the liquid displacement cell having a capacity of 500 mAh at a current of 200 mA: (a) Control experiment without the addition of PbO. (b) After the addition of 2 molar percentage of PbO into the electrolyte. (c) Efficiencies of both experiments. (d) Comparison of capacity vs. the potential for the best performing charge-discharge cycle.

2.3.2 Impact of mitigation on the impedance of the cell

Electrochemical Impedance Spectroscopy (EIS) was used to further characterize the performance of the cell. A higher impedance of the cell results in lower voltage efficiency, in turn, lower round-trip energy efficiency. It is important to quantify the overall impedance of the cell and then further analyze it to get the contribution of each component. Initially, the impedance curve obtained from EIS measurements was fitted on a Randles circuit which helps to analyze the first semi-circle highlighting the ohmic resistance and charge-transfer resistance of the cell. The Randles circuit fittings were used as the starting point to get values for the model of the equivalent circuit. The impedance curve was further fitted to the equivalent circuit model considering the physical phenomena incurred in the cell.

Since existing reported results were not available, the EIS measurements were validated using the Kronig-Kramers test (K-K test) as shown in Figure S 11.2. This test informs about the steady-state condition of the electrochemical system. If the investigated system is dynamic (*i.e.* frequently changing with time) then this test fails. This can happen due to the effect of aging, temperature change, non-equilibrium initial state, *etc*. Failure of the K-K test usually means that no good fit can be obtained using the equivalent circuit method. The Kronig-Kramers test ensures causality, linearity, and stability: Here, causality signifies that the recorded response is only related to the excitation signal generated by the potentiostat during measurement. Linearity signifies that the recorded response is linear and the perturbation small enough to avoid any change in the open circuit potential of the cell during measurement. Finally, stability highlights that the electrochemical system is not changing the state-of-charge (SOC) with respect to time [116,117]**.**

The measurements were successfully validated by the K-K test and fitted to the equivalent circuit as shown in Figure 2.7. The inductance of wires between the cell, glove box, and potentiostat is denoted by L_1. The *x*-intercept of the Nyquist plot indicates the ohmic contribution of the cell and is denoted in the equivalent circuit by the resistive component R_S. The latter combines the ohmic resistances of the cathode, electrolyte, membrane, anode, and current collectors. The double-layer effect at the interfaces of the electrolyte with anode/cathode is modeled using an analogy of RC_{CPE} circuits, where C_{CPE} is a Constant Phase Element (CPE). The fitted parameters helped to estimate the overall

impedance of the cell by using the commonly applied circuit analysis of the RC circuit [118].

The equivalent circuit fits the individual impedance curves very well - Figure 2.7. The EIS parameters used in the equivalent circuit model were determined with good accuracy - Table 2.1. The errors for each parameter are within the 95 % confidence interval according to the equivalent circuit analysis in ZView and lie within the Chi-squared criteria ($< 1 \times 10^{-3}$). There is a negligible effect of PbO addition on the ohmic resistance of the cell which indicates that neither the electrolyte layer thickness changes nor the conductivity of the electrolyte. In comparison to this, the anodic impedance increased by *ca.* 32 % (from 592 mΩ to 783 mΩ) because the charge transfer resistance increased at the anode due to the additional side reactions. The cathodic impedance decreased, which is possibly associated with the physicochemical properties of the melt ($LiCl$-KCl-$PbCl_2$-Pb_2OCl_2) and also because of the availability of more Pb^{2+} ions. Interestingly, this trade-off allowed to maintain the overall impedance of the cell, which is almost the same when adding PbO to the electrolyte. This finding is also supported by the earlier results showing that the columbic efficiency increased without any effect on the voltage efficiency.

2.3.3 Impact of mitigation on the polarization of the cell

The polarization curve analysis is based on the standard electrochemical technique of Linear sweep voltammetry (LSV) for characterizing the performance of the battery and provides information about the performance losses in the cell under operating conditions. The generalized polarization curve of a battery is given in supplementary information as shown in Figure S 11.1. The peaks of the polarization curve highlight the limiting current density and limiting power that can be achieved from this particular cell. The curve obtained while discharging the cell indicate the useful parameters of activation overpotentials (η_a), ohmic losses (η_o) and mass transport (η_m) overpotentials. These values can be extracted using the ohmic resistance from the impedance analysis.

The polarization curve obtained while charging the cell from 0.4 V to 2.2 V at a scan rate of 10 $mV \cdot s^{-1}$ is shown in Figure 7. The control experiment (without PbO) achieved a limiting current density of 575 $mA \cdot cm^{-2}$ and limiting power up to 2.53 W whereas the remedy experiment (with PbO) achieved a limiting current density of 831 $mA.cm^{-2}$ and limiting power of 3.66 W. Moreover, the polarization curve was obtained while discharging the cell from the SOC = 80 % to 20 %, which is the range of

varying the potentials from 1.8 V to 0.3 V. The activation overpotential is negligible because of the fast kinetics at liquid-liquid interfaces. Ohmic resistance values obtained from EIS were used to get iR-free curves which help to quantify the ohmic overpotential (η_o); the remaining curve is the effect of the mass-transport overpotential (η_m). The values of the various overpotentials are shown in Figure 8. The gains in the performance of the cell are also evident in these results.

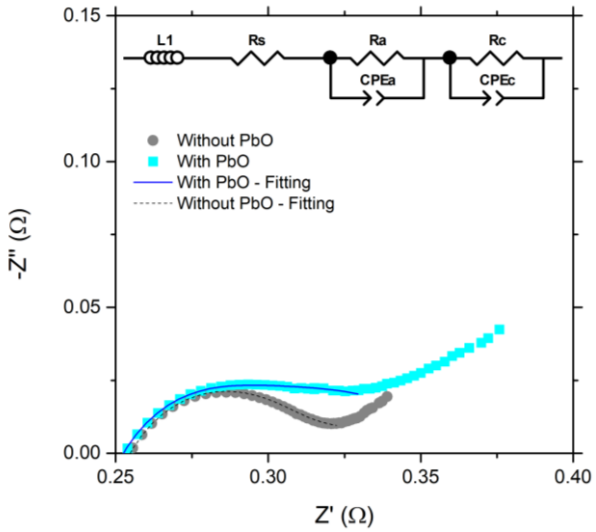


Figure 2.7 Impedance curve obtained by electrochemical impedance spectroscopy in the frequency range from 2.5 kHz to 1 Hz having an amplitude of 10 mV. The inset shows the equivalent circuit model used for curve fitting.

Table 2.1 Fitting parameters and RC circuit impedance analysis of the equivalent circuit for the impedance curves shown in Figure 2.7.

	Without PbO		With PbO	
Elements	Value	Error (%)	Value	Error (%)
	Fitted Parameters			
L_1 (mH)	2.16×10^{-3}	0.37	2.08×10^{-3}	1.12
R_s (Ω)	2.56×10^{-1}	0.02	2.54×10^{-1}	0.05
R_a (Ω)	6.48×10^{-2}	0.55	8.46×10^{-2}	0.84
CPE_a (mF)	4.65×10^{2}	0.29	4.69×10^{1}	0.65
R_c (Ω)	6.59×10^{-2}	0.08	5.31×10^{-2}	0.31
CPE_c (mF)	2.99	0.21	2.77	0.8
Chi-Squared (Criteria < 1×10^{-3})	5.7×10^{-7}		5.3×10^{-6}	
	RC-circuit Impedance Analysis			
$\lvert Z_{RC,a} \rvert$ (Ω)	5.92×10^{-4}		7.83×10^{-3}	
$\lvert Z_{RC,c} \rvert$ (Ω)	6.58×10^{-2}		5.31×10^{-2}	
$\lvert Z_{CELL} \rvert$ (Ω)	3.22×10^{-1}		3.15×10^{-1}	

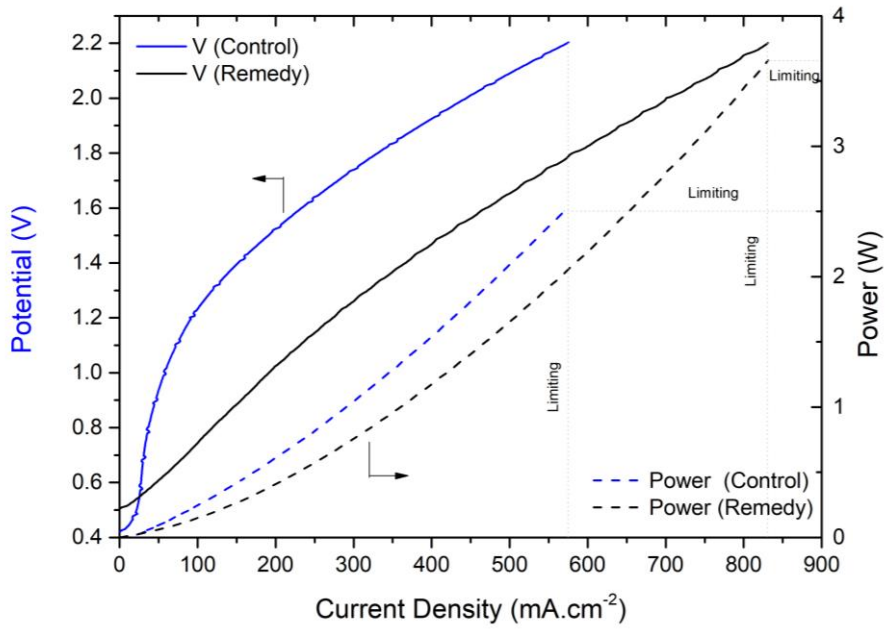


Figure 2.8 Polarization curves while charging the cell from 0.4 V to 2.2 V. The solid lines represent voltage as a function of current density and the dotted lines represent power as a function of current density (mA·cm^{-2}). The active area of the cell is 2 cm^2.

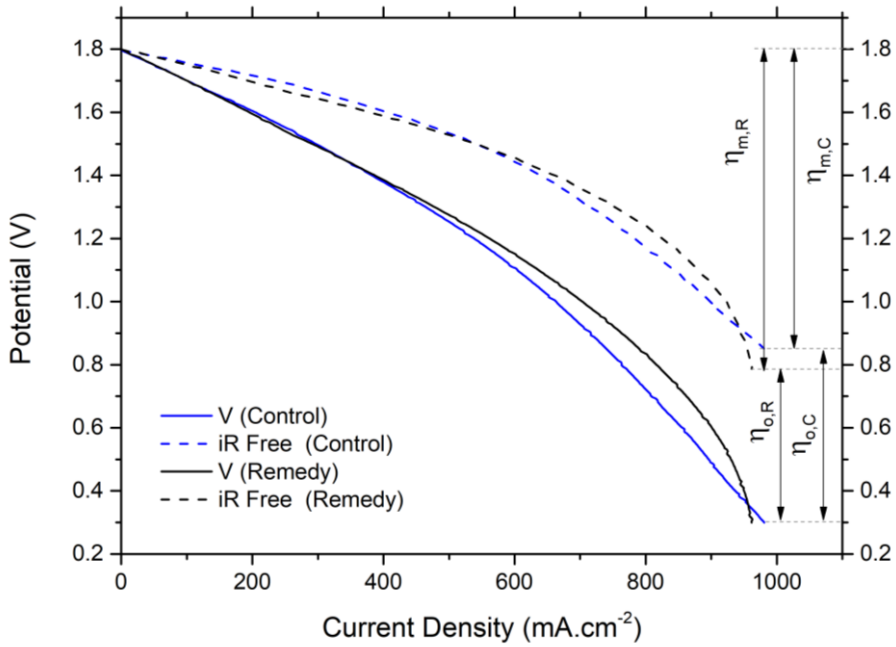


Figure 2.9 Polarization curves while discharging the cell from 1.8 V to 0.3 V at a scan rate of 10 mV·s^{-1}. The solid lines represent voltage as a function of current density and the dotted lines represent iR-free curves.

2.4 Conclusion

A formulation involving Faraday's law and the Nernst-Planck equation leads to a relationship, which signifies that the self-discharge current density is directly proportional to the diffusion coefficient. This directs this study to the solution of adding lead oxide (PbO) into the electrolyte. The latter was helpful to reduce the diffusion coefficient as well as the Pb ion concentration by providing two additional side reactions. The limiting current density and power were improved from 575 $mA \cdot cm^{-2}$ to 831 $mA \cdot cm^{-2}$ and from 2.53 W to 3.66 W, respectively. The addition of PbO decreases the ohmic losses, but the mass transport overpotentials increased due to the effect of PbO on the diffusion of Pb^{2+} in the electrolyte. The equivalent circuit model is used to estimate the contribution of impedance by the contacts and interfaces. The remedial actions reported here lead to the highest reported columbic efficiency for liquid displacement batteries, *i.e.* an increment from 91 % to 97 % without affecting the voltage efficiency. The addition of PbO allows for decreasing the diffusion-controlled self-discharge process by complementing the faradaic function of the membrane through additional reversible side reactions.

(Blank)

Part II

Chapter 3

In-situ crossover diagnostics to assess membrane efficacy

3. *In-situ* crossover diagnostics to assess membrane efficacy

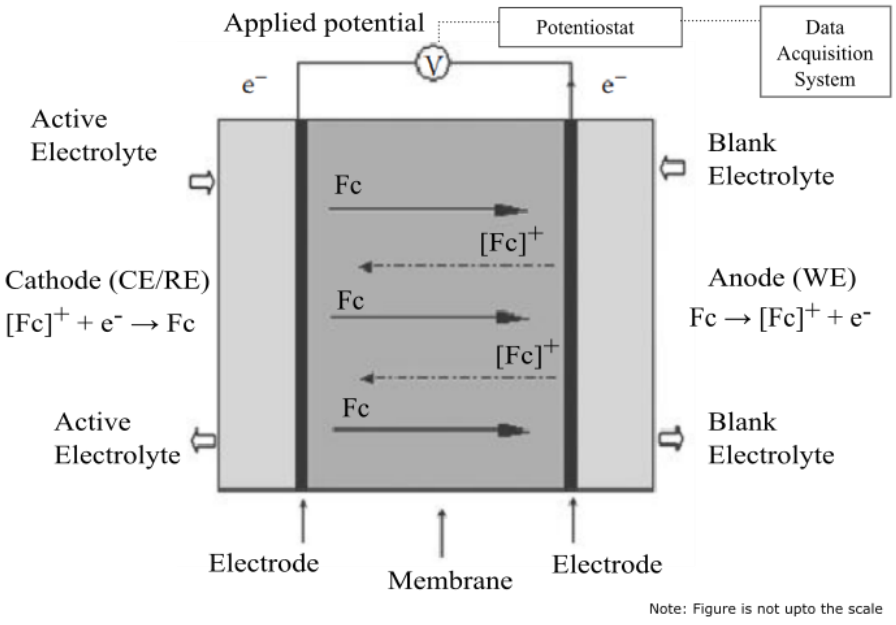
Adapted from the following articles:

K. Mushtaq, A. Mendes, "In-situ crossover measurements for vanadium-based non-aqueous redox flow battery", 239th ECS Meeting (June 2021), Chicago, USA.
URL: https://ecs.confex.com/ecs/239/meetingapp.cgi/Paper/147222

K. Mushtaq, T. Lagarteira, A.A. Zaidi, A. Mendes, "In-situ crossover diagnostics to assess membrane efficacy for non-aqueous redox flow battery", J. Energy Storage. 40 (2021) 102713.
URL: https://doi.org/10.1016/j.est.2021.102713

The redox species crossover through the membrane is problematic since it leads to capacity loss and lower coulombic efficiency. It needs to be readily quantified before any commercial application of the non-aqueous redox flow battery (NAqRFB). An *in-situ* electrochemical method is introduced and further validated through an *ex-situ* method and performance characterization. The feasibility of ferrocene is checked and reported as a model probing species. Among ion exchange membranes, a lower crossover molar flux rate is obtained from Nafion 117 and FAPQ-375-PP (2.18 and 0.75 $\mu mol \cdot h^{-1} \cdot cm^{-2}$). The model redox species – $V(acac)_3$ – was used for the performance assessment of NAqRFB. The coulombic efficiency was 86.6 % and the voltage efficiency of 65.8 %. The ohmic and mass transport overpotentials affecting the performance of NAqRFB were 0.46 V and 1.44 V. The crossover rate obtained from the LSV technique concerns materials and cells under real working conditions. This technique has the potential to become a reference testing method to determine the crossover and aid in selecting the best performing membrane, in the RFB field. As a membrane diagnosis tool, this technique allows *in-situ* determination of crossover without the need for disassembling the devices.

Graphical Abstract



3.1 Introduction

The large-scale integration of renewable electricity in a grid leads to instability problems that can be overcome by the incorporation of effective energy storage systems. This requires the use of technologies that can easily and efficiently convert electricity in a storable form of energy, such as stationary batteries. In this regard, lithium-ion batteries and redox flow batteries (RFBs) emerged as promising candidates. As compared to enclosed batteries (*e.g.*, lithium-ion, Na-S battery), the RFB architecture offers several advantages including the ability to decouple the power (stack size) from the energy capacity (electrolyte volume), a high ratio of active-to-inactive materials, simplified manufacturing, longer service life with full charge/discharge cycles, and improved safety. Because of their low energy density and integrated design requirements, RFBs are best suited for megawatt-scale energy storage with long charge/discharge durations (*ca.* 4–5 hours) [119].

At present, the most developed RFB system is the aqueous all-vanadium RFB (VRFB), which uses water-soluble vanadium ions in different oxidation states as redox-active species. First conceptualized in 1986 [20], this technology still enjoys considerable interest from the research community. RFB has a low energy density as compared to batteries where the energy is stored in solid electrodes such as Li-ion, Nickel Metal Hydride (Ni-MH), and Ni-Cd batteries. All of these have volumetric energy densities higher than 100 $Wh{\cdot}L^{-1}$, whereas the highest reported for aqueous VRFB was around 55.16 $Wh{\cdot}L^{-1}$ [120]. This was only achieved by a reported study using the maximum possible 3 M concentration of vanadium [120] but commercial versions have 25 to 30 $Wh{\cdot}L^{-1}$. The upper bound in the energy density (U_{MAX}, $Wh{\cdot}L^{-1}$) for an RFB can be estimated by equation (3.1) [23]:

$$U_{\mathrm{MAX}} = \frac{1}{2} E_{\mathrm{OCP}} n F C_{\mathrm{A}} \qquad (3.1)$$

where n is the number of electrons transferred per molecule of redox species during the redox reaction, E_{OCP} is the open circuit potential (V), C_A is the maximum concentration of the redox species ($mol{\cdot}L^{-1}$) and F is Faraday's constant (26.8 $Ah{\cdot}mol^{-1}$).

Equation (3.1) shows that energy density can be enhanced by increasing the concentration of redox species, increasing the cell potential, or by increasing the number of involved electrons in the reaction. Non-aqueous electrolytes (based on ionic liquids, deep eutectic solvents, and organic solvents) are being investigated to increase energy

density by providing wider electrochemically stable windows [25] and higher solubility of active species. Additionally, this allows searching for new redox species that are incompatible with aqueous electrolytes due to low solubility, chemical reactivity, or redox potentials outside of the stability window. Moreover, a diverse range of supporting electrolytes and molecular solvents that can be tailored to specific redox chemistry can be used for this application. Summing up altogether, these benefits can lead to higher energy density resulting in lower costs of energy storage [26].

Vanadium acetylacetonate, $V(acac)_3$, was reported as the "redox species" [39] for NAqRFB operation and is also being used as a commercially available model reagent to study the performance of NAqRFB-cell. The battery reactions of the vanadium-based non-aqueous electrochemistry are given below in the discharging direction [40].

$$[V(IV)(acac)_3]^+ + e^- \rightleftharpoons V(III)(acac)_3, E_C = 0.45\ V\ vs.\ Ag/Ag^+ \qquad (3.2)$$

$$V(III)(acac)_3 + e^- \leftrightharpoons [V(II)(acac)_3]^-, E_A = -1.75\ V\ vs.\ Ag/Ag^+ \qquad (3.3)$$

The efficient operation of the non-aqueous redox flow battery (NAqRFB) requires a selective membrane that prevents the crossover of the charged storage molecules (redox species) to minimize self-discharge or mixed potentials; actually, the crossover-induced capacity loss remains one of the most challenging problems for non-aqueous redox flow battery [121]. At the same time, the membrane must enable high ionic conductivity (ions from supporting electrolyte) to lower ohmic losses. The identification of a highly conductive, yet selective membrane is of paramount importance for the market penetration of RFBs [121]. Although the membrane should be extremely selective, for allowing years of continuous operation, the truth is that all commercially used membranes allow to some extent redox species permeation, especially when a thinner membrane is pursued to ensure high ionic conductivity. In terms of capacity retention, the reactant that crosses directly through the membrane is oxidized or reduced without providing electrical work, leading to lower efficiency. Therefore, crossover in a redox flow cell and its impact on cell operation is a critical phenomenon that needs to be quantified and mitigated in the development of redox flow cells.

Most commercially available ion-exchange membranes were designed for fuel cell systems and have been used for aqueous redox flow batteries. Moreover, NAqRFB is less mature than their aqueous counterpart and the development of non-aqueous redox chemistries has far outpaced the development of membranes/separators. Nearly all the

solid-electrode batteries (Li-ion, Na-ion, NiMH, *etc.*) have a nonaqueous-based electrolyte barrier. Depending on the chemistry, NAqRFB has been using either nano-porous (*i.e.* <100 nm pores) separators or ion-exchange membranes. The porosity of the separator allows the passage of the balancing ion but inherits the disadvantage of leaving the door wide open also for redox species to pass through. Ion-exchange membranes were favored to reduce this effect since they allow only either positive or negative charged species to cross but at the expense of higher costs and low ionic conductivity [122].

The crossover test of redox species for non-aqueous electrolytes was reported by Liang Su [121] using the diffusion-based H-cell. That cell was having redox species at one side and the other side without redox species. Samples were collected after a certain period of intervals and then the concentration of redox species was measured using cyclic voltammetry. Other methods [123,124] were reported to account for the contribution, but they still need *ex-situ* analytical methods.

In comparison, an electrochemical technique based on linear sweep voltammetry (LSV), is most frequently used to estimate gas crossover through membranes for the technology of Proton-exchange membrane fuel cells (PEMFCs). LSV is a method where the response of redox species is measured in terms of current by sweeping the potential between the working electrode (WE) and a reference electrode (RE). It can be applied directly under different and realistic fuel cell operating conditions [125]. During testing, a linear potential scan is applied to the fuel cell electrode to obtain a limiting current, which is used for calculating the crossover rate. This standard technique can be adapted to quantify the electrochemical crossover of redox species through membrane assembled in a NAqRFB. Ferrocene is used in this study as a model "probing species" to perform crossover measurements. It had been continuously used as a standard reference in the field of electrochemistry while working with non-aqueous solvents [126].

The negative side (containing redox species i.e. ferrocene as probing species) serves as RE as well as a counter electrode (CE) and the positive side (containing the blank electrolyte, without ferrocene) serves as WE. The potential was linearly swept at a very low scan rate while passing electrolytes at a very low flow rate. Under the chosen potential range, ferrocene ions that permeate the membrane, from negative to positive side, should be oxidized under mass-transfer limited conditions. This allowed obtaining a limiting oxidation current density, which is related to the ferrocene crossover. Since a blank electrolyte was introduced into the positive side, any current response should be

assigned to the electrochemical oxidation of ferrocene that permeates the membrane. This leads to the following redox reactions at the electrodes, as indicated in Figure 3.1.

Counter-electrode (negative side, cathode):

$$[Fc]^+ + e^- \rightleftharpoons Fc \tag{3.4}$$

Working-electrode (positive side, anode):

$$Fc \rightleftharpoons [Fc]^+ + e^- \tag{3.5}$$

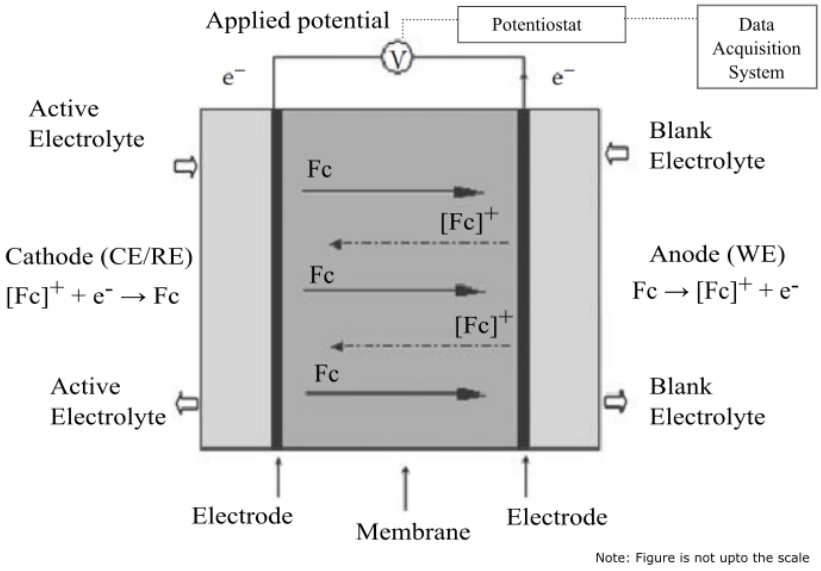


Figure 3.1 Schematic for the principles of crossover measurements in non-aqueous redox flow battery having ferrocene as probing species, $TEABF_4$ as supporting electrolyte, and acetonitrile as solvent.

The crossover of ions through an ion exchange membrane is described by the Nernst Planck equation. This model comprehends three mass transport contributions: diffusion, migration, and convection:

$$J_i = -D_i \frac{\partial C_i}{\partial x} - \frac{n_i F}{RT} D_i C_i \frac{\partial \varepsilon}{\partial x} + C_i v \tag{3.6}$$

where the subscript i refers to the redox species, J_i is the crossover molar flux, D_i is the diffusion coefficient, $\frac{\partial C_i}{\partial x}$ is the concentration gradient of the redox species, n_i is the number of electrons participating in the reaction, R is the gas constant, T is the absolute temperature, $\frac{\partial \varepsilon}{\partial x}$ is the potential gradient across the membrane, and v is the velocity of the

solution. Based on the limiting current density, ferrocene crossover – J_i – can be determined from Faraday's law [127].

$$J_i = \frac{(i_{\text{diffusion}} \approx i_{\text{lim}})}{z_i F} \tag{3.7}$$

where $i_{\text{diffusion}}$ is the current density due to concentration gradient, i_{lim} is the transport limiting current density obtained from the LSV measurement, and F is the Faraday's constant.

The LSV measurement is performed at the very low value of scan rate and flow rate [128]. The contribution of migration and convection terms of equation (3.6) become negligible and the limiting current density from the LSV measurement remains dominated only by diffusion-based current density - as mentioned in equation (3.7) [129,130]. Similar phenomena are also reported elsewhere for PEMFCs having hydrogen on one side and electrochemically inert nitrogen on the other side [131,132].

This technique will allow researchers to account for the contribution of the diffusion-based crossover. The results were further confirmed by measuring the permeance of redox ions using an *ex-situ* method. The crossover rate obtained from the LSV technique concerns materials and cells under real working conditions. This technique has the potential to become a reference testing method to determine the crossover and aid in selecting the best performing membrane, in the RFB field. As a membrane diagnosis tool, this technique allows *in-situ* determination of crossover without the need for disassembling the devices.

3.2 Experimental Methods

3.2.1 Electrolytes

Tetraethylammonium tetrafluoroborate, 99 %, $TEABF_4$, acquired from Alfa Aesar; Vanadium(III) acetylacetonate, 97 %, $V(acac)_3$ acquired from Sigma-Aldrich; Acetonitrile, 99.8 %, anhydrous acquired from Sigma Aldrich; ferrocene, 99 %, Fc acquired from Alfa Aesar were used as received. All experiments were conducted using non-aqueous electrolytes composed of acetonitrile as solvent and $TEABF_4$ as supporting electrolyte salt. Ferrocene was used as a "probing species" and $V(acac)_3$ as a "redox species". The concentration of supporting electrolytes was kept to be 0.1 M for all experiments to get uniform conductivity of electrolytes. The electrolyte without ferrocene was named blank electrolyte. Blank electrolyte (**A1**) consist of, acetonitrile + $TEABF_4$

0.1 M. The working electrolyte (**B1**) used for crossover measurement consist of, acetonitrile + $TEABF_4$ 0.1 M + Fc 0.05 M. The flow-cell electrolyte **(C1**) consist of, acetonitrile + $TEABF_4$ 0.1 M + $V(acac)_3$ 0.02 M. The voltammetry studies were performed using the electrolytes (**B2 and C2**) consist of acetonitrile + $TEABF_4$ 0.1 M + Fc 5 mM and acetonitrile + $TEABF_4$ 0.1 M + $V(acac)_3$ 5 mM.

3.2.2 Membranes

Ion-exchange membranes especially designed and fabricated as per the requirements of the non-aqueous redox flow batteries are not available commercially. Therefore, commercial membranes were used in this study, and their properties are mentioned in Table 3.1. The as-received cation exchange membranes (CEM) were pre-treated to exchange H^+ with TEA^+. The membranes were immersed for 18 hours in a 200 cm^3 solution containing 1 M TBAOH in methanol supplied by Aldrich, USA. These TBA^+-loaded membranes were further equilibrated for 1 day in an anhydrous 200 cm^3 solution of 0.1 M $TEABF_4$ in acetonitrile for conversion to TEA^+-form. The as-received anion exchange membranes (AEM) were soaked for 1 day in a 200 cm^3 of 0.1 M $TEABF_4$ in acetonitrile.

Table 3.1 Characteristics of the selected commercial membranes.

Description	Composition	Thickness (µm)	Intended Application
Nafion 117 (CEM)	PFSA / PTFE copolymer	183	Aqueous batteries and fuel cells
Nafion 115 (CEM)	PFSA/PTFE copolymer	127	VRFB and other batteries/fuel cells
FAPQ-375-PP (AEM)	Fluorinated and PP Reinforced	70	Aqueous Flow batteries
FAP-450 (AEM)	Fluorinated	50	Aqueous Flow batteries
FAP-330-PE (AEM)	Fluorinated and PE Reinforced	30	Aqueous Flow batteries

Acronyms: (CEM) = Cation Exchange Membrane, (AEM) = Anion Exchange Membrane, PFSA = Perfluorosulfonic acid, PTFE = Polytetrafluoroethylene.

3.2.3 Treatment of electrodes

Commercial PAN-based Sigracell battery felt (GFD 4.6 EA) was acquired from SGL Carbon. The manufacturer claims excellent chemical resistance and inertness with high porosity and good electrical conductivity. All experiments were conducted using this

4.6 mm thick electrode. The electrodes were cut to size and the thermal activation was performed according to the procedure reported in the literature [133]. Briefly, the as-received electrodes were washed with de-ionized (DI) water and immersed in 2.7 M sulfuric acid for 26 hours. Then, boiled in DI water to remove traces of acid, thoroughly washed with DI water, and dried in an oven for 30 mins at 120 ^{o}C. Further, the electrodes were heat-treated in a muffle furnace under atmospheric air. The batch was kept at 450 ^{o}C for 16 hours and immediately taken out of the furnace for cooling down to room temperature.

3.2.4 Cyclic Voltammetry of redox species

Voltammograms were recorded using a glassy carbon electrode (GC, Metrohm), as a working electrode, in a 50 ml three-electrode cell configuration. Electrolytes **B2** and **C2** were used to perform all the measurements. Electrode Biologic RE-7, filled with 0.01 M $AgNO_3$ + 0.1 M TBAP + Acetonitrile, was used as reference electrode. Platinum wire served as a counter-electrode. All experiments were performed under the nitrogen atmosphere. Autolab potentiostat (PG302STAT) was used to record all the data and Nova software was used for the voltammograms analysis.

3.2.5 *In-situ* and *Ex-situ* measurements for the crossover of probing species

The electrolyte was pumped from the reservoirs using an Ismatec MCP Standard peristaltic pump. Dry nitrogen was continuously bubbled to prevent the oxidation of electrolytes. Electrochemical measurements were performed using a Zahner Zennium's workstation by Zahner Elektrik, Germany. The cell was connected to the workstation in a 2-electrode configuration, where WE is connected to the positive half cell and CE is connected to the negative half cell. The negative half-cell was connected to a reservoir having the probing species (electrolyte **B1** as negolyte) and the positive half-cell was connected to the blank electrolyte (electrolyte **A1** as posolyte). Each measurement was done with a fresh positive electrode and fresh blank electrolyte. Electrolyte with the probing species and without the probing species (blank electrolyte) was circulated across the cell at a low flow rate of 4 ml·min^{-1}. The experimental setup is shown in Figure 1.9 (a).

UV-Vis spectra were recorded on a Shimadzu Spectrophotometer for *ex-situ* measurements. The characteristic absorption wavelength of ferrocene for UV-vis analysis is *ca.* 441 nm [134]. The calibration curves obtained through measurements at different concentrations were used further to get the unknown concentration from samples [135].

The samples from the blank electrolyte were collected after each *in-situ* electrochemical crossover measurement for different membranes. Since it was collected after each LSV, so the results of the UV-vis spectrum can be co-related.

3.2.6 NAqRFB assembly and assessment

A fuel cell from Pragma Industries was modified into a flow cell, changing bipolar plates and nitrile rubber O-rings, which were replaced by PTFE O-rings for compatibility with the used non-aqueous solvents. Serpentine flow-fields were used in this work; the choice of flow-field may affect the crossover of the redox species. The treated carbon felt (SGL 4.6 EA) were placed on each of the flow fields. Membranes mentioned in Table 3.1 were used as a separator between positive and negative half-cells. Teflon gaskets sealed the membranes and electrodes into the cell. Electrodes were compressed 35 %, providing a final thickness for the electrodes of 3 mm.

The flow experiments were performed in a glove box having with a dry nitrogen environment, to ensure the minimum effect of humidity [136]. Two Schott GL45 bottles served as reservoirs. The 25 ml of posolyte (electrolyte **C1**) and negolyte (electrolyte **C1**) were used in the flow cell experiments. The flow circuit is the same as shown in Figure 1.9. Impedance measurements were recorded at 10 mV of amplitude and OCP (at 1.2 V) across the frequency range of 250 kHz to 1 Hz using the Zahner workstation. Potentiostatic measurements were performed to acquire polarization data from 0.5 V to 2.5 V at a scan rate of 20 $mV \cdot s^{-1}$. The ohmic resistance contribution from the wires – 0.02 Ω – was subtracted from all polarization and impedance measurements. Data obtained from charge/discharge cycling enabled the calculation of Coulombic, Voltage, and Energy efficiencies (η_{CE}, η_{VE}, and η_{EE}, respectively) using the equations (2.4), (2.5), and (2.6).

3.3 Results and Discussions

3.3.1 Feasibility of Ferrocene as probing species

The feasibility of ferrocene as probing species was tested before utilizing it for *in- situ* crossover measurements of different membranes. Ferrocene has only two valency states (Fc and Fc^{+}) as compared to vanadium which has four valency states (V^{2+}, V^{3+}, V^{4+}, and V^{5+}). Using ferrocene as a probing species eliminates the possibility of recording current from multiple oxidations states of vanadium ion while performing LSV, which can be misinterpreted as current from crossed species. More importantly, it was recently

reported that $V(acac)_3$ is very sensitive to the presence of moisture and proceeds into a parasitic reaction of forming $VO(acac)_2$ [136]. Even for other redox species, this is a big concern for the NAqRFB researchers and forces them to work in the controlled environment of the glovebox having dry Nitrogen, unlike the conventional aqueous RFB which can be operated efficiently without the need of any glovebox. The requirement of a controlled environment will be the main hurdle for the commercial application of NAqRFB. Since ferrocene has a negligible effect from moisture and it enabled the measurement of crossover from a redox flow-cell operating without using a glove box. This will help researchers to check the membrane before starting the operation of a NAqRFB inside the glovebox. So in the future, this method can also be applied easily for commercial applications of NAqRFB.

Cyclic Voltammetry (CV) analysis was performed to show that there is no side reaction of ferrocene with supporting electrolyte ($TEABF_4$) and it confirms the redox potential for the non-aqueous system used in this study. The value of potential and current at the highest and lowest points of the curve were referred to as peak potential and peak current. The value of peak potential for a redox couple of Fc^+/Fc remains the same at varying scan rates, confirming the reversibility of this reaction – Figure 3.2 (a). The average of the cathodic and anodic peak potential values is equal to the value of the redox potential of the reaction, which is 0.126 V *vs.* Ag^+/Ag.

3.3.2 Crossover of probing species by different membranes

The optimization of parameters was necessary because this technique was never used for any non-aqueous redox flow cell. Each experiment was performed using a fresh working electrode (WE) to ensure there were no traces of any probing species in the electrode. The difference in potential across the two half cells was associated with differing concentrations of ferrocene and blank electrolyte, as the cell behaves like a concentration cell. Since the redox potential of the ferrocene is *ca.* 0.126 V *vs.* Ag^+/Ag, so preliminary tests were performed with wider potential to determine the most suitable range of potential differences for LSV measurements. The potential difference of 0.25 V was found to be adequate to ensure that the complete response of crossed species was recorded by reaching the plateau.

The blank electrolyte is electrochemically inert and it was confirmed by performing LSV on the cell having blank electrolytes on both sides. The resulting voltammogram displayed a nearly negligible constant current of *ca*. 0.00787 $mA \cdot cm^{-2}$ as

shown in Figure 3.2 (b). For optimizing the scan rate value, several LSVs were performed at different scan rates. Higher scan rates result in a pronounced peak current leading to a less well-defined current plateau due to fast oxidation of accumulated Fc in the blank electrolyte while smaller scan rates result in longer test durations for the same potential range. A scan rate of 100 $\mu V \cdot s^{-1}$ was chosen to be adequate because obtained voltammograms have a well-defined plateau and all measurements in this study were performed at this scan rate. The measurements lasted around 70 to 90 minutes and no variation in the volume of the blank electrolyte was observed during the LSV measurements, which highlights that membrane had no gross leaks.

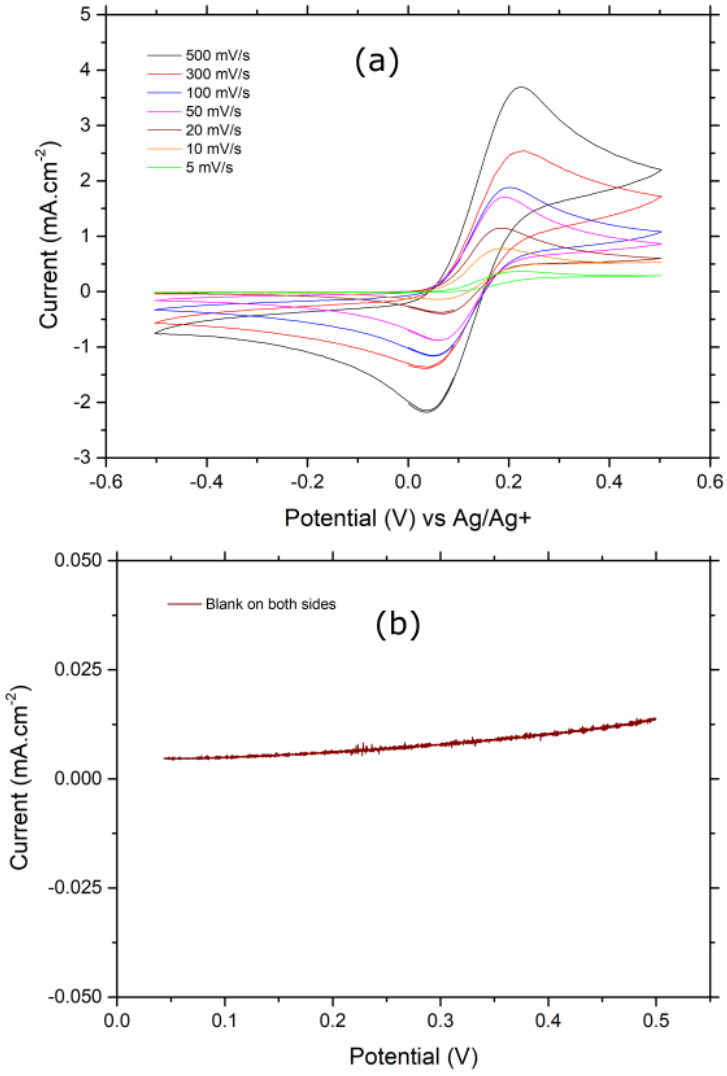


Figure 3.2 (a) Cyclic voltammogram of Ferrocene as probing species in a three-electrode setup having glassy carbon as the working electrode, platinum wire as the counter electrode, and Ag/Ag^{+} as the non-aqueous reference electrode. (b) Voltammogram displayed a nearly negligible constant current of having an average of ca. 0.00787 $mA \cdot cm^{-2}$.

The methodology to quantify crossover presented in this study was applied to all the membranes mentioned in Table 3.1 having a varying thickness, reinforcement, and composition. Voltammograms resulting from the crossover measurements are shown in Figure 3.3. The crossover molar flux of ferrocene ion (Fc^{+}) through each membrane is mentioned in Table 3.2.

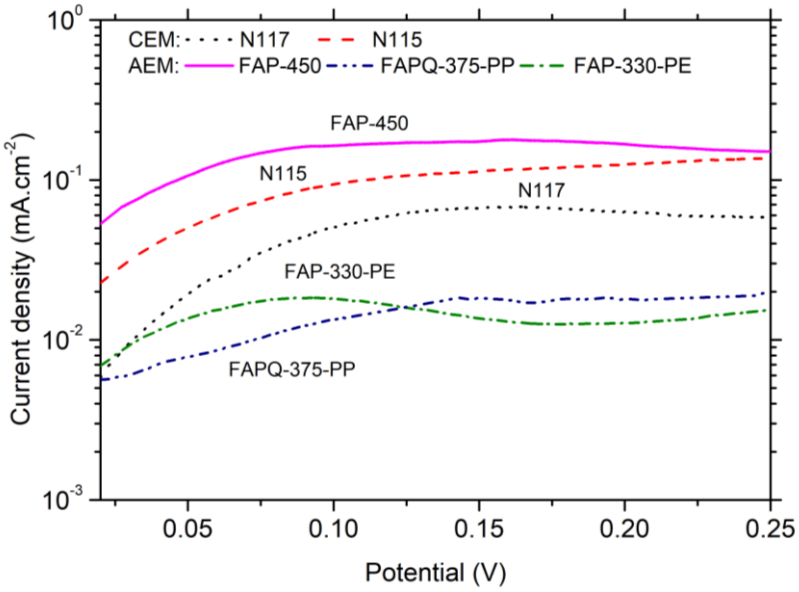


Figure 3.3 Crossover molar flux rate of ferrocene as probing species. LSV voltammograms were performed at 100 $\mu V \cdot s^{-1}$ from cells assembled with each of the membranes.

Table 3.2 Crossover molar flux rates for ferrocene as probing species

Membranes	Dry Thickness (µm)	Molar Flux ($\mu mol \cdot h^{-1} \cdot cm^{-2}$)
Nafion 117 (CEM)	183	2.18
Nafion 115 (CEM)	127	5.09
FAPQ-375-PP (AEM)	70	0.75
FAP-450 (AEM)	50	5.61
FAP-330-PE (AEM)	30	0.58

The crossover molar flux of $V^{4+/3+}$ as probing species is shown in Figure 3.4. The voltammograms were performed at 50 $\mu V \cdot s^{-1}$ for the membranes of Nafion 117 and Nafion 115. The value of the crossover molar fluxes were 4.65 and 8.82 $\mu mol \cdot h^{-1} \cdot cm^{-2}$, respectively. The trend is similar but the ratio between the crossover of vanadium and ferrocene is almost twice. The measurement was started from the initial oxidation state

of V^{3+} and the current was measured from the oxidized state of V^{4+}. There is a possibility that V^{4+} can be further oxidized into V^{5+} and this leads to the higher value of measured limiting current density. So, this highlights a limitation that if redox species have multiple oxidation states, then the recorded currents from additional oxidation states may be misinterpreted as crossover molar flux. This possibility was eliminated by the use of ferrocene which gives the benefit of having only one oxidation state.

Ionic conduction in ion-exchange membranes is based on electrostatic repulsion/attraction upon the establishment of an electrical field. The non-aqueous electrolytes do not contain protons (H^+), so the redox reaction is balanced by exchanging cation (TEA^+) referred to as charge carriers which were supplied by supporting electrolyte salt ($TEABF_4$). The CEMs comprise a fluorinated polymer with sulfonic negatively charged sites having an affinity to TEA^+ ion. The oxidized probing species (Fc^+) were also positively charged particles, so higher crossover was observed in the same thickness of CEMs when compared to AEMs. Contrary to CEM, the AEMs have positively charged amino groups that allow the exchange of anion (BF_4^-) and electrostatically repel all the cations (TEA^+ and Fc^+). This phenomenon is referred to as the Donan-exclusion effect.

Increasing the thickness of CEMs decreases the crossover but at the cost of loss in ionic conductivity. Additionally, NAqRFB is already suffering from non-aqueous electrolytes having less conductivity (*ca.* 35 $mS \cdot cm^{-1}$) as compared to their aqueous counterparts (*ca.* 300 $mS \cdot cm^{-1}$). Usually, the higher crossover results in lower coulombic efficiency (η_{CE}) of the NAqRFB, and higher ohmic resistance causes lower voltage efficiency (η_{VE}).

Uniformly, all the membranes had shown larger swelling in non-aqueous electrolytes as compared to their behavior in aqueous electrolytes. All of the AEMs have the same chemical composition as fluorinated hydrocarbon polymers, so the difference in swelling is mainly affected by the presence of reinforcement. The reinforcement typically decreases porosity and provides mechanical strength. The reinforced AEMs (such as FAP-330-PE and FAPQ-375-PP) had shown lower crossover rates. The thickness of FAP-450 is higher than the FAP-330-PE membrane but the results of the crossover are quite different. The membranes having reinforcement are preferred due to the reduced swelling and resultantly lower crossover [137,138].

In the case of CEMs, the response of crossover measurement is following the thickness of the membrane. In the case of reinforced AEMs, the voltammogram for FAP-330-PE reached a plateau *at ca.* 0.075 V. Similarly, FAPQ-375-PP reached a plateau

around 0.15 V, which is also higher than for the other membranes. Further study regarding the optimization of scan rates toward a lower value is recommended to get plateau like the other membranes.

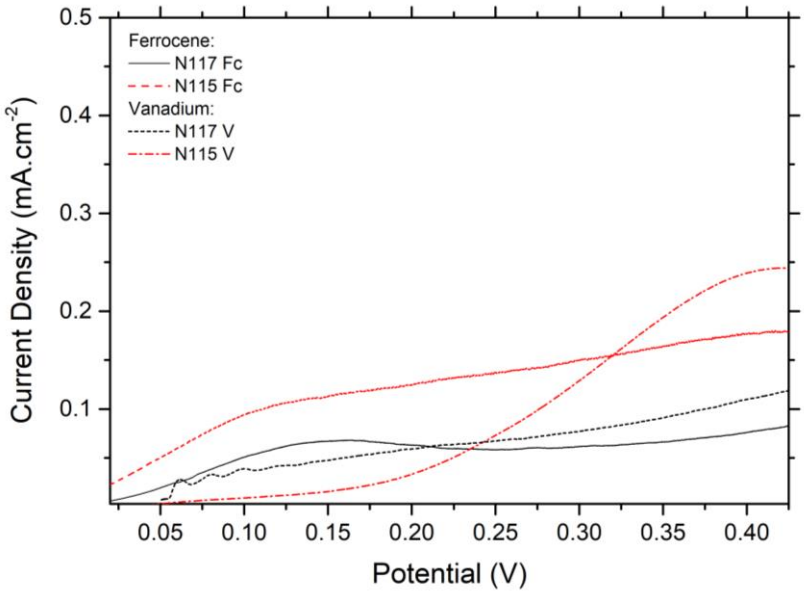


Figure 3.4 Crossover molar flux of $V^{4+/3+}$ as probing species. LSV voltammograms were performed at 50 $\mu V \cdot s^{-1}$ from cells assembled with each of the membranes. This gives crossover molar flux of 8.82 $\mu mol \cdot h^{-1} \cdot cm^{-2}$ and 4.65 $\mu mol \cdot h^{-1} \cdot cm^{-2}$ for Nafion 115 and Nafion 117 respectively. The trend is similar and almost twice the molar flux difference between Nafion 117 and Nafion 115, like the measurement taken using the ferrocene as probing species.

3.3.3 *Ex-situ* validation for the crossover of probing species

To corroborate the presented LSV methodology, the UV-vis spectrum was obtained for each of the samples taken after each *in-situ* measurement for all the membranes. The results were validated by finding the permeance of ferrocene using the *ex-situ* technique based on UV-vis spectroscopy. The membrane permeability to ferrocene was determined using a method similar to the dual chamber direct permeation cell. Equation (3.8) corresponds to the diffusive permeability as reported in the literature [116, 117]. Given that change of ferrocene concentration in the donor reservoir (catholyte) was very low, ferrocene concentration history in the receiver reservoir (anolyte) can be described by Fick's law [141]:

$$V\frac{dc_{\mathrm{R}}(t)}{dt} = P\frac{A}{\ell}[c_{\mathrm{D}}(t) - c_{\mathrm{R}}(t)] \approx P\frac{A}{\ell}[c_{\mathrm{D}}(0) - c_{\mathrm{R}}(t)] \qquad (3.8)$$

where V is the volume of the receiver reservoir, c_D is the initial ferrocene concentration in the donor reservoir (anolyte), which is assumed constant and equal to the

initial concentration – $c_D(t) \approx c_D(0)$, $c_R(t)$ is the ferrocene concentration in the receiver reservoir (catholyte), P is the permeance of the membrane, ℓ is the thickness of the membrane, A is the active area of the membrane and t is the time. Integrating equation (3.8) we obtain equation (3.9), which is used to calculate permeance of membranes to ferrocene:

$$P = -\frac{V_R \ell}{At} ln\left(1 - 2\frac{C_R(t)}{C_D(0)}\right) \quad (3.9)$$

The characteristic absorption wavelength of ferrocene for UV-vis analysis is *ca*. 441 nm as shown by the dotted line in Figure 3.5 (a). The calibration curves are given in supplementary information as Figure 3.5 (b). The absorbance depends on the concentration of probing species present in the sample. The absorbance values are matching with the trend of crossover molar flux rate as shown in Figure 3.3. The permeance to ferrocene together with the electrochemical crossover is shown in Figure 3.6 for the studied membranes. Though the scales are different, this figure shows that for the cation as well as for the anion exchange membranes both methods are directly proportional.

3.3.4 Characterization of $V(acac)_3$ as redox species

Cyclic Voltammetry (CV) analysis was performed to confirm the redox potentials, reversibility, and to assess diffusion coefficients. Voltammograms shown in Figure 3.7 were performed on vanadium-based non-aqueous electrolytes to investigate the fundamental electrochemical properties of the V^{3+}/V^{2+} and V^{4+}/V^{3+} redox flow battery chemistry. The value of the potential at the highest/lowest current density is referred to as peak potential. The value of peak potential for both redox couples (V^{3+}/V^{2+} and V^{4+}/V^{3+}) remains the same for the tested scan rates, which signifies that the condition of reversibility of reaction is satisfied – Figure 3.7 (a) and (b). The average of the cathodic and anodic peak potential value is equal to the value of redox potential (E_{REDOX}) for both couples. The difference between the redox potentials of the redox couple gives the overall cell potential, E_{CELL} = 2.2 V as shown in Figure 3.7 (b). The ratios of anodic and cathodic peak current values were close to unity, as shown in Figure 3.7 (c). Thus, the mass transport coefficient of the redox couple was assumed to display the same magnitude as the electrochemical rate constant. The peak currents were analyzed using Randles-Sevcik analysis at scan rates from 20 $mV \cdot s^{-1}$ to 100 $mV \cdot s^{-1}$. The linear dependence of peak

currents with the square root of the scan rate – Figure 3.7 (d) – enabled us to find the diffusion coefficient for this electrochemical system using the following equation:

$$i^{\mathrm{p}}_{\mathrm{ox/red}} = (2.69 \times 10^5) \cdot n^{\frac{3}{2}} \cdot A \cdot D^{1/2}_{\mathrm{ox/red}} \cdot C^{1/2}_{\mathrm{ox/red}} v^{1/2} \qquad (3.10)$$

where, $i^{p}_{\mathrm{ox/red}}$ is peak current density (mA·cm^{-2}), n is the number of electrons participating in the reaction, A is the area of the working electrode, D is the diffusion coefficient, $C_{\mathrm{ox/red}}$ is the bulk concentration of the solution and v is the scan rate.

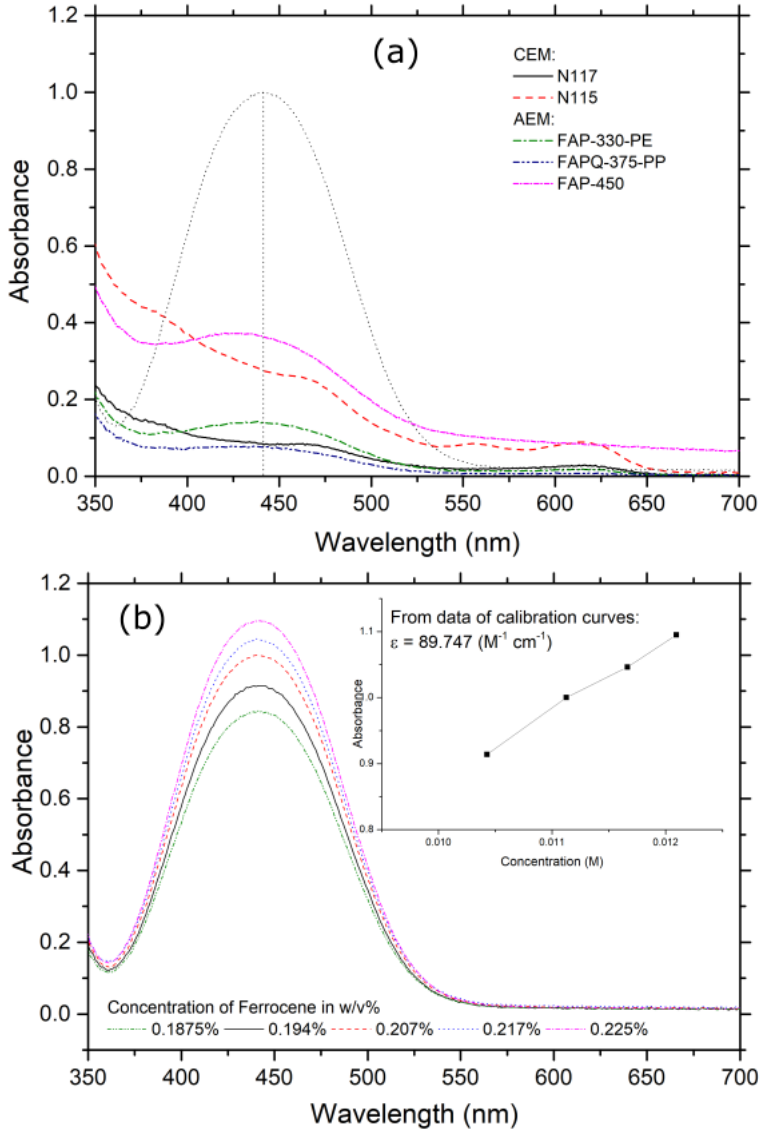


Figure 3.5 (a) UV-vis spectrum for samples collected after each LSV measurement. Inset shows the analysis of data from calibration curves leading to the determination of the molar absorption coefficient (ε = 89.747 M^{-1}·cm^{-1}). (b) UV-vis spectrum is used as calibration curves to follow the Beer-Lambert equation and to determine the value of epsilon.

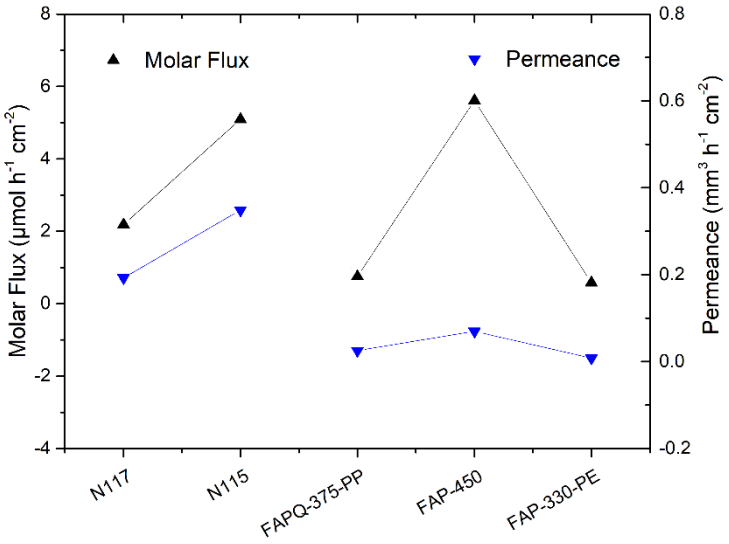


Figure 3.6 Comparison between the permeance to ferrocene and the electrochemical crossover for the selected cation and anion membranes. Lines were added for guiding the eyes.

Equation (3.10) is used to calculate diffusion coefficients for both redox couples V^{3+}/V^{2+} and V^{4+}/V^{3+}. The analysis using the cathodic peak currents measured at varying scan rates leads to the value of 7.88×10^{-6} $cm^2 \cdot s^{-1}$ and 7.31×10^{-6} $cm^2 \cdot s^{-1}$ for the redox couples of V^{3+}/V^{2+} and V^{4+}/V^{3+} respectively. The values are comparable to reported literature [39] which signifies the redox species has no side reaction and the electrolyte is suitable for the flow-cell testing. The additional peak at -1.25 V *vs.* Ag^+/Ag remains visible when CV was performed in the absence of redox species $V(acac)_3$. This is shown in the inset of Figure 3.7 (a) and the voltammogram of acetonitrile shows that this solvent is stable within the potential range of ± 2 V. Therefore, the additional peak can be safely associated with the supporting electrolytes. Similar behavior is also observed elsewhere [27] and suggests that the associated reactions do not involve the redox species.

3.3.5 Impact of crossover on the performance of a flow-cell

The trend of the crossover molar flux obtained through studied *in-situ* measurement is FAP-450 > Nafion 115 > Nafion 117 > FAPQ-375-PP > FAP-330-PE. Excessive swelling was observed for the FAP-450 membrane and also electrolyte imbalance was observed which obstructed to perform the charge-discharge cycling (CDC). The cell having FAPQ-375-PP and FAP-330-PE membrane was tested but it was observed that a layer of redox species get deposited on the hydrocarbon-based anion exchange membranes and obstructed CDC. The condition of the membrane is shown in

Figure S 11.4 and similar behavior was observed by Yihan Zhen while using these membranes with the same electrochemistry [142].

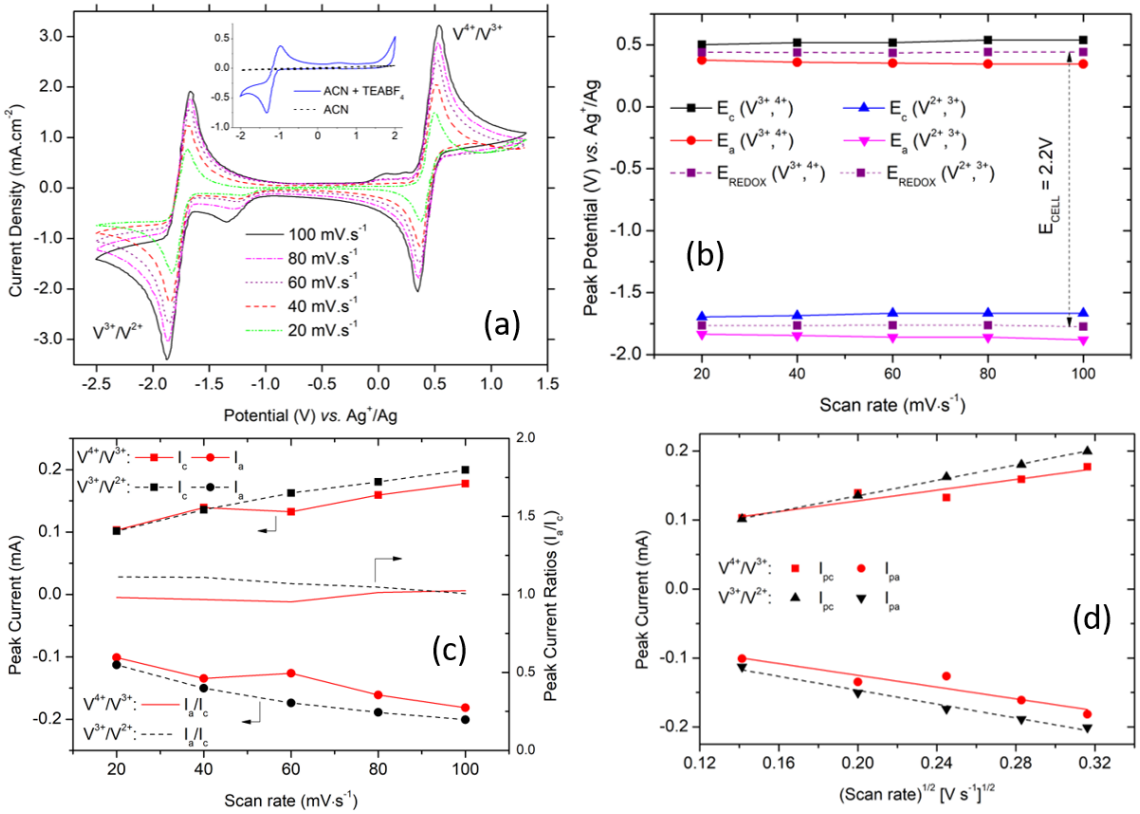


Figure 3.7 (a) Cyclic voltammogram as a function of scan-rate in the range of 20 mV·s^{-1} to 100 mV·s^{-1} of V^{3+}/V^{2+} and V^{4+}/V^{3+} (b) Peak potentials and redox potential for the V^{3+}/V^{2+} and V^{4+}/V^{3+} redox couple, (c) Peak currents and their current ratios (I_c/I_a), (d) Randles-Sevcik analysis for $V(acac)_3$ oxidation and reduction.

The performance of a flow-cell equipped with membranes of Nafion 117 and Nafion 115 was further characterized using 25 charge-discharge cycles. The upper cut-off potential of 1.9 V was established to eliminate the possibility of forming vanadyl acetylacetonate [$VO(acac)_2$] at the positive electrode [143]. State of Charge (SOC) was defined as a function of open-circuit potentials (OCP) and it was measured after each half cycle. The cell was operated with cut-off potentials of 1 V to 2.5 V, including a margin for overpotentials (*ca.* 0.2 V). It was loaded with electrolyte C1 and the performance was examined as a function of constant cycling current density of 1.23 mA·cm^{-2} – corresponds to a discharge rate (C-rate) of 0.67C, where C is the capacity of the cell.

The excerpt of charge-discharge cycles with cells assembled with Nafion 117 and Nafion 115 are shown in Figure 3.8 (a) and (b). The coulombic efficiency of the cell having Nafion 115 (η_{CE} = 83.3 %) and Nafion 117 (η_{CE} = 86.6 %) is comparable to the

results of electrochemical crossover. However, the cell having Nafion 115 has a capacity loss of about 55 % in 25 cycles. Whereas, the capacity loss is also observed in the Nafion 117 which is about 35 % in 25 cycles.

Generally, any loss in the concentration of redox species leads to loss of capacity. The reason behind the capacity loss is usually the presence of side reactions and/or crossover through the membrane. The results of cyclic voltammetry of the redox species indicated that there are no side reactions within this potential range. However, if the battery is overcharged, *i.e.* some V^{4+} is oxidized to V^{5+}, it is no longer possible to revert it to V^{3+} during discharging (reduction). Eventually, the battery will keep losing capacity at every charge-discharge cycle. This can be avoided by keeping the loading potential below 2.27 V [144].

The redox species are also sensitive to environmental oxygen and moisture. Their presence promotes the formation of vanadyl acetylacetonate - $VO(acac)_2$, especially from V^{3+}, which originates capacity fade in every cycle. Since this study was performed within the glove box, the environmental degradation of the electrolyte will be similar for both cells, having Nafion 115 and Nafion 117. Together with other factors, the electrochemical crossover leads to the loss of capacity in both cells.

The voltage efficiency (η_{VE} = 58.5 % and 65.8 % for cells having Nafion 115 and Nafion 117, respectively) is mainly affected by the overpotentials, which can be further divided into activation, ohmic, and mass transport; these can be obtained from the polarization curves (*i*V-curves) and electrochemical impedance spectroscopy (EIS) analysis. The high-frequency intercept is indicative of ohmic losses; it includes ohmic resistances from all the physical components of the cell such as wires, connectors, current collectors, bipolar plates, electrodes, and membranes. The contribution of the ohmic resistances of all components of NAqRFB-cell except electrolyte and membrane is shown in Figure S 11.3 at different compression ratios. Since the felt electrodes are physically porous and softer than the other electrodes (such as carbon paper or metallic foam), the effect of compression is also important and should be established considering its effect on the overall ohmic losses. The measurements indicate that configuration 'C' – *cf.* Figure S 11.3 – is feasible and an electrode having 35 % compression in dry conditions has 29 mΩ of resistance. The Nyquist plot can be corrected by this value to get only the effect of membrane and electrolyte for high-frequency intercept.

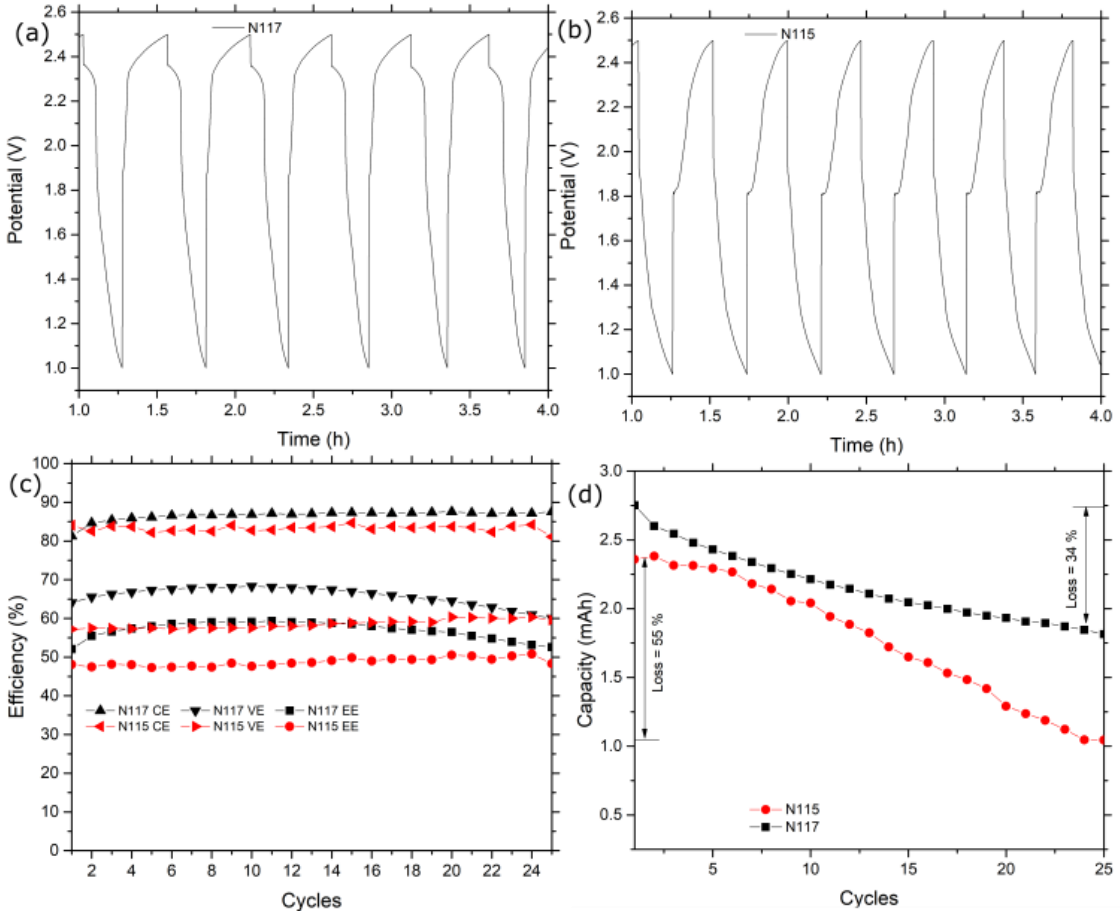


Figure 3.8 Charge-discharge curves at 2 mA·cm^2 at flowrate of 20 cm^3·min^{-1} having nonaqueous electrolyte (Acetonitrile + 0.05 M V(acac)$_3$ + 0.1 M TEABF$_4$) (a) and (b) Three hour expcerpt of charge-discharge cycles of cell having Nafion 117 and Nafion 115 (c) Coulombic, potential and energy efficiency for each cycle (d) Capacity for each cycle during charging and discharging and indicating capacity loss of 34% and 55% in the cell having Nafion 117 and Nafion 115 respectively.

The electrochemical impedance of the operating cell was recorded at E_{OCP} = 1.5 V as shown in Figure 3.9 (a). The impedance curve highlights ohmic contribution and mass transport losses. The value of the high-frequency intercept indicates the ohmic contribution of 67.8 Ω·cm^2 and 65.9 Ω·cm^2 for cells having Nafion 115 and Nafion 117. This contribution can be further decreased through optimization of cell components and also by increasing the concentration of supporting salt. These actions result in a higher value of the voltage efficiency. The polarization response of the NAqRFB-cell was recorded by charging the cell from 0.3 V to 2.5 V at the scan rate of 20 mV·s^{-1} as shown in Figure 3.9 (b). The limiting current density is proportional to the capacity of the battery, which is defined by the concentration of the redox species present in the electrolyte. The electrolyte used in this study offers the theoretical capacity of 13.5 mAh and the limiting

current density is higher in the case of Nafion 117 (14 mA·cm^{-2}) than Nafion 115 (12.6 mA·cm^{-2}) as shown in Figure 3.9 (b). The cells can reach a limiting power rating of 253 mW and 228 mW for the Nafion 117 and Nafion 115 respectively.

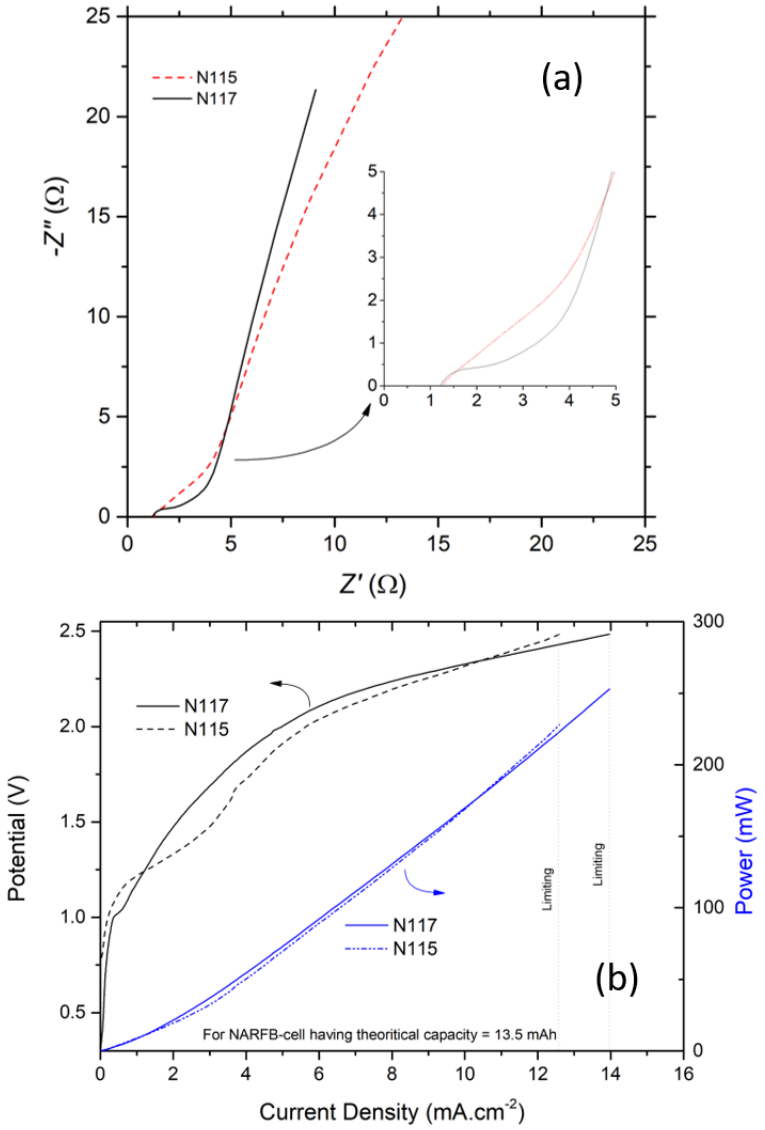


Figure 3.9 (a) Electrochemical impedance curve (-Nyquist Plot) for the cells having Nafion 117 and Nafion 115 (b) Polarization curve analysis at a scan rate of 20 mV·s^{-1} for the cells having Nafion 117 and Nafion 115.

3.4 Conclusion

This study presented a framework for the determination of crossover leading to a systematic diagnostic of membrane for non-aqueous redox flow battery. Ferrocene is reported as a model probing species for *in-situ* crossover measurement. The trend of the crossover molar flux obtained through studied *in-situ* measurement was found to be FAP-450 > Nafion 115 > Nafion 117 > FAPQ-375-PP > FAP-330-PE. It was further compared

with the crossover molar flux rate obtained while using $V^{+4/+3}$ as probing species and was found to be 4.65 and 8.82 μmol·h^{-1}·cm^{-2} for Nafion 117 and Nafion 115 respectively. The trend is similar but the ratio between the crossover of vanadium and ferrocene is almost twice for both the membranes. This highlights the limitation of this technique that if redox species having multiple oxidation states are used, the recorded currents from additional oxidation states may be misinterpreted as crossover molar flux. This possibility was eliminated in this study by using ferrocene which has only one oxidation state. The results of *in-situ* and *ex-situ* measurements show that for the cation as well as for the anion exchange membranes both methods are directly proportional.

The CV analysis using the cathodic peak currents measured at varying scan rates leads to the value of 7.88 × 10^{-6} cm^2·s^{-1} and 7.31 × 10^{-6} cm^2·s^{-1} for the redox couples of V^{3+}/V^{2+} and V^{4+}/V^{3+} respectively. The results signify that there is no side reaction and the electrolyte is suitable for the flow-cell testing. The coulombic efficiency (η_{CE}) of the cell having Nafion 115 (η_{CE} = 83.3 %) and Nafion 117 (η_{CE} = 86.6 %) is comparable which indicates the membrane is performing and the battery is operating successfully. However, the cell having Nafion 115 has a capacity loss of about 55 % in 25 cycles. Whereas, 35 % capacity loss was observed for the cell having Nafion 117. The crossover effect is deteriorating the performance of the cell. The voltage efficiency (η_{VE} = 58.5 % and 65.8 % for cells having Nafion 115 and Nafion 117, respectively) is mainly affected by the overpotentials. The value of the high-frequency intercept indicates the ohmic contribution of 67.8 Ω·cm^2 and 65.9 Ω·cm^2 for cells having Nafion 115 and Nafion 117. The electrolyte used in this study offers the theoretical capacity of 13.5 mAh and limiting current density is higher in the case of Nafion 117 (14 mA·cm^{-2}) than Nafion 115 (12.6 mA·cm^{-2}). The cells can reach a limiting power rating of 253 mW and 228 mW for the Nafion 117 and Nafion 115 respectively.

The presented *in-situ* technique will allow researchers to account for the contribution of diffusion-driven crossover. The quantification of the crossover directly from the flow cells complements the improvement in the design/optimization. Since there is no need for disassembling of the cell, it can be used as a diagnostic tool to assess the realistic membrane situation under real working conditions. This technique has the potential to become the basic testing method and can also aid in membrane diagnostics for other electrochemical systems.

Chapter 4

Composite membranes

4. Composite membranes

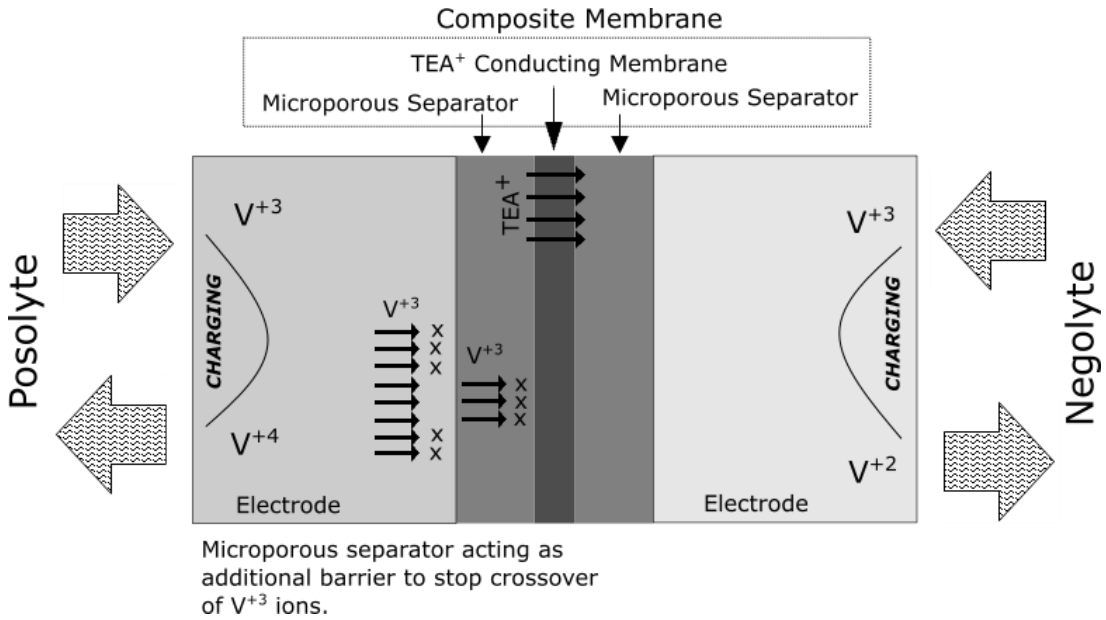
Adapted from the following articles:

K. Mushtaq, A. Mendes, "Hybrid Membrane Leading to Improved Ionic Selectivity for Non-Aqueous Redox Flow Battery", 239th ECS Meeting (June 2021), Chicago, USA.
Link: https://iopscience.iop.org/article/10.1149/MA2021-013231mtgabs

K. Mushtaq, A. Mendes, "Composite membrane for non-aqueous redox flow battery", Electrochimica Acta. (Under Review)

Porous separators display no or very low selective transport of ionic species, allowing redox species of negolyte and posolyte to short circuit. Thicker ion-exchange membranes are being used in non-aqueous redox flow batteries to avoid these disadvantages but at the cost of higher ohmic losses. Interestingly, these disadvantages can be overcome by incorporating a thin ion-exchange (IE) layer sandwiched between pair of microporous membrane separators. The performance of composite membrane presented in this study as a proof-of-concept. The sandwiched membrane allows the use of the thinnest reinforced IE membrane Nafion HP, whereby mechanical strength is ensured by the layers of microporous separators (Celgard 4560 or Celgard 2500). $V(acac)_3$ based non-aqueous electrolyte is used as model chemistry to assess the performance of the membranes. Composite membranes achieved a TEA^+ conductivity of 2.53 $mS \cdot cm^{-1}$, a permeability to Vanadium(III) of 2.76×10^{-9} $cm^2 \cdot s^{-1}$, and selectivity of the balancing cation to the redox cations of 2306. The composite membrane performed better during the battery cycling leading to η_{CE} = 82 %, η_{VE} = 84 %, and η_{EE} = 69 %, compared with Nafion 115 which performed with η_{CE} = 84 %, η_{VE} = 57 %, and η_{EE} = 48 %.

Graphical Abstract



Sketch of a non-aqueous redox flow-cell using the described composite membrane.

4.1 Introduction

Despite the several advantages mentioned in last chapter, one of the most challenging problems for this type of battery is the availability of an efficient membrane for the non-aqueous electrolytes. The ideal membrane should prevent the crossover of redox species while providing higher ionic conductivity. The identification of a highly conductive, yet selective membrane, is of paramount importance for the market penetration of RFBs [145]. Generally, perfluorosulfonic acid (PFSA) ion-exchange membrane (IEM having thickness > 89 µm) is often chosen for NAqRFB providing a trade-off between mechanical strength, ion permeability, and ohmic resistance. Thicker membranes have the advantage of higher mechanical strength and lower crossover rates. However, higher ohmic resistances are expected from thicker membranes which eventually leads to lower performance of the battery and higher material cost.

To address these challenges, porous separators were being considered as an alternative to ion-exchange membranes. These separators are successfully being used for lithium-ion batteries and lead-acid batteries. Unlike PFSA membranes (cation exchange membranes, CEM) and hydrocarbon membranes (anion exchange membranes, AEM), the porous separators have submicrometer pore size. These separators have usually no inherent ion-exchange sites but become conductive when soaked in organic solvents because their internal porosity becomes loaded with the supporting electrolyte and solvent [146]. The high ionic conductivity combined with remarkably low cost makes them promising for RFB applications. However, there are two major disadvantages in using porous separators for the RFB systems [147–149]. Under pressure difference, porous membranes display convective flow causing the volumetric imbalance of electrolytes between the reservoirs. Also, these membranes show no or very low ionic selectivity because of the non-existence of any ion-exchange sites [147–149]. These are the main reasons that porous separators show lower coulombic efficiency and cycling performance than ion-exchanging membranes.

Interestingly, both disadvantages can be overcome by incorporating a thin ion exchange (IE) membrane sandwiched between two microporous separators. A proof-of-concept for such a composite membrane for the non-aqueous redox flow battery is introduced in this study. Within this study, composite membrane refers to a membrane made of a cation-exchange membrane (Nafion HP) sandwiched by two microporous membranes (Celgard C4560 or C2500). This sandwich allows the use of the thinnest

reinforced Nafion HP membrane (20.3-µm thick) since the microporous separators provide the necessary mechanical strength. In addition, the separator layers act as a barrier to reduce the influx of the solvent whereas the ion-exchange membrane is responsible for the selectivity while keeping the ohmic resistance to the lowest level.

Vanadium acetylacetonate - $V(acac)_3$ - is being used as model redox species for the study of non-aqueous redox flow battery (NAqRFB). It has reversible redox reactions for couples of V^{2+}/V^{3+} (*i.e.*, the negolyte *ca.* -1.75 V *vs* Ag/Ag^{+}) and V^{3+}/V^{4+} (*i.e.* posolyte *ca.* 0.45 V *vs* Ag/Ag^{+}). The ability of this electrolyte to start the battery from the same valency state - V^{3+} - in both half-cells, makes it more appealing. The easy dissolution of these redox species in an organic solvent and its commercial availability at a fair price makes it a promising candidate for future commercial versions of non-aqueous redox flow batteries. The half-cell reactions of the vanadium-based non-aqueous electrochemistry are given in the discharging direction – equations (3.2) and (3.3) [40].

The sketch of a non-aqueous redox flow using the described composite membrane for the vanadium chemistry is displayed in Figure 4.1, where TEA^{+} (tetraethylammonium ion) is the balancing ion.

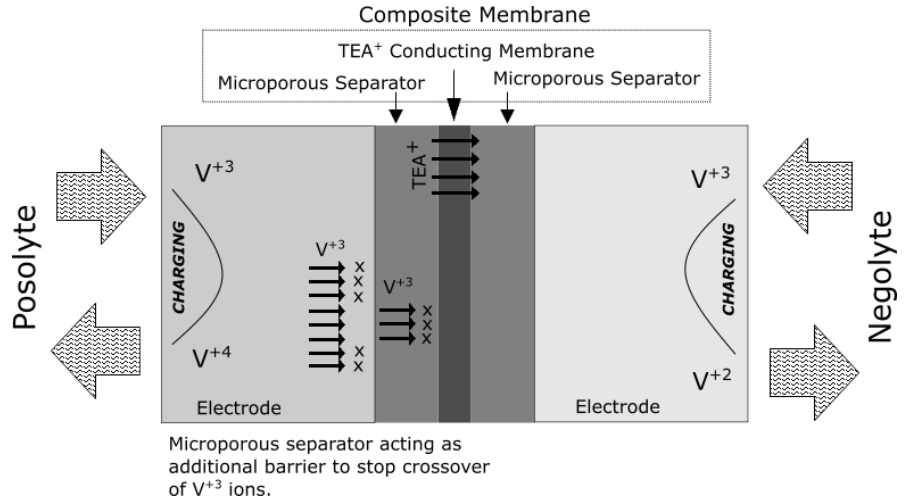


Figure 4.1 Sketch of a non-aqueous redox flow using the described composite membrane.

4.2 Experimental

4.2.1 Electrolytes

Tetraethylammonium tetrafluoroborate, 99%, $TEABF_4$ acquired from Alfa Aesar; Vanadium(III) acetylacetonate, 97%, $V(acac)_3$ acquired from Strem chemicals and Acetonitrile, anhydrous, 99.8%, ACN, acquired from Sigma Aldrich were used as received. All experiments were conducted using non-aqueous electrolytes made of

acetonitrile (ACN) as solvent and $TEABF_4$ as supporting electrolyte. The posolyte without any redox species was referred to as a blank electrolyte. Blank electrolyte (A1) consists of $TEABF_4$ on ACN at 0.1 M. The negolyte (B1) used for crossover measurement and flow-cell electrolyte consists of ACN + $TEABF_4$ 0.1 M + $V(acac)_3$ 0.02 M. Lower concentrations of redox species is recommended to perform voltammetry studies [150]; therefore, electrolyte (B2) consisting of ACN + $TEABF_4$ 0.1M + $V(acac)_3$ 5 mM was used.

4.2.2 Electrodes

Commercial PAN-based Sigracell battery felt (GFD 4.6 EA) was acquired from SGL Carbon. The manufacturer claims excellent chemical resistance, inertness, open porosity of 94 %, the electrical resistivity of < 5 Ω·mm, and area-specific resistance of 0.15 $\Omega \cdot cm^2$. All experiments were conducted using this 4.6 mm thick electrode. The electrodes were cut to size, washed using ethanol, and then dried for 2 hours at 120 ^oC.

4.2.3 Membranes

Reinforced Nafion HP electrolyte membrane was chosen because of the high cation conductivity and sufficient stability. The reinforced membrane was used to avoid the effect of swelling, which is commonly observed for non-reinforced thinner membranes like Nafion 212 or 211. Nafion 115 was also employed to compare the performance results. The properties of the membranes and separators used in the study are listed in Table 3.1. The prepared composite membranes were labeled as C45-HP-C45 and C25-HP-C25; they contain a Nafion HP membrane sandwiched between a pair of Celgard Separator C4560 and C2500 respectively.

The ionic conductivity of ion-exchange membranes in aqueous environments has been studied for more than two decades; comparatively, much fewer reports exist for non-aqueous systems. The through-plane ionic conductivity of a membrane can be measured by electrochemical impedance spectroscopy (EIS). Normally, a single electrolyte (SSE) arrangement is used [151], where the electrolyte is continuously recirculated from the anode to the cathode. The redox species entering the cell at the anode are oxidized and then reduced at the cathode, allowing to keep a constant SOC (50 %). The mathematical relationship to calculate the conductivity of the membrane ($S \cdot cm^{-1}$) is given below [145]:

$$\kappa_m = \frac{\ell}{(R_2 - R_1)A} \tag{4.1}$$

where R_1 is the cell resistance without the membrane, R_2 is the cell resistance with the membrane, ℓ is the membrane wet thickness, and A is the active area of the membrane.

Table 4.1 Properties of the used membranes.

Description	Composition	Thickness (µm)	Pore Size (µm)	Intended application as per manufacturers
Celgard 4560 (Separator)	Microporous monolayer PP, laminated to PP nonwoven fabric	110	0.064	Lithium batteries
Celgard 2500 (Separator)	Microporous Monolayer Membrane PP	25	0.064	Energy storage systems
Nafion HP (CEM)	PFSA / PTFE copolymer	20	-	Fuel cells
Nafion 115 (CEM)	PFSA / PTFE copolymer	127	-	Aqueous batteries and fuel cells
C45-HP-C45	C4560 | Nafion HP | C4560	240	-	Prepared by this work
C25-HP-C25	C2500 | Nafion HP | C2500	70	-	Prepared by this work

Acronyms: (CEM) = Cation Exchange Membrane, PFSA = Perfluorosulfonic acid, PTFE = Polytetrafluoroethylene, PP = Polypropylene

4.2.4 Cyclic Voltammetry of redox species

Voltammograms were recorded using a glassy carbon electrode (GC, Metrohm) as a working electrode, in a 50 ml three-electrode cell configuration. Electrolyte B2 was used to perform all the measurements. Electrode Biologic RE-7, filled with 0.01 M $AgNO_3$ + 0.1 M TBAP + Acetonitrile, was used as reference electrode. Platinum wire served as a counter-electrode. All experiments were performed under a nitrogen atmosphere. Autolab potentiostat (PG302STAT) was used to record all the data and Nova software was used for the voltammograms analysis.

4.2.5 *In-situ* crossover measurement of redox species

The technique of *in-situ* crossover measurement was used as reported in the literature [152]. The peristaltic pump (Ismatec MCP Standard) was used to supply electrolytes to the flow cell. Electrochemical measurements were performed using the workstation of Zennium (Zahner Elektrik, Germany). The cell was connected in a two-electrode configuration, where Working Electrode (WE) is connected to the positive side and Counter Electrode (CE) is connected to the negative side. The negative half-cell was connected to a reservoir having the redox species (electrolyte B1 as negolyte) and the

positive half-cell was connected to the blank electrolyte *i.e.* without any redox species. Each measurement was done with a fresh positive electrode and fresh blank electrolyte. The electrolyte was circulated across the cell at a low flow rate of 3 ml·min^{-1}. The experimental setup is shown in Figure 1.9 (b).

4.2.6 NAqRFB assembly and assessment

A fuel cell from Pragma Industries was modified into a flow cell after changing some components like bipolar plates, O-rings, and gaskets. The carbon felt electrodes were compressed to 35 %, providing a final thickness of 3 mm. The flow experiments were performed in a glove box having a dry nitrogen environment, to minimize the parasitic effect of humidity [136]. Two Schott GL-25 bottles served as reservoirs; 20 ml of posolyte (electrolyte B1) and negolyte (electrolyte B1) were used in the flow cell experiments. The flow circuit is the same as shown in Figure 1.9 (b). Impedance measurements were recorded at open circuit potential (around 1.5 V) with a signal amplitude of 20 mV of amplitude and a frequency range from 100 mHz to 250 kHz, using the Zahner workstation. Potentiostatic measurements were performed to acquire polarization data from 0.1 V to 2.2 V at a scan rate of 20 mV·s^{-1}. Data obtained from charge/discharge cycling (CDC) enabled the calculation of Coulombic, Voltage, and Energy efficiencies (η_{CE}, η_{VE}, and η_{EE}, respectively) for each cycle using equations (2.4), (2.5), and (2.6).

4.3 Results and Discussions

4.3.1 Battery electrolyte characterization

Cyclic Voltammetry (CV) analysis was performed to confirm the redox potentials, reversibility, and to assess diffusion coefficients. Voltammograms shown in Figure 4.2 were performed on vanadium-based non-aqueous electrolytes to investigate the fundamental electrochemical properties of the V^{3+}/V^{2+} and V^{4+}/V^{3+} non-aqueous electrochemistry. The value of the potential at the highest/lowest current density is referred to as peak potential. The value of peak potential for both redox couples (V^{3+}/V^{2+} and V^{4+}/V^{3+}) remains the same for the tested scan rates, indicating that the condition of reversibility of reaction is satisfied – Figure 4.2 (a) and (b). The average of the cathodic and anodic peak potential value is equal to the value of redox potential (E_{REDOX}) for both couples. The difference between the redox potentials of the redox couple gives the overall cell potential, E_{CELL} = 2.2 V as shown in Figure 4.2 (b). The ratios of anodic and cathodic

peak current values were close to unity, as shown in Figure 4.2 (c); this means that the electrochemical reactions are controlled by the mass transport of the redox species. The voltammograms were analyzed using the Randles-Sevcik model at scan rates from 20 mV·s^{-1} to 100 mV·s^{-1}. The linear dependence of peak currents with the square root of the scan rate – Figure 4.2 (d) – allowed the quantification of the diffusion coefficient for this electrochemical system through the following equation [39]:

$$i^{\mathrm{p}}_{\mathrm{ox/red}} = (2.69 \times 10^5) \cdot n^{\frac{3}{2}} \cdot A \cdot D^{1/2} \cdot C^{O\frac{1}{2}} \cdot v^{1/2} \qquad (4.2)$$

where, $i^{\mathrm{p}}_{\mathrm{ox/red}}$ is peak current density (mA·cm^{-2}), n is the number of electrons participating in the reaction, A is the area of the working electrode, D is the diffusion coefficient, $C_{\mathrm{ox/red}}$ is the bulk concentration of the solution, and v is the scan rate.

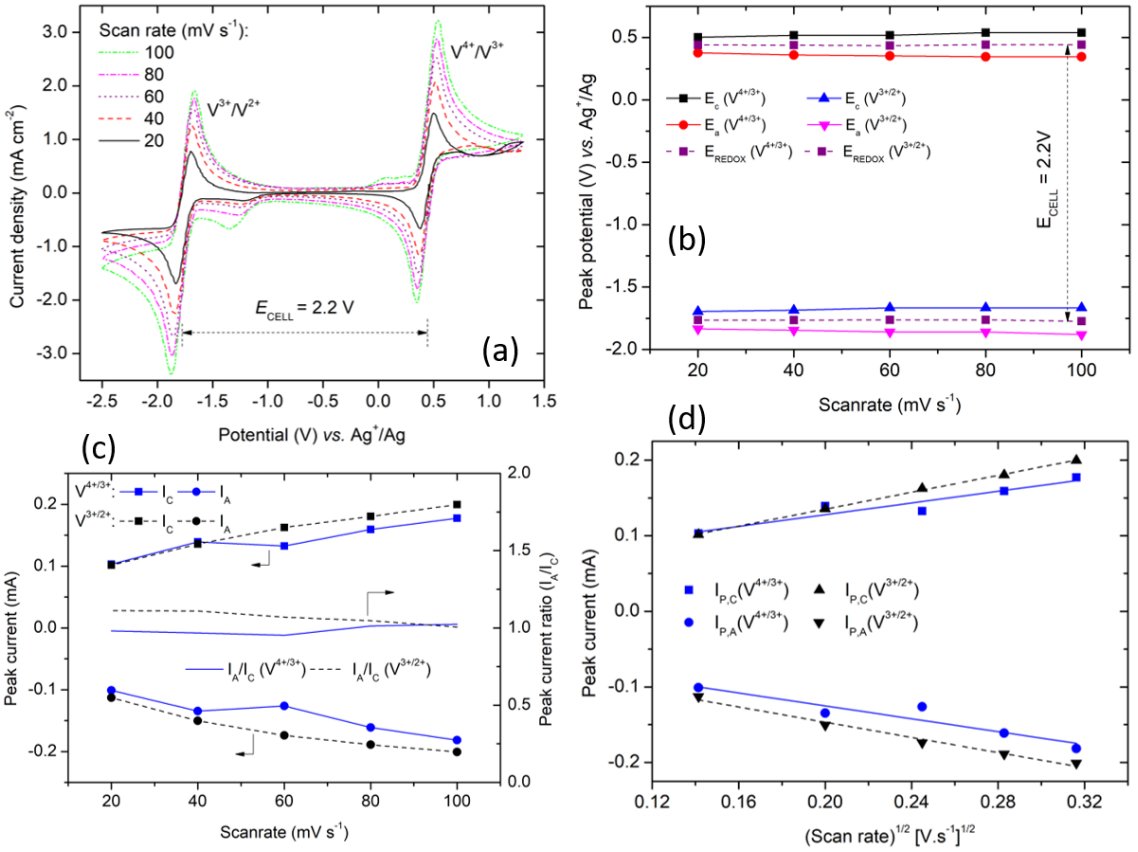


Figure 4.2 (a) Cyclic voltammogram as a function of scan-rate in the range of 20 mV·s^{-1} to 100 mV·s^{-1} of V^{3+}/V^{2+} and V^{4+}/V^{3+} (b) Peak potentials and redox potential for the V^{3+}/V^{2+} and V^{4+}/V^{3+}redox couple. (c) Peak currents and their current ratios (d) Randles-Sevcik analysis for $V(acac)_3$ oxidation and reduction.

Equation (4.2) is used to calculate diffusion coefficients for both redox couples V^{2+}/V^{3+} and V^{3+}/V^{4+}. The analysis using the cathodic peak currents measured at varying

scan rates leads to the diffusivity values of 7.88×10^{-6} $cm^2 \cdot s^{-1}$ and 7.31×10^{-6} $cm^2 \cdot s^{-1}$ for the redox couples of V^{3+}/V^{2+} and V^{4+}/V^{3+}, respectively. The values are comparable to reported literature [39] which indicates that there is no side reaction and the electrolyte is suitable for the flow-cell testing.

4.3.2 Ionic conductivity of membranes

The impedance measurements, at high frequency (250 kHz) were performed on the cell assembled with just the two bipolar plates, in short-circuit to get the ohmic contribution for bipolar plates, current collectors, and workstation wires, *i.e.*, 21.05 mΩ. Then, the cell was assembled with the two bipolar plates and the two electrodes at 35 % compression (without membrane), and the ohmic resistance increased to the value of 37.32 mΩ. This resistance was decreased to the value of 26.1 mΩ after flowing the electrolyte from the same assembly. The cells were finally assembled including the membrane and the electrical conductivity measured again. The tabulated values of the partial and total conductivities are given in supplementary information. The membrane conductivity values were calculated using equation (4.1) and shown in Figure 4.3.

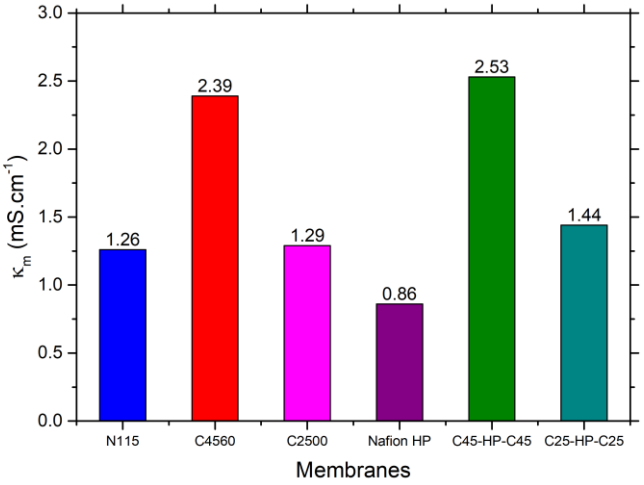


Figure 4.3 Conductivity of the membranes. Composite membranes are designated as C45-HP-C45 and C25-HP-C25.

The conductivity measurements were done using a single electrolyte flow arrangement which eliminates the effect of the crossover. The results of Figure 4.3 show that composite membranes have higher electrical conductivity. However, the relationship between conductivity and the crossover of the active species is a more important parameter while selecting the membrane for any battery application.

4.3.3 Membrane conductivity, crossover of redox species, and selectivity

The performance of any RFB can be improved by decreasing the crossover of redox species and increasing the membrane conductivity. The latter is the inherent characteristics of the membrane and it is difficult to change them independently. But same membranes can behave differently in various electrochemical systems. Therefore, it is of particular interest to understand the relationship between membrane conductivity and the crossover of redox species. Assuming a cation exchange membrane displaying negligible anion permeation, we can define the ideal selectivity (α) of the membrane as [145]:

$$\alpha = \frac{R_{\mathrm{A}}}{R_{\mathrm{m}}} \tag{4.3}$$

where R_{A} is the overall area-specific ohmic resistance of the membrane to the cation permeation of the redox species and R_{m} is the area-specific ohmic resistance of the membrane to the ionic permeation of the balancing cation. The analogy of ohm's law can be used to further express R_{A} as given below:

$$R_{\mathrm{A}} = \frac{RT}{i_{\mathrm{A}}\, F} \tag{4.4}$$

where i_{A} is the permeation current of the redox species, which can be further formulated as [145,153]:

$$i_{\mathrm{A}} = n\,\frac{F}{A}\,\frac{dn_{\mathrm{A}}(t)}{dt} = \frac{nFD_{\mathrm{A}}\left[C_{\mathrm{A,b}} - \left(C_{\mathrm{A},x} \approx 0\right)\right]}{\ell} \approx \frac{nFD_{\mathrm{A}}C_{\mathrm{A,b}}}{\ell} \tag{4.5}$$

n is the number of electrons associated with permeating species. In this work, $n = 1$ is used because only one electron is transferred per reactant species. F is the Faraday constant (96485 C·mol^{-1}); A is the area; n_{A} is the molar flux of redox species; $\mathrm{d}n_{\mathrm{A}}(t)/\mathrm{d}t$ is the crossover rate of redox species (mol·s^{-1}); D_{A} is the permeation diffusivity; $C_{\mathrm{A,b}}$ is the concentration of the permeating redox cation at the anode side; $C_{\mathrm{A},x}$ is the concentration of the permeating redox cation at the cathode side – permeation side; ℓ is the thickness of the membrane.

If one assumes that the number of redox species going across the membrane is much smaller than that of the original redox species in the bulk solution ($n_{\mathrm{A,x}} \ll n_{\mathrm{A,b}}$), R_{m} can be expressed as:

$$R_{\mathrm{m}} = \frac{\ell}{\kappa_{\mathrm{m}}} \tag{4.6}$$

where κ_m is the membrane conductivity ($S \cdot m^{-1}$) and ℓ is the membrane thickness. Therefore, combining equation (3) to (6), ideal selectivity (α) can be expressed as:

$$\alpha = \frac{RT}{F^2 C_{A,b}} \frac{\kappa_m}{D_A} \quad (4.7)$$

The crossover current (i_A), as indicated in equation (4.5), was measured using an *in-situ* crossover measurement methodology as described elsewhere [128]. Briefly, the negative side (containing V^{3+} as redox species) serves as counter-electrode (CE) and the positive side (containing the blank electrolyte *i.e.*, without any redox species) serves as a working electrode (WE). The potential was linearly swept at a very low scan rate ($50\ \mu V \cdot s^{-1}$). Under the chosen potential range, vanadium ions that permeate the membrane, from negative to positive side, should be oxidized under mass-transfer limited conditions, *i.e.*, the diffusion limiting current density should be related to the amount the vanadium permeation through the membrane. This leads to the following redox reactions (4.8) and (4.9) at the electrodes.

Counter-electrode (negative side, cathode):

$$V^{4+} + e^- \rightleftharpoons V^{3+} \quad (4.8)$$

Working-electrode (positive side, anode):

$$V^{3+} \rightleftharpoons V^{4+} + e^- \quad (4.9)$$

Separators (Celgard C4560 and C2500) are showing good conductivity values but the results - Figure 4.4 – highlight that a plateau is not reached and the value of current was kept increasing, indicating a large crossover. For the case of Nafion 115, the low value of crossover current indicates less permeability of redox species across the membrane. Nafion HP is the closest neighbor of the composite membranes but it does not display physical strength to be used in the flow cell. Also, charge-discharge cycling is not possible due to the fragility of the membrane in the acetonitrile-based non-aqueous electrolyte. The combination of Nafion HP sandwiched between separators provides physical strength along with the added advantage of reduced swelling. The results highlight that the prepared composition membranes help to reduce the crossover of redox species.

The permeation of the redox species was calculated using equation (4.5) and plotted against the membrane conductivity, as shown in Figure 4.5. Ideally, the best membrane should exhibit high conductivity and low crossover permeation. The

composite membranes are performing quite well concerning both, conductivity (2.53 $mS \cdot cm^{-1}$ and 1.44 $mS \cdot cm^{-1}$ for C45-HP-C45 and C25-HP-C25, respectively) and crossover permeation (5.11×10^{-9} $cm^2 \cdot s^{-1}$ and 2.76×10^{-9} $cm^2 \cdot s^{-1}$ for C45-HP-C45 and C25-HP-C25 respectively). These results are by far better than the state-of-the-art values existing in the literature [154]; namely by S. Tung by preparing the nanoporous aramid nanofiber separator to overcome similar challenges. They got the conductivity of 0.10 $mS \cdot cm^{-1}$ and crossover permeation of 0.82×10^{-7} $cm^2 \cdot s^{-1}$. Furthermore, Liang Su [145] simulated that the best performance of non-aqueous redox flow battery (*i.e.* η_{CE} > 97 % and η_{VE} > 91.4 %) can be achieved by using the membrane having the values of conductivity and crossover permeation to be *ca.* 1.1 $mS \cdot cm^{-1}$ and 3.42×10^{-8} $cm^2 \cdot s^{-1}$ respectively. The composite membranes prepared in this work are performing better these benchmark values.

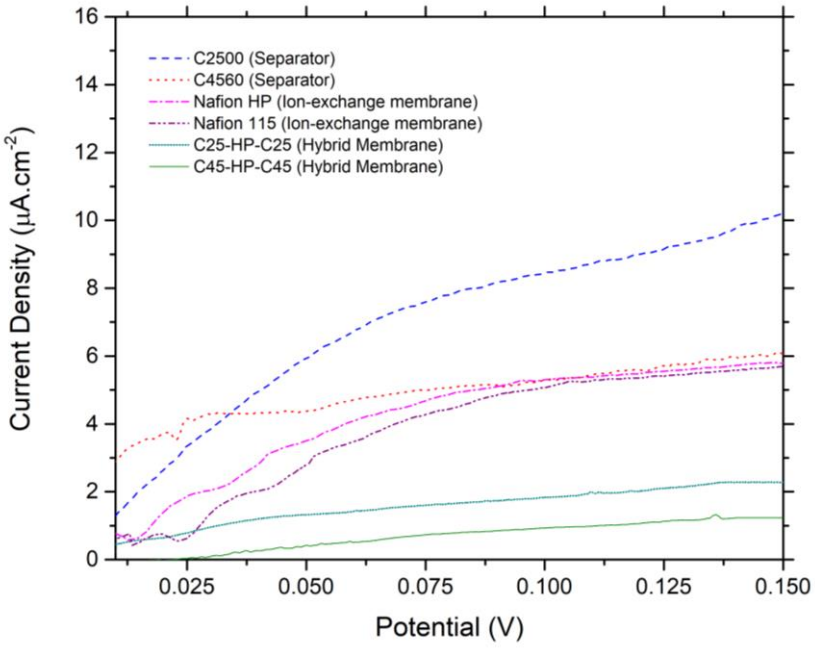


Figure 4.4 Crossover measured current density at the scan rate of 50 $\mu V \cdot s^{-1}$ and flow rate of 3 $ml \cdot min^{-1}$. Working electrode having blank electrolyte consisting of 0.1 M $TEABF_4$ + Acetonitrile and counter electrode having electrolyte with active species of 0.02 M $V(acac)_3$ + 0.1 M $TEABF_4$ + Acetonitrile.

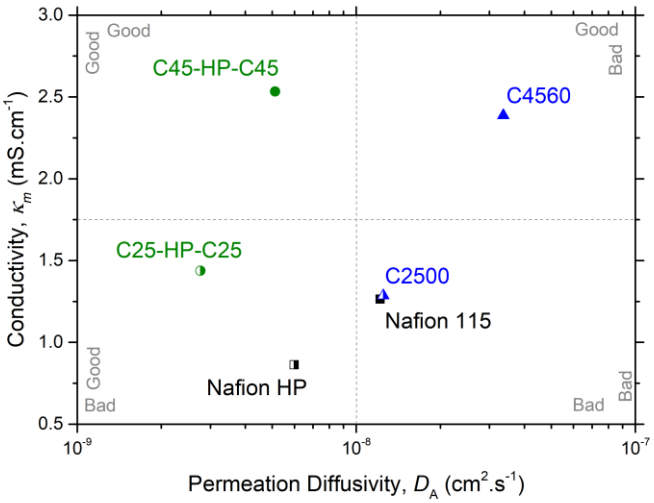


Figure 4.5 The conductivity of membranes as a function of the permeation diffusivity (D_A) of vanadium ions. The conductivity values are obtained from Figure 4.3 and D_A numbers are derived from Figure 4.4.

4.3.4 Impact of composite membrane on the performance of redox flow cell

It was observed that Nafion 212 showed excessive swelling and high crossover, while reinforced membrane Nafion HP displayed minimal swelling. The composite membranes, C45-HP-C45 and C25-HP-C25, and Nafion 115 displayed also suitable behavior when inserted in the redox cell. These membranes were inserted in a redox cell loaded with $V(acac)_3$ as posolyte and negolyte. The cell was then cycled between 1 V to 2.5 V until reaching 50 % of state-of-charge (SOC).

In batteries terminology, the discharge current is often mentioned as C-rate, which is a measure of the rate at which a battery is discharged relative to its maximum capacity. This parameter allows normalizing discharging rate with battery capacity. A 1C rate means that the particular value of current will discharge the entire capacity of the battery in 1 hour. Manufacturers commonly rate alkaline and lead-acid batteries at a very low C-rate (usually 0.05C or 20-hour discharge). A recent article by Siu in Tung reported the performance of the RFB having the same electrochemistry as of this reported at the C-rate 0.2C [154]. But, in this study, it was tested at a higher C-value (C-rate = 0.84C, where C is the total thermodynamic capacity of the cell, *ca.* 10.42 mAh) to assess the performance of the device. In terms of constant cycling current density, this corresponds to 1 $mA \cdot cm^{-2}$. Employing such harsh operating conditions highlights the effect of ohmic

losses, crossover, and mass transport overpotentials caused by the under-study membranes.

The results of flow-cells having the composite membrane were compared with the cell incorporating Nafion 115 and shown in Figure 4.6. The cell having the composite membrane C45-HP-C45, it averaged η_{CE} = 82 %, η_{VE} = 84 % , and η_{EE} = 69 %: whereas, for the cell equipped with composite membrane C25-HP-C25, it averaged to η_{CE} = 88 %, η_{VE} = 67 %, and η_{EE} = 59 %. These results are better than the performance of the cell when equipped with ion-exchange membrane Nafion 115 (η_{CE} = 84 %, η_{VE} = 57 %, and η_{EE} = 48 %). Recent articles [154] also reported similar values of η_{CE} and attributed the lower value to the crossover through the membrane. As mentioned above, the crossover values for membranes C45-HP-C45, C25-HP-C25, and Nafion 115 are relatable to the values of η_{CE}.

An excerpt of 2 hours from the battery cycling was shown in Figure 4.6 (d), (e), and (f). It was observed that the cycles duration are shrinking with cycling time. This effect is more evident for C25-HP-C25 as compared to Nafion 115, which may be ascribed to the irreversible formation of $VO(acac)_2$ in the posolyte reservoir, which is a parasitic non-reversible side reaction for this electrochemistry [143]. This effect can be avoided by keeping the upper cut-off potential below 2.3 V to eliminate the possibility of forming vanadyl acetylacetonate, $VO(acac)_2$. The presence of oxygen and moisture can also trigger this reaction. This effect can be identified performing a cyclic voltammogram of the electrolyte before and after the addition of a small amount of moisture (H_2O) and also only by exposure to dry oxygen. The possible sources of these contaminants are residual water in the chemical reactants and solvents, water absorbed on cell components (such as electrodes, bipolar plate, and/or membrane), or also the water vapor trapped inside the N_2-filled glove box. Since capacity retention is not the focus of the present study, this issue will be investigated in-depth in future works.

The CDC results show that the main difference between the cells is in the value of η_{VE}. It is mainly affected by the activation overpotentials, ohmic and mass transport efficiency losses; their contribution can be quantified using polarization analysis based on linear sweep voltammetry (LSV) and impedance analysis based on electrochemical impedance spectroscopy (EIS) measurements.

4.3.5 Impedance and polarization analysis

EIS was performed at the end of the charge-discharge cycling (at SOC = 50 %) for each membrane. Further analysis was conducted fitting the equivalent circuit model in Figure 4.7 to the impedance curves. The inductance of the wires is denoted by L_1 and R_S is the ohmic contribution of the cell which is dominated by the membrane. The interfaces of electrode-electrolyte present at the anode and cathode are represented by using a parallel combination of R_a and R_c with CPE_a and CPE_c, respectively. The equivalent circuit fits the individual impedance curves (Figure 4.7) very well. The EIS parameters used in the equivalent circuit model could be determined with good accuracy (Table 4.2). The errors for each parameter are within the 95 % confidence interval according to the equivalent circuit analysis in ZView and remain within the Chi-squared criteria ($< 1 \times 10^{-3}$).

The *x*-intercept of the Nyquist plot indicates the ohmic contribution of the cell and is denoted in the equivalent circuit by the resistive component R_S. The variation for each assembly is the membrane has different thicknesses. So, the ohmic contribution should be different as expected. Since the EIS measurements were taken after charge-discharge cycling for each cell having new electrodes. Therefore, the pattern of the impedance curve is slightly different highlighting that there is a slight influence of membrane on the electrode-electrolyte interface as well. The inductance (L_1) represents the inductive behavior of the potentiostat wires which is similar for all the membranes. The fitted parameters can help to estimate the overall impedance of the cell by using impedance analysis of the RC circuit.

The cell impedance is lowest for the C25-HP-C25 but the high value of crossover makes it less appealing. The cell assembly having C45-HP-C45 suffers from higher anodic charge transfer resistance which usually arises from the electrode-electrolyte interface and not because of the membrane-electrolyte interface. Therefore, composite membrane C45-HP-C45 possesses the ability to further reduce the overall cell impedance and can be chosen for further optimization of the cell performance.

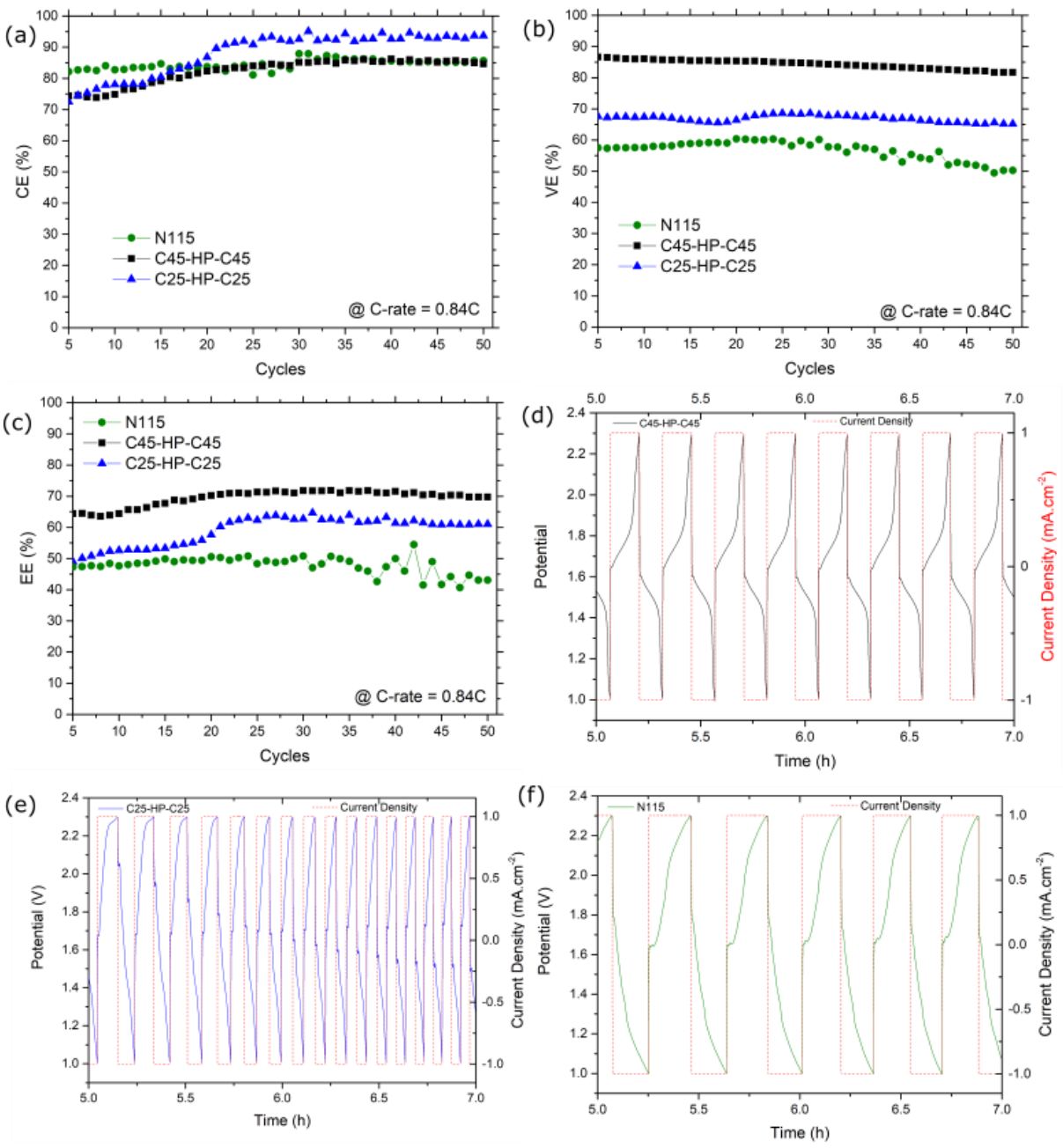


Figure 4.6 Charge-discharge cycling of redox flow cell having vanadium based non-aqueous electrolyte - 0.02 M $V(acac)_3$ + 0.1 M $TEABF_4$ + Acetonitrile - flowing at 30 ml·min^{-1} operating at C_{rate} = 0.84C (a) coulombic efficiency (b) voltage efficiency (c) energy efficiency (d) Excerpt from the 50 cycles performed on composite membrane C45-HP-C45 (e) Excerpt from the 50 cycles performed on composite membrane C25-HP-C25 (f) Excerpt from the 50 cycles performed on nafion membrane N115.

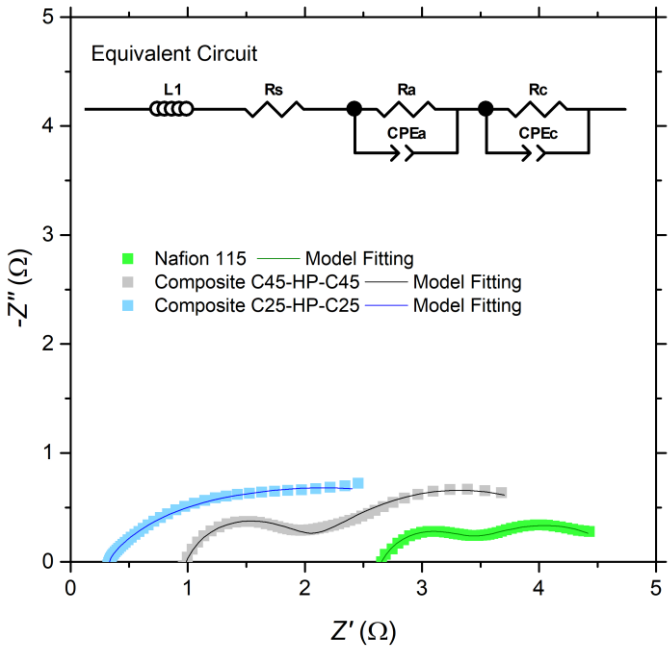


Figure 4.7 Impedance spectroscopy performed after charge-discharge cycling at SOC = 50 % (OCP = 1.5 V), electrolyte flowing at 30 ml·min^{-1}, and having an active area of 7.29 cm^2. The -Nyquist plotted as scatter plot and lines represent the corresponding equivalent circuit fitting on each curve.

Table 4.2 Fitting parameters and RC circuit impedance analysis of the equivalent circuit for the impedance curves shown in Figure 4.7.

	Membranes					
Elements	C25-HP-C25		C45-HP-C45		N115	
	Value	Error (%)	Value	Error (%)	Value	Error (%)
	Fitted Parameters					
L_1 (mH)	3.72×10^{-4}	0.63	4.45×10^{-4}	0.459	4.06×10^{-4}	0.62
R_s (Ω)	0.332	0.26	0.997	0.594	2.655	0.03
R_a (Ω)	0.702	1.12	1.249	1.261	1.041	0.11
CPE_a (mF)	1.674	3.41	0.00836	4.996	0.0052	2.13
R_c (Ω)	2.965	1.95	2.634	0.282	1.368	0.48
CPE_c (mF)	9.425	1.53	23.87	1.873	2.234	1.36
Chi-Squared (Criteria < 1E-03)	1.3×10^{-4}		4.3×10^{-6}		2.9×10^{-4}	
	RC-circuit Impedance Analysis					
$\lvert Z_{RC,a}\rvert$ (Ω)	0.014		0.637		0.760	
$\lvert Z_{RC,c}\rvert$ (Ω)	0.186		0.026		0.206	
$\lvert Z_{CELL}\rvert$ (Ω)	0.533		1.661		3.622	

The highest limiting current density that can be achieved by the NAqRFB-cell under these operating conditions was measured using polarization curves as shown in Figure 4.8. The cell equipped with membrane C25-HP-C25 can reach up to 98 $mA \cdot cm^{-2}$ (which corresponds to C_{RATE} = 13C, where C is the maximum capacity, *i.e.*, 53 mAh for 0.1 M $V(acac)_3$ electrolyte used for polarisation measurements) whereas C45-HP-C45 has achieved 64 $mA \cdot cm^{-2}$ (which corresponds to C_{RATE} = 8.7C). Both composite membranes are performing better than Nafion 115, which achieved 21 $mA \cdot cm^{-2}$ (corresponding to C_{RATE} = 3C). The highest reported current density in the optimized conditions for the aqueous-based VRFB is 1000 $mA \cdot cm^{-2}$ [155] (which corresponds to the C-rate = 8.5 C, where C is the ideal capacity, *i.e.*, 858 mAh or 42.8 $Ah \cdot L^{-1}$ for commercially available 1.6 M $VOSO_4/V_2(SO_4)_3$ based aqueous electrolyte [156]) and commercial VRFB is operated at the current density of 80 $mA \cdot cm^{-2}$ (which corresponds to C_{RATE} = 0.68C having 1.6 M electrolyte). This means that even at unoptimized conditions, the charge/discharge response rate of $V(acac)_3$-based NAqRFB (C-rate = 13C) equipped with either composite membrane is better than aqueous VRFB (which have maximum C-rate = 8.5C and commercial C-rate = 0.68C).

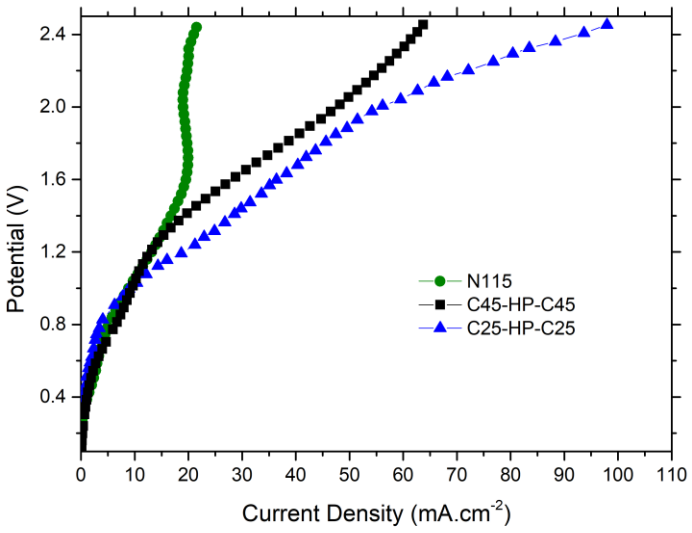


Figure 4.8 Polarization curves for the NAqRFB while sweeping in the range of 0.1 V to 2.5 V at the scan rate of 20 $mV \cdot s^{-1}$ and electrolyte flowing at 30 $ml \cdot min^{-1}$.

4.3.6 Linking selectivity of membrane and flow cell efficiency

The maximum energy efficiency of the RFB can be quantitatively linked to the selectivity of the membrane. Wei Xie [153] derived the following simplified equation, which relates maximum energy efficiency with the membrane selectivity:

$$\eta_{\mathrm{EE,max}} = \left(1 - \sqrt{\frac{\phi RT(1+\tau)(1+\tau^{-1})}{\alpha F E_{\mathrm{OCP}}}}\right)^2 \qquad (4.10)$$

where $\eta_{\mathrm{EE,max}}$ is the maximum efficiency of a flow battery, T is the absolute temperature, τ is the ratio between charge to discharge times, α is the selectivity of the membrane, and E_{OCP} is the open-circuit potential; provided the area-specific resistance is dominated by the membrane which is the present case. The proportionality constant ϕ depends on the reactions associated with crossover and the charge carried by the exchanging species for which selectivity is defined, which is V^{4+} in the present study as per equation (4.10). For a vanadium-based RFB with equal fluxes of all vanadium species across the membrane $\phi = 4$ [157]. Equation (4.10) can be applied when polarization is linear and parasitic crossover occurs by diffusion.

The ideal trend of energy efficiency as a function of selectivity ($\eta_{\mathrm{EE,max}}$ *vs.* α) is shown in Figure 4.9. This highlights the margin for improvement to enhance the performance of composite membranes. Future approaches should address thinner composite membranes prepared using a chemical binder between layers or by applying a pressure; this helps to reduce the ohmic losses.

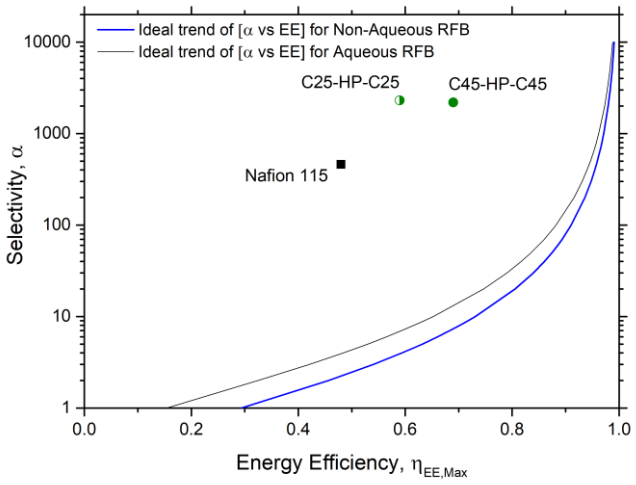


Figure 4.9 Ideal trend of round trip energy efficiency as a function of membrane selectivity.

4.4 Conclusion

The selectivity of the porous separator is enhanced by using a sandwiched ion-exchange layer. This composite membrane performed better than a single layer of porous separator or membrane. The composite membranes are performing quite well concerning both, conductivity (2.53 $mS \cdot cm^{-1}$ and 1.44 $mS \cdot cm^{-1}$ for C45-HP-C45 and C25-HP-C25, respectively) and crossover permeation (5.11×10^{-9} $cm^2 \cdot s^{-1}$ and 2.76×10^{-9} $cm^2 \cdot s^{-1}$ for C45-HP-C45 and C25-HP-C25 respectively). The composite membrane also performed better during the charge-discharge cycling. The cell having the composite membrane C45-HP-C45, it averaged η_{CE} = 82 %, η_{VE} = 84 %, and η_{EE} = 69 %: whereas, for the cell equipped with composite membrane C25-HP-C25, it averaged to η_{CE} = 88 %, η_{VE} = 67 %, and η_{EE} = 59 %. These results are better than the performance of the cell when equipped with ion-exchange membrane Nafion 115 (η_{CE} = 84 %, η_{VE} = 57 %, and η_{EE} = 48 %). The cell impedance is lowest for the C25-HP-C25 but the high value of crossover makes it less appealing. The composite membrane C45-HP-C45 possesses the ability to further reduce the overall cell impedance and can be chosen for further optimization of the cell performance. The composite membrane C25-HP-C25 allowed to achieve a high limiting current density of 98 $mA \cdot cm^{-2}$ from the cell which corresponds to the high discharge response C_{RATE} = 13C as compared to the highest achieved for aqueous VRFB (i.e. C_{RATE} = 8.5C). The ideal trend of energy efficiency as a function of selectivity highlights that there is a margin for improvement in cell performance while using composite membranes. For future studies, this proof-of-concept composite membrane can be fabricated using more compactness either by using pressure or some binders.

Blank Page

Chapter 5

Parasitic reaction free electrodes

5. Parasitic reaction free electrodes

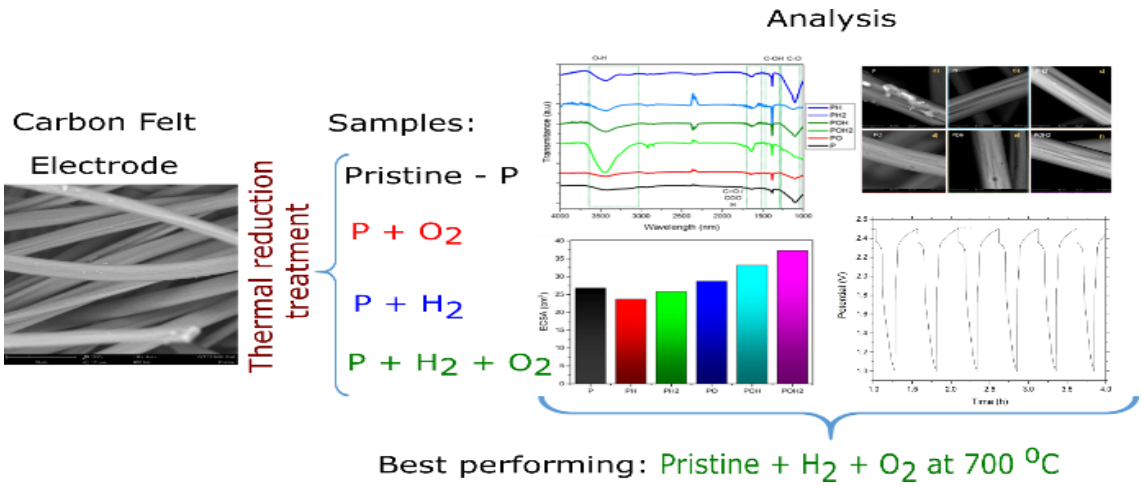
Adapted from the following articles:

K. Mushtaq, S. Delgado, A. Mendes, "Thermal Hydrogen Treatment of Electrodes for Performance and Stability Enhancement of Non-Aqueous Redox Flow Batteries", 239th ECS Meeting (June 2021), Chicago, USA.
Link: https://iopscience.iop.org/article/10.1149/MA2021-013232mtgabs

K. Mushtaq, S. Delgado, A. Mendes, "Parasitic reaction free electrodes for high performance and stability in non-aqueous redox flow batteries", Journal of Energy Chemistry, Elsevier (Under review).

The meticulous study was carried out to understand the sudden cell capacity loss and noticeable degradation of non-aqueous vanadium flow batteries (NAqRFB). The presence of moisture and/or oxygen on both the electrolyte and carbon felts was confirmed to trigger a parasitic reaction that favors the formation of irreversible $VO(acac)_2$ which in turn hinders the performance of NAqRFBs. The main sources for this parasitic reaction were studied and it was found that one of the culprits refers to the use of oxygen-rich electrodes. A disruptive technique was deployed to fix this degradation mechanism and thus increase the lifetime of the battery, which consists of using a tailored and microstructural carbon felt surface modification based on a hydrogen reduction treatment. The impact of such reduction treatment on the structure and chemistry of the electrodes was studied by performing morphological characterizations such as scanning electron microscopy and FT-IR spectroscopy. The electrochemical surface area (ECSA) of the electrodes was obtained and it was discovered that the resulting oxygen-less carbon felts prepared by H_2 treatment at 700 ^oC aid to increase the ECSA and lessen electronic resistances, which results in the observed boost of overall performance. The modified electrodes allowed a coulombic efficiency of η_{CE} = 90%, a voltage efficiency of η_{VE} = 57%, the energy efficiency of η_{EE} = 52% and a stable average capacity of 10.42 mAh throughout 45 charge/discharge cycles, which is the largest ever reported stability for such a system. The maximum current density increased up to 60 % compared to the system equipped with pristine, non-modified electrodes. The proposed technique paves the way for the future optimization and market penetration of this technology.

Graphical Abstract



Sequential thermal reduction treatment of carbon felt by O_2 followed by H_2 results into oxygen-less high performing electrodes.

5.1 Introduction

The transition toward a climate-neutral society requires fundamental changes in the way energy is being transformed, stored, and used. This motivates the increasing trend for the implementation of renewable energy systems and electric battery vehicles (EBV) encouraging the development of energy storage systems, especially batteries. The EU's total CO_2 footprint in 2019 reached 6.7 tons per person, according to Eurostat [1]. Unsurprisingly, from 2010 to 2021, battery demand grew by 30 % annually and reached a volume of 280 GWh in 2021 [158]. This tendency is expected to keep growing, at an estimated 25 % annual rate, to reach a volume of 2035 GWh in 2030 [158]. Still, to reach the sustainability goals, batteries must exhibit ultra-high performance surpassing their capabilities set today by the European Green Deal [159], the lifetime of these devices and their performance should be much improved.

The market for high-energy-density rechargeable batteries is currently dominated by lithium-ion chemistries. However, the present generation of Li-ion batteries (LIBs) is approaching their performance limits. Without a breakthrough, battery performance and production will not keep up with the developments necessary to build a climate-neutral society. While LIBs will continue to play a major role in the energy storage landscape, alternative technologies are required for enabling the creation of future sustainable batteries and lay the foundation for European competitiveness during the energy transition. Recent studies, [4] projected the lowest levelized cost of storage (LCOS) for nine electricity storage technologies from 2015 to 2050; the top two technologies are LIBs and redox flow batteries (RFB).

Vanadium acetylacetonate - $V(acac)_3$ - is being used as model redox species for the study of vanadium-based non-aqueous redox flow battery (V-NAqRFB) [23]. The half-cell reactions of the vanadium-based non-aqueous electrochemistry, loaded with a solvent/supporting electrolyte of acetonitrile/$TEABF_4$, are mentioned in discharging direction in equations (3.2) and (3.3) [160]. Despite the high potential of this chemistry, 2.2 V, the electrolyte is very sensitive to moisture and oxygen [161], which triggers the parasitic side reactions. These parasitic side reactions are responsible to consume the concentration of redox species which in turn results in loss of capacity and operational current density. In the RFB, sources of moisture might arise from residual water on chemical reagents, solvents, or even that is absorbed on the components of the cell, besides the water vapor inside the glove box. A dry nitrogen atmosphere should be used

to protect the electrolyte from any environmental moisture. Nonetheless, it was observed that even maintaining the electrolyte in a fully inert atmosphere or operating inside a purged glovebox is not sufficient to maintain stability during battery operation [161]. The sudden cell failure should then root in the components of the cell; the authors suspected carbon felts / bipolar plates as a possible source of oxygen since they normally display a surface containing a high concentration of oxygenated functional groups [96].

Hydrogen is known as a powerful reducing agent which can be employed to remove these oxygen groups. Therefore, the impact of different pre-treatments on the carbon felts morphology and performance for the V-NAqRFB was assessed in this work. Mainly, the effect of using pristine carbon felt electrodes from SGL (4.6 GFD) – referred to as P, oxygen treated electrodes – referred to as PO, hydrogen treated electrodes – referred to as PH, and a combination of oxygen followed by a hydrogen treated electrodes – referred to as POH, were studied. These electrodes were then characterized concerning the morphology and surface chemistry, by SEM and FTIR, and concerning the electrochemical performance in a NAqRFB-cell, by impedance spectroscopy and polarization measurements. This study allowed to decipher the relation between the surface chemistry of each electrode and the stability of the cell and its electrochemical activity.

5.2 Experimental Methods

5.2.1 Materials

Tetraethylammonium tetrafluoroborate, $TEABF_4$ from Alfa Aesar, 99%; Vanadium(III) acetylacetonate, $V(acac)_3$ from Strem chemicals, 97%; and Acetonitrile, ACN from Sigma Aldrich, anhydrous, 99.8% were used as received. All experiments were conducted using non-aqueous electrolytes composed of acetonitrile (ACN) as solvent and $TEABF_4$ as supporting electrolyte. The flow-cell electrolyte consists of "ACN + $TEABF_4$ 0.5 M + $V(acac)_3$ 0.1 M", referred to in this study as A1. The voltammetry studies were performed using the electrolytes consisting of "ACN + $TEABF_4$ 0.1 M + $V(acac)_3$ 0.02 M", referred to in this study as A2. The composite membrane consists of layers of the separator from Celgard and Nafion membrane in the order of C2500 | Nafion HP | C2500 is referred to as C25-HP-C25 in this study. The electrodes were purchased from Sigracell, SGL Carbon, 4.6 mm of thickness.

5.2.2 Preparation of the electrodes

Different heat and acid treatments were applied to as-received carbon felt samples, as indicated in Table 5.1.

Table 5.1. Treatments applied to as-received electrodes

Reference	Steps of preparation
Pristine (P)	Cleaning with ethanol and dried in the oven at 80 ^{o}C for 2 hours
Pristine with thermal treatment in O_2 environment (PO)	Boiled in 1 M H_2SO_4 for 12 hours. Washed with DI water and dried in an oven for 2 hours at 120 ^{o}C. Placed inside a furnace for 10 hours at 400 ^{o}C having an oxygen-rich environment. Reached the room temperature inside the furnace.
Pristine with thermal treatment in H_2 environment at (PH / PH2)	Cleaning with ethanol and dried in an oven at 80 ^{o}C for 2 hours. Placed in a tube furnace under a hydrogen flow rate of 190 ml min^{-1} for 10 hours at 400 ^{o}C (For PH2, Temperature = 700 ^{o}C). Reached the room temperature inside the furnace.
Pristine with thermal treatment in O_2 followed by H_2 (POH / POH2)	PO samples were placed in a tube furnace having hydrogen at a flow rate of 190 ml min^{-1} for 10 hours at 400 ^{o}C (For POH2, at 700 ^{o}C). Reached the room temperature inside the furnace.

5.2.3 Morphology characterization

The surface morphologies of the carbon felt electrodes were analyzed using a field emission scanning electron microscope SEM (PhenomPro XL). SEM images were obtained at different magnifications (up to 12500x) to decipher features at the nanoscale. The surface functionalization groups on the carbon felt were identified using Fourier-transform infrared spectroscopy FT-IR, (Bruker VERTEX70) in the 400 – 4000 cm^{-1} range at room temperature using air as sweep gas at 8 ml min^{-1}. The surface fibres of the felts were firstly ground using a mortar and pestle, then diluted in KBr in a weight percent ratio of 1:200 and afterward, placed in the transmission apparatus.

5.2.4 Electrochemical characterization

5.2.4.1 Configuration of 3-electrode cell

Cyclic voltammograms (CVs) were retrieved by varying the scan rate from 2.5 mV s^{-1} to 100 mV s^{-1} (2.5, 10, 20, 50, 100 mV s^{-1}) and within the range of -2.4 V to -1.0 V in the configuration of three electrodes cell. The volume of 50 ml for electrolyte A2 was used, 6 mm diameter from each CF sample was placed in a gold tip and submersed in the electrolyte serving as a working electrode; an electrode Biologic RE-7, filled with

0.01 M $AgNO_3$ + 0.1 M TBAP + Acetonitrile operated as reference electrode and the counter-electrode was a platinum wire. A Zahner Zennium potentiostat equipped with Thales software enabled the recording of the voltammograms under an inert (N_2) saturated atmosphere. The effect of the purging gas on the electrolyte was studied to verify the stability of V^{3+}/ V^{2+} and V^{4+}/ V^{3+} redox species and the reversibility of the reactions under inert (N_2) and oxidative (O_2) environment using a glassy carbon (GC, Metrohm) in the three-electrode cell. An accelerated stress test (AST) was performed to assess the impact of oxygen group functionalities on the surface of the different CFs and screen their impact on the reversibility of the reactions of interest. This protocol encompassed the cycling of the electrodes PO and POH2 from -2.1 V to 1.4 V at 100 mV s^{-1} in N_2 purged electrolyte.

5.2.4.2 Redox flow-cell assembly

A commercial fuel cell from Pragma Industries was modified into a flow-cell, by introducing bipolar plates from Roy Carbon having serpentine flow-field; nitrile rubber O-rings were replaced by PTFE O-rings for compatibility with the non-aqueous solvents used in this study. The carbon felt (SGL 4.6 EA) were placed on each of the flow-fields and sealed by the Teflon gaskets. An electrode compression of 34% was ensured which results in a final thickness of 3 mm. The flow experiments were performed in a glove box under a dry nitrogen environment. Two Schott GL25 bottles served as reservoirs. The 20 ml of posolyte (electrolyte A1) and negolyte (electrolyte A1) were circulated at the flowrate of 30 ml·min^{-1}. The flow circuit is depicted in Figure 1.9 (b). Impedance measurements were recorded at 10 mV of amplitude and OCP (around 1.5 V) across the frequency range of 250 kHz to 100 mHz using a Zahner workstation. Potentiostatic measurements were performed to acquire polarization data from 0.1 V to 2.5 V at a scan rate of 20 mV·s^{-1}. Data obtained from charge/discharge cycling (CDC) enabled the calculation of Coulombic, Potential, and Energy efficiencies (η_{CE}, η_{VE}, and η_{EE}, respectively) using equations (2.4), (2.5), and (2.6).

5.3 Results and discussions

5.3.1 Environmental moisture and oxygen effect on the stability of redox species

The non-aqueous electrolyte A2, containing dissolved redox species $V(acac)_3$, was characterized in a three-electrode cell equipped with a glassy carbon performing as a working electrode to screen the electrolyte stability when exposed to oxygen or

moisture. Figure 5.1 displays the cyclic voltammograms of pristine and contaminated non-aqueous electrolyte A2. Figure 5.1 (a) displays the cyclic voltammogram of pristine electrolyte; this voltammogram indicates that the redox reaction is reversible with a cell potential of 2.2 V. Deionized (DI) water was added gradually to the electrolyte to mimic the increment of relative humidity (RH). The stability of redox pairs – $V^{3+/2+}$ and $V^{4+/3+}$ *cf*. equations (3.2) and (3.3) - was assessed in the presence of moisture, as shown in Figure 5.1 (b) and (c). Both anodic and cathodic peaks for the redox couple $V^{3+/2+}$ vanished upon the addition of solely 50 ppm DI water. The latter highlights that even the atmospheric moisture - *ca.* RH = 35.6 % @ 25 °C - can degrade the electrolyte, especially for the $V^{3+/2+}$ redox couple. On the other hand, the redox couple of $V^{4+/3+}$ is comparatively less sensitive and therefore, degraded slowly until 2500 ppm - Figure 5.1 (c); nonetheless, upon the addition of 375 000 ppm, there was an evident peak reduction and even loss of reversibility. The addition of water dilutes the electrolyte which affects the peak current values but the loss achieved surpasses greatly the effect of dilution. Therefore, it is crucial to use a dry atmosphere to keep the electrolyte stable. Since $V^{4+/3+}$ remains stable, it can be used as a posolyte, combined with a suitable negolyte. The proposed reaction mechanism for the parasitic formation of $VO(acac)_2$ is given below [143]:

$$V(acac)_3{}^{+} + H_2O \rightarrow VO(acac)_2 + Hacac + H^{+} \qquad (5.1)$$

The saturated electrolyte with O_2 caused the rise of additional peaks which indicated a strong influence for the reaction's shift towards the formation of parasitic $VO(acac)_2$ as can be seen in Figure 5.1 (d). Thus, keeping a dry and oxygen-free atmosphere is of utmost importance for maintaining a stable battery operation. Interestingly, it was found that the reversibility of species on the working electrode (WE) depends on the exposure time to the oxygenated electrolyte. The effect is negligible up to 20 minutes but extremely critical after 4 h. The aged electrolyte could not be regenerated after 4 h of nitrogen bubbling; the anodic/cathodic peak current densities decreased *ca*. 67% and additional peaks for $VO(acac)_2$ (-2.1 V and -1.9 V) became apparent in Figure 5.1 (d). The following reaction mechanism was proposed to happen in parallel with the reduction of molecular oxygen [143]:

$$4V(acac)_3 + 2H_2O + O_2 \leftrightharpoons 4VO(acac)_2 + 4Hacac \qquad (5.2)$$

5.3.2 Electrochemical Surface Area of modified electrodes

The combined thermal treatment of the carbon felt electrodes under an oxygen atmosphere (400 °C, 10 h) followed by a treatment under and hydrogen atmosphere (400 °C, 10 h – referred to as POH) was performed for extensively removing the attached oxygen functional groups. An additional set of samples was prepared to assess the impact of the treatment at higher temperatures, 700 °C and 10 h under H_2 flow (referred to as PH2 and POH2). The electrochemical activity of each carbon felt (CF) sample for the redox couple V^{3+}/V^{2+} was analyzed by cyclic voltammetry using a three-electrode cell at 25 °C, as detailed in *c.f.* section 1.4.1. Figure 5.2 (a) shows the CVs of samples P, PH, PO and POH immersed in V^{3+}/V^{2+} redox couple in 0.1 M $TEABF_4$ + 0.02 M $V(acac)_3$ + Acetonitrile electrolyte, at the scan rate of 10 $mV \cdot s^{-1}$.

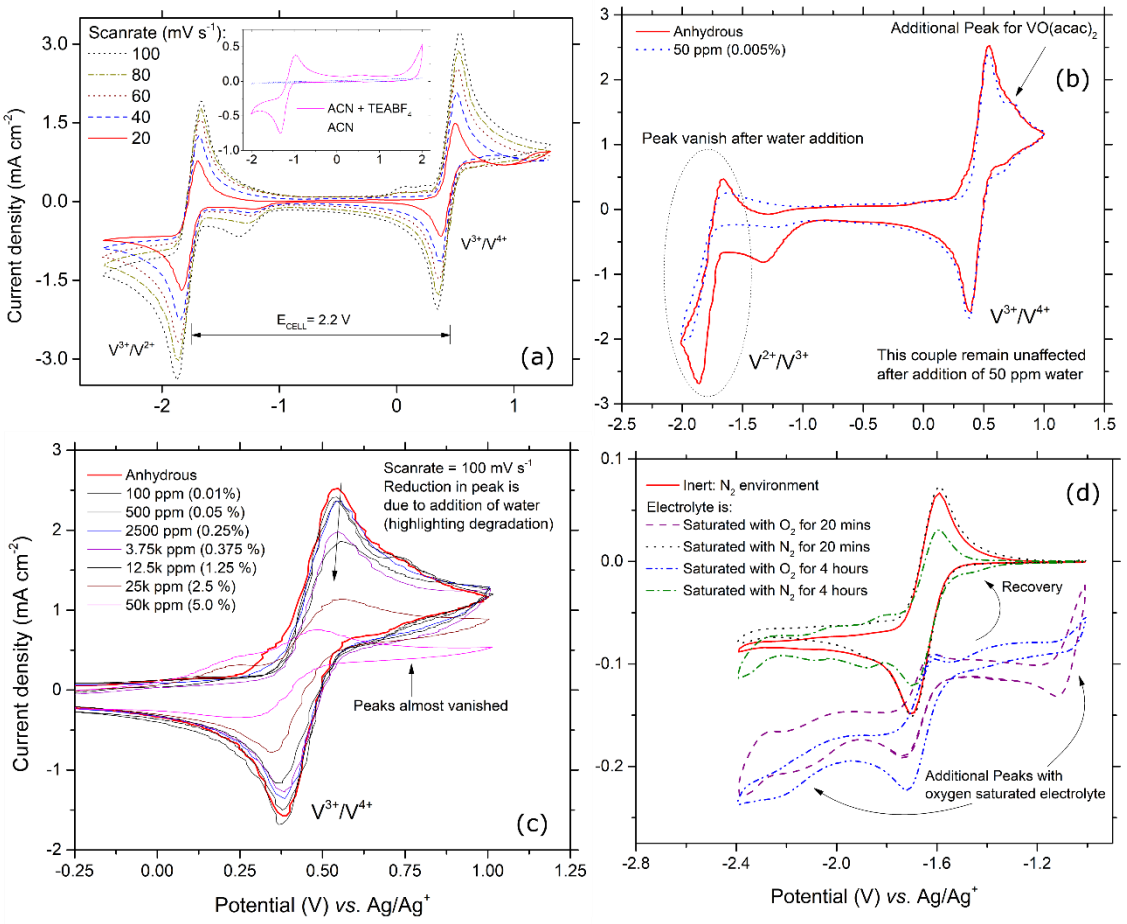


Figure 5.1 Voltammogram using 3-electrode cell configuration (a) for the non-aqueous electrolyte having redox species $V(acac)_3$ without any contamination (b) highlighting the effect of gradually adding moisture (water) on the redox couples a) V^{3+}/V^{2+} and V^{4+}/V^{3+} depicting the parasitic product $VO(acac)_2$ (c) V^{4+}/V^{3+} at different moisture concentrations (100 ppm – 50k ppm) (d) Degradation test was performed from inert nitrogen (N_2) environment to oxygen (O_2)

saturation for 20 minutes and then repeated with saturation for 4 hours, first with O_2 and then recovered by N_2.

From the spectra plotted in Figure 5.2 (a), it can be observed that peak currents for $V^{3+/2+}$ are higher for POH electrodes – anodic peak reaches currents of *ca.* 10.13 mA, followed by oxygen treated carbon felts PO – the anodic peak of 9.53 mA; P and PH electrodes display the worse anodic peak performance. At first glance, these results show that the treatment applied to the POH electrode allows increasing the number of active sites needed for the redox reaction. Interestingly, the mild oxidative treatment (400 °C for 10 h under airflow, PO) allows the growing of more surface oxygen functional groups, namely functional groups C=O and C-OH [95], which demonstrate greater catalytic activity compared to the pristine sample. Figure 5.2 (b) shows the voltammograms recorded at 10 $mV \cdot s^{-1}$, concerning the impact of increasing the thermal treatment temperature (from 400 °C to 700 °C) during the reduction treatment under H_2 flow. The increase of the thermal treatment temperature modified the surface chemistry to produce more active electrodes (POH2 > POH > PH2 > PH).

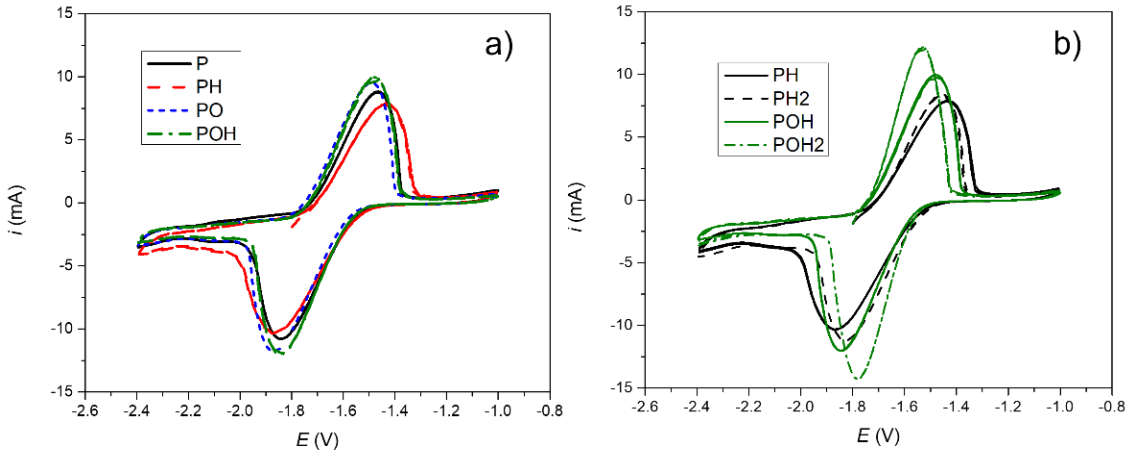


Figure 5.2 Cyclic voltammograms for screening the effect a) of the heat treatment environment in Pristine (P), Pristine + Hydrogen treated @ 400 °C (PH), Pristine + Oxygentreated @ 400 °C (PO), Pristine + Oxygen + Hydrogen treated @ 400 °C (POH) carbon felts at 10 $mV \cdot s^{-1}$; b) the effect of increasing the temperature from 400 °C in PH and POH to 700 °C in PH2 and POH2 at 10 $mV \cdot s^{-1}$.

These results pair with those obtained upon the estimation of the electrochemical active surface area (ECSA), using the Randles-Sevcik equation; this equation assumes that mass transport phenomena occur solely by diffusion mechanisms [162].

Anodic/cathodic peak currents are related to the square root of the scan rate, at 25 °C, as described in the following equation (5.3).

$$Ip = 2.69 \times 10^5 \cdot A \cdot D^{\frac{1}{2}} \cdot n(\alpha n)^{\frac{1}{2}} \cdot \gamma^{\frac{1}{2}} \cdot C_0 \quad (5.3)$$

where I_p is the anodic peak current of oxidation peaks, n is the number of exchanged electrons (1 in this case), α represent the transfer coefficient *i.e.* 0.5, A represents the ECSA, C_0 is the initial concentration of the electroactive probe species, D is the diffusion coefficient of the molecule and γ is the scan rate. From our previous work from CV analysis using the cathodic peak currents measured at varying scan rates, a diffusion coefficient of 7.88×10^{-6} cm^2 s^{-1} for the redox couple of V^{3+}/V^{2+} could be obtained [40]. As shown in Figure S 11.6, nearly for all electrode samples, except for PO, the corresponding current peaks are proportional to the square root of the scan rate. The latter result suggests that besides diffusion processes there might be an additional adsorption step governing the redox reaction behavior for PO electrode [163]. The slope of the Randles Sevcik plots - Figure S 11.8 - was used to get ECSA values for each sample electrode. Figure 5.3 highlights these values and by comparing with pristine CF, it can be concluded that there is an improvement of *ca.* 24% after a pre-treatment consisting of oxidation followed by a reduction step at 400 °C (POH). If the temperature for the reduction is increased up to 700 °C, then the improvement is *ca.* 39% (POH2). The higher slope - Figure S 11.8 - is also the indication of faster kinetics / mass transfer at the POH2 electrode.

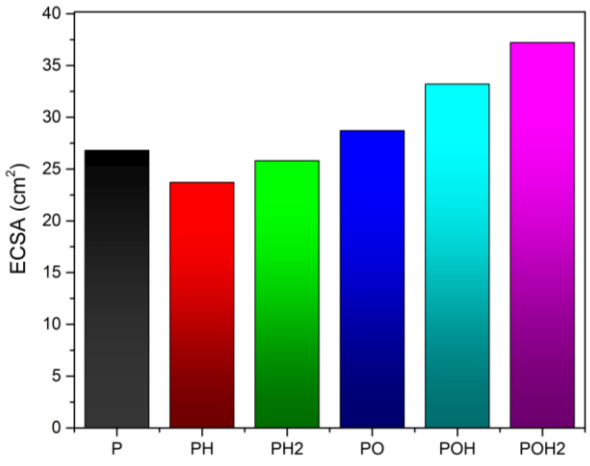


Figure 5.3 Comparison of electrochemical surface areas obtained by CV analysis from Randles-Sevick study for P, PH, PH2, PO, POH, and POH2 carbon felts.

5.3.3 Impact of surface modifications on the redox reaction reversibility

To assess the impact of the thermal treatments on the reversibility of the modified carbon felts towards the redox couple, the ratio between the anodic and cathodic peak current densities was examined (I_{pa}/I_{pc}). The redox reaction reversibility is considered to be improved when the ratio I_{pa}/I_{pc} approaches the value of 1 [164]. Amongst all the studied CFs, the closest unit value pertains to POH2 followed by POH, which demonstrates a significant improvement compared to the pristine carbon felt or even comparable to the CF treated under oxygen flow (PO), as shown in Table 5.2. Additionally, peak to peak potential separation ($\Delta E = E_{pc} - E_{pa}$) analysis also provide accurate information about the reversibility towards a specific reaction and therefore the less the separation – ΔE - the more reversible the reaction [164,165]. Thus, reduced electrodes such as POH2 (245 mV) and PH2 (366 mV) followed by POH (370 mV) display the smallest peak-to-peak separation. Again, increasing the thermal treatment temperature (POH2 and PH2 *vs.* POH and PH) appears to also improve the electrochemical reversibility significantly towards the redox reaction couple.

Table 5.2 Summary of electrochemical parameters determined by CV for P, PH, PH2, PO, POH and POH2 CFs for V^{2+}/V^{3+} redox couple in 0.1 M $TEABF_4$ + 0.02 M $V(acac)_3$ + Acetonitrile electrolyte at the scan rate of 10 mV s^{-1}.

Electrode type	I_{pa} (mA)	I_{pc} (mA)	E_{pa} (V)	E_{pc} (V)	I_{pa}/I_{pc}	ΔE (mV)
P	8.5	10.26	-1.46	-1.85	0.83	385
PH	7.92	10.35	-1.44	-1.86	0.77	422
PH2	8.43	10.57	-1.46	-1.83	0.80	366
PO	9.53	11.77	-1.49	-1.88	0.81	386
POH	10.13	12.09	-1.48	-1.85	0.84	370
POH2	12.10	14.19	-1.53	-1.78	0.85	245

5.3.4 Electrode stability on the presence of oxygen-rich/free surface

An accelerated stress test (AST) - Figure S 11.9 - was performed under N_2 purged electrolyte in a three-electrode cell. This test consisted of cycling the potential from - 2.1 V to 1.4 V at 100 mV·s^{-1} for 700 cycles for both PO and POH2, which are high-performing electrodes in terms of ECSA and reversibility towards the redox couple, Figure S 11.9. The main goal is to assess whether the presence of pseudocapacitive oxygen groups on the surface of the carbon hinders the electrochemical reversibility of

the reaction of interest as the environment is completely oxygen-free and therefore solely the oxygen functional groups on the CF surface will be responsible for causing any performance loss. Moreover, the potential was cycled until such positive potentials (up to 1.4 V) to mimic the potential at which the irreversible species forms, typically, 0.75 *vs.* Ag/Ag^+ [30,161] – *cf.* equations (5.1) and (5.2) – and thus allow to identify the electrode more prone for developing $VO(acac)_2$ parasitic species.

From Figure 5.4, it can be observed that there is a drop of nearly 46 % in the I_{pa}/I_{pc} ratio for the PO electrode as compared to solely *ca*. 20 % for the POH2 electrode – after 700 cycles which corresponds to *ca*. 20 h. Besides, by analyzing the peak to peak separation data (ΔE) from Table 5.3, it is observed that upon the accelerated stress test, the ΔE appears to diminish and thus improve (25 % for PO and 34 % for POH2), most likely due to the creation of additional surface defects or higher porosity from the repetitive cycling [166].

The presented results highlight that the surplus of oxygen-containing groups at the carbon felts surfaces hinders the performance of non-aqueous RFB, despite these functional oxygen groups being generally considered to improve the performance of the aqueous RFB [30]. In the present non-aqueous RFB, the presence of such groups triggers the formation of parasitic $VO(acac)_2$ and strongly hinders the battery capacity.

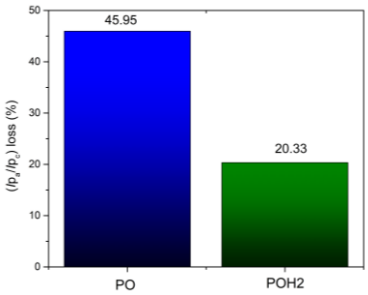


Figure 5.4 Loss of reversibility (I_{pa}/ I_{pc}) ratio after AST/degradation test for PO and POH2.

Table 5.3 Summary of electrochemical parameters determined by CV for PO and POH2 CFs for V^{3+}/V^{2+} redox couple in 0.1 M $TEABF_4$ + 0.02 M $V(acac)_3$ + Acetonitrile electrolyte at the scan rate of 10 mV·s^{-1} at the beginning of life (BoL) and upon the AST/stability test.

	I_{pa} (mA)	I_{pc} (mA)	E_{pa} (V)	E_{pc} (V)	I_{pa}/I_{pc}	ΔE (mV)
PO BoL	9.53	11.77	-1.49	-1.88	0.81	386
PO AST	4.551	10.46	-1.53	-1.82	0.44	290
POH2 BoL	12.10	14.19	-1.53	-1.78	0.85	245
POH2 AST	6.169	9.08	-1.57	-1.73	0.68	162

5.3.5 Morphology characterization applied to prepared electrodes

The characterizations were performed to assess the effect of hydrogen/oxygen treatment on the surface chemistry of the carbon felts. FT-IR spectra of the various treated carbon felts are shown in Figure 5.5. All carbon felt samples show four similar bands; a strong band attributed to the stretching vibration of (C-O) groups in the region between ~1200-1100 cm^{-1} related to alcohol/phenol groups. A broader band appearing in the range of 1470-1380 cm^{-1} is due to a series of overlapping absorption bands related to the deformation vibration of surface hydroxyl groups (C-OH) and in-plane vibrations of C-H in several C=C-H structures; these are considered as typical for carbon materials. In the region of ~1620 to 1600 cm^{-1}, a band is originated due to the conjugated C=C stretching vibrations and carbonyl (C=O) groups [167].

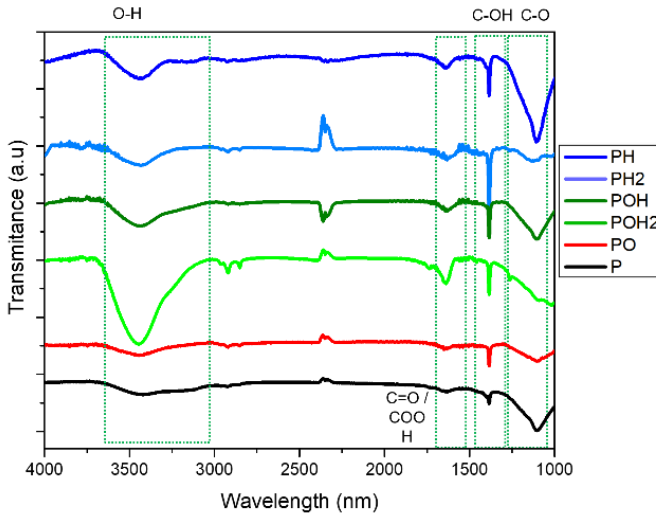


Figure 5.5 FTIR performed on samples of carbon felt. Legend: Pristine (P), Pristine + Oxygen treatment (PO), Pristine + Hydrogen treatment at 400 °C (PH), Pristine + Hydrogen treatment at 700 °C (PH2), PO + Hydrogen treatment at 400 °C (POH), and PO + Hydrogen treatment at 700 °C (POH2).

In the spectra of the carbon materials, the band of stretching vibrations (3600-3100 cm^{-1}) was due to surface hydroxylic groups (O-H) and vibration modes from the moisture adsorbed on the sample [168]. The strong broader peaks for samples pristine (P) and air/oxidation treatment (PO) are due to the superposition of the vibration of hydroxyl groups that arise when the carbon is highly oxidized [169]. The latter indicates that the heat treatment under an atmosphere of oxygen at 400 °C allowed to increase the amount of oxygen functional groups in the carbon felts which is evident from the broader bands

in this region (3600-3100 cm^{-1}). Whereas the samples that were reduced in hydrogen (PH, PH2, POH, and POH2) show narrower peaks, and thus are likely to have fewer amount of surface OH groups.

Figure 5.6 shows the SEM images of all electrodes. In Figure 5.6 (a) to (c), there are noticeable differences between the pristine carbon felt (PAN-based GFD4.6EA) and samples PH and PH2. The pristine carbon felt shows a pronounced grooved and coarse surface. The treatment under hydrogen atmosphere at 400 °C and 700°C originated a clean and smooth homogeneous surface.

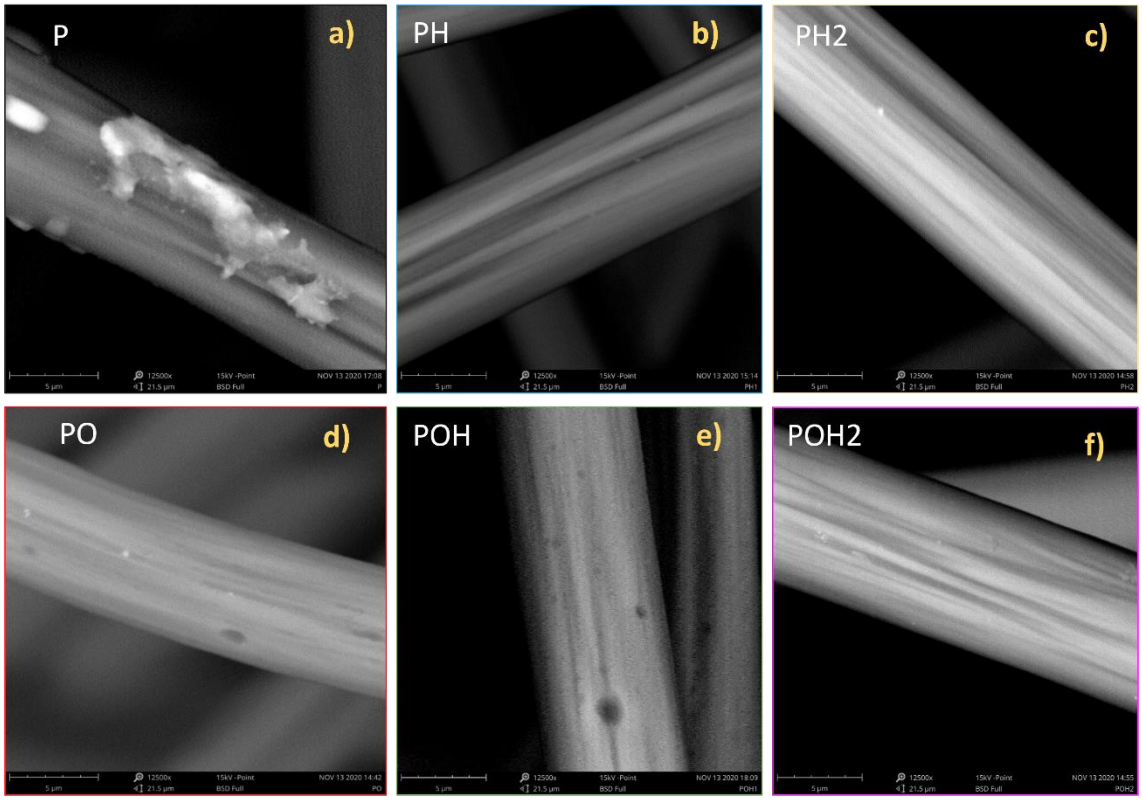


Figure 5.6 SEM images of carbon felts at 12500 X; a) pristine (P), b) Pristine + Hydrogen treatment at 400 °C (PH), c)), Pristine + Hydrogen treatment at 700 °C (PH2), d) Pristine + Oxygen treatment (PO) d), PO + Hydrogen treatment at 400 °C (POH), and f) PO + Hydrogen treatment at 700 °C (POH2).

Electrodes that were previously subjected to a soaking step in sulfuric acid - PO, POH, and POH2 - display roughened fibers with larger surface area, as can be confirmed by the greater ECSAs obtained – *cf.* Figure 5.3. Most likely, the chemical treatment is harsh for the surface, generating too many defects. The acid treatment followed by thermal treatments, firstly under airflow and secondly under hydrogen flow, generate additional porosity onto the fibers, which is apparent from the significant increase in the amount of dark large dots in Figure 5.6 (e). Nonetheless, the corresponding sample treated

at 700 °C *i.e.* for POH2, seems to have a smoother surface. Oxidative thermal treatments are generally performed to increase the number of oxygen functional groups. By applying a thermal treatment in an oxygen environment followed hydrogen environment, it is expected that these functional groups are removed and many surface defects are created – *i.e.* for POH, POH2. These expectations were confirmed from the ECSA (Figure 5.3) and FTIR analysis (Figure 5.5).

5.3.6 Performance of the redox flow cell

Charge-discharge cycling (CDC) is a key electrochemical test to assess the performance of the NAqRFB-cell assembled with the electrodes here in the study. The discharge current is often expressed as C-rate, which is a measure of the rate at which a battery is discharged relative to its nominal capacity. This parameter allows normalizing discharging rate with the battery capacity. A 1C rate means that the particular value of current will discharge the entire capacity of the battery in 1 hour. Manufacturers commonly rate alkaline and lead-acid batteries at a very low C-rate (usually 0.05C or 20-hour discharge). A recent article by Siu in Tung [154] a NAqRFB with the same electrochemistry as of the present work was characterized at a C-rate of 0.2C; in the present work a C-rate of 1.35C was considered (where the nominal capacity of the cell is *ca.* 33.5 mAh), which corresponds to a discharge rate of 6.2 $mA \cdot cm^{-2}$. Employing such harsh operating conditions will highlight the effect of ohmic losses and mass transport overpotentials caused by the under-study electrodes.

Composite membrane, bipolar plates, current collectors, and flow conditions were kept the same throughout this study. The performance of the cell equipped with each pair of electrodes in the study is shown in Figure 5.7. The performance of pristine electrodes – P – was taken as a reference for comparison purposes. Overall, the electrode samples treated under a hydrogen atmosphere display a better performance compared to the results of pristine electrodes and PO electrodes. Interestingly, the coulombic efficiency – η_{CE} – of PO surpasses that of the pristine – P – sample after 30 charge/discharging cycles (CDC), whereas the capacity of the cell reaches solely a rather negligible 2.0 mAh – Figure 5.7 (a). This steep drop upon solely 10 CDC – Figure 5.7 (d) – was assigned to the formation of the parasitic species ($VO(acac)_2$) due to the reaction triggered between redox species and the oxygen functional groups at the microstructure of carbon felts. As the cell is operated at constant current, it is expected that the C-rate increases alongside the capacity decay for PO, as it reached a C-rate of 22C in the 30^{th} cycle and 180C by the end

of CDC – 45th cycle. The seemingly rapid charge/discharge of the cell – Figure 5.7 (a) - covers the adverse effects of the mentioned parasitic reaction as such a behavior might be misinterpreted as good performance.

Electrode PO also displays a larger ECSA compared with electrodes PH and PH2 - Figure 5.3 – and initially reaches a higher capacity – *ca.* 23 mAh – which steeply drops however by the 45th cycle to *ca.* 0.25 mAh. The behavior of the cell equipped with PO electrodes is similar to the results obtained for the 3-electrode cell; the ECSA was initially higher but when exposed to the accelerated aging experiment, the reversibility of the reaction dropped significantly to *ca*. 46 % (*cf.* Figure 5.4). This supports the hypothesis that the parasitic vanadyl precipitates are formed due to the surface chemistry of the carbon felt, which is rich in oxygen functional groups. The formation of greenish crystal precipitates was also observed at the surface of the PO *post-mortem* electrodes, as shown in Figure S 11.12. Upon further investigations, it was found that the solubility of $VO(acac)_2$ is 0.06 M in acetonitrile [143], which is significantly lower as compared to $V(acac)_3$, and hence, $VO(acac)_2$ easily precipitates [170]. Moreover, this unexpected overlayer of $VO(acac)_2$ causes 6-fold higher (from *ca.* 2.5 Ω to 15 Ω) charge transfer resistance at the PO electrode, which is noticeable in the EIS spectra – Figure 5.8 (b) – recorded at 1.5 V after the CDC. In this regard, it is possible to confirm that the presence of an oxygen-rich electrode sparks the generation of $VO(acac)_2$, parasitic species, which blocks the active sites of the electrode making the charge transfer resistance increase substantially. Ohmic resistance also increases for PO with CDC due to the presence of such parasitic precipitates at the surface of the PO electrode and deposition on the membrane surface, which condemns both ionic conductivity and increases interfacial contact resistance of the cell – *cf.* Figure 5.8 (a) inset *vs.* Figure 5.8 (b) inset. No precipitates were observed for the remaining *postmortem* electrodes. The higher overall PO impedance entails the lowest potential (η_{VE}) and energy efficiencies (η_{EE}) achieved.

The cell assembled with PH electrodes displays a coulombic efficiency of η_{CE} = 98%, a voltage efficiency of η_{VE} = 58%, and an energy efficiency of η_{EE} = 57%, which is similar to the cell equipped with POH electrodes. The average cell capacity over the 45 CDC while equipped with PH electrodes was *ca.* 6.14 mAh, which is poorer than the cell performance equipped with POH2 electrodes, which is *ca.* 10.42 mAh, yet still providing a fairly stable operation. This indicates that the oxygen-free electrodes are beneficial to increase the stability of the cell. A lower value of the capacity was expected for the cell

equipped with PH electrodes because they displayed the lowest ECSA. Increasing the temperature of the H_2 reduction treatment boosted the ECSA and therefore, both PH2 and POH2 electrodes exhibit a higher capacity compared with their counterparts, PH and POH, as seen in Figure 5.7 (d). A thermal treatment with only hydrogen reduces the manufacturing steps to produce oxygen-less electrodes, however, POH2 electrode is the one that displayed the best performance. The acid treatment followed by oxygen treatment helps to introduce the surface defects and abundant oxygen functional groups. These latter groups are then reduced under a hydrogen atmosphere at 700 ºC. Although the energy efficiency of the cell using POH2 electrodes (η_{EE} = 52%) falls behind the one using POH electrodes (η_{EE} = 56%), it achieved much higher capacity during the initial cycles (*ca.* 30 mAh) stabilizing afterward, at almost twice the value compared to POH – *cf.* Figure 5.7 (d). Furthermore, the ohmic resistance – R_Ω – increase between cycle 0^{th} and cycle 45^{th} - Table S 11.2 - is smaller for the cell using POH2 (*ca.* 43%) and POH (*ca.* 91%) electrodes compared with for pristine (*ca*. 162%) and PO (*ca.* 123%) electrodes. A lower ohmic resistance increase implies that the graphitization level of the POH2 electrode was higher which contributes to an enhanced electrical contact between the electrode surface and the bipolar plates, *cf*. Figure 5.6. Moreover, the increment in R_Ω, which is common to all electrodes, was assigned to the degradation of the Nafion composite membrane – C25-HP-C25. A previous work [40] denoted the importance of using separators to minimize crossover effects of vanadium V^{2+} species and to reduce the degradation effects.

The highest limiting current density - Figure 5.9 - was achieved with POH2 (*ca.* 104 mA cm^{-2}) followed by PH2 (ca. 93 mA cm^{-2}). These values correspond to a C-rate = 22C and 20C respectively, where C is 33.5 mAh – nominal capacity. This highlights that cells equipped with electrode POH2 are capable to be operated at the largest to date reported limiting current density for this system – 104 mA cm^{-2}.

The state-of-the-art and highest reported current density are *ca.* 100 mA cm^{-2} for a similar electrochemical system by J. Saraidaridis, 2018, [171]. These authors assigned the observed current density to the strict control of environmental moisture in the glovebox (max. 250 ppm of humidity) and further to the supply of the chemicals, *i.e.* the credit was given to the good sealing of the bottles that contained the chemicals, from Strem in the UK, as compared to Sigma Aldrich. Good sealing of the bottles helps to prevent the formation of $VO(acac)_2$ (Vanadyl acetylacetonate), which is a parasitic species. But these conditions are similar to the second-highest performing V-NAqRFB, which was operated by I.L. Escalante-García, [161], achieving merely 10 mA·cm^{-2}; yet,

these authors observed an enormous capacity loss of 90% after solely 10 CDC, despite having run the experiments inside a glove-box (max. 250 ppm of humidity) and using electrolytes of high purity. The only major difference between both studies is the pre-treatment applied to electrodes. *J. Saraidaridis et al*, *applied* pre-treated carbon-felt electrodes at 250 ^{o}C for 48 h under vacuum, whilst, *I.L. Escalante-García*, [161] used as-received electrodes without considering any further treatment. These results support the conclusions of the present study, *i.e.* the electrolyte parasitic species are formed from the oxygen functional groups presented in the electrodes. It should be emphasized that the glove-box used in our laboratory contained *ca.* 6000 ppm of humidity and 100 ppm of oxygen, which highlights that the effect of electrodes is far more relevant than the environmental conditions. The conclusions of this work enable the easy preparation of electrodes using standard industrial processes and motivate battery specialists to forward one step closer to the implementation of vanadium-based non-aqueous redox flow battery as a promising technology for energy storage.

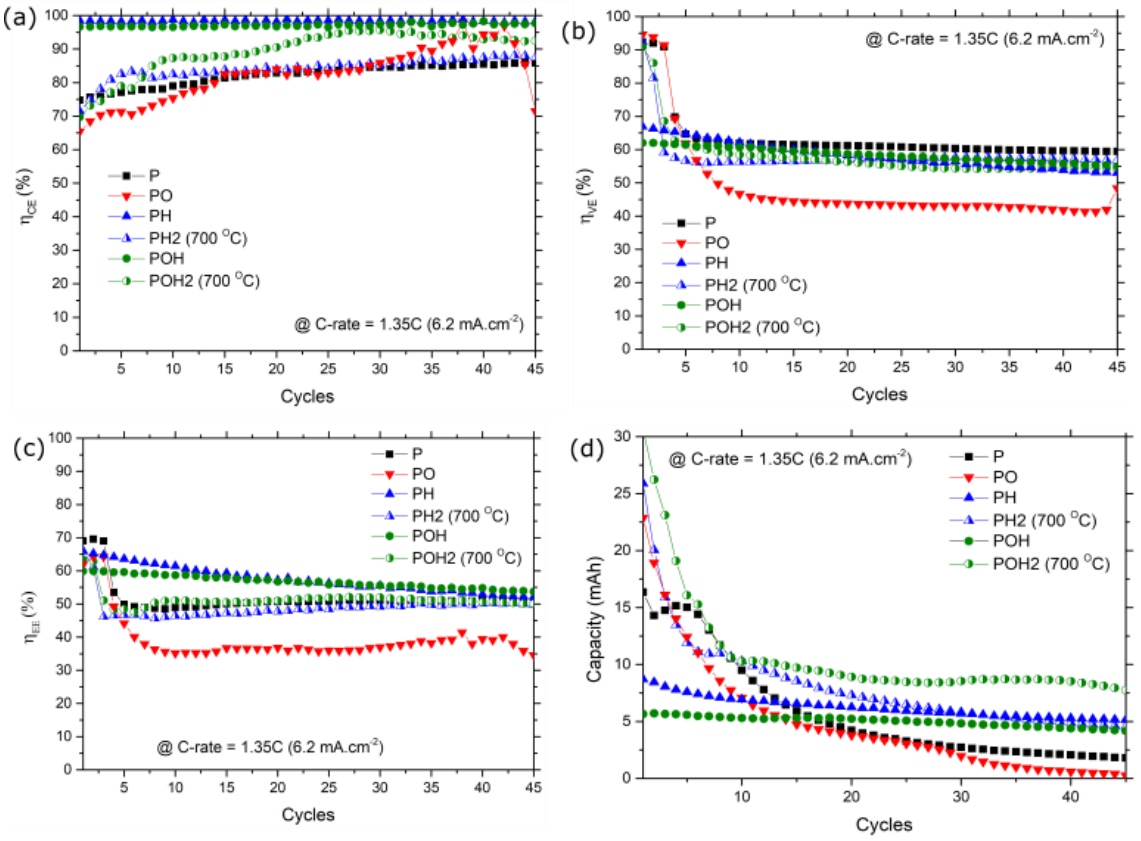


Figure 5.7 Performance of V-NAqRFB assembled with prepared electrodes operating at the flow-rate of 30 ml min^{-1} at the C-rate of 1.35C i.e. 6.2 mA cm^{-2} (a) Coulombic Efficiency (η_{CE}) (b) Voltage efficiency (η_{VE}) (c) Energy Efficiency (η_{EE}) (d) Capacity for each cycle.

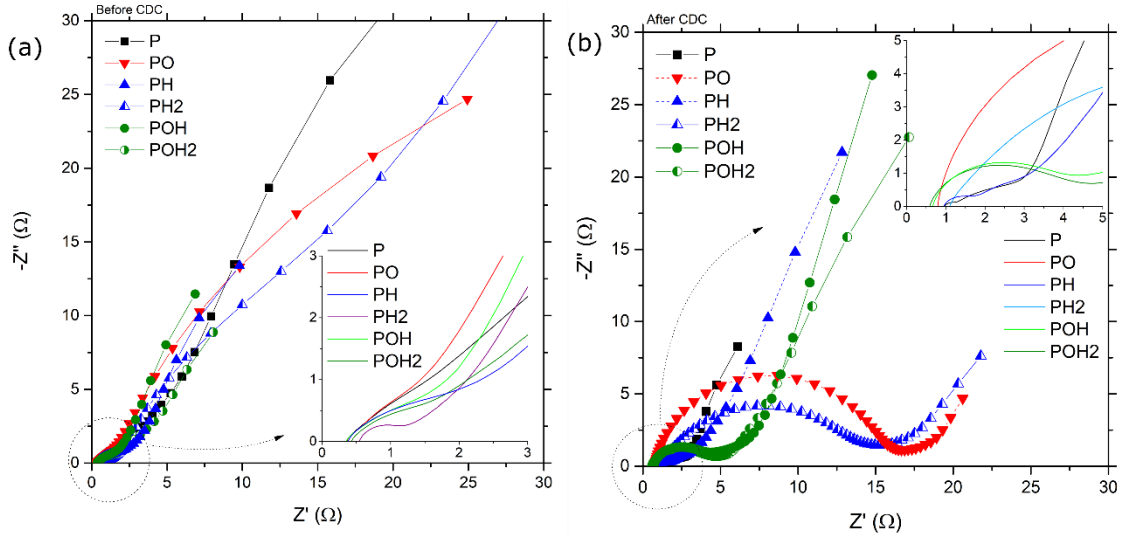


Figure 5.8 Impedance curves obtained through electrochemical impedance spectroscopy performed at E_{OCP} = 1.5 V from 250 kHz to 100 mHz with an amplitude of 10 mV. (a) Performed before charge-discharge cycling (b) Performed after charge-discharge cycling.

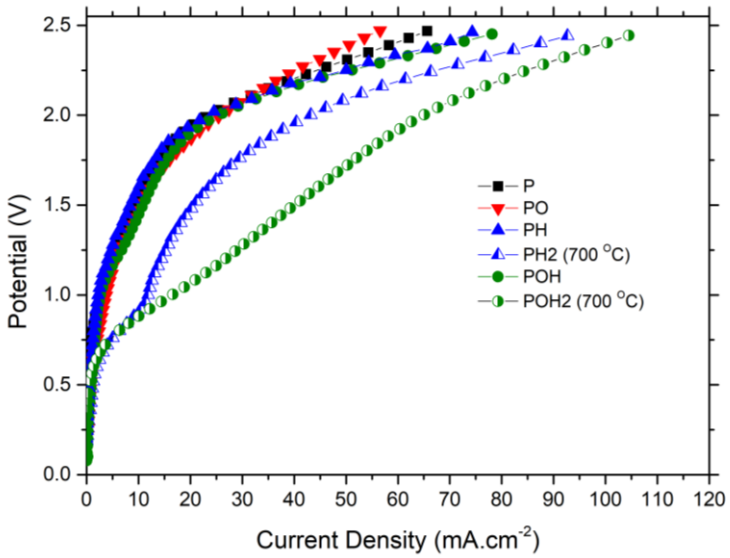


Figure 5.9 Polarization curves obtained while linear sweeping in the range of 0.1 V to 2.5 V at the scan rate of 20 mV s^{-1} and electrolyte flowing at 30 ml min^{-1}

5.4 Conclusion

Vanadium acetylacetonate $V(acac)_3$ is being used as model redox species for the study of non-aqueous redox flow battery. It dissolves easily in most of the organic solvents, besides its commercial availability at a fair price. Nonetheless, merits are usually accompanied by some demerits. The presence of moisture/oxygen in the environment triggers the irreversible formation of parasitic species $VO(acac)_2$, which causes rapid battery capacity loss. Accordingly, the electrolyte must be kept in an inert atmosphere

such as dry nitrogen. Nonetheless, it was observed that even keeping a strictly controlled inert gas over the electrolytes, the stability of the batteries was still rather low. It was observed a prominent loss in the anodic/cathodic peak current densities to *ca.* 67 % and rise of additional redox peaks (at -2.1 V, -1.9 V, and 0.75 V *vs.* Ag/Ag^{+}) upon bubbling the electrolytes with oxygen and by adding DI water in a 3 electrode-configuration cell. This study proposes for the first time that carbon felt electrodes, were a major source of oxygen since they often display an oxygen-rich surface of oxygen functional groups.

The carbon felt electrodes were then submitted to a set of different treatments for removing these oxygen functional groups and for increasing the surface area (morphology). The best performance was obtained when the electrodes were treated at 400 °C under oxygen, followed by a treatment at 700 °C under hydrogen atmosphere – POH2 sample, which displayed an increase of 34 % of the ECSA compared to the pristine sample. The cell equipped with POH2 electrodes outperformed all those reported in the literature for similar systems, achieving efficiencies of *ca.* η_{CE} = 90%, η_{VE} = 57%, and η_{EE} = 52%. More importantly, the capacity of the cell remained stable at *ca.* 10.42 mAh and also achieved the highest reported limiting current density of *ca.* 104 mA cm^{-2}.

The results of this work highlight the critical relevance of the chemisorbed oxygen at the surface of the carbon electrodes for the performance of the vanadium NAqRFB; oxygen-free electrodes or electrodes containing inert oxygen functional groups should be used. Since the chemisorbed oxygen functional groups are quite important for allowing the redox species to anchor and exchange electrons at the electrode surface, research should progress onto assessing the effect of inert carbon surface dopants, where nitrogen appears as a very promising candidate.

Blank Page

Chapter 6

Carbon felt electrodes augmented with nanoparticles

6. Carbon felt electrodes augmented with nanoparticles

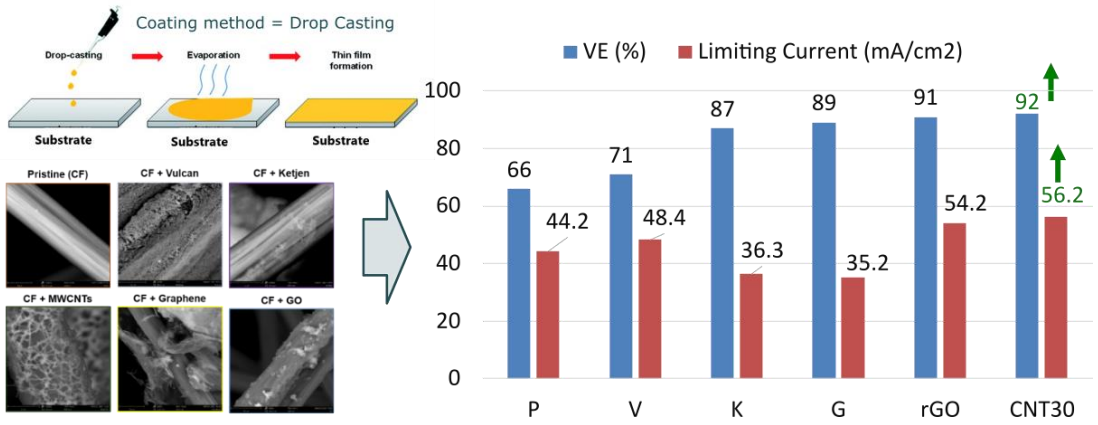
Adapted from the following articles:

K. Mushtaq, S. Delgado, A. Mendes, "Nanoparticles Coated Electrodes for Vanadium-Based Non-Aqueous Redox Flow Battery", 240th ECS Meeting (October 10 – 14, 2021), USA.
Link: https://iopscience.iop.org/article/10.1149/MA2021-0251924mtgabs/meta

K. Mushtaq, S. Delgado, A. Mendes, "Carbon felt electrodes augmented with nanoparticles for non-aqueous redox flow battery", Journal of Energy Storage, Elsevier (Under review).

The non-aqueous electrolytes are getting attention as a way to increase the energy density of a redox flow battery. Pristine carbon felt electrodes, available commercially, often display high overpotentials when running the electrochemical reactions in non-aqueous medium. Hence, it is crucial to develop stable high-performance electrodes, displaying low activation overpotentials, low ohmic losses and porosity for a uniform distribution of the flowthrough electrolyte. This study acknowledges the influence of using attached carbon-based nanoparticles to the fibers of the supporting carbon felt electrodes. The use of reduced graphene oxide, graphene, multi-walled carbon nanotubes (CNT), carbon black Vulcan XC72 and Ketjen carbon nanoparticles bounded to the support carbon felt electrode using a Nafion ionomer was assessed. Post-mortem analysis revealed that the nanoparticles remained attached to the fibers even after intense charge-discharge cycling. The carbon felt containing CNT added to the fibers displayed the best performance on running the charge / discharge electrochemical reactions while achieving a 23 % higher energy efficiency compared to commonly used electrodes.

Graphical Abstract



6.1 Introduction

The exponential growth in the human population is driving the continuous increase in energy demand. Aside from the population growth, the energy sector has been encouraged to maximize the use of renewable energy sources for electricity production due to emerging environmental concerns. This stimulates the deployment of economical energy storage technologies utterly necessary for managing the intermittency of renewable energy sources and to develop reliable electrical power systems solely based on these sources. Recent studies [40,172] projected the lowest Levelized cost of storage (LCOS) by 2050 for nine electricity storage technologies. The top two ranked technologies are lithium-ion batteries and redox flow batteries (RFB). The electrochemical operation of the RFB is similar to a fuel cell but it has the advantage of not using expensive noble metals and enabling low-cost manufacturing. Especially, it is a captivating technology for large-scale energy storage applications because energy capacity and power output can be independently upscaled by simply increasing the volume of electrolyte tanks or by adding more stacks, respectively. This flexibility also reduces the capital cost of the battery for any future expansion.

Non-aqueous electrolytes are being investigated to increase the energy density by providing a wider electrochemical window [25] and for allowing higher solubility for active species. This also enables the development of new redox species, incompatible with aqueous electrolytes due to their limited solubility, chemical reactivity, or redox potentials that are outside the stability window of water (*i.e.* Cell potential > 1.6 V). This application can also make use of a wide range of supporting electrolytes and molecular solvents that can be tuned to specific redox chemistry. Summing up altogether, these advantages promise an increased energy density and cheaper energy storage [26].

Non-aqueous redox flow battery (NAqRFB) is still in the nascent phase and technology is only now progressing towards successful prototype versions of the cells. The redox species of Vanadium acetylacetonate – $V(acac)_3$ – are considered a reference to assess electrodes and membranes because of their commercial availability [23]. This reference compound demonstrates reversible redox reactions for V^{3+}/V^{2+} (*i.e.* negolyte *ca.* -1.75 V *vs.* Ag/Ag^{+}) and V^{4+}/V^{3+} (*i.e.* posolyte *ca.* 0.45 V *vs.* Ag/Ag^{+}). The flexibility of this redox species to charge from the same valency state (V^{3+}) on both half cells makes it quite appealing [40]. The half-cell reactions of the vanadium-based non-aqueous

electrochemistry are mentioned in equations (3.2) and (3.3) in discharging direction [161].

The electrodes play an essential role in the redox reaction mechanism by providing electrochemically active sites and any improvement in electrodes leads to lower activation overpotentials [87]. The battery's performance significantly depends on the number of available active sites on the electrodes where the electrochemical reactions take place [88]. Typically, pristine electrodes used for aqueous RFB are highly associated with poor activity towards vanadium redox reactions, and therefore several attempts were reported to increase the carbon material electroactivity, by applying acid leaching [93], nitrogenation treatments [94], or even thermal pre-treatments [95]. Moreover, bulk metal-based electrocatalyst, including Pd, Ir, Pt, Bi nanoparticles, were tested supported in graphite/carbon felts for aqueous vanadium redox batteries and revealed enhanced charge-transfer rates at the interface of the electrode and electrolyte owing to the better electrical conductivity of metallic nanoparticles [105].

Conventional electrode materials, such as carbon felt [73], graphite felt [98], carbon paper [99], and carbon cloth [100] rely on beneficial porous structures with fair electrical conductivity, great chemical stability, and good corrosion resistance [101]. The widely used carbon felt materials offer reliable electrical conductivities for NAqRFB but fail to offer lower activation overpotentials; this power catalytic activity is related to the presence at the surface of the carbon fibers of many electrochemically inert carbon bonds besides the low surface area, and poor wettability [92]. Hence, it is essential to develop high-performance, robust electrodes, specially designed to improve the electrochemical activity of redox species in non-aqueous electrolytes. The active surface augmentation using attached nanoparticles is been gaining considerable attention for improving the reaction kinetics and electrochemical surface area (ECSA) while boosting the electrical conductivity.

There are fewer studies related to the active surface augmentation of the carbon felt electrodes using attached nanoparticles (NPs), which correlate the influence of the microstructure of different NPs, several Ionomer/Carbon ratios, application of noble metals as a catalyst, and their effect on the performance of the NAqRFB. Reduced graphene oxide (rGO), graphene (G), multi-walled carbon nanotubes (CNT), carbon black Vulcan XC72 (V), and carbon black as Ketjen (K), were used to assess their performance in a NAqRFB. The electrodes coated with the selected carbon particles were prepared using a facile and fast drop-casting coating technique. Nafion ionomer served

as a binder, and it was also optimized to get the best performance. The performance of the battery was also compared with the use of carbon felt electrodes loaded with platinum-based reduced graphene oxide (Pt-rGO) particles. The findings of this work contribute for paving the way to the development of electrodes for a future battery stack having reduced size and resulting in lower overall capital expenditure. This encourages the pilot-scale commercialization of the non-aqueous redox flow battery.

6.2 Experimental Methods

6.2.1 Materials

Tetraethylammonium tetrafluoroborate 99 %, $TEABF_4$ from Alfa Aesar, Vanadium(III) acetylacetonate 97%, $V(acac)_3$ from Strem chemicals, and Acetonitrile anhydrous 99.8 %, (ACN) from Sigma Aldrich, were used as received. All experiments were conducted using non-aqueous electrolytes composed of acetonitrile as solvent and $TEABF_4$ as supporting electrolyte. Electrolyte consisting of ACN + $TEABF_4$ 0.1 M + $V(acac)_3$ 0.02 M, referred in this study to as A1, was used to perform voltammetry studies in a three-electrode configuration cell. A membrane consisting of a sandwich of commercial membranes Celgard 4560 | Nafion HP | Celgard 4560 was used in all experiments [40]. The flow-cell electrolyte consisted of ACN + $TEABF_4$ 0.5 M + $V(acac)_3$ 0.1 M, referred in this study to as A2. The electrodes were purchased from Sigracell, SGL Carbon GFD, and have a thickness of 4.6 mm.

6.2.2 Preparation of Electrodes

The pristine (P) carbon-felt electrodes received from Sigracet were thoroughly washed with ethanol and dried in an oven for 2 hours at 120 ^{o}C. Several samples were prepared by depositing the different carbon nanoparticles onto the washed carbon felts, *i.e.* Vulcan XC72 from Cabot Corp. (V); multi-walled carbon nanotubes from Nanoinnova (CNT); Ketjenblack EC 600 from Sigma Aldrich (K); reduced graphene oxide from Sigma Aldrich (rGO); and graphene nanoplatelets, 6-8 nm from Sigma Aldrich (G). Ink formulations were prepared by mixing 96 mg of carbon nanoparticles with 64 ml isopropyl alcohol, IPA, 70 % from Merck KGaA, and a Nafion ionomer suspension (5 wt. %, Quintech); the ionomer/carbon particles ratio was 30 wt.%. The ink was placed in an ultrasonic bath for 20 minutes to ensure uniform dispersion of the nanoparticles, followed by 20 minutes of mixing using an ultrasonication bath with a needle probe. Throughout the mixing steps, an ice bath was used to avoid any evaporation

of the solvent. The coating ink was drop cast - 1 ml each time - on the preheated surface of each carbon felt, maintained at 100 ^{o}C. The loading of carbon nanoparticles on the final weight of the carbon felt corresponded to *ca*. 11 ± 0.5 %.

Further drying was performed in a tube furnace at 120 ^{o}C for 4 hours while flowing hydrogen at 100 ml·min^{-1}. The ionomer concentration in the ink formulation containing nanoparticles of CNT was varied from an ionomer to carbon particle ratio of 5 wt. % to 30 wt.%. The ensuing preparation steps mentioned above were repeated to finalize these electrodes. Electrodes loaded with Pt-rGO nanoparticles were also prepared using this method.

6.2.3 Cyclic Voltammetry

Voltammograms were measured using a 3-electrode cell assembled; the prepared carbon felt samples were used as working electrodes (WE), a platinum wire served as a counter electrode (CE) and a Biologic RE-7 electrode, filled with 0.01 M $AgNO_3$ + 0.1 M TBAP + Acetonitrile, was employed as a reference electrode (RE). The electrodes were immersed in 50 ml of electrolyte A1. Several scan rates were applied namely, 2.5 mV·s^{-1}, 10 mV·s^{-1}, 20 mV·s^{-1}, 50 mV·s^{-1}, and 100 mV·s^{-1}, and used to retrieve kinetic parameters concerning the reaction. All the experiments were performed in a saturated nitrogen electrolyte. The Zahner Zennium workstation was used to record all the data and Thales software served to analyze the voltammograms.

6.2.4 Physicochemical characterization

The surface morphologies of the carbon felts were analyzed by SEM (PhenomPro XL). The SEM was coupled to an (EDX) energy-dispersive x-ray spectroscopy Peltier cooled Si (Li) detector to quantify the chemical elements in the *post-mortem* membranes. SEM images were obtained at different magnifications (340 x, 2650 x, and 6400 x) to analyze micro and nanoscale features. The functional groups of the membranes before and after CDC were characterized using a FT-IR - Bruker VERTEX70 - in the 400–4000 cm^{-1} range at room temperature using air as sweep gas at 8 ml·min^{-1}.

6.2.5 Redox flow-cell assembly and electrochemical assessment

A fuel cell from Pragma Industries was adapted into a flow cell by placing graphite bipolar plates of wide channels and by switching conventional nitrile rubber o-rings to PTFE materials display the required stability. The carbon felt electrodes were placed on each flow field in an equivalent geometric area of 7.29 cm^2. Teflon gaskets, with a

thickness of 3 mm, was used to guarantee the sealing of the cell. The electrodes were compressed to 34 % of their initial thickness. The flow cell experiments were performed inside a glove box with a saturated dry nitrogen atmosphere. The experimental setup is shown in Figure 1.9; each bottle has 25 ml of electrolyte A2 as posolyte and of negolyte. The impedance measurements were recorded using an amplitude of 10 mV at open circuit potential ($E_{OCP} \approx 1.5$ V) across the frequency range of 100 mHz to 250 kHz. Potentiostatic measurements were performed to acquire polarization data in the cutoff range up to 2.6 V at a scan rate of 20 mV·s^{-1}. Data obtained from charge/discharge cycling (CDC) enabled the calculation of Coulombic, Voltage, and Energy efficiencies (η_{CE}, η_{VE}, and η_{EE}, respectively) for each cycle by using the equations (2.4), (2.5), and (2.6).

6.3 Results and discussions

6.3.1 Characterization of electrolyte

The first requirement of any electrolyte of a redox flow battery is to display a fast reversible redox reaction at the surface of a carbon-based electrode. Electrolyte A2 was assessed using a three-electrode cell. The voltammograms - Figure S 11.13 (a), see *supplementary information* – were obtained by cycling the potential from -2.5 V to 1.5 V *vs.* Ag/Ag$^+$. The obtained voltammograms are direct evidence of the reversibility of the redox reactions of vanadium species dissolved in acetonitrile and $TEABF_4$ (*i.e.* supporting electrolyte). It offers a cell potential difference of E_{CELL} = 2.2 V; with increasing scan rates the value of peak-to-peak potential separation for each redox couple V^{2+}/V^{3+} and V^{3+}/V^{4+} remains constant. The Randles-Sevcik plots - Figure S 11.13 d) – show that the peak currents are a linear function of the square root of the scan rate, which corroborates with the condition of reversibility [163]. Therefore, the Randles-Sevcik model was employed to obtain the diffusion coefficients; the computed values are (7.65 ± 0.85) × 10^{-6} cm^2·s^{-1} for V^{3+}/V^{2+} and (4.5 ± 0.4) × 10^{-6} cm^2·s^{-1} for V^{4+}/V^{3+} at room temperature (25 °C), obtained using the following equation (6.1) [173]:

$$I_P = 2.69 \times 10^5 A \cdot D^{\frac{1}{2}} \cdot n(\alpha \cdot n)^{\frac{1}{2}} \cdot \gamma^{\frac{1}{2}} \cdot C_0 \qquad (6.1)$$

where I_P is the anodic peak current (oxidation), n is the number of exchanged electrons, *i.e.*, n = 1 for this study, α = 0.5 [40], which represents the charge transfer coefficient, A refers to the electrode area, C_0 is the initial concentration of the electroactive probe species, D is the diffusion coefficient of the molecule, and γ is the scan rate. The silica gel was introduced in the electrolyte flasks for capturing moisture, with a 4 wt. %

concentration. The cyclic voltammogram, as shown in Figure S 11.24, highlights the improvement in the current peak and shows no parasitic reactions.

6.3.2 Characterization of augmented electrodes

The pristine carbon felt was loaded with nanoparticles in a ratio of 11 % to the total weight of the carbon felt. Nafion ionomer was added as a binder to allow the adhesion of the nanoparticles to the carbon felt surface and extend the ion conductive pathway. The performance of each sample was compared with that of a non-modified pristine electrode in a 3-electrode cell. The goal was to assess the reversibility of the redox reactions on the electrodes and to study the effect of the carbon nanoparticles coating on the electrochemical reaction rate. Samples with 3 mm in diameter were placed in a gold tip (WE) and CVs were recorded at several scan rates in a 3-electrode cell configuration. The Randles Sevcik plots - Figure S 11.14 - show that Vanadium redox reaction is mainly governed by a diffusion mechanism in all prepared electrodes, as concluded from the linear relation between the anodic peak currents and the square root of the scan rate [174]. Coating the carbon felts with different types of carbon nanoparticles originated distinct electrochemical performances owing to their different features. The slopes of graphene and MWCNTs decorated carbon felts are greater than the pristine and the Ketjen electrode samples; it should be concluded that the ionic transport is faster for samples loaded with graphene and MWCNTs.

A redox reaction is considered reversible when the ratio of anodic to cathodic peak currents stay around I_{PA} / I_{PC} = 1 and peak potential separation, $\Delta E < 59$ mV, otherwise it is considered irreversible [175] . The obtained ΔE values – Table 6.1 and Figure 6.1 – are beyond the mentioned limit which indicate that the electrode-electron-transfer process is irreversible. Equations (6.2) and (6.3), firstly derived by Gokhshtein [176], were used to determine the reaction rate constant (K^0) for the case of totally irreversible reactions:

$$E_0 = \frac{\sum_{i=1}^{m}(E_{\mathrm{PA},i} - E_{\mathrm{PC},i})}{2 \cdot m} \qquad (6.2)$$

$$I_P = 0.227 \cdot n \cdot F \cdot A \cdot C^O \cdot K^0 \cdot e^{(-\alpha \cdot f \cdot (E_\mathrm{P} - E_\mathrm{O}))} \qquad (6.3)$$

where, E_0 is the equilibrium potential, E_{PA} is the anodic peak potential, E_{PC} is the cathodic peak potential, m is the total number of peaks, I_P is peak current, F is Faraday's constant, A is the area of the electrode, C^O is the concentration of electrolyte, and α is the charge

transfer coefficient. The plot of $\ln|I_P|$ $vs.$ $|(E_P - E_O)|$ determined at different scan rates has a slope of $-\alpha \cdot f$ and an intercept proportional to K^0. The value for K^0 can be obtained from the intercept without driving the value for α. The K^0 values for oxidation and reduction processes of both negolyte and posolyte sides for the pristine carbon felt and for the Ketjen decorated carbon felts are the smallest, while the reaction rate is much faster in CNT-30 coated carbon felts, which outperforms graphene-based and other prepared electrodes. The detailed analysis is mentioned in the *supplementary information*.

The addition of CNT or graphene nanoparticles to the cathode or anode sides appears to improve both the mass transfer (lower ohmic resistance) and reaction kinetics (lower activation overpotential) involved at each electrode. Concerning the electroactivity - K^0 from Table 6.1, for the charging step, graphene-coated electrodes perform the best, while reducing V^{3+} to V^{2+} at the negative side – cathode (0.28 cm·s^{-1}). On the other hand, CNT-electrodes perform the best at the positive side during the oxidation reaction, V^{3+} to V^{4+} - anode (0.023 cm·s^{-1}). During the discharging step, the electrode loaded with CNT outperforms the electrode loaded with graphene at the negative side (8.06 cm·s^{-1} vs 6.44 cm·s^{-1}), and at the posolyte, the graphene, and Vulcan -based electrodes deliver the fastest reaction rates for the reduction reaction (0.284 cm s^{-1}). However, overall CNT-coated carbon felts perform the best when running a NAqRFB-cell.

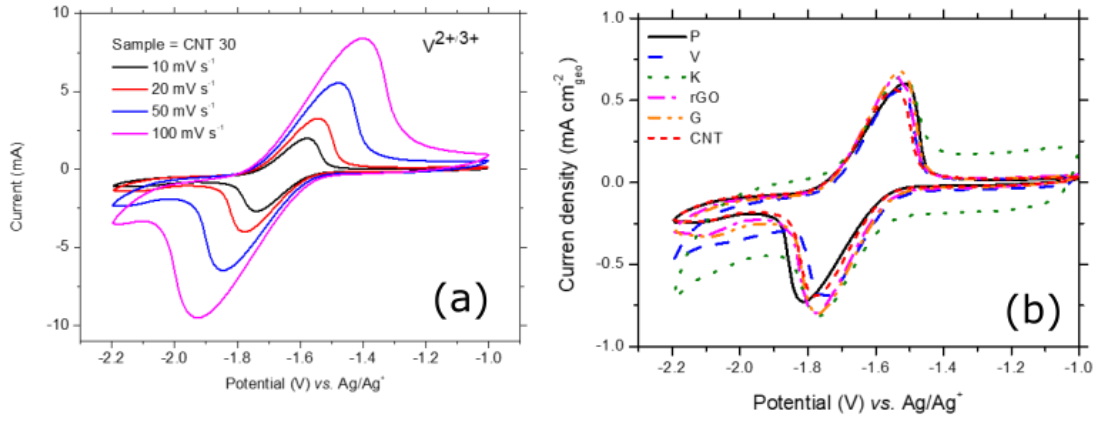


Figure 6.1 Cyclic voltammogram in a 3-electrode configuration cell, using platinum wire as a counter electrode, and Ag/Ag$^+$ as a reference electrode. The electrolyte was 0.1 M $TEABF_4$ + 0.02 M $V(acac)_3$ + Acetonitrile for V^{2+}/V^{3+} reaction i.e. for negolyte. (a) Measurements at various scan rates for the same sample of CNT 30 (b) Measurements at 20 mV·s^{-1} for each sample.

The morphology of pristine and coated carbon felt at several magnifications, 340 x, 2650 x, and 6400 x is illustrated in Figure 6.2 and Figure 6.3. The pristine sample, Figure 6.3 (g-i) reveals that the fibers are entangled and possess a clean and smooth

surface. The coating of nanoparticles generates a rougher surface and a more significant proportion of defects suggesting the existence of a larger number of active sites for the redox reactions. The latter also shows that the ionomer, in the ratio of I/C = 30 wt. %, is effective and offers good binding of the carbon nanoparticles to the felt fibers.

Table 6.1 Peak to peak potential separation, peak current ratios, recorded at 20 mV·s^{-1} and fitting result for the reaction rate constants of oxidation V^{2+}/V^{3+} (negolyte) and reduction, V^{3+}/V^{4+} (posolyte) processes on different electrodes obtained using Equation (9).

	I_{PA} (mA)	$-I_{PC}$ (mA)	E_{PA} (V)	E_{PC} (V)	I_{PA}/I_{PC}	ΔE (mV)	K_A^0 (cm·s^{-1}) Oxidation	K_C^0 (cm·s^{-1}) Reduction
Negolyte								
Pristine	3.66	3.98	-1.46	-1.81	0.92	290	1.70	0.19
Vulcan	3.39	3.73	-1.52	-1.75	0.91	215	4.12	0.27
Ketjen	3.19	3.45	-1.52	-1.77	0.92	245	1.37	0.17
Graphene	4.12	4.27	-1.51	-1.77	0.96	241	6.44	0.28
rGO	3.92	4.27	-1.50	-1.78	0.92	243	4.85	0.27
CNT30	3.54	3.83	-1.54	-1.77	0.92	230	8.06	0.25
Posolyte								
Pristine	2.95	2.72	0.69	0.38	1.08	307	0.018	0.137
Vulcan	2.55	1.95	0.64	0.45	1.31	187	0.007	0.284
Ketjen	2.44	2.17	0.64	0.44	1.12	203	0.014	0.148
Graphene	3.07	2.69	0.64	0.44	1.14	207	0.011	0.284
rGO	3.40	3.05	0.64	0.42	1.12	219	0.018	0.260
CNT30	3.20	2.83	0.65	0.41	1.13	239	0.023	0.175

In terms of adhesion of the nanoparticles, the drop-casting method was highly effective, mainly for rGO and CNT coated electrodes, as they demonstrated extensive dispersion of nanoparticles on their fibers, Figure 6.2 (a-c) and Figure 6.3 (a - c), respectively. Vulcan nanoparticles, with a primary particle diameter of 30 nm, offered a very dense coating that may contribute to enhanced electrical conductivity but simultaneously to pore's blockage. Simultaneously, Figure 6.3 (d-f) shows the immense graphene nanoparticles adhered to the fibers with agglomerates of *ca.* 80 µm in diameter. The interaction of these nanoparticles with the Nafion ionomer produced larger secondary particles because of aggregation and agglomeration phenomena [177]. The electrodes prepared with CNT have a spiderweb-like microstructure, extraordinarily uniform, and overall, this coating did not generate as many agglomerates as the remaining. The coatings with Ketjen nanoparticles were not successful as the carbon felt fibers were barely covered.

Post-mortem analysis reveals that the coating method is reliable because the nanoparticles remain attached to the fibers even after intense charge-discharge cycling -

Figure S 11.19. Ketjen coated electrodes depict a much different microstructure, throughout the charge-discharge cycling, some leaching of the Ketjen nanoparticles occurred. The carbon felt containing CNT shows a similar morphology when it was aged compared with when it was fresh.

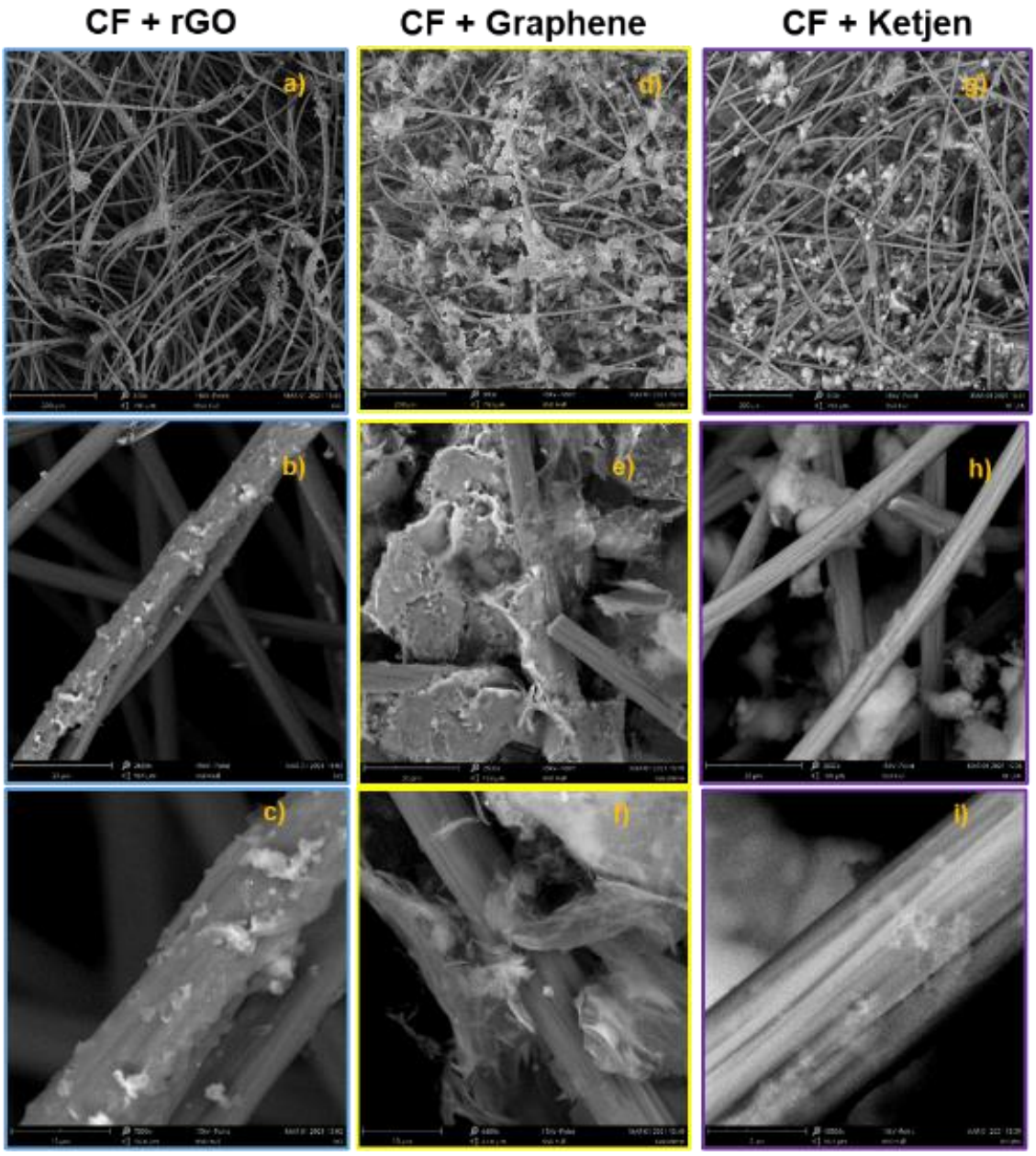


Figure 6.2 Surface morphology of carbon fibers of carbon felts with rGO nanoparticles at (a) 340 x (b) 2500 x and (c) 7600 x magnification; graphene nanoparticles at (c) 340 x (d) 2500 x and (e) 7600 x magnification and Ketjen at (f) 340 x (g) 2500 x and (h) 7600 x magnification. The loading of the modified carbon felts with nanoparticles was maintained at 11 % of the total weight with an I/C of 30 wt. %.

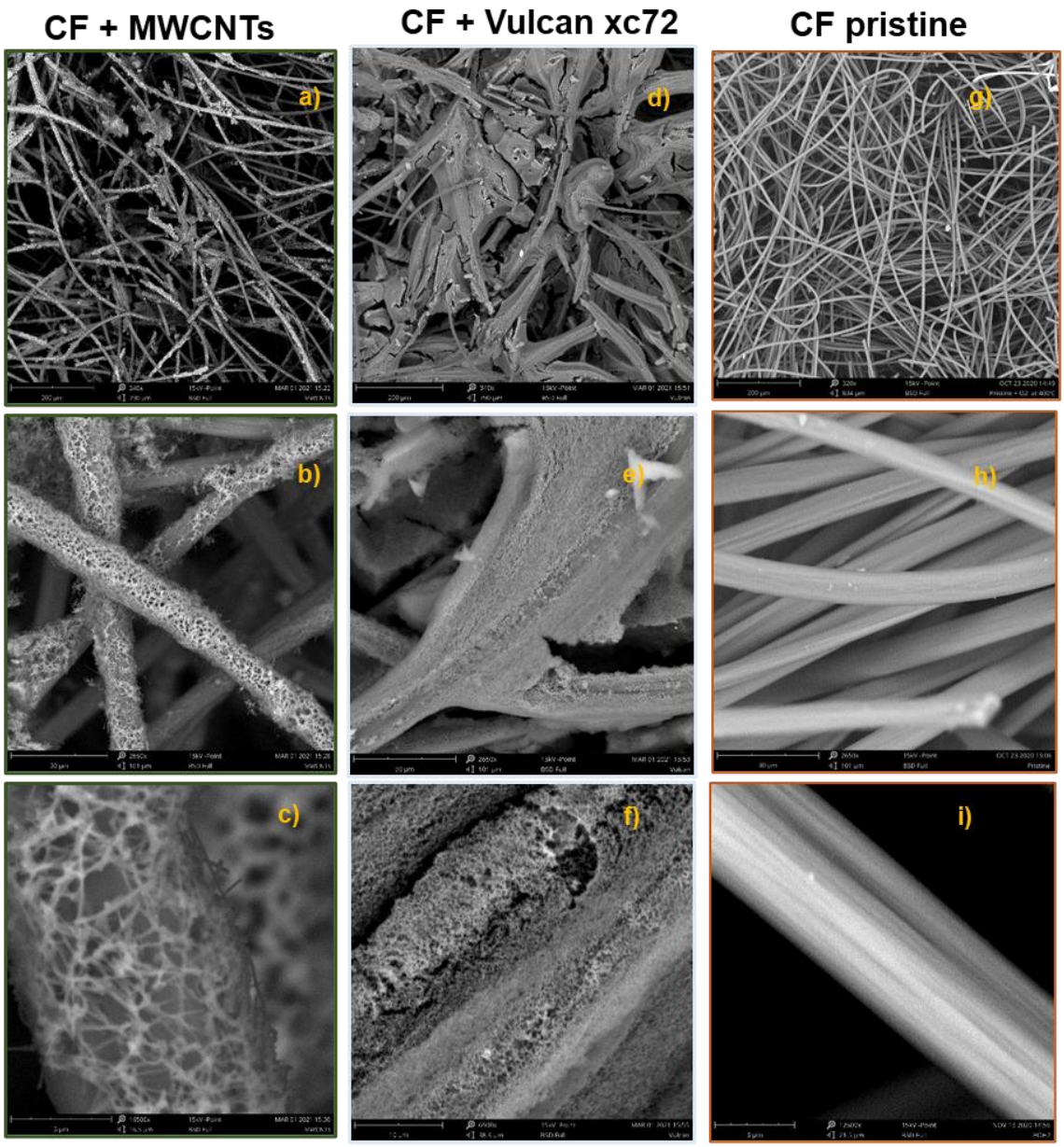


Figure 6.3. Surface morphology of carbon fibers of carbon felts with CNT at (a) 340 x (b) 2500 x and (c) 7600 x magnification; Vulcan XC7 nanoparticles at (c) 340 x (d) 2500 x and (e) 7600 x magnification and the pristine carbon felt at (f) 340 x (g) 2500 x and (g) 7600 x magnification. The loading of coated nanoparticles was maintained at 11 % of the total weight with an I/C of 30 wt. %.

6.3.3 Performance of electrodes in the redox flow cell

Charge discharge cycling (CDC) was used to assess the performance of the redox flow cell. The cell was assembled using each of the coated carbon felts and further operated for 25 cycles at a C-rate of C/2, *i.e.*, equivalent to the current density of 4.2 $mA \cdot cm^{-2}$. The results obtained for the pristine felt were used as the benchmark. A polarization curve was obtained in charging mode before cycling the battery, to measure

the limiting current density obtained with each set of electrodes. The *iR*-free corrected polarization curves were obtained after battery cycling to estimate the ohmic losses. The high-frequency intercept was obtained from the impedance spectra (- Nyquist Plot), which represented the value of the ohmic resistance of the cell.

The charge-discharge cycling (CDC) performance for the cell equipped with each electrode sample is shown in Figure 6.4. The electrodes coated with Vulcan nanoparticles performed better during the initial 9 cycles – η_{EE} = 72 %; at cycle 10th there is a drop in the energy efficiency from 72 % to 44 %, continuing to decrease afterward. On the other hand, the coulombic efficiency (η_{CE}), which quantifies the ability to store and retrieve the same amount of electric charge, is the lowest for the cell equipped with Vulcan- electrodes, *ca.* η_{CE} = 77.1 % averaged for 25 cycles. The posolyte V^{3+} oxidized to V^{4+} during battery charging and the electroactivity of Vulcan coated electrodes for oxidation is the lowest, *i.e.* K^0 = 0.007 cm·s^{-1}. This can cause an imbalance between the oxidized and reduced redox species. So, there is a rapid drop in the performance after oxidizing the initially available concentration of V^{3+}.

The cell equipped with Ketjen coated electrodes offered increased efficiency and capacity retention, compared to Vulcan-electrodes. This particle type is also from the same family of carbon black nanoparticles, but the dispersion of these nanoparticles was far from dense in comparison to Vulcan particles. Besides, the manufacturer claims [178] that the coatings remain stable with Ketjen nanoparticles since higher shear forces are necessary to break the agglomerates attached to the carbon felt fibers. SEM images from before and after cycling also confirm this behavior – *cf.* Figure 6.2 (g) and Figure S 11.18. The energy efficiency of the cell equipped with Ketjen-electrodes is η_{EE} = 71.4 % for 25 cycles, higher than for Vulcan-electrode and pristine samples, but lower than for the graphene, rGO, and CNT-based electrodes, *cf.* Figure 6.4 (c). The cell efficiencies, when assembled with graphene-coated electrodes and with reduced graphene-oxide coated electrodes, exhibit η_{CE} = 83.1 %, η_{VE} = 89.1 %, η_{EE} = 74 % and η_{CE} = 83 %, η_{VE} = 90.7 %, η_{EE} = 75.2 %, respectively. Also, the limiting current density achieved by the rGO-electrodes is *ca.* 23 % (54.25 mA·cm^{-2}) higher than the graphene-based electrodes (35.2 mA·cm^{-2}) – *cf.* Figure 6.6 (a).

The CNT-based electrode achieved remarkable performance, and the overall attained efficiencies, averaged for 25 cycles were: η_{CE} = 81.7 %, η_{VE} = 91.8 %, and η_{EE} = 74.8 % - Figure 6.4; this electrode also provided the highest cell limiting current

density - 56.2 mA·cm^{-2} - Figure 6.6 - while delivering the lowest ohmic losses, 369 mV. Multi-walled carbon nanotubes (MWCNT) are a unique form of carbon nanotubes in which multiple single-walled carbon nanotubes are nested inside one another. Figure 6.3 shows the morphology of MWCNT coated electrodes, plenty of long nanotubes are tangled together in a pattern like a spider-web. The distribution of sp^2 sites in MWCNT is responsible for higher electrical conductivity [176]. The boost in the performance of cells having CNT-electrodes was assigned to the combination of higher electronic conductivity together with higher electroactivity, K^0. The uniform dispersion of the MWCNT across the carbon felt helped to minimize the mass transport losses, while adhesion provided the best electrical conductivity throughout the cycles [179,180].

CNT-electrodes and rGO-electrodes demonstrated a similar limiting current density measured before the charge-discharge cycling, *i.e.,* 56.2 and 54.2 mA·cm^{-2}, respectively. After the charge-discharge cycling, the effect of ohmic losses became very significant for rGO-electrode, as the limiting current density dropped by *ca.* 10 % compared to the CNT-electrode, as shown in Figure 6.6 (b). The looseness of the rGO particles from the carbon felt fibers should explain the increase in ohmic losses - Figure 6.6 b - due to the more electronic resistance at the particle/fiber interface.

Table 6.2 Ohmic and charge transfer resistances from the first semi-circle of impedance curves taken before and after charge-discharge cycling of cell equipped with each sample electrodes.

	Before CDC		After CDC			
Electrodes	R_o (Ω)	R_{CT} (Ω)	R_o (Ω)	% less w.r.t P	R_{CT} (Ω)	% less w.r.t P
Pristine	0.64	4.16	1.87	-	7.55	-
Vulcan	0.69	1.97	1.72	8 %	0.57	92 %
Ketjen	0.55	1.39	1.43	24 %	1.5	80 %
Graphene	0.65	6.07	1.41	25 %	3.95	48 %
rGO	0.63	4.96	1.6	14 %	6.16	18 %
CNT	0.69	3.71	1.02	45 %	2.82	63 %

Acronyms: w.r.t = with respect to; R_o = Ohmic resistance; R_{CT} = Charge transfer resistance; CDC = Charge discharge cycling

The impedance spectra of the cell equipped with the pristine electrodes are shown in Figure 6.5. The ohmic contribution for the pristine electrode before and after CDC was nearly the same. However, there is a significant increase in the charge transfer resistance

of the cell from *ca.* 2.32 Ω to 7.91 Ω, which is the biggest change among all electrodes and utterly condemns the CDC performance of the cell. The coating of carbon nanoparticles assists in lowering the charge transfer resistance to significantly lower values compared with the pristine electrodes, as indicated in Table 6.2. The cell equipped with CNT-electrodes exhibits not only the lowest ohmic resistance (R_0) compared to the cell equipped with the pristine-electrode but also the lowest charge transfer resistance (R_{CT}) compared to electrodes pristine, graphene, and rGO. These electrochemical results for the NAqRFB are aligned with the morphological analysis and follow the trend observed for the reaction rate constant values.

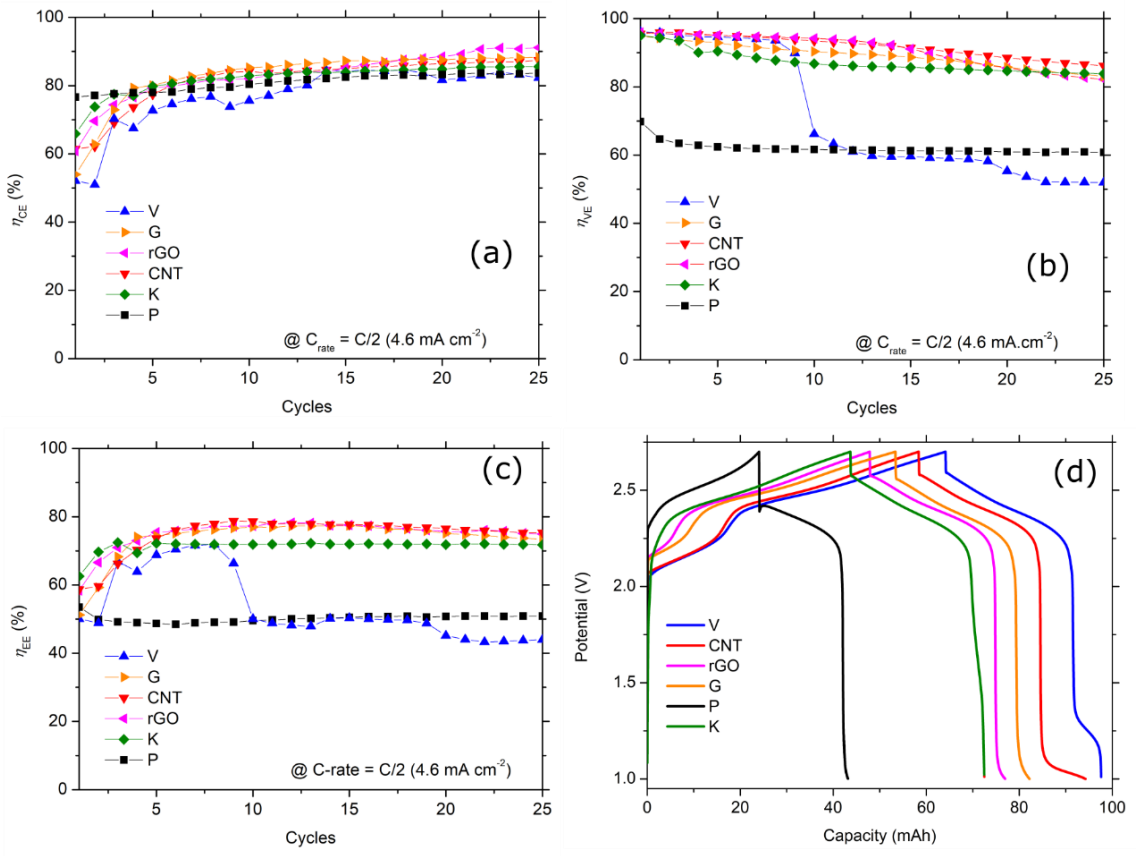


Figure 6.4 Charge discharge cycling of the NAqRFB-cell assembled with each sample of electrodes coated with nanoparticles of Vulcan Carbon Black - V, Ketjen Carbon Black - K, Carbon Nanotubes - CNT, Graphene Oxide - rGO and Graphene - G. Results are compared with Pristine electrodes - P. (a) Coulombic Efficiency, (b) Voltage Efficiency, (c) Energy Efficiency, (d) Recorded potential of 2nd cycle as a function of capacity.

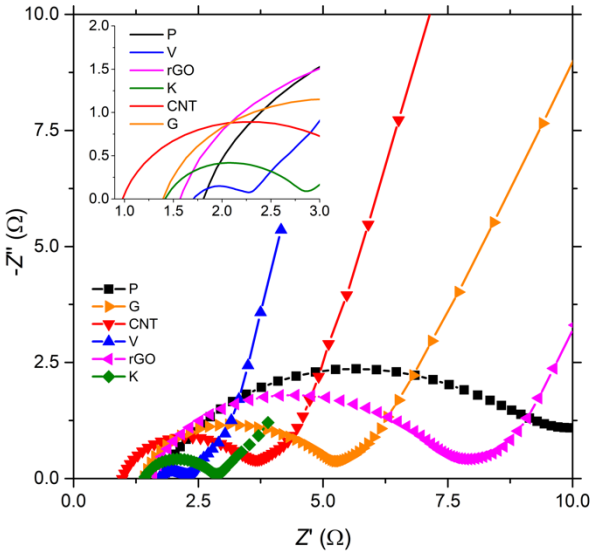


Figure 6.5 Impedance curves measured after CDC through electrochemical impedance spectroscopy (EIS) in the range of 100 mHz to 250 kHz at an amplitude of 10 mV while the cell was maintained at E_{OCP} = 1.5 V.

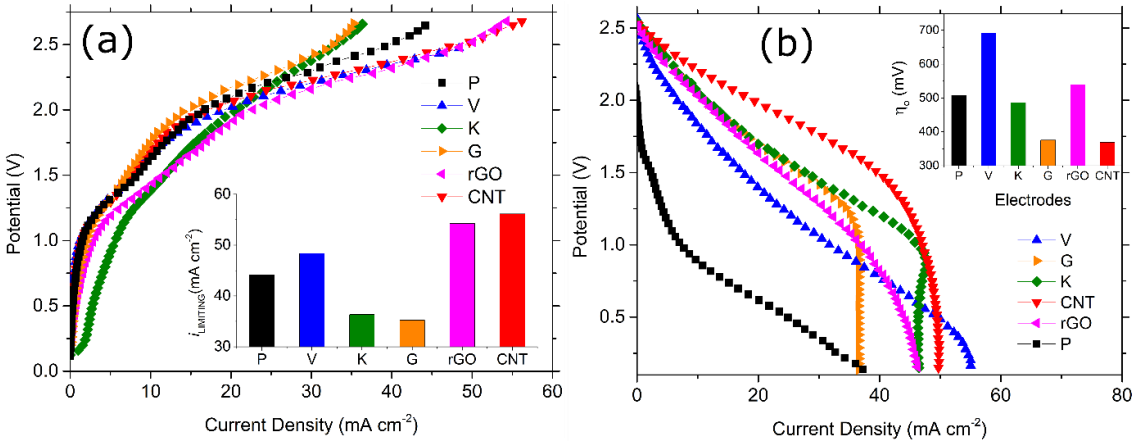


Figure 6.6 iV-curves of the NAqRFB-cell (a) Polarization in charging mode was performed before CDC through scanning at 10 mV·s^{-1} from 0.1 V to 2.5 V; (b) Polarization in discharging mode was performed after CDC by scanning at 10 mV·s^{-1} from 2.5 V to 0.1 V.

6.3.4 Optimization of Nafion ionomer concentration in the CNT-electrodes

The influence of the Ionomer/Carbon (I/C) ratio on the electrode microstructure and the electrochemical performance has been thoroughly studied for electrochemical devices such as PEM fuel cells (PEMFCs), mainly concerning the interaction of perfluorinated sulfonic acid-based ionomers with Pt/C catalysts [181,182]. Typically, for PEMFCs using carbon-based electrocatalysts, the optimal concentration of Nafion ionomer lies in the range ratios of 0.22 - 0.30 concerning the total mass of metal catalyst [183]. The optimum ionomer concentration highly depends on the type and dimensions

of the used carbon supports [24]. The trade-off study was performed to optimize the concentration of the binding – ionomer – in the coating ink, which was applied to the best performing CNT-electrode. Compositions of 5 wt.%, 15 wt.%, and 30 wt.% of Nafion ionomer were assessed, referred to as CNT5, CNT15, and CNT30. Higher coverage with CNT particles was reached increasing the concentration of ionomer. Samples CNT15 and CNT30 demonstrated minimal or no loss of nanoparticles after 30 charge-discharge cycles, while sample CNT5 lost almost all the originally attached CNT particles – *cf*. *supplementary information*, Figure S 11.18 to Figure S 11.22.

Impedance and polarization analyses were performed before and after 30 cycles of charge-discharge @ 4.6 $mA \cdot cm^{-1}$. Figure 6.7 shows the energy performance of the NAqRFB equipped with pristine electrodes and electrodes CNT5, CNT15 and CNT30, along with a CDC assay; CNT5, CNT15, and CNT performed similarly after 25 cycles, respectively η_{EE} = 73.1 %, η_{EE} = 73.8 %, and η_{EE} = 74.8 %, while the pristine performed η_{EE} = 52.4 %. Moreover, the capacity retention improved with the ionomer concentration, as shown in Figure 6.10 and discussed in the next sections. On the other hand, the charge-transfer resistance (R_{CT}) values of the coated-electrodes (CNT30, CNT15, and CNT5) decrease up to 67 %, 77 %, and 76 %, respectively, compared to the pristine-electrodes.

The mass transport kinetics of the redox species decreased with the ionomer concentration, as assessed by the onset of the limiting current. Following, CNT15, CNT30, CNT5 display an onset limiting current which is respectively 19 %, 27 % and, 28.4 % early compared with the NAqRFB equipped pristine electrodes. The addition of CNT helps to lower the ohmic losses, which decreases *ca.* 29 % compared with the pristine electrodes for all modified electrodes – CNT5, CNT15, and CNT30; the ohmic losses decreased from (508 ± 5) mV to (365 ± 5) mV. Considering the trade-off between adhesion/stability, mass-transport losses, and ohmic losses, the CNT15 electrode seems to display the best performance.

6.3.5 Application of noble metals as catalyst

Besides adding carbon nanoparticles to the carbon fibers of the carbon felt electrodes, one may think about using nanoparticles of noble metals. Metals such as Au, Pt, Ru, and Ir have been reported showing improved results for the case of vanadium redox flow batteries – aqueous-based [183]. The role of supported nanoparticles platinum was then assessed in the present study, namely, it was added to the carbon fibers of the carbon felt electrodes graphene oxide platelets loaded with 8 wt.% of platinum

nanoparticles (Pt-rGO). CDC results using a NAqRFB cell equipped Pt-rGO-electrodes are shown in Figure 6.9. These electrodes show benefits mostly concerning the charge transport, as seen from the lower R_{CT} obtained (*cf.* Figure 6.9 d) and also lower activation overpotentials in charging mode (*ca.* 1.25 V for Pt-rGO *vs.* 1.40 V for rGO @ 10 mA·cm^{-2}) and discharging mode (*ca.* 0.21 V for Pt-rGO *vs.* 0.52 V for rGO @ 10 mA·cm^{-2}).

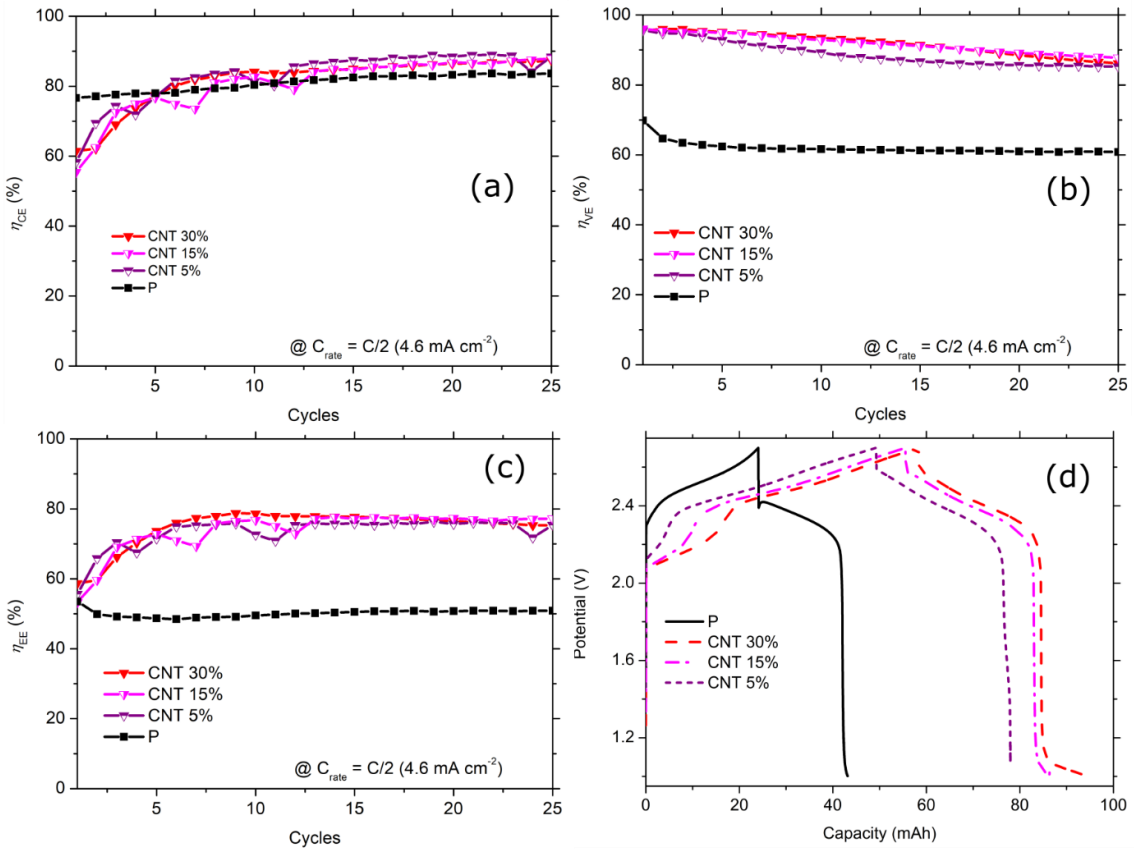


Figure 6.7 Charge discharge cycling for the CNT-electrode samples. Electrodes were prepared using ink having 5 wt. %, 15 wt. %, and 30 wt. % concentration of Nafion ionomer. (a) Coulombic efficiency, (b) Voltage efficiency, (c) Energy Efficiency, (d) Charge-discharge curve for the second cycle.

The polarization curve in discharging mode - Figure 6.9 f - shows a steep drop in the performance of Pt rGO-electrodes at high current densities due to starvation, whereas the same trend was not observed for the pristine-electrodes; this starvation happens earlier for the Pt-rGO-electrode at *ca.* 1.75 V, as compared to rGO-electrode - *ca.* 0.94 V. For the case of Pt-rGO-electrodes, as the cell was continued to be discharged at 20 mV·s^{-1}, the current density starts reducing, indicating that more electrolyte is required to avoid starvation. Further studies should be performed to assess the optimum flow rate due to the drastic performance reductions at high currents. According to the *iV*-curves, the

limiting current density assessed as the *x*-intercept reads 121.7 mA·cm^{-2} for Pt-rGO and 60.3 mA·cm^{-2} for rGO, which is respectively 252 % and 74 % higher as compared to pristine electrodes (*i.e.*, 34.6 mA·cm^{-2}). Pt-rGO-electrodes show less ohmic losses in charging - Figure 6.9 e - and discharging - Figure 6.9 f – modes. The performance of the NAqRFB-cell equipped with electrodes loaded with Pt-rGO is higher compared to when equipped with pristine electrodes; however, the performance of Pt-rGO-electrodes is only slightly higher than the rGO-electrodes but lower than CNT15-electrodes, which contains no platinum – Table 6.3.

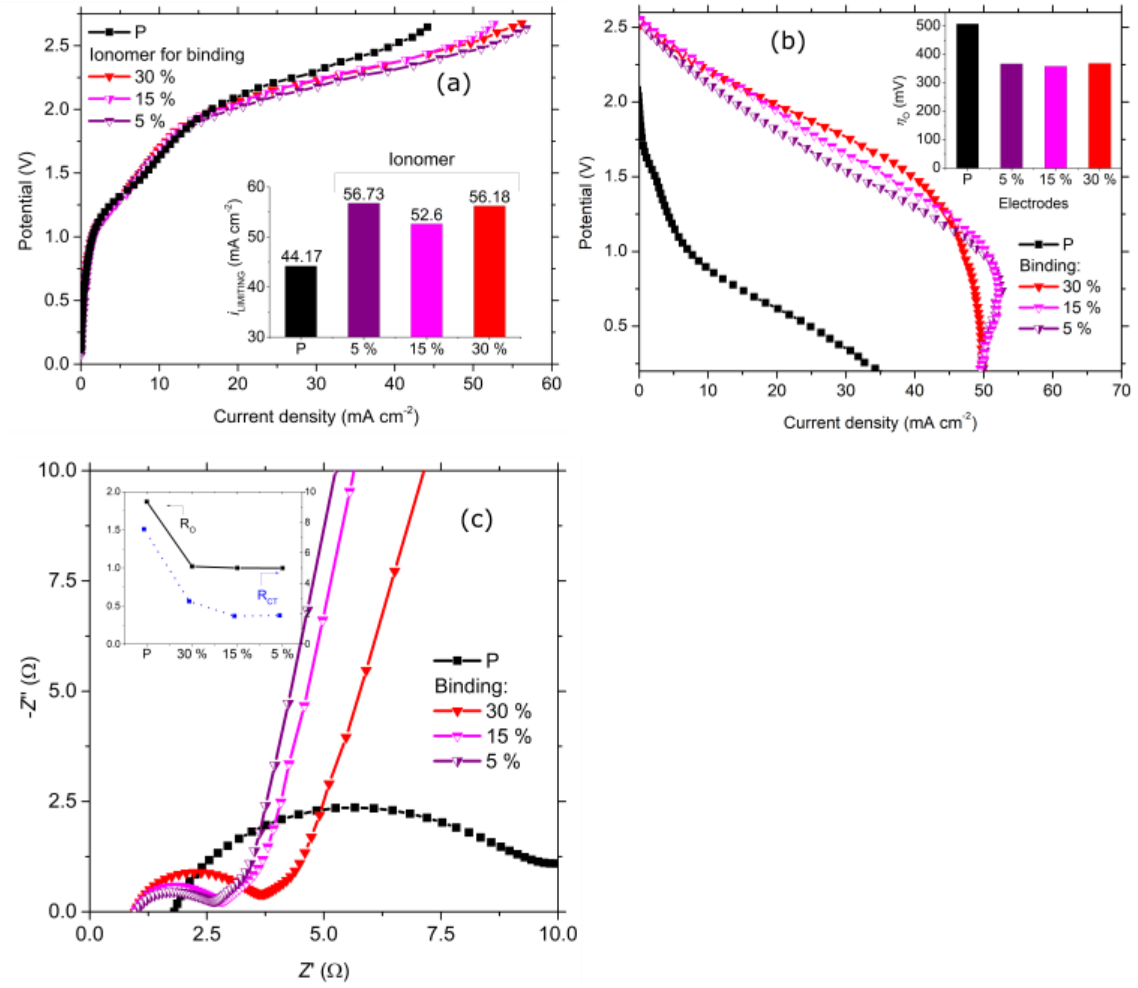


Figure 6.8 NAqRFB equipped with MWCNT based electrode. Sample electrodes were prepared at 5 wt. %, 15 wt. %, and 30 wt. % addition of Nafion ionomer as binding solution. The impedance curves were retrieved after CDC at 1.5 V from 250 kHz to 100 mHz at 10 mV AC amplitude. (a) & (b) Polarization curves in charge/discharge modes. (c) Impedance curves and the inset show the values of ohmic resistance R_O and charge transfer resistances R_{CT} (Lines are added in the inset).

6.3.6 Storage capacity fade

The presence of moisture and oxygen in vanadium NAqRFB triggers an irreversible parasitic reaction that typically generates vanadyl acetylacetonate – $VO(acac)_2$ – which severely condemns the stability of the cell [77,171,184]; in contrast, redox couple V^{3+}/V^{4+}, in contact with the positive electrode, typically withstand better these adverse conditions. The tuning of the electrodes to get an oxygen-free surface provides facile kinetics towards the redox reactions, as shown elsewhere by the authors [185]. Commercial as-received carbon felts (pristine), are a source of oxygen that shortens the battery life. The parasitic reaction which originates $VO(acac)_2$ can be mitigated using thermally reduced carbon felt electrodes under a hydrogen atmosphere [185]. Similarly, in this work, a hydrogen reduction treatment was applied to the prepared electrodes to lower the available oxygen-based functional groups at the surface of the electrodes. However, because of the limited stability of the applied Nafion ionomer, which is stable only up to 150 ^{o}C [186], the thermal reduction was performed at 120 °C for 4 h, and not at 400 °C as described elsewhere [185]. Because of that, storage capacity fade, which is mostly related to the formation of parasitic $VO(acac)_2$ species, was observed – Figure 6.10.

Actually, all the NAqRFB cells, equipped with the prepared electrodes, showed a capacity drop after 10 cycles and energy density loss, as shown in Figure 6.10. *Post-mortem* FTIR of the membrane performed before and after the charge-discharge cycling show no significant difference as shown in Figure S 11.25. Overall, compared with the pristine electrodes, the cell equipped with CNT30 - electrodes outperform all the remaining achieving 3.2 fold higher storage capacity, measured at the end of the CDC test. The performance in terms of storage capacity is as follows CNT30 > Vulcan > rGO > Ketjen > CNT15 > Graphene > CNT5 > Pt-rGO > Pristine at the end of charge-discharge cycle *i.e.* 25th cycle.

6.4 Conclusion

Electrodes are critical components in NAqRFB as they are related to the activation overpotentials and ohmic losses. Pristine carbon felt, however, display low electroactivity and research on how to improve its electroactivity is required. The most obvious strategy is increasing their electrochemical surface area by coating the carbon felt fibers with electronic and electrocatalytic active elements. This work assessed the role of carbon nanoparticles Vulcan, Ketjen, graphene, rGO, CNT and also platinum supported on

graphene. A facile and fast drop-casting coating technique was developed to prepare the modified electrodes. Nafion ionomer was added to the nanoparticles for adhesion to the fibers of carbon felt and the optimum Nafion ratio in the electrode was studied. The best performing electrodes, coated with CNT, displayed an energy efficiency of *ca.* 22.4 % higher as compared with pristine electrodes. The adhesion of the nanoparticles prepared through the drop-casting method was robust, and this technique is scalable to manufacture electrodes for larger geometric areas.

The carbon fibers coated with CNTs display a spider-web configuration, which certainly was the most responsible for its better performance compared with the other carbon nanoparticles. The closest performing added particle was graphene, which coating layer displays also an open porous morphology. Besides other properties, it was concluded that the shape of the added nanoparticles was of critical relevance to determine their performance, which should be mostly related to the morphology of formed agglomerates over the surface of the supporting carbon fibers. On the other hand, Pt-rGO nanoparticles displayed only a slightly better performance of rGO. CNT-electrodes demonstrated widespread dispersion of nanoparticles on their fibers, which is proportional to a higher number of active sites to perform the redox reactions. The latter was confirmed by the 4.7 fold higher electrochemical reaction rate constant – K^0, as compared to pristine electrodes. Adding the ionomer in a ratio of 15 wt. % was effective and offers good binding of the carbon nanoparticles to the felt fibers. This allowed increasing the number of triple-phase boundaries, which results in a 34.4 % reduction in the charge-transfer resistance compared to the pristine electrodes. This study contributes to paving the way toward pilot-level commercialization of non-aqueous redox flow batteries.

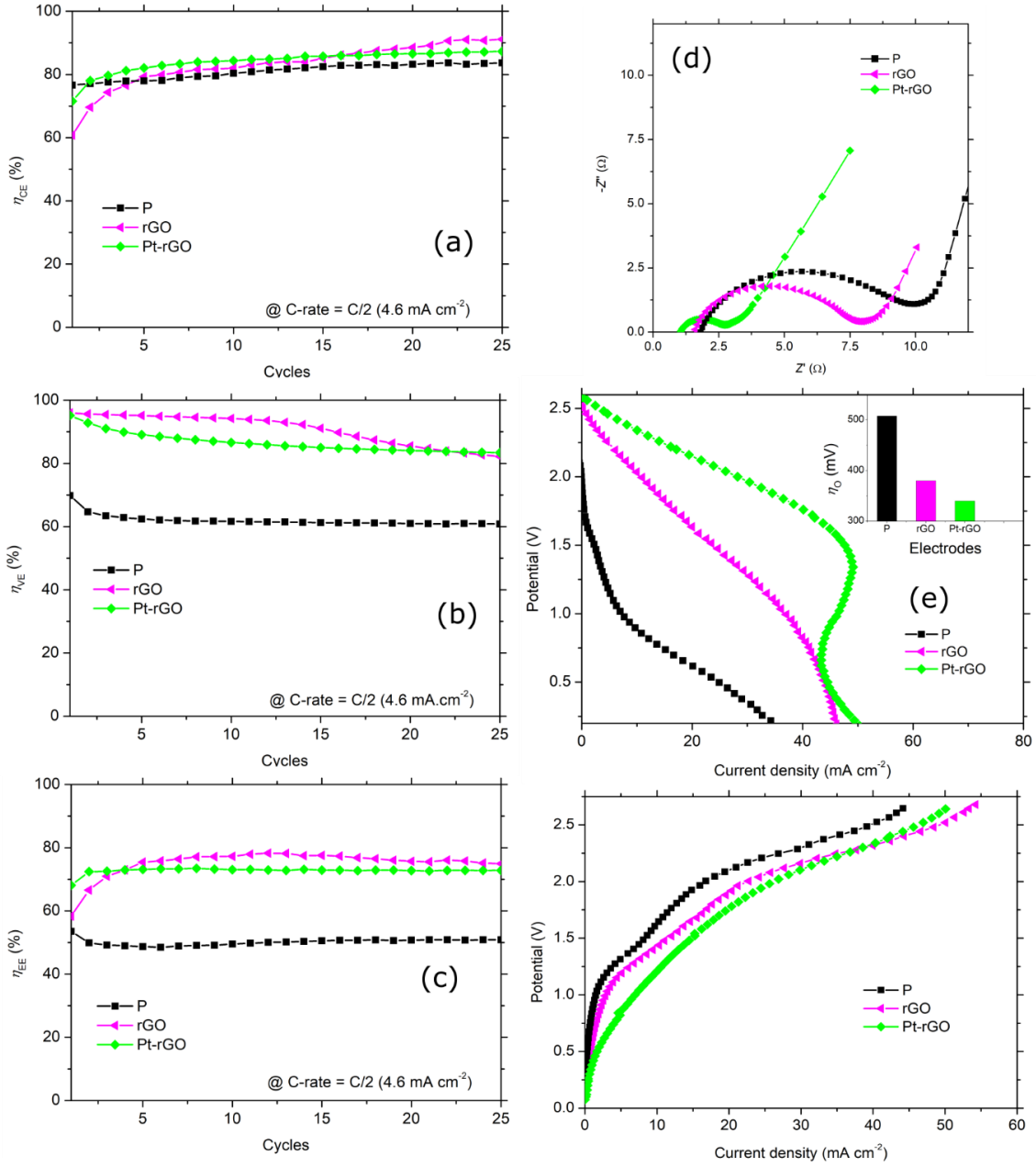


Figure 6.9 NAqRFB-cell equipped with the electrodes coated with rGO and Platinum as a catalyst, Pt-rGO electrode. (a) Coulombic efficiency (b) Voltage efficiency (c) Energy efficiency (d) Impedance curve (e) Polarization in discharging mode (f) Polarization in charging mode.

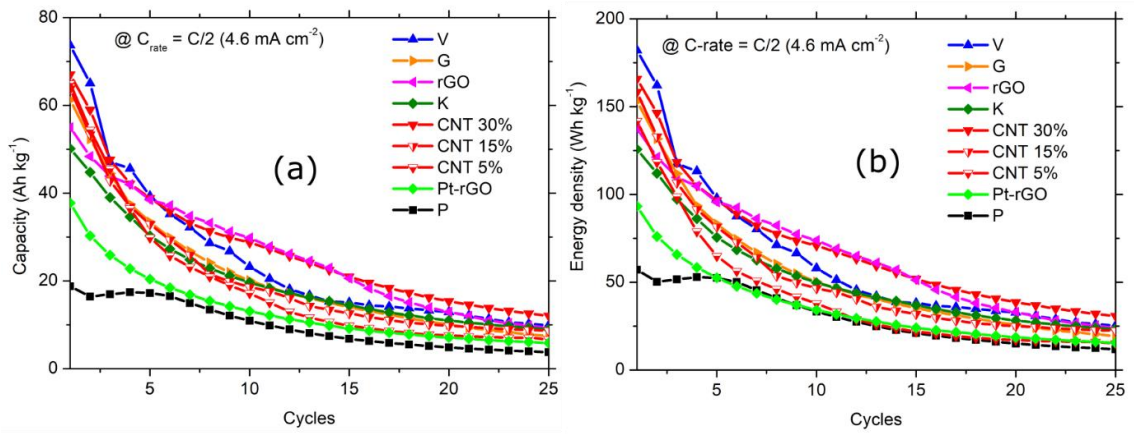


Figure 6.10 NAqRFB-cell assembled with each sample of electrodes operated at C-rate = C/2, i.e., 4.6 mA·cm^{-2} at the flow rate of 30 ml·min^{-1} (a) Capacity (b) Energy density

Table 6.3 Summary of the results of the NAqRFB-cell equipped with each of the coated electrodes and optimization of the electrodes containing varying ink composition having Nafion ionomer binding solution.

Electrodes	η_{CE} %	η_{VE} %	η_{EE} %	i_{LIM} mA·cm^{-2}	η_O mV	R_O Ω	R_{CT} Ω
Pristine	80	65.7	52.4	44.2	508	1.87	7.55
Vulcan	77.1	70.8	53.5	48.4	618	1.72	0.57
Ketjen	82.1	87.2	71.4	36.3	486	1.43	1.5
Graphene	83.1	89.1	74	35.2	376	1.41	3.95
rGO	83	90.7	75.2	54.2	380	1.6	6.16
CNT30	81.7	91.8	74.8	56.2	369	1.02	2.82
CNT15	80.6	91.8	73.8	52.6	359	1.02	1.85
CNT5	82.8	88.7	73.3	56.7	367	1	1.88
Pt-rGO	84.2	86.6	72.7	50.1	340	1.06	1.77

Acronyms: η_{CE} = Coulumbic efficiency; η_{VE} = Voltage efficiency; η_{EE} = Energy efficiency; i_{LIM} = limiting current density; η_O = Ohmic overpotentials; R_O = Ohmic resistance; R_{CT} = Charge transfer resistance.

Chapter 7

Aluminum ion based NAqRFB

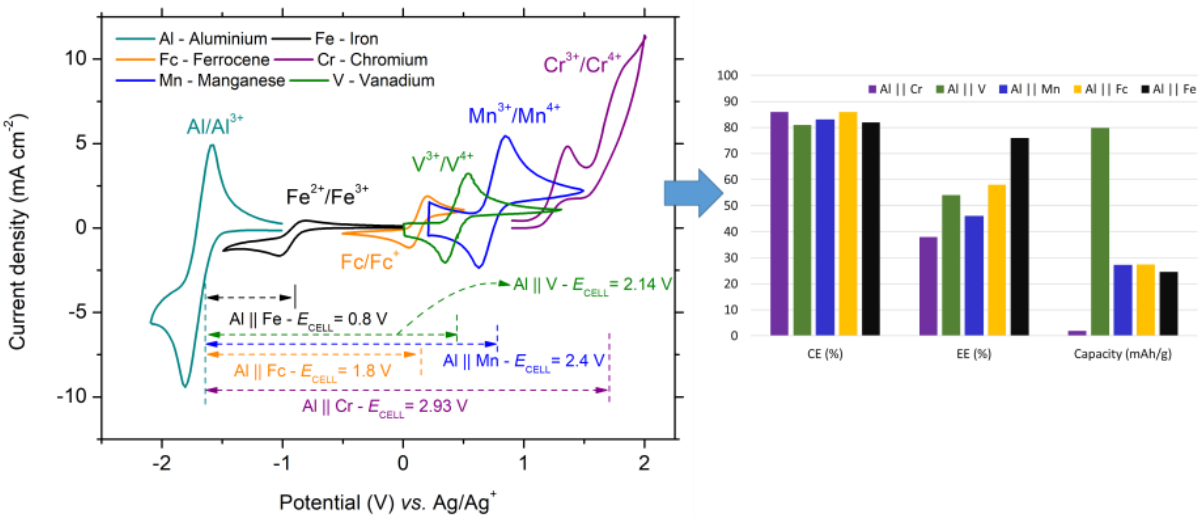
7. Aluminum ion based NAqRFB

Adapted from the following article:

K. Mushtaq, S. Delgado, A. Mendes, "Novel Aluminum-Ion Based Non-Aqueous Redox Flow Battery", 240th ECS Meeting (October 10-14, 2021), Digital Meeting, USA.
Link: https://iopscience.iop.org/article/10.1149/MA2021-0251925mtgabs

The global implementation of renewable energy technologies requires the use of low environmental impact and locally available materials. In particular, for energy storage, Li-ion battery (LIB) technology is presently the leading technology, though it requires the use of lithium, cobalt, phosphates, and graphite, all considered critical raw materials by the EU commission. In contrast to LIBs, redox flow batteries can use different electrolyte chemistries with minimal adaptations, making them suitable to take advantage of locally available raw materials. Aluminium-ions (Al^{3+}), which offers high energy density and a high value of negative redox potential, i.e., -1.7 V *vs.* Ag^{+}/Ag, is the most abundant metal and more evenly distributed over the Earth's crust. An aluminum-ion-based non-aqueous redox flow battery was introduced in this study as a proof-of-concept. The aluminum redox ion is used as negolyte coupled with the posolyte based on the redox ions of several metal acetylacetonates - M(acac), namely M = Cr, V, Mn, Fe, and Ferrocene (Fc), in detail Al || Cr, Al || V, Al || Mn, Al || Fc, and Al || Fe with cell potential differences of 2.93 V, 2.15 V, 2.4 V, 1.8 V, and 0.8 V, respectively. The Al || Mn battery demonstrated a stable performance up to 50 cycles and an energy density of *ca.* 60 $mWh \cdot g^{-1}$ based on the mass of unsaturated negolyte. Aluminum-based batteries have the potential to be the candidate for the new generation of NAqRFBs. The aluminum-based family of electrolytes for non-aqueous RFB are reported for the first time and paves the promising way for very high-energy density and low-cost batteries.

Graphical Abstract



7.1 Introduction

The emerging inspiration to achieve a climate-neutral society encourages researchers to find sustainable and innovative ways to store energy in different forms. Currently, Li-ion battery (LIB) technology is a widespread technology used to store energy and efficiently convertible into electricity. The LIBs' upstream supply chain comprises materials such as lithium, cobalt, graphite, iron, and phosphates [187,188]. The global implementation of renewable energy technologies requires the use of large amounts of specific materials which must be abundant, have a low environmental impact, and preferably local. In the case of LIB, the required materials are geographically limited to a few countries, while lithium, cobalt, graphite, and phosphorous are already classed as "critical" by the EU [187]. Critical raw materials as shown in Figure 7.1 are required for the EU to meet the European Green Deal's climate goals. The goal of zero net greenhouse gas emissions by 2050 will necessitate electrification initiatives and the diversification of energy sources, which will necessitate a massive increase in raw materials. The LIB production growth rate increases annually by 5 %, and the remaining global lithium resource can only support lithium use until 2079 [189]. As a result, alternative battery systems, based on other elements, including sodium, magnesium, and aluminum, have gotten much attention in recent years [190,191].

In contrast to the intercalation-based electrochemistry of the LIBs, the reaction mechanism of the redox flow battery (RFB) enables storing active redox species in the electrolyte instead of storing them at the electrodes. The amount of energy stored in the battery is proportional to the concentration of active redox species and to the amount of the electrolyte used. The redox reactions happen at the electrode surface assembled inside the battery, while the electrolyte, containing the active redox species, flows through the electrodes from the adjacent reservoirs. Minimal single-cell design variations are required to use different electrolyte chemistries. This flexibility enables the use of the electrolyte by choosing the active redox species from locally abundant transition metals such as iron, aluminum, manganese, vanadium, iron, among others.

Non-aqueous redox flow battery (NAqRFB) technology opens the window of using redox species outside the electrochemical stability range of aqueous electrolytes. An ideal redox species should be i) abundant; ii) cheap; iii) provide fast multiple electron transfer per reacting molecule; iv) high solubility in the chosen solvent, and v) possess reversible kinetics. The relationship between the abundance of commonly used metals for

energy storage technologies and their prices – Figure S 11.26 – provides a prima-facie for selecting metals for the next generation of batteries. This thirst is quenched by aluminum-ions (Al^{3+}), which have high natural abundance, wide availability, ease of processing (including recycling), low cost, the high theoretical volumetric energy storage capacity – 8056 $mAh \cdot cm^{-3}$, high gravimetric energy density – 2981 $mAh \cdot g^{-1}$, and high value of negative redox potential, -1.65 V [192]. Al-based batteries can compete with existing cell electrochemistry for both primary (non-rechargeable) and secondary (rechargeable) applications. The concept of rechargeable aluminum-ion batteries (AIBs) has been advocated for several decades, with the potential to share the realm with lithium-ion batteries (LIBs) for large-scale applications [190].

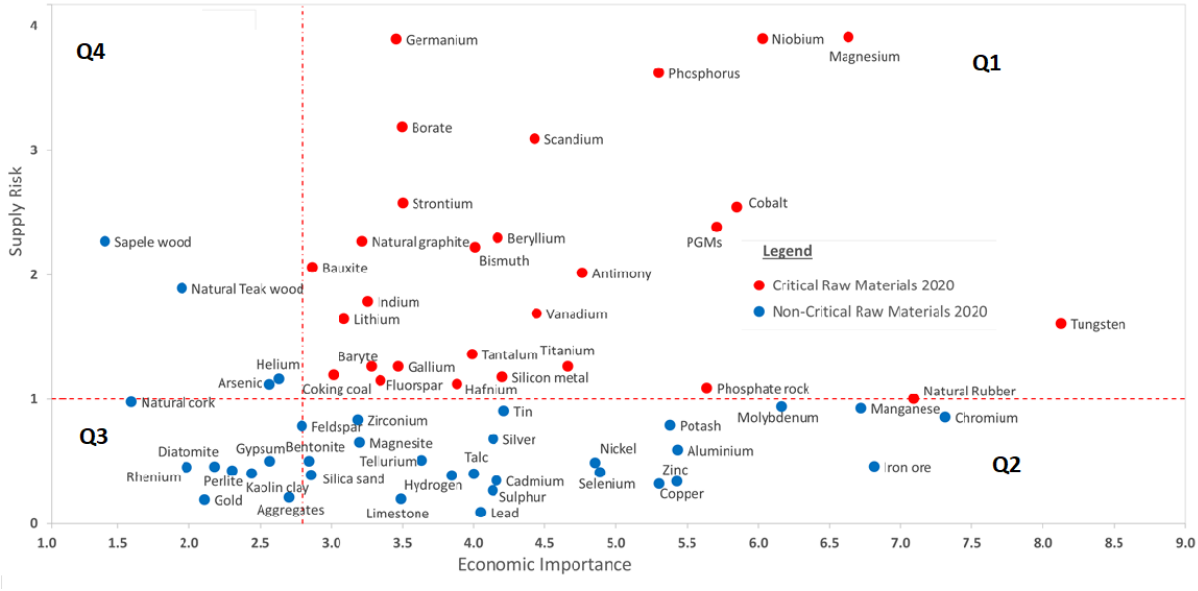


Figure 7.1 Materials in Q1 are categorized by European Union as Critical Raw Materials for the year 2020. Materials from Q2 should be targeted for future technologies [187].

Aluminum is an active battery material, first used in the Buff cell in the 1850s [192] when it was combined with a carbon cathode. Aluminum anodes were studied in a variety of aqueous media, ranging from saline cells to Leclanche-type dry cells [193]. The Al - O_2/air battery concept was initially suggested in 1962, and Al - Cl_2 rechargeable cells on molten salt electrolytes were disclosed in 1988 [194]. These cells were conceptually interesting but they corrode and passivate easily. This prompted extensive research into the ways to overcome these challenges for both aqueous and non-aqueous cells. The development of Al-ion batteries (AIBs) in 2011 [195] aimed at addressing this challenge and research in this area has mostly been focused on understanding the reaction processes seeking suitable cathodes. In the domain of Al-based

batteries, Al-air batteries (AABs) are the most common primary batteries today, whereas AIBs are the most common secondary batteries.

Many of the research on AABs or AIBs that have been published conclude with claims of high energy density materials and/or effective demonstrations of the technology. However, such assertions have almost always overlooked the full implementation of the stated chemistry in practical cells. As per the author's information, the use of aluminum ions for redox flow batteries was never addressed. Therefore, an aluminum-ion-based non-aqueous redox flow battery was introduced in this study as a proof-of-concept using a practical cell. The aluminum redox ion is used as negolyte coupled with the posolyte based on the redox ions of metal acetylacetonates: M(acac), where, M = Chromium (Cr), Vanadium (V), Manganese (Mn), Iron (Fe), and Ferrocene (Fc).

7.2 Experimental Methods

7.2.1 Materials

Tetraethylammonium tetrafluoroborate, $TEABF_4$, was acquired from Alfa Aesar, anhydrous acetonitrile (ACN), 99.8%, was acquired from Sigma Aldrich and used without further purification as supporting electrolyte and solvent, respectively. Vanadium(III) acetylacetonate, $V(acac)_3$, 97 %, was acquired from Strem Chemicals; Chromium (III) acetylacetonate, $Cr(acac)_3$; aluminum acetylacetonate, $Al(acac)_3$; manganese acetylacetonate, $Mn(acac)_3$; iron acetylacetonate, $Fe(acac)_3$; and ferrocene, Fc were acquired from Alfa Aesar. The voltammetry studies were performed using the electrolytes consisting of ACN + $TEABF_4$ 0.1 M + redox species 0.02 M, referred in this study as A1. A membrane consisting of a sandwich of commercial membranes Celgard 4560 | Nafion HP | Celgard 4560 was used in all experiments [40]. The electrodes were purchased from Sigracell, SGL Carbon, having a thickness of 4.6 mm.

7.2.2 Cyclic Voltammetry

Voltammograms were measured using a glassy carbon electrode (GC, Metrohm), as a working electrode, in a 50 ml three-electrode cell configuration. Electrolyte A1 was used to perform all the measurements. Electrode Biologic RE-7, filled with 0.01 M $AgNO_3$ + 0.1 M TBAP + Acetonitrile, was used as reference electrode. Platinum wire served as a counter-electrode. All experiments were performed under a nitrogen

atmosphere. Zahner Zennium potentiostat was used to record all the data, and Thales software was used for the voltammograms analysis.

7.2.3 Redox flow-cell assembly and assessment

A fuel cell from Pragma Industries was modified into a flow cell, changing bipolar plates and nitrile rubber o-rings; these latter were replaced by PTFE o-rings for compatibility with the non-aqueous solvents. Serpentine flow fields were used in this work and as-received carbon felt (SGL 4.6 EA) were placed on each of the flow fields. A composite membrane was used as a separator between positive and negative half-cells. Teflon gaskets sealed the membranes and electrodes into the cell. Electrodes were compressed to 34 %, providing a final thickness of 3 mm for the electrodes. The flow-cell experiments were performed in a glove box with a dry nitrogen environment, and two Schott GL25 bottles served as reservoirs. The experiments were performed using 25 ml of each positive/negative electrolyte and the flow circuit is shown in Figure 1.9 (b). Impedance measurements were recorded at 20 mV of amplitude and state-of-charge (SOC) of 50 % across the frequency range of 250 kHz to 100 mHz using the Zahner workstation.

7.3 Results and discussions

7.3.1 Electrochemical characterization of electrolyte

The reversibility of the redox ions in the electrolyte is compulsory and crucial for the operation of any NAqRFB. Cyclic voltammetry (CV) - Figure 7.2 - was performed for the non-aqueous electrolytes having acetonitrile as solvent and $TEABF_4$ as supporting electrolyte. The redox couples of Al^{3+}/Al, Cr^{5+}/Cr^{4+}, V^{4+}/V^{3+}, Mn^{4+}/Mn^{3+}, Fc^{+}/Fc, and Fe^{3+}/Fe^{2+} were assessed as negolyte and posolyte for the NAqRFB-cell. The redox species proved to be reversible on a glassy carbon working electrode (GCE) and exhibit redox potentials (*vs.* Ag^{+}/Ag) of -1.7 V, 1.23 V, 0.45 V, 0.7 V, 0.13 V, and - 0.9 V, respectively, as shown in Figure 7.2. The following redox pairs were selected: Al || Cr, Al || V, Al || Mn, Al || Fc, and Al || Fe, with cell potential differences of 2.93 V, 2.15 V, 2.4 V, 1.8 V, and 0.8 V, respectively. The governing half-cell reactions leading to the corresponding cell potentials (E_{CELL}) are given below for the mentioned chemistries in the discharging direction.

Posolyte:

$$[Cr(IV)(acac)_3]^+ + e^- \rightleftharpoons Cr(III)(acac)_3, \quad E_P = 1.23\ V\ vs.\ Ag^+/Ag \tag{7.1}$$

$$[V(IV)(acac)_3]^+ + e^- \rightleftharpoons V(III)(acac)_3, \quad E_P = 0.45\ V\ vs.\ Ag^+/Ag \tag{7.2}$$

$$[Mn(IV)(acac)_3]^+ + e^- \rightleftharpoons Mn(III)(acac)_3, \quad E_P = 0.7\ V\ vs.\ Ag^+/Ag \tag{7.3}$$

$$Fc^+ + e^- \rightleftharpoons Fc, \quad E_P = 0.13\ V\ vs.\ Ag^+/Ag \tag{7.4}$$

$$[Fe(III)(acac)_3]^O + e^- \rightleftharpoons [Fe(II)(acac)_3]^-, \quad E_P = -0.9\ V\ vs.\ Ag^+/Ag \tag{7.5}$$

Negolyte:

$$[Al(III)(acac)_3] + 3e^- \rightleftharpoons Al + 3(acac)^-, E_N = -1.7\ V\ vs.\ Ag^+/Ag \tag{7.6}$$

The diffusion coefficient of the redox reactions highlights the kinetics of the reactions. The Randles-Sevcik plots (i_P *vs.* $v^{1/2}$) – Figure S 11.27 to Figure S 11.31 – shows that the peak currents are a linear function of the square root of the scan rate, which corroborates with the condition of reversibility [163]. Therefore, the Randles-Sevcik model was employed to find the diffusion coefficients, using the following equations (7.7) to (7.9) [173]:

$$i_P = 0.4463 \cdot n \cdot F \cdot A \cdot C^O \cdot \left(\frac{n\,F\,v\,D}{R\,T}\right)^{\frac{1}{2}} \tag{7.7}$$

$$\text{Slope} = \left[0.4463\,n\,F\,A\,C^O\left(\frac{n\,F\,D}{R\,T}\right)^{\frac{1}{2}}\right] \tag{7.8}$$

$$D = \left(\frac{\text{Slope}}{0.4463\,n\,F\,A\,C^O}\right)^2 \frac{R\,T}{n\,F} \tag{7.9}$$

where, i_P is peak current, n is the number of electrons participating in the reaction, A is electrode surface area, C^O is electrolyte concentration, v is scan rate, D is diffusion coefficient, F is Faraday's constant, R is gas constant, T is the temperature. The experiment was performed at 293 K using a glassy carbon working electrode having an area of 0.0707 cm^2.

The solvent and supporting electrolyte are not active in the range from ± 2 V *vs.* Ag^+/Ag. The redox species of Al^{3+}/Al offered the lowest negative potential and feasibility as negolyte. The higher value of the diffusion coefficient - Table 7.1 - points

towards the facile kinetics of the redox reactions. The redox couple of Mn^{4+}/Mn^{3+} offers a diffusion coefficient better than others, followed by V^{4+}/V^{3+}, and Fe^{3+}/Fe^{2+}. The redox species of Cr^{4+}/Cr^{3+} show quasi-reversible kinetics and exhibit different diffusion coefficients for anodic and cathodic processes, *i.e.* 1.33×10^{-5} $cm^2 \cdot s^{-1}$ and 4.36×10^{-8} $cm^2 \cdot s^{-1}$, respectively. The ferrocene (Fc^+/Fc) offers the best reversibility but it has slower kinetics, which makes it unappealing for being used in the NAqRFB.

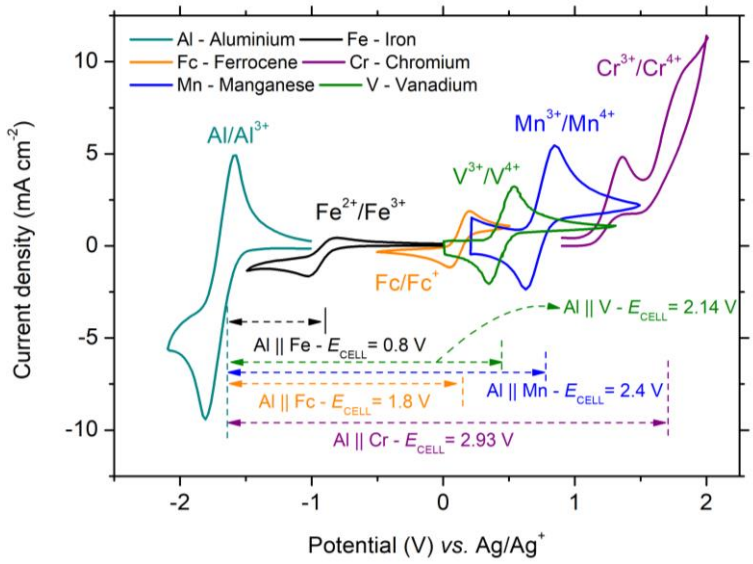


Figure 7.2 Cyclic voltammetric analysis of redox species having respective cell potentials.

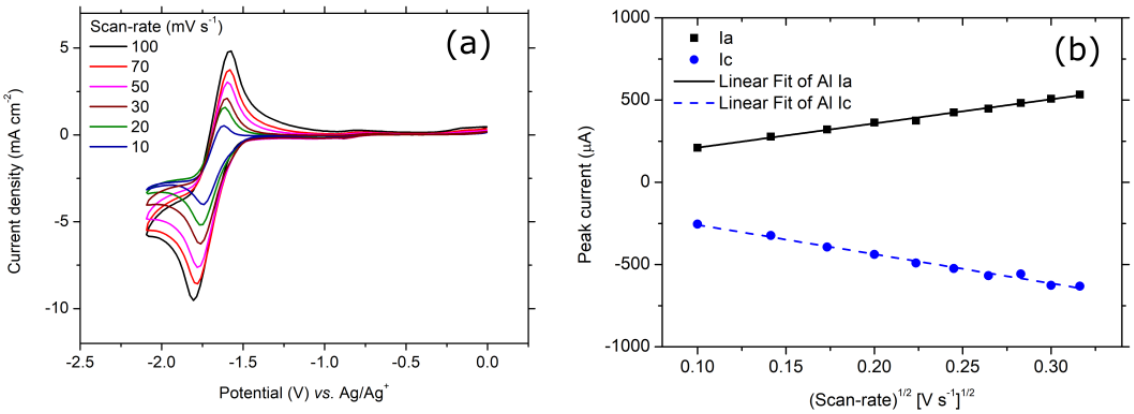


Figure 7.3 Cyclic voltammetry analysis of $Al(acac)_3$ (a) Voltammograms (b) Randles-sevcik plots (i_P vs. $v^{1/2}$) showing reversibility condition.

Table 7.1 Diffusion coefficients of redox couples

Redox Couples	Redox Potentials, E_{REDOX} (V *vs.* Ag^{+}/Ag)	Diffusion Coefficient, D ($cm^2 \cdot s^{-1}$)
Al^{3+}/Al	-1.70	2.92×10^{-6}
Cr^{4+}/Cr^{3+}	1.23	4.36×10^{-8}
V^{4+}/V^{3+}	0.45	4.30×10^{-6}
Mn^{4+}/Mn^{3+}	0.70	4.40×10^{-6}
Fc^{+}/Fc	0.13	9.81×10^{-8}
Fe^{3+}/Fe^{2+}	-0.90	6.81×10^{-6}

7.3.2 Battery cycling performance

The storage capacity of the NAqRFB-cell is related to the concentration of redox species and the volume of the electrolyte used at this concentration. The charging or discharging current should be chosen according to the electrochemical performance of the cell. For a given device, electrochemical cell, and storage volume tanks, it is possible to use parameter C-rate, where C is the theoretical capacity, for comparing the energy performance of different electrolytes. The value of C-rate = 1C, is when the battery is discharged completely in 1 hour (*i.e.* state-of-charge, SOC = 0 %). In this study, all systems were characterized at C-rate = C / 2. The concentration of redox species for negolyte was 0.05 M and 0.15 M for posolyte, which leads to the theoretical capacity of *ca.* 4.02 $Ah \cdot L^{-1}$ for both electrolytes; for comparison, the volumetric capacity of commercial vanadium electrolyte, with a vanadium concentration of 1.6 M, is *ca.* 21.4 $Ah \cdot L^{-1}$.

Each experiment was conducted using fresh electrodes and membranes to isolate the effect of using different electrolytes. Few charge-discharge cycles (CDC) are shown from Figure S 11.32 to Figure S 11.36 and the results are summarized in Table 7.3, for each redox system. The Al || Cr redox system displays the highest cell potential but it offers the lowest energy efficiency, η_{EE} = 37.9 %, which is *ca.* 37 % less than for Al || Fe redox system *i.e.* η_{EE} = 75.6 %. The voltammogram of $Cr(acac)_3$ – Figure S 11.31 – highlights that this redox system displays only a quasi-reversible behavior. Although the highest energy efficiency was offered by Al || Fe, the cell potential difference is the lowest *i.e.* 0.8 V and the storage capacity is also similar to Al || Mn redox system and 30 % lower than Al || V redox system as indicated in Table 7.3.

Electrochemical impedance spectroscopy (EIS) was performed at 50 % state-of-charge and after charge-discharge cycling. The fitting of an equivalent circuit to the impedance plot helps to identify the contribution of each half-cell loaded with different posolytes and negolytes. The interfaces of electrode-electrolyte at the anode and cathode are represented by two RC circuits, using CPEs, as is illustrated in Figure 7.5 (b). The value from the *x-axis* intercept of the Nyquist plot is taken as the series resistance of the cell (R_S), which comprehends the resistances offered by current collectors, bipolar plates, electrodes, and membrane. In the case of Al || Mn cell, it was necessary to add a finite Warburg element to fit the experimental Nyquist plot. The equivalent circuit fits quite accurately the experimental Nyquist plot, as illustrated in Figure 7.5 (a), and the model parameters are shown in Table 7.2. The errors for each parameter are within the 95 % confidence interval and comply with the Chi-squared criteria of less than 1×10^{-3}. The shape of each impedance curve is different which highlights the influence of the redox species.

The series resistance (R_S) of the cells remains within the range of 1.53 ± 0.32 **Ω**, except for Al || Fc cell which has 5.36 **Ω**. *Post-mortem* analysis showed that Nafion HP membrane changed its appearance from transparent to brownish – Figure S 11.37 – which was assigned to the sorption of Fc, making the membrane far less conductive. The high charge transfer impedances also affected the cycle time of the Al || Cr cell because it reached the cut-off potentials in just 10 min, which resulted in the lowest capacity of 1.9 $mAh \cdot g^{-1}$ as per the mass of the redox species Al^{3+}.

7.3.3 Storage capacity fade

Capacity retention is critical for any battery, which should display an acceptable lifetime. Improving capacity retention is a struggling research topic of non-aqueous redox flow batteries. Capacity fade is related to physical mechanisms such as (a) cell leakage; (b) membrane crossover; and chemical mechanisms such as (c) electrolyte degradation, (d) parasitic reactions. The in-house flow cell was optimized to prevent any leakage of the electrolyte but still, there are some losses because of the tendency of acetonitrile-based electrolytes to diffuse through gaskets. This happens slowly and acetonitrile gets evaporated leaving crystalline residues at the edges of the gaskets. A simple test was performed to isolate the effects of leakage by circulating electrolytes across Al || V cell for seven days. Despite this, total volume loss even after seven days of the experiment was insignificant, smaller than 1 cm^3. The capacity loss and performance of the cell went

together, which indicates that there is no benefit of pre-conditioning the cell. It can be concluded that cell leakage is not responsible for the observed capacity fade.

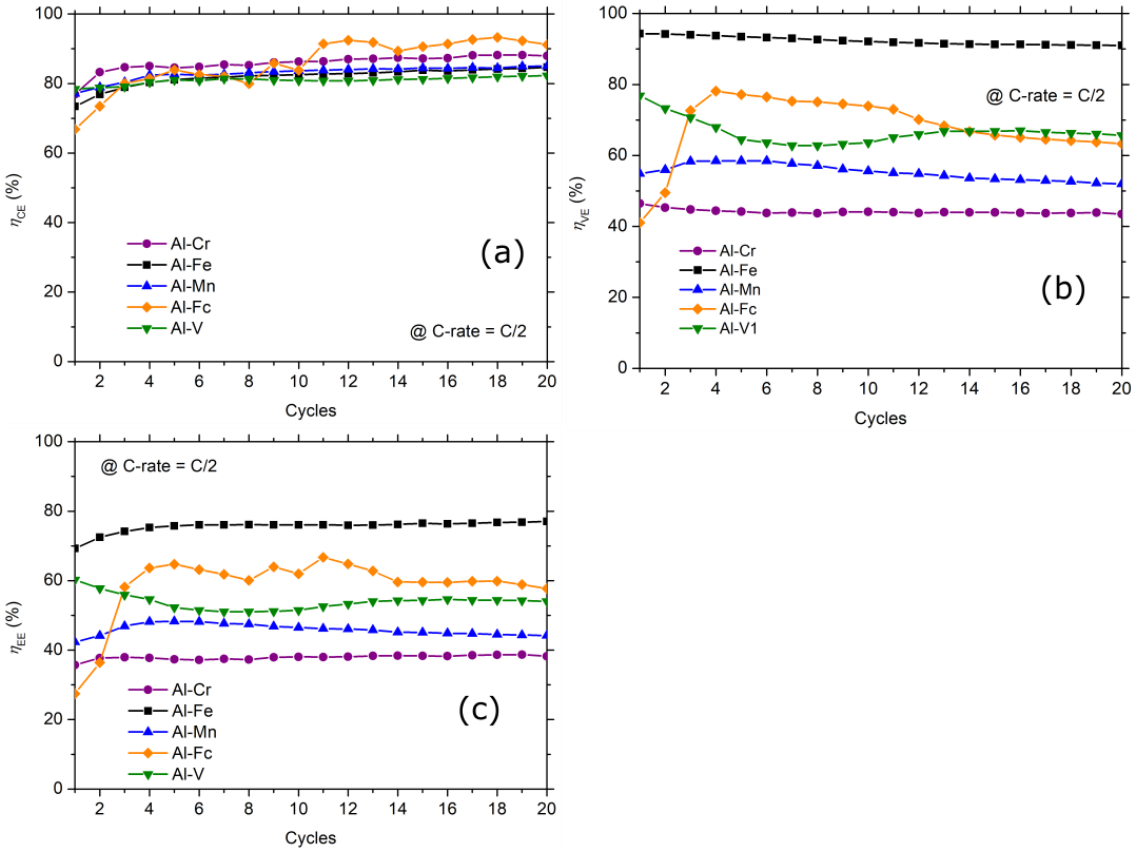


Figure 7.4 Charge-discharge cycling of cells each having negolyte as $Al(acac)_3$ and posolyte of $Cr(acac)_3$, $Fe(acac)_3$, $Mn(acac)_3$, $V(acac)_3$, and Ferrocene. (a) Coulombic efficiency (b) Voltage efficiency (c) Energy efficiency.

Further investigations were performed using cyclic voltammetry, which can provide insights into the electrochemical stability of the electrolyte. The voltammogram of the fresh electrolytes – Figure 7.2 – highlighted that there were no parasitic reactions before (dis)charge cycling. The morphological results by SEM - Figure S 11.39 - highlight that there was no noticeable degradation of the carbon felts after the charge-discharge cycling. Therefore, the most probable reason is the membrane crossover of the redox species. *Post-mortem* voltammograms were obtained for each posolyte and negolyte after performing the charge-discharge cycling in a 3-electrode cell. Glassy carbon was used as a working electrode to qualify the membrane permeation of redox species – Figure 7.7. The voltammograms of the electrolytes of cell Al || Cr are shown in Figure 7.7 (a). The negolyte, which contains Al^{3+} redox species, show no additional peaks at the positive side highlighting that redox species of $Cr^{3+/4+}$ did not permeate the membrane. The negolyte peak A_N^2 / C_N^2 and peak A_P^3 / C_P^3 from posolyte match with the peak at -1.145 V *vs.* Ag/Ag^+

measured from the blank electrolyte – Figure S 11.38. The blank electrolyte contains 0.1 M of $TEABF_4$ in acetonitrile and no redox species. Therefore, the permeation redox species is then small for Al || Cr cell which also displayed the lowest capacity fade of *ca.* 2.36 % per cycle; the performance of the cell is limited by the quasi-reversible kinetics of the chromium-based redox species.

Similarly, for cell Al || V cell the negolyte has no additional peaks other than the peak for Al^{3+}/Al, which indicates that vanadium is not permeating toward the negative side – Figure 7.7 (b). Whereas, the posolyte exhibits peak A_P^3 / C_P^3 related to V^{4+} / V^{3+} at - 1.75 V *vs.* Ag/Ag^+, which do not match with any peak of negolyte. Peaks A_P^2 / C_P^2 and A_N^2 / C_N^2 match with the blank electrolyte - Figure S 11.38. Therefore, the permeation of redox species is not also significant for the Al || V cell and the capacity fade of *ca.* 2 % per cycle. Further investigations highlighted that the posolyte having V^{4+}/V^{3+} is prone to a parasitic reaction with any moisture and/or oxygen present in the system which leads to the capacity fade by forming $VO(acac)_2$ [161].

The unsaturated solutions were used for the electrolyte during this study, so the storage capacity and energy density shown in Figure 7.6 are only based on the concentration of redox species used for the negolyte. It should be noted that maximum storage capacity and maximum energy density offered by these cells should also be determined using the maximum solubility of the redox species in the respective solvent, which will be the scope of future studies.

The voltammograms of cell Al || Mn are mentioned in Figure 7.7 (c). Again, peaks A_P^3 / C_P^3 and A_N^2 / C_N^2 match with the blank electrolyte - Figure S 11.38. Peak A_N^4/ C_N^4 from negolyte matches with peak A_P^1 / C_P^1 from posolyte, which indicates that Al^{3+} is permeating the membrane. On the other hand, there is no peak from posolyte matching with the redox potential of Al/Al^{3+}, indicating that redox species of manganese are not permeating the membrane. The negolyte is showing an additional irreversible peak, A_N^3, near to the 0 V *vs.* Ag/Ag^+, which also matches with peak A_P^2 / C_P^2 of posolyte. This explains the capacity fade of *ca.* 3.1 % per cycle of cell Al || Mn, but the performance stabilizes after the sixth cycle at the value of 29 $mAh \cdot g^{-1}$, similar to that of Al || Fe cell. The voltammograms of cell Al || Fe - Figure 7.7 (e) – show no cross-peaks indicate low crossover; this observation matches with the low fading rate of Al || Fe cell which is *ca.* 2.83 % per cycle.

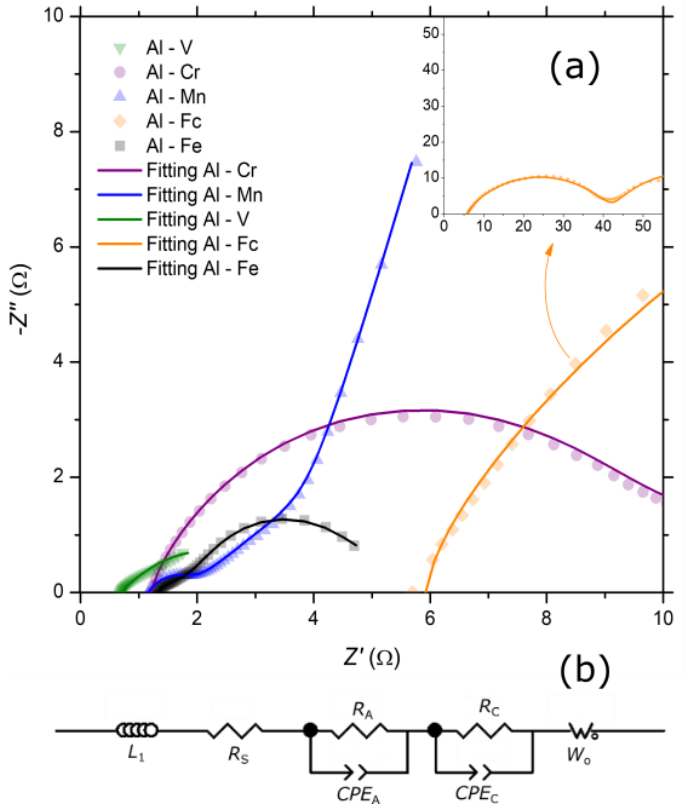


Figure 7.5 Electrochemical impedance spectroscopy measured in the range of 100 mHz to 250 kHz at AC amplitude of 20 mV. (a) Impedance curves (b) Equivalent circuit used for impedance curve fitting.

Table 7.2 Parameters of the equivalent circuit fitted on the impedance curves for each cell.

Elements	Battery types				
	Al || Cr	Al || Mn	Al || V	Al || Fc	Al || Fe
	Fitted parameters				
R_S (Ω)	1.21	1.22	1.85	5.361	1.33
R_A (Ω)	7.77	1.35	3.5	36.96	5.031
C_A (F)	1.3×10^{-5}	1.3×10^{-6}	1.14×10^{-2}	3.2×10^{-6}	2.2×10^{-1}
n_A	0.78	0.68	0.38	0.64	0.7
R_C (Ω)	3.1×10^{1}	3.38×10^{-1}	0.822	36.93	1.952
C_C (F)	1.1	8.39×10^{-3}	3.05×10^{-3}	1.96×10^{-2}	1.14×10^{-2}
n_C	0.27	1	0.77	0.69	0.71
W_{O1} (Ω)	NA	4.3	NA	NA	NA
Chi-Squared (Criteria < 10^{-3})	1.79×10^{-4}	2.41×10^{-4}	5.87×10^{-5}	4.83×10^{-4}	2.95×10^{-5}

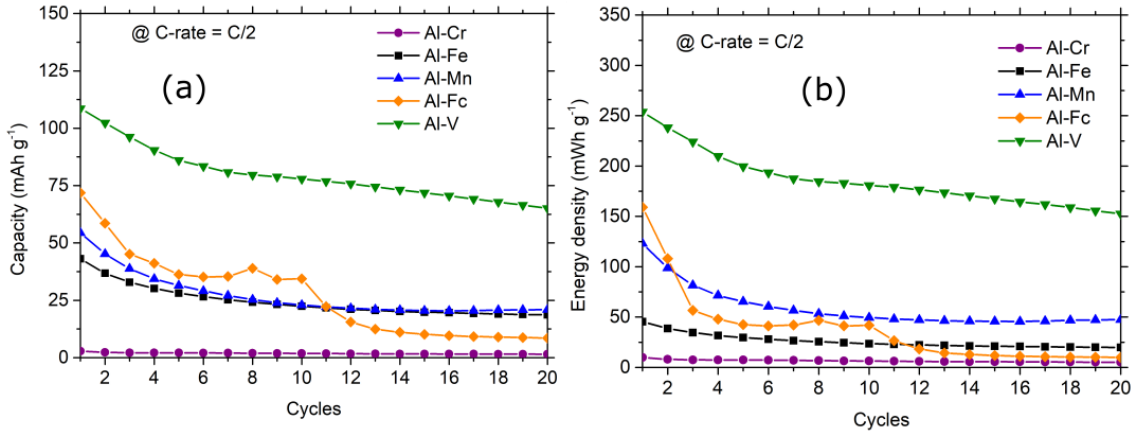


Figure 7.6 NAqRFB-cells having mentioned electrolytes. (a) Capacity and (b) Energy density are calculated using the mass of redox species used for negolyte.

Cell Al || Fc displayed a high storage capacity of 71.8 mAh·g^{-1} during the first cycle but then the capacity faded at *ca.* 4.4 % per cycle, which was the highest fading rate. Peaks A_P^3 / C_P^3 and A_N^2 / C_N^2 match with the blank electrolyte - Figure S 11.38. The voltammogram of the negolyte is not showing any additional peak other than Al/Al^{3+} redox couple, which indicates that Fc is not permeating the membrane. There is also no peak at the posolyte side matching with the redox potential of Al/Al^{3+}, indicating that aluminum is not permeating the membrane. Therefore, the permeation of redox species is small or negligible for cell Al || Fc but the posolyte shows an additional irreversible peak, C_P^2, which may be related to the very high storage fading rate observed for cell Al || Fc.

Table 7.3 Summary of the 20 charge-discharge cycles for each battery type having mentioned posolyte and negolyte.

Type	E_{CELL} (V)	η_{CE} (%)	η_{VE} (%)	η_{EE} (%)	Capacity (mAh·g^{-1})	Energy density (mWh·g^{-1})
Al || Cr	2.93	85.9	44.2	37.9	1.9	6.5
Al || V	2.15	80.9	66.6	53.9	79.8	185.7
Al || Mn	2.4	83.0	55.3	45.9	27.1	58.9
Al || Fc	1.8	85.8	67.9	58.5	27.4	38.1
Al || Fe	0.8	81.9	92.3	75.6	24.6	25.9

Acronyms: E_{CELL} = Cell potential; η_{CE} = Coulombic efficiency; η_{VE} = Voltage efficiency; η_{EE} = Energy efficiency; Capacity and energy density are calculated using the mass of redox species Al^{3+} and for unsaturated solutions.

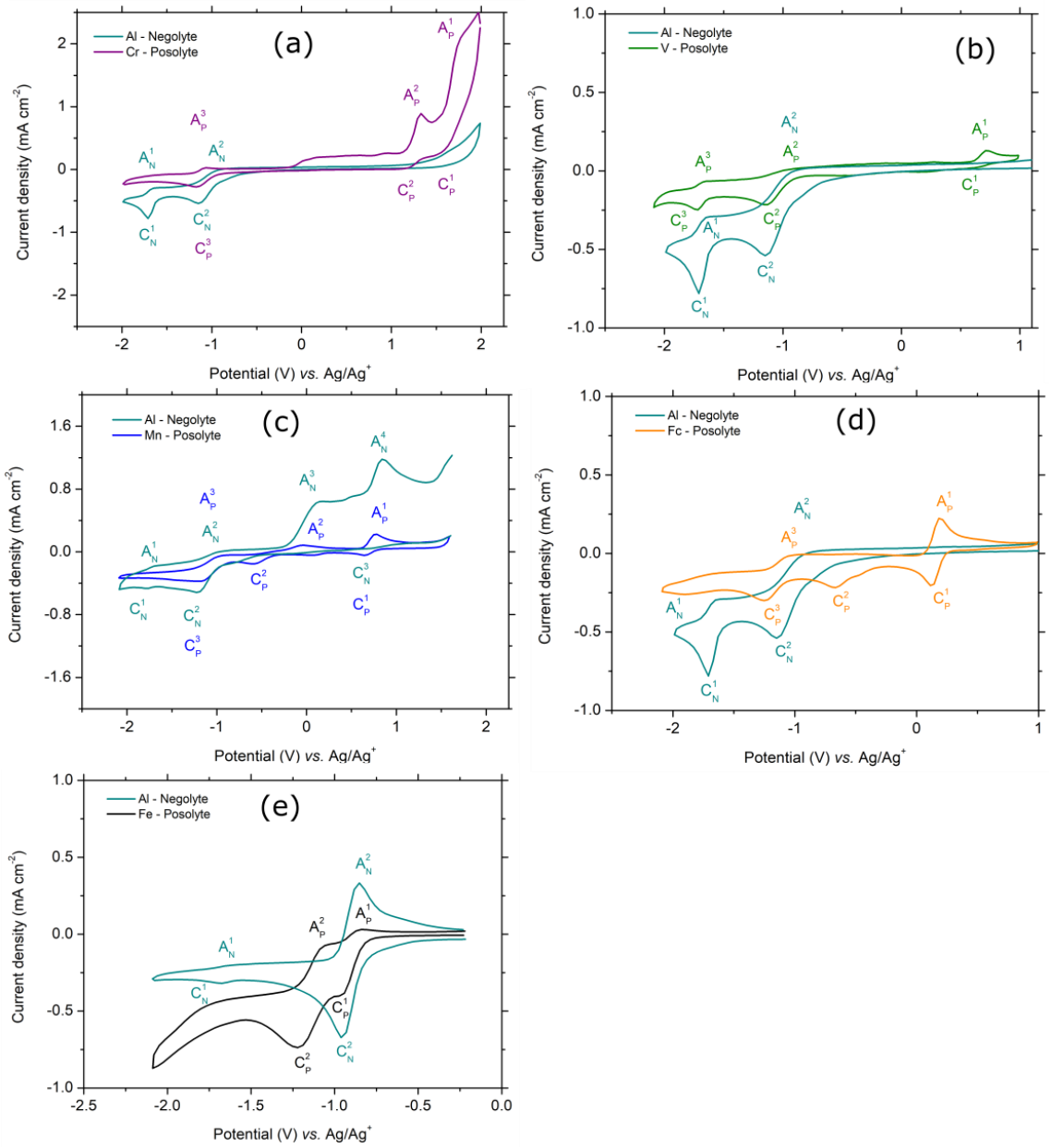


Figure 7.7 Voltammograms taken after charge/discharge cycling for the NAqRFB-cells having mentioned negolytes and posolytes. (a) Al || Cr (b) Al || V (c) Al || Mn (d) Al || Fc (e) Al|| Fe.

7.4 Conclusion

The aluminum-based non-aqueous redox flow cell was introduced in this study as a proof-of-concept. The aluminum redox was used as negolyte coupled with a posolyte based on the redox ions of metal acetylacetonates M(acac), where, M = Chromium (Cr), Vanadium (V), Manganese (Mn), Iron (Fe), and Ferrocene (Fc). The new chemistries for NAqRFBs are Al || Cr, Al || V, Al || Mn, Al || Fc, and Al || Fe with cell potential differences of 2.93 V, 2.15 V, 2.4 V, 1.8 V, and 0.8 V, respectively. At the maximum

solubility of 0.2 M for $Al(acac)_3$ in Acetonitrile can offer batteries having energy density of Al||Cr = 47.1 $Wh \cdot L^{-1}$, Al || V = 34.5 $Wh \cdot L^{-1}$, Al || Mn = 38.6 $Wh \cdot L^{-1}$, Al || Fc = 14.5 $Wh \cdot L^{-1}$, and Al || Fe = 6.4 $Wh \cdot L^{-1}$. These values can be increased further by using Al^{3+}- ion having higher solubility.

A composite membrane, made of two layers of microporous separator Celgard C4560 and one ion-exchange membrane Nafion HP, displaying a reduced permeability to redox species Al^{3+}, was used in this work. Cells Al || V and Al || Mn exhibited the most promising performance. These cells offered cell potentials of 2.15 V and 2.4 V, respectively; which is 34 % and 50 % higher potential than the aqueous commercial all-vanadium aqueous RFB. Cell Al || Cr displayed 83.1 % higher potential than all-vanadium aqueous RFB.

Cell Al || V displayed a current efficiency of η_{CE} = 81 %, an energy density of 185.7 $Wh \cdot kg^{-1}$, and storage capacity of 79.8 $mAh \cdot g^{-1}$, based on the mass of redox species used for unsaturated negolyte. This cell displayed a limiting current density of 46 $mA \cdot cm^{-2}$. This chemistry showed a voltage efficiency of η_{VE} = 67 % and energy efficiency of η_{EE} = 54 %, indicating high ohmic losses, especially in the membrane. Furthermore, the Al || Mn cell demonstrated a stable performance up to 50 cycles and the second-highest energy density of *ca.* 60 $mWh \cdot g^{-1}$ (based on the mass of aluminum at the unsaturated negolyte). Future studies are in progress for increasing the energy density of the most promising cells – Al || V and Al || Mn, based on the volume of saturated electrolyte.

Blank Page

Chapter 8

Bio-inspired eco-friendly negolyte

8. Bio-inspired eco-friendly negolyte

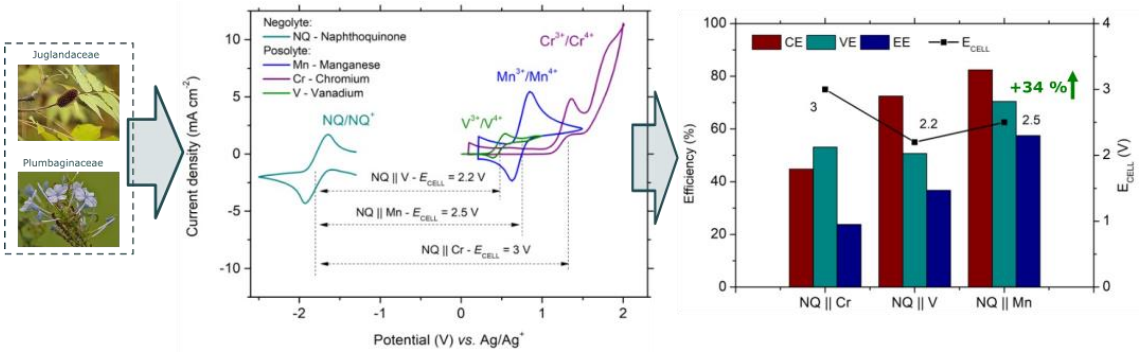
Adapted from the following articles:

K. Mushtaq, A. Mendes, "Step toward eco-friendly green source of non-aqueous electrolytes for redox flow battery", 240th ECS Meeting (October 10-14, 2021), Digital Meeting, USA.
Link: https://ecs.confex.com/ecs/240/meetingapp.cgi/Paper/153625

Márcia S. Santos, Luciana Peixoto, K. Mushtaq, et. al., "Bioelectrochemical energy storage in a Microbial Redox Flow Cell", Journal of Energy Storage, Volume 39, July 2021, 102610, Elsevier.
Link: https://www.sciencedirect.com/science/article/pii/S2352152X21003522.

Redox flow battery (RFB) technology is one of the promising candidates for large-scale grid systems. Present commercial RFB technology is based on redox reactions of electroactive metal-based species, which are constrained by abundance, cost, and environmental issues. These challenges are prompting scientists to look into organic-based technologies as an alternative. On the other hand, water electrochemical window is *ca.* 1.6 V, which limits the energy density of these devices. For working beyond this limit, the use of non-aqueous electrolytes is required, the so-called non-aqueous RFB (NAqRFB). Among the organic-based redox species, quinones and anthraquinones have been demonstrating great potential as negolyte in NAqRFB due to their great stability and low environmental impact. Among all the reported quinones with potential for being used in NAqRFB, 1,4 naphthoquinone (NQ) has not been properly addressed. This work studies NQ redox ion as negolyte coupled with metal acetylacetonates, M(acac), where, M = Chromium (Cr), Vanadium (V), Manganese (Mn), as posolytes. NQ || Mn cell offered a performance of η_{EE} = 57.5 % and reached a limiting current density of 6.7 mA·cm^{-2} for a cell having only 0.06 M of the redox species. Furthermore, NQ || Cr cell demonstrated a stable performance up to 20 cycles and the energy capacity of *ca.* 63.6 mWh and capacity fade is negligible.

Graphical Abstract



8.1 Introduction

The efficient utilization of energy from non-exhaustive resources without adverse effects on the environment is the only pathway for sustainable development. The intermittent nature of renewable energy sources such as sunlight and wind requires a large-scale energy storage system to mitigate the intermittency noise in the power grid. Redox flow battery (RFB) technology is one of the promising candidates for large-scale grid systems. Commercial RFBs are based on the redox reactions of electroactive metals, which are constrained by material abundance, cost, and environmental issues. These issues are prompting scientists to look into organic-based technologies as potential metal-free battery alternatives. Organic-based materials offer structural diversity of organic molecules to adjust the electrolyte materials' thermodynamics and redox characteristics, in addition to low cost and scalability. This opens the door to the development of green and sustainable energy storage devices.

The electrochemical potential operating window for the water remains within 1.6 V and operating beyond this operational limit destabilizes the system unless the water is replaced with some alternate organic solvents. The scientific community addressed this issue by introducing the non-aqueous RFB (NAqRFB). This technology opens the window of using redox species outside the electrochemical stability range of aqueous electrolytes. An ideal redox species should be i) abundant; ii) cheap; iii) provide fast multiple electron transfer per reacting molecule; iv) high solubility in the chosen solvent, and v) possess reversible kinetics.

Quinones is the most redox-active moieties found in natural organic materials, and they play a critical role in biological electron transport [196–198]. They are a class of molecules that are formed from aromatic compounds like benzene or naphthalene and have a fully conjugated cyclic diketone structure with a redox reaction based on the rearrangement of the conjugated double bond. A series of quinones such as 1,4-benzoquinone (BQ), 1,4-naphthoquinone (NQ), 9,10-phenanthrenequinone (PQ), anthraquinone (AQ), and 5,12-naphthace-nequinone (NAQ) were investigated elsewhere [199], to study the relationship between their molecular structures and electrochemical properties. AQ [200] is getting attention to be used as an organic alternative for aqueous-based RFB but it has less solubility for non-aqueous electrolytes of acetonitrile or dimethylacetamide. Whereas, 1,4-naphthoquinone (NQ) exhibited good solubility and

possess good electrochemical characteristics, which make it an attractive candidate for a bio-inspired eco-friendly negolyte [199].

"Naturally occurring 1,4-naphthoquinones are widely distributed in nature, especially in several families of plants such as Plumbaginaceae, Juglandaceae, Ebenaceae, Boraginaceae, Dioncophyllaceae, Ancistrocladaceae, Iridaceae, Verbenaceae, Scrophulariaceae, Avicenniaceae, Balsaminaceae, Bignoniaceae, Gentianaceae, and Droseraceae, and in addition also being present in algae, fungi, some animals, and products of metabolism in some bacteria" [201]. Plumbagin (5-hydroxy-2-methyl-1,4-naphthoquinone) is a bioactive chemical found in Indian and Chinese medicinal plants belonging to the Plumbaginaceae, Droseraceae, and Ebenaceae families [202]. Plumbagin is usually isolated from plant material by solvent extraction of coarsely powdered roots with increasing polarity solvents using a cold percolation process [203]. The methods of plant cell culture have been used in recent years to boost its yield due to its medicinal relevance. The early development of plumbagin-rich tuberous roots has a great deal of potential for plant cultivation through commercial horticulture [204].

The term "vitamin K" represents a set of molecules that share a 2-methyl-1,4-naphthoquinone ring structure but differ in the length and saturation of their isoprenoid side chains. NQ has high natural abundance, wide availability, ease of processing (including recycling), low cost, and high value of negative redox potential, -1.75 V *vs.* Ag/Ag^{+}. NQ-based batteries can compete with existing cell electrochemistry for both primary (non-rechargeable) and secondary (rechargeable) applications. The concept of rechargeable quinone-based batteries has the potential to share the realm of batteries for large-scale applications.

Many of the research on organic redox species that have been published conclude with claims of high energy density materials and/or effective demonstrations of the technology. However, such assertions have almost always overlooked the full implementation of the stated chemistry in practical cells. As per the author's information, the use of 1,4 Naphtoquinone ions for redox flow batteries was rarely addressed. Therefore, an NQ-ion-based non-aqueous redox flow battery was introduced in this study as a proof-of-concept. The NQ redox ion is used as negolyte coupled with the posolyte based on the redox ions of metal acetylacetonates: M(acac), where, M = Chromium (Cr), Vanadium (V), Manganese (Mn). The theoretical energy capacity offered by each cell NQ || Cr, NQ || Mn, and NQ || V based on the thermodynamic solubility of 1 M of NQ in DMA [199] is 80.4 $Wh \cdot L^{-1}$, 67 $Wh \cdot L^{-1}$, and 59 $Wh \cdot L^{-1}$, respectively.

8.2 Experimental Methods

8.2.1 Materials

Tetraethylammonium tetrafluoroborate, $TEABF_4$, was acquired from Alfa Aesar, N, N - Dimethylacetamide (DMA), 99 %, was acquired from Sigma Aldrich and used without further purification as supporting electrolyte and solvent, respectively. Vanadium(III) acetylacetonate, $V(acac)_3$, 97 %, was acquired from Strem Chemicals; Chromium (III) acetylacetonate, $Cr(acac)_3$; manganese acetylacetonate, $Mn(acac)_3$; 1,4 - Naphtoquinone 97 %, NQ, were acquired from Alfa Aesar. A membrane consisting of a sandwich of commercial membranes Celgard 4560 | Nafion HP | Celgard 4560 was used in all experiments [40]. The electrodes were purchased from Sigracell, SGL Carbon, having a thickness of 4.6 mm.

8.2.2 Cyclic Voltammetry

Voltammograms were measured using a glassy carbon electrode (GC, Metrohm), as a working electrode, in a 50 ml three-electrode cell configuration. The voltammetry studies were performed using the electrolytes consisting of DMA + $TEABF_4$ 0.1 M + redox species 0.02 M. Electrode Biologic RE-7, filled with 0.01 M $AgNO_3$ + 0.1 M TBAP + Acetonitrile, was used as reference electrode. Platinum wire served as a counter-electrode. All experiments were performed under a nitrogen atmosphere. Zahner Zennium potentiostat was used to record all the data, and Thales software was used for the voltammograms measurements.

8.2.3 Redox flow-cell assembly and assessment

An in-house-made flow cell was used for experimental testing of the cell. It was a modified version of the fuel cell from Pragma Industries. The wider channels of flow field were introduced to facilitate the liquid flow and all of the nitrile rubber components were replaced by PTFE material for compatibility with the non-aqueous solvent. Serpentine flow fields were used in this work and carbon felt electrodes were placed on each of the flow fields. A composite membrane was used as a separator between positive and negative half-cells. Teflon gaskets were used to seal the membrane-electrode assembly (MEA). Electrodes were compressed to 34 %, providing a final thickness of 3 mm. The experiments were performed in a glove box with a dry nitrogen environment, and two Schott GL25 bottles served as reservoirs. The volume of 25 ml was used for each posolyte / negolyte and the flow circuit is shown in Figure 1.9. Impedance measurements

were recorded at 20 mV of AC amplitude and state-of-charge (SOC) of 50 % across the frequency range of 250 kHz to 100 mHz using the Zahner workstation. Potentiostatic measurements were performed to acquire polarization data at the scan rate of 20 mV s^{-1}.

8.3 Results and discussions

8.3.1 Electrochemical characterization of electrolyte

The reversibility of the redox ions in the electrolyte is crucial for the operation of any NAqRFB. Cyclic voltammetry (CV) - Figure 8.1 - was performed for the non-aqueous electrolytes having DMA as solvent and $TEABF_4$ as supporting electrolyte. The redox couples of NQ^+/NQ, Cr^{4+}/Cr^{3+}, V^{4+}/V^{3+}, and Mn^{4+}/Mn^{3+} were assessed as negolyte and posolyte. The redox species are reversible on a glassy carbon working electrode (GCE) and exhibit the redox potentials (*vs.* Ag/Ag^+) of -1.75 V, 1.23 V, 0.45 V, and 0.7 V, respectively. The redox species were paired into the cells having electrochemistry of NQ || Cr, NQ || Mn, and NQ || V , which results in the cell potential differences (E_{CELL}) of *ca.* 3 V, 2.5 V, and 2.2 V , respectively. The governing half-cell reactions in the discharging direction are given below.

Posolyte:

$$[Cr(IV)(acac)_3]^+ + e^- \rightleftharpoons Cr(III)(acac)_3, \qquad E_P = 1.23\ V\ vs.\ Ag^+/Ag \qquad (8.1)$$

$$[V(IV)(acac)_3]^+ + e^- \rightleftharpoons V(III)(acac)_3, \qquad E_P = 0.45\ V\ vs.\ Ag^+/Ag \qquad (8.2)$$

$$[Mn(IV)(acac)_3]^+ + e^- \rightleftharpoons Mn(III)(acac)_3, \qquad E_P = 0.7\ V\ vs.\ Ag^+/Ag \qquad (8.3)$$

Negolyte:

$$NQ^+ + e^- \rightleftharpoons NQ, \qquad E_N = -1.75\ V\ vs.\ Ag/Ag^+ \qquad (8.4)$$

The diffusion coefficient of the redox reactions highlights the kinetics of the reactions. The Randles-Sevcik plots (i_P *vs.* $v^{1/2}$) – Figure 8.2 to Figure 8.5 – shows that the peak currents are a linear function of the square root of the scan rate, which corroborates with the condition of reversibility [163]. Therefore, the Randles-Sevcik model was employed to find the diffusion coefficients, using the following equations [173]:

$$i_P = 0.4463\ n\ F\ A\ C^O \left(\frac{n\ F\ v\ D}{R\ T}\right)^{\frac{1}{2}} \qquad (8.5)$$

$$\text{Slope} = \left[0.4463\, n\, F\, A\, C^{O} \left(\frac{n\, F\, D}{R\, T}\right)^{\frac{1}{2}}\right] \tag{8.6}$$

$$D = \left(\frac{\text{Slope}}{0.4463\, n\, F\, A\, C^{O}}\right)^{2} \frac{R\, T}{n\, F} \tag{8.7}$$

where, i_P is peak current, n is the number of electrons participating in the reaction, A is electrode surface area, C^O is electrolyte concentration, v is scan rate, D is diffusion coefficient, F is Faraday's constant, R is gas constant, T is the temperature (K). The experiment was performed at 293 K using a glassy carbon working electrode having an area of 0.0707 cm^2.

The solvent and supporting electrolyte are not active in the range from ± 2 V *vs.* Ag^+/Ag. The redox species 1,4-Naphthoquinone have two redox couples of NQ offering - 1.75 V *vs.* Ag^+/Ag and - 0.93 V *vs.* Ag^+/Ag and feasible to be used as negolyte. Both redox couples are reversible and have a good value of the diffusion coefficient - Table 8.1 - pointing towards the facile kinetics of the redox reactions.

Table 8.1 Diffusion coefficients of redox couples

Redox Couples	Redox Potentials, E_{REDOX} (V *vs.* Ag/Ag^+)	Diffusion Coefficient, D_A ($cm^2 \cdot s^{-1}$)	Kinetics
NQ^+/NQ	-1.75	2.45×10^{-6}	Reversible
NQ^{2+}/NQ^+	-0.93	2.45×10^{-6}	Reversible
Cr^{4+}/Cr^{3+}	1.23	3.34×10^{-6}	Quasi-reversible
V^{4+}/V^{3+}	0.45	6.13×10^{-7}	Reversible
Mn^{4+}/Mn^{3+}	0.75	1.70×10^{-7}	Reversible
Mn^{3+}/Mn^{2+}	-0.40	1.70×10^{-7}	Quasi-reversible

Manganese acetylacetonate also offers two redox couples, which are indicated in Figure 8.5 (a), labeled as A1/C1 for Mn^{3+}/Mn^{2+} at -0.4 V *vs.* Ag/Ag^+ and labeled as A3/C3 for Mn^{4+}/Mn^{3+} at 0.75 V *vs.* Ag/Ag^+ and have similar values like it is reported elsewhere [205]. There is also one additional peak labeled as A2/C2 having a redox potential of *ca.* - 0.083 V *vs.* Ag/Ag^+, which was also observed by Sleightholme [205] and was assigned to the presence of H_2O as contamination. Since the cyclic voltammetry was performed at very low concentrations, the effect of any contamination will also be appeared as significant. Further investigations are important to identify the origin of this peak but it

was not considered parasitic because of the reversible behavior of this ambiguous redox couple.

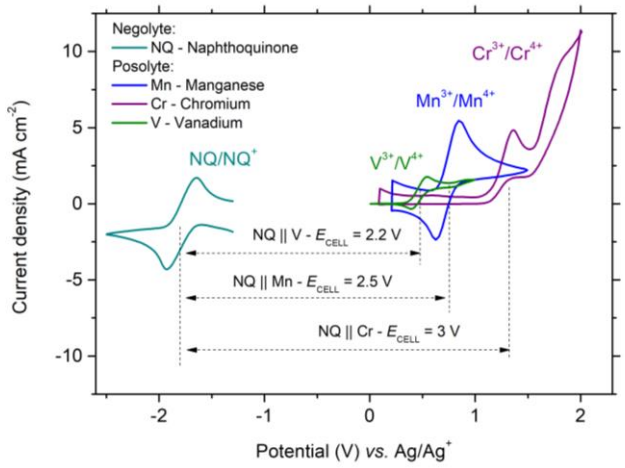


Figure 8.1 Cyclic voltammograms of the redox species having respective cell potentials.

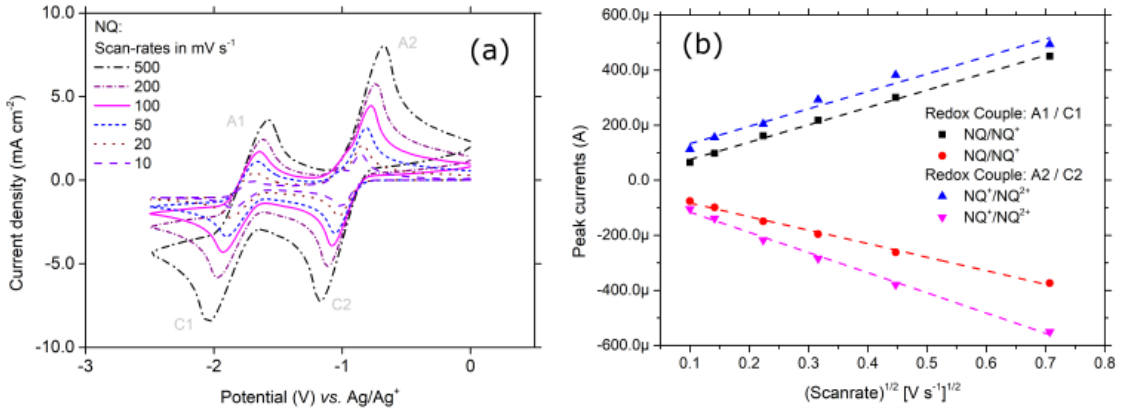


Figure 8.2 Cyclic voltammetry analysis of 1,4-Naphthoquinone (a) Voltammograms (b) Randles-sevcik plots (i_P vs. $v^{1/2}$) showing the linear relationship for the condition of kinetic reversibility.

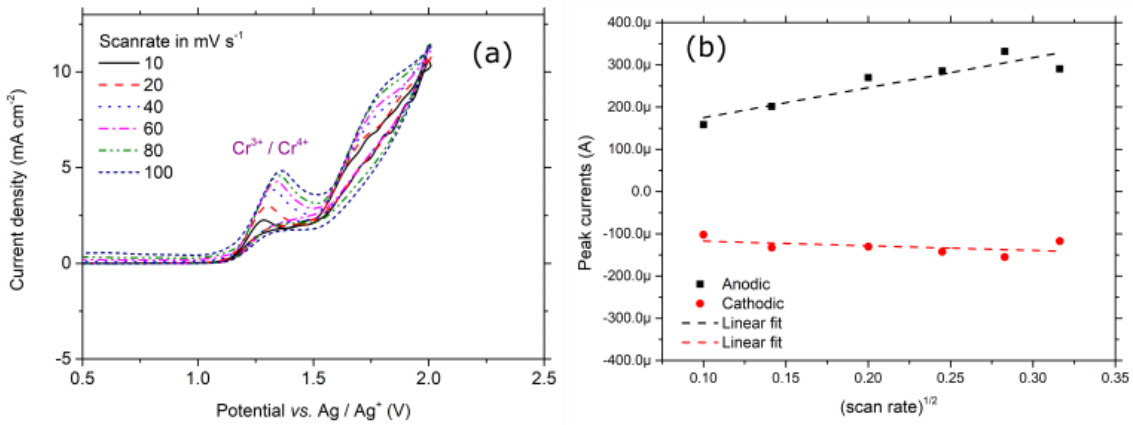


Figure 8.3 Cyclic voltammetry analysis of Chromium acetylacetonate. (a) Voltammograms (b) Randles-sevcik plots (i_P vs. $v^{1/2}$) showing the linear relationship for the condition of kinetic reversibility.

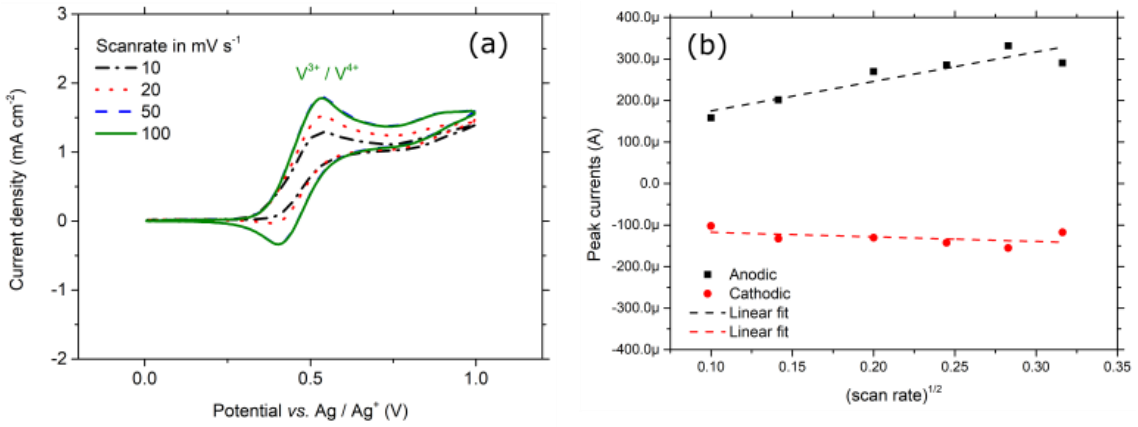


Figure 8.4 Cyclic voltammetry analysis of Vanadium acetylacetonate. (a) Voltammograms (b) Randles-sevcik plots (i_P vs. $v^{1/2}$) showing the linear relationship for the condition of kinetic reversibility.

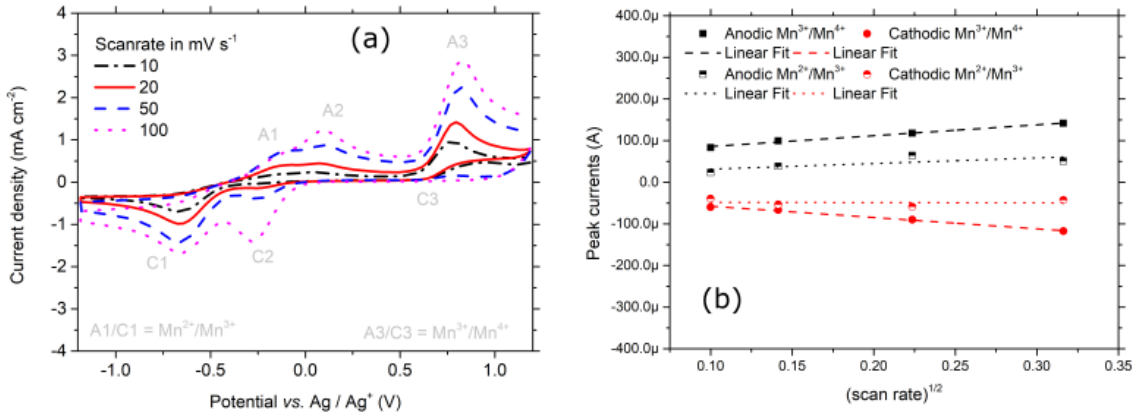


Figure 8.5 Cyclic voltammetry analysis of Manganese acetylacetonate. (a) Voltammograms (b) Randles-sevcik plots (i_P vs. $v^{1/2}$) showing the linear relationship for the condition of kinetic reversibility.

8.3.2 Battery cycling performance

The storage capacity of the cell is proportional to the redox species concentration and the volume of the electrolyte employed at that concentration. The charging or discharging current should be determined by the electrochemical performance of the cell. Charge-discharge cycling (CDC) was performed at 1.4 mA·cm^{-2}, which corresponds to C-rate = C / 5. The same concentration of 0.06 M of redox species was used for negolyte and posolyte to keep the similar theoretical storage capacity of 40.2 mAh. Each experiment was performed using fresh electrodes and membranes to isolate the effect of using different electrolytes. The fifty hours extract of charge-discharge cycles are shown from Figure S 11.40 to Figure S 11.42 and results are summarized in Table 8.4. Cell NQ || Cr has the highest cell potential but it offers the lowest energy efficiency of

η_{EE} = 23.8 %, which is *ca.* 33.7 % less than cell NQ || Mn which has an energy efficiency of *ca.* η_{EE} = 57.5 %. The voltammogram of $Cr(acac)_3$ - Figure 8.3 - highlights that the redox reaction is quasi-reversible, which is also evident through lowest coulombic efficiency of the cell.

Electrochemical impedance spectroscopy (EIS) was performed at 50 % state-of-charge and after charge-discharge cycling. The fitting of an equivalent circuit on the impedance curves helped to identify the contribution of each half-cell having different posolytes and negolytes. The interfaces of electrode-electrolyte at the anode and cathode are represented by two RC circuits, using constant phase elements (CPEs), as is illustrated in Figure 8.7 (b). There was a good fit of the equivalent circuit to the individual impedance curves as shown in Figure 8.7 (a). The parameters used in the equivalent circuit model were determined with good accuracy as illustrated in Table 8.3. The errors for each parameter are within the 95 % confidence interval and comply with the Chi-squared criteria of less than 1×10^{-3}. The value from the *x-axis* intercept of the Nyquist plot for high frequencies was taken as the series resistance of the cell (R_S), which comprehends the resistances offered by current collectors, bipolar plates, electrodes, and membrane of the cell. The trajectory of each impedance curve is different which highlights the influence of the redox species. The polarization response of a redox flow battery highlights the sources of overpotentials and helps to identify the causes of performance loss. In general, the potential drop is associated with (a) activation overpotential; (b) ohmic losses associated with contact and charge transport resistances; and (c) mass transfer limiting currents [206].

The series resistance (R_S) of the cells NQ || Cr and NQ || V was in the range of 3.605 ± 0.075 **Ω**, except 35 % less for cell NQ || Mn. Impedance curves taken from EIS measurements were plotted as (–)Nyquist plots. For a current density of *ca.* 1.4 mA cm^{-2}, the ohmic losses derived from the series resistance are highlighted in Figure S 11.43 and summarized in Table 8.2. The cell NQ || Cr exhibits the highest ohmic losses of 47.5 mV, followed by NQ || V and NQ || Mn with 42.4 mV and 23 mV, respectively. The polarization curve of each cell is shown in Figure 8.6 (f). Below 0.7 V, cell NQ || Mn is already in the starvation phase with a limiting current density of 7.7 $mA \cdot cm^{-2}$, and it is 46.8 % higher in value than NQ || Cr cell.

Table 8.2 Polarisation analysis for each cell indicating current density at the flow-limiting condition and ohmic losses at 1.4 mA·cm^{-2}.

Type	Limiting current density ($mA \cdot cm^{-2}$)	Ohmic losses (η_O) (mV)
NQ || Cr	5.86	47.5
NQ || V	5.34	42.4
NQ || Mn	6.70	23

Table 8.3 Parameters of the equivalent circuit from Figure 8.7 (b) fitted on the impedance curves of Figure 8.7 (a) for each type of NAqRFB-cell.

Elements	Battery types		
	NQ || Cr	NQ || Mn	NQ || V
	Fitted parameters		
L_1 (mH)	4.37×10^{-4}	5.13×10^{-4}	3.23×10^{-4}
R_S (Ω)	3.53	2.345	3.68
R_A (Ω)	40.01	11.41	26.47
C_A (F)	1.0×10^{-2}	1.34×10^{-3}	1.51×10^{-3}
R_C (Ω)	285.4	35.82	96.61
C_C (F)	1.36×10^{-2}	1.10×10^{-2}	1.68×10^{-2}
Chi-Squared (Criteria < 10^{-3})	5.21×10^{-4}	6.63×10^{-4}	4.15×10^{-4}
	Impedance analysis using RC-circuit elements		
$\lvert Z_{RC,\,A}\rvert$ (Ω)	0.795×10^{-3}	5.93×10^{-3}	5.23×10^{-3}
$\lvert Z_{RC,\,C}\rvert$ (Ω)	1.17	1.446	0.947
$\lvert Z_{CELL}\rvert$ (Ω)	4.70	3.796	4.632

8.3.3 Storage capacity fade

Any battery that is expected to last an acceptable lifetime must retain its capacity. Improving the capacity retention of non-aqueous redox flow batteries is a challenging research topic. Physical mechanisms such as cell leakage and membrane crossover, as well as chemical ones such as cell degradation and parasitic reactions, can cause capacity fading. Although the in-house flow cell was modified to avoid any electrolyte leakage, there are still considerable losses due to the ability of DMA-based electrolytes to permeate through gaskets. A simple test was performed to identify the effect of leakage by flowing electrolytes across the NQ || Cr cell for seven days. Despite this, even after seven days of testing, the total volume loss was negligible, *i.e.* less than 0.5 cm^3. The capacity loss and

performance of the cell were identical, indicating that pre-conditioning the cell has no benefit. This concludes that the observed capacity fading was not due to cell leakage.

The unsaturated solutions were used for the electrolyte during this study, so the storage capacity and energy density shown in Figure 8.6 (d, e) are only based on the concentration of redox species used for the negolyte. It should be noted that maximum storage capacity and maximum energy density offered by these cells should also be determined using the maximum solubility of the redox species in the respective solvent, which will be the scope of future studies.

The cell NQ || Cr displayed negligible loss in storage capacity as shown in Figure 8.6 (d, e). However, the cells NQ || V and NQ || Mn displayed capacity fade after 14 and 6 cycles, respectively. The voltammogram of the fresh electrolytes – Figure 8.1 – highlighted that there were no parasitic reactions before (dis)charge cycling. The morphological results though SEM - Figure S 11.45 - highlights that there is no noticeable degradation in the carbon felts after charge-discharge cycling. Therefore, the most probable reason for capacity fade is the membrane crossover of redox species.

The cyclic voltammetry can be used as a diagnostic tool to find out the permeation of redox species through the membrane. This crossover of redox species can be the main contributor to the observed storage capacity fade as shown in Figure 7.6 (d, e). *Post-mortem* voltammograms were measured using a 3-electrode cell for each posolyte and negolyte using the samples taken after the charge-discharge cycling.

The voltammogram of the RFB equipped with electrolytes of NQ || V and NQ || Mn are shown in Figure 8.8 (a) and (b). The peak labelled as A_P^1 / C_P^1 is matching with voltammogram – Figure S 11.44 – of blank electrolyte ($TEABF_4$ + DMA), *i.e.* without any redox species. From Figure 8.8 (a), the negolyte peak labelled as A_N^2 / C_N^2 is matching with the peak of V^{4+}/V^{3+} at 0.45 V *vs.* Ag/Ag^+, however there is no peak of posolyte matching with redox potential of NQ/NQ^+. This indicates that vanadium ion crossed the membrane which results in the capacity loss of 18 % from the initial capacity of 83.25 $mAh \cdot g^{-1}$ or 20 mAh. Further research revealed that the posolyte containing V^{4+}/V^{3+} is susceptible to a parasitic reaction with any moisture and/or oxygen present in the system, resulting in capacity fade via the formation of $VO(acac)_2$ [161]. From Figure 8.8 (b), the negolyte is showing additional peaks other than the NQ^+/NQ labelled as A_N^2 / C_N^2, A_N^3 / C_N^3, and A_N^4 / C_N^4, which are matching with the redox potentials of manganese redox couples. Also, the posolyte exhibit only one peak labelled as A_P^1 / C_P^1,

which is relavant to blank electrolyte. Therefore, the cell equipped with the electrolytes of NQ || Mn exhibit higher loss in capacity upto 47 % from its initial capcity of 83.25 mAh·g^{-1} or 20 mAh.

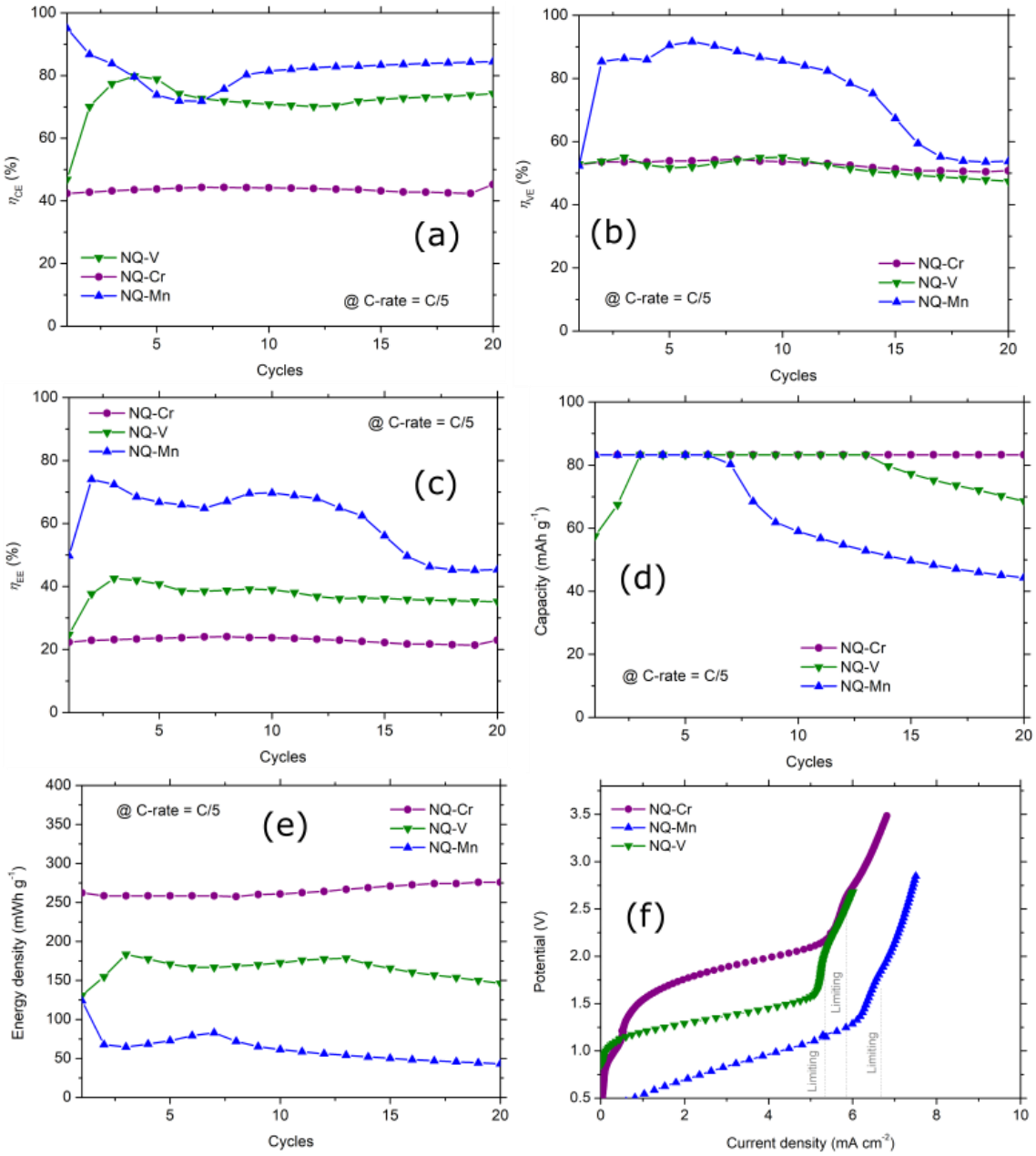


Figure 8.6 Charge-discharge cycling of cells each having negolyte as NQ and posolyte of $Cr(acac)_3$, $Mn(acac)_3$, and $V(acac)_3$. (a) Coulombic efficiency, (b) Voltage efficiency, (c) Energy efficiency, (d) Capacity, (e) Energy density were calculated using the mass of redox species used for negolyte i.e. NQ, and (f) Polarization response indicating limiting current density of the cells having 0.06 M concentration and flow rate of 30 ml·min^{-1}.

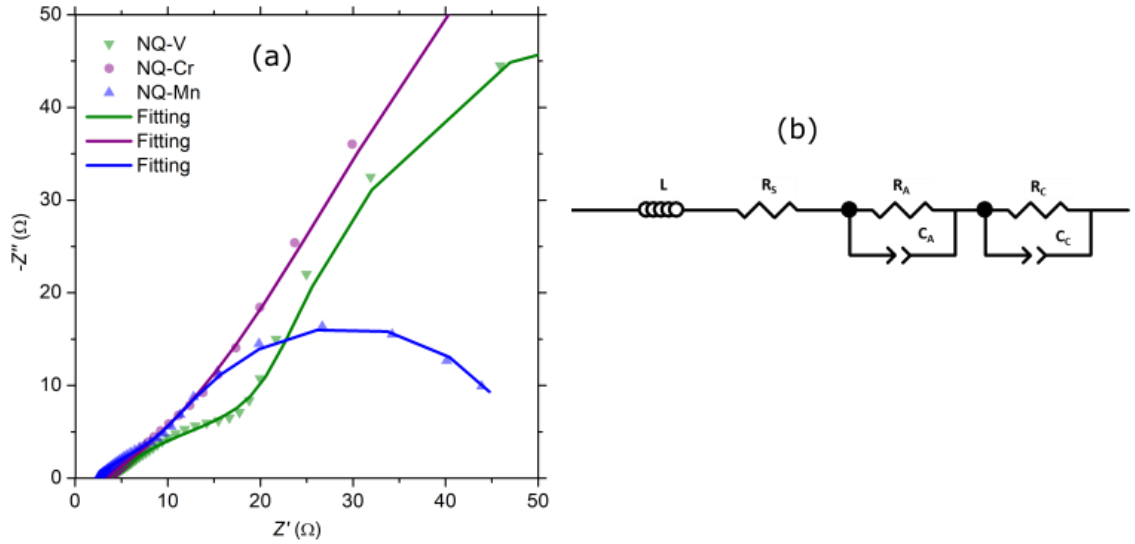


Figure 8.7 Electrochemical impedance spectroscopy measured in the range of 100 mHz to 250 kHz at AC amplitude of 20 mV. (a) Impedance curves, (b) Equivalent circuit used for impedance curve fitting.

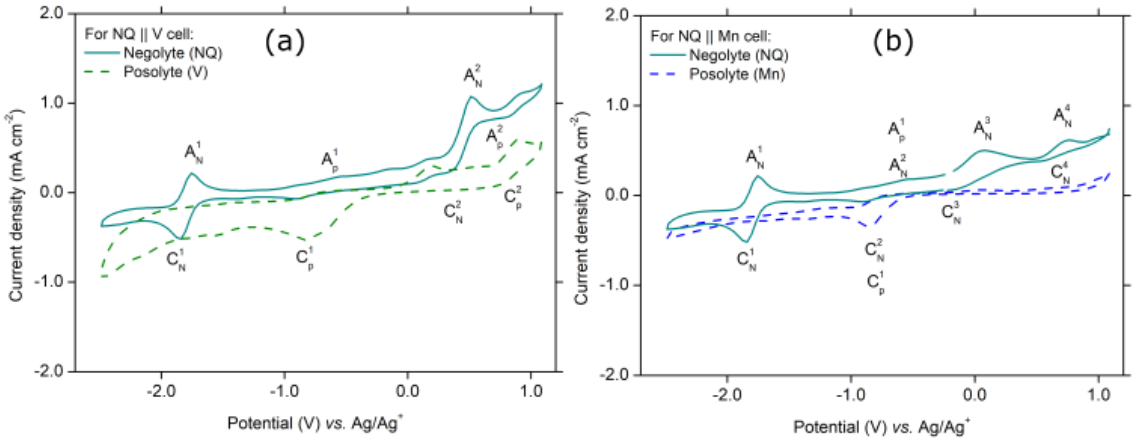


Figure 8.8 Voltammograms taken after charge/discharge cycling for the NAqRFB-cells having mentioned negolyte and posolyte. (a) NQ || V (b) NQ || Mn.

Table 8.4 Summary of the 26 charge-discharge cycles for each type having mentioned posolyte and negolyte.

Type	E_{CELL} (V)	η_{CE} (%)	η_{VE} (%)	η_{EE} (%)	Capacity ($mAh \cdot g^{-1}$)	Energy density ($mWh \cdot g^{-1}$)
NQ || Cr	3.5	44.8	53.1	23.8	79.4	249.9
NQ || V	2.2	72.5	50.7	36.7	75.3	159.5
NQ || Mn	2.5	82.4	70.4	57.5	58.4	57.7

Acronyms: E_{CELL} = Cell potential; η_{CE} = Coulombic efficiency; η_{VE} = Voltage efficiency; η_{EE} = Energy efficiency, Note: Capacity and energy density are calculated based on mass of redox species of the unsaturated negolyte, *i.e.* NQ^{+}/NQ having concentration of 20 mM.

8.4 Conclusion

The naphthoquinone-based non-aqueous redox flow battery was introduced in this study as a proof-of-concept. The naphthaquinone redox ion was used as negolyte coupled with the posolyte based on the redox ions of metal acetylacetonates M(acac), where, M = Chromium (Cr), Manganese (Mn), and Vanadium (V). The use of the mentioned metals at the posolyte while keeping naphthaquinone at the negolyte were considered for the first time for NAqRFBs. In detail, NQ || Cr, NQ || Mn, and NQ || V cells display potential differences of 3.0 V, 2.5 V, and 2.2 V, respectively. These cell potentials are 87 %, 56 %, and 37 % higher than the aqueous commercial all-vanadium RFB technology. The theoretical specific capacities offered by these cells at 1 M concentration of redox species are 80.4 $Wh \cdot L^{-1}$, 67 $Wh \cdot L^{-1}$, and 59 $Wh \cdot L^{-1}$, respectively, based on the mass of redox species used for unsaturated negolyte. The composite membrane was used in this study, which was made of ion-exchange layer of Nafion HP sandwiched between two layers of microporous separator Celgard C4560. This membrane successfully enabled to decrease permeability of the membrane toward redox species of NQ.

The cells NQ || Cr, NQ || Mn, and NQ || V offered storage capacities of 79.4, 75.3, and 58.4 mAh g^{-1}, based on mass of redox species used for unsaturated negolyte. In terms of energy efficiency, the NQ || Mn cell offered an energy efficiency of η_{EE} = 57.5 %, and limiting current density of 6.7 $mA \cdot cm^{-2}$ for a cell loaded with 0.06 M of the redox species. Furthermore, the NQ || Cr cell demonstrated a stable performance up to 20 cycles and energy density of *ca.* 250 $mWh \cdot g^{-1}$ based based on mass of redox species used for unsaturated negolyte.

Chapter 9

Retrospectives, Conclusions, and Prospectives

9. Retrospectives, Conclusions, and Perspectives

"The value of an idea lies in the using of it.", Thomas Edison

9.1 Retrospectives

The next generation of energy storage systems will be the one offering high energy densities. Non-aqueous systems enable conventional redox flow battery to cross the barrier of water splitting reaction and challenge researchers to design batteries having potentials higher than 1.6 V. This thesis is a step towards the development of such non-aqueous electrochemical energy storage technologies. This work was aimed to develop and investigate liquid metal displacement battery (LDB) and non-aqueous redox flow battery (NAqRFB).

Literature review of the existing research articles is presented, which highlights the key challenges such as (i) self-discharge defect of liquid displacement batteries; (ii) lack of facile *in-situ* technique to quantify crossover through membranes of NAqRFB; (iii) lack of highly conductive and selective membranes for non-aqueous electrolytes; (iv) parasitic reactions affecting the stability of the electrolyte and the capacity retention; (v) electrodes offering slow kinetics and low electrochemical surface area and; (vi) identifying low-cost and abundant redox species for non-aqueous electrolytes.

Although the development of batteries having non-aqueous electrolytes has sparked worldwide attention, there are still these significant challenges needed to be overcome before any pilot-scale implementation. Liquid displacement batteries is a promising technology, though displaying fast self-discharge. Chapter 2 addresses challenge no. (i) by complementing the faradaic function of the membrane through additional reversible side reactions. Chapter 3 targets challenge no. (ii) by developing an *in-situ* technique for quantifying the crossover, whereas Chapter 4 targets challenge no. (iii) by introducing a composite membrane as a proof-of-concept. Chapters 5 and 6 address challenges no. (iv) and (v), by using modified electrodes. Novel electrolytes are presented as proof-of-concept batteries in Chapters 7 and 8 addressing challenge no. (vi).

9.2 Conclusions

Liquid metal displacement batteries are promising but their performance is affected by the defect of self-discharge. The formulation involving Faraday's law and the Nernst-Planck equation explain the self-discharge current density which is directly proportional to the diffusion coefficient of the crossing species. This directed this study to add lead oxide (PbO) into the electrolyte. The latter was helpful to reduce the diffusion coefficient as well as the Pb ion concentration by providing two additional side reactions. The remedial actions reported here lead to the highest reported columbic efficiency for liquid displacement batteries, *i.e.* an increment from 91 % to 97 % without affecting the voltage efficiency.

This work developed a technique for determining crossover and also provide a framework for a systematic membrane diagnostic of NAqRFB. Ferrocene is reported as a model probing species for *in-situ* crossover measurement. The trend of the crossover molar flux obtained through studied *in-situ* measurement was found to be FAP-450 > Nafion 115 > Nafion 117 > FAPQ-375-PP > FAP-330-PE. The presented *in-situ* technique allows researchers to account for the contribution of diffusion-driven crossover.

Porous separators display very low selective transport of ionic species, allowing redox species of negolyte and posolyte to short circuit. Thicker ion-exchange membranes are then being used in non-aqueous redox flow batteries to avoid these disadvantages but at the cost of higher ohmic losses. The selectivity of the porous separator was enhanced by using a sandwiched ion-exchange layer. A composite membrane having layers of microporous separator Celgard C4560 / C2500 and ion-exchange membrane Nafion HP was used. This composite membrane performed better than a single layer of porous separator or membrane. The composite membranes C45-HP-C45 performed quite well concerning both, conductivity and crossover permeation.

Vanadium acetylacetonate $V(acac)_3$ dissolves easily in most of the organic solvents, besides its commercial availability at a fair price. Nonetheless, merits are usually accompanied by some demerits. The presence of moisture/oxygen in the environment triggers the irreversible formation of parasitic species $VO(acac)_2$, which causes rapid battery capacity loss. Accordingly, the electrolyte must be kept in an inert atmosphere such as dry nitrogen. Nonetheless, it was observed that even keeping a strictly controlled inert gas over the electrolytes, the stability of the batteries was still rather low. This study

proposed for the first time that carbon felt electrodes were a major source of oxygen since they often display an oxygen-rich surface. The carbon felt electrodes were then submitted to a set of different treatments for removing these oxygen functional groups and for increasing the surface area. The best performance was obtained when the electrodes were treated at 400 °C under oxygen, followed by a treatment at 700 °C under hydrogen atmosphere, which displayed an increase of 34 % of the ECSA compared to the pristine sample. The cell equipped with such electrodes outperformed all those reported in the literature for similar systems and the capacity of the cell remained stable at *ca.* 10.42 mAh.

The role of carbon nanoparticles was assessed using Vulcan, Ketjen, graphene, rGO, CNT, and also platinum supported on graphene. A facile and fast drop-casting coating technique was developed to prepare the modified electrodes. Nafion ionomer was added to the nanoparticles for adhesion. The best performing electrodes, coated with CNT nanoparticles, displayed an energy efficiency of *ca.* 22.4 % higher as compared with pristine electrodes. CNT particles coated carbon fibers display a spider-web configuration, which certainly was most responsible for its better performance. The Pt-rGO nanoparticles displayed only a slightly better performance than rGO-electrode. CNT-electrodes demonstrated widespread dispersion of nanoparticles on their fibers, which is proportional to a higher number of active sites to perform the redox reactions. The latter was confirmed by the 4.7 fold higher electrochemical reaction rate constant – K^0, as compared to pristine electrodes. Adding the ionomer in a ratio of 15 wt. % was effective and offers good binding of the carbon nanoparticles to the felt fibers. This allowed increasing the number of triple-phase boundaries, which results in a 34.4 % reduction in the charge-transfer resistance compared to the pristine electrodes.

In contrast to lithium-ion batteries which use critical elements, the redox flow batteries can use different electrolyte chemistries with minimal adaptations, making them suitable to take advantage of locally available raw materials. Aluminium-ions (Al^{3+}), which offers high energy density and a high value of negative redox potential, i.e., -1.7 V *vs.* Ag/Ag^{+}, is the most abundant metal and more evenly distributed over the Earth's crust. The aluminum-ion-based non-aqueous redox flow cell was introduced as a proof-of-concept. The aluminum redox ion was used as negolyte coupled with the posolyte based on the redox ions of metal acetylacetonates M(acac), where, M = Chromium (Cr), Vanadium (V), Manganese (Mn), Iron (Fe), and Ferrocene (Fc). Cells equipped with Al || V and Al || Mn exhibited the most promising performances.

RFB technology is one of the promising candidates for large-scale grid systems. Present commercial RFB technology is based on the redox reactions of electroactive metals, which are constrained by material abundance, cost, and environmental issues. These issues are prompting scientists to look into organic-based technologies as potential metal-free battery alternatives. This opens the door to the development of green and sustainable energy storage devices. NAqRFB technology opens the window of using redox species outside the electrochemical stability range of aqueous electrolytes. The naphthoquinone-based redox system was introduced in this study as a proof-of-concept using a practical cell. The naphthoquinone redox ion was used as negolyte coupled with the posolyte based on the redox ions of metal acetylacetonates M(acac), where, M = Chromium (Cr), Manganese (Mn), and Vanadium (V). This insertion leads to the generation of novel chemistries, such as NQ || Cr, NQ || Mn, and NQ || V with cell potential differences of 3.0 V, 2.5 V, and 2.2 V, respectively. The theoretical energy capacity offered by each cell NQ || Cr, NQ || Mn, and NQ || V based on the thermodynamic solubility of 1 M of NQ in DMA [199] is 80.4 $Wh \cdot L^{-1}$, 67 $Wh \cdot L^{-1}$, and 59 $Wh \cdot L^{-1}$, respectively. The cell NQ || Cr demonstrated a stable performance up to 20 cycles and the energy density of *ca.* 250 $mWh \cdot g^{-1}$ based on 0.06 M concentration of redox species used for unsaturated negolyte NQ.

9.3 Perspectives

This thesis opens up several accounts for interesting future works and the propositions are given below, bearing in mind the presented results.

- The performance of a liquid metal displacement battery having electrochemistry based on the Pb ions was presented. This battery can also be operated using other molten metals and molten electrolytes. More environmental sustainable metal-oxides should be studied for providing reversible side reactions which minimise the self-discharge challenge.
- The quantification of the crossover directly from the flow cells complements the improvement in the design/optimization. Since there is no need for disassembling of the cell, it can be used as a diagnostic tool to assess the realistic membrane situation under real working conditions. Further testing of this technique on battery stacks can lead to thought-provoking results.

- The ideal trend of energy efficiency as a function of selectivity highlighted that there is a margin for improvement in cell performance while using composite membranes. For future studies should address the commercial availability of such composite membranes.
- The results of parasitic-reaction-free electrodes highlighted the critical relevance of the chemisorbed oxygen at the surface of the carbon electrodes to the performance of the vanadium-based NAqRFB. Oxygen-free electrodes or electrodes containing inert oxygen functional groups should be used. Since the chemisorbed oxygen functional groups are quite important for allowing the redox species to anchor and exchange electrons at the electrode surface, research should progress onto assessing the effect of inert carbon surface dopants, where nitrogen appears as a very promising candidate.
- The adhesion of the nanoparticles prepared through the drop-casting method was robust, and this technique is scalable to manufacture electrodes for larger geometric areas. This technique should be implemented on electrodes having a larger geometric area.
- Novel proof-of-concept fully operational Aluminium-based redox flow battery is reported for the first time. Future studies should address higher concentrations to reach the theoretical energy density limit, complemented with the study of the effect of using treated/coated electrodes, optimization of flowrates, the effect of using different membranes, aiming to devise chemistries suitable for industrialization.
- Naphthoquinone-based redox flow battery is also reported for the first time in this thesis. Future research should include testing higher concentrations, as well as a thorough investigation of other factors, such as using the treated or coated electrodes, to determine the practicality of Napthoquinone-based RFBs as the next generation of NAqRFBs.

Quoting Thomas Edison,

"When you have exhausted all possibilities, remember this: you haven't."

10. References

[1] G. Clark, D. Jacks, Coal and the Industrial Revolution, 1700–1869, Eur. Rev. Econ. Hist. 11 (2007) 39–72. https://doi.org/10.1017/S1361491606001870.

[2] J.S. Walker, Writing the History of Nuclear Energy: The State of the Art, Dipl. Hist. 9 (1985) 377–383. https://doi.org/10.1111/J.1467-7709.1985.TB00545.X.

[3] J.L. Roeder, What We Learned From the Oil Crisis of 1973: A 30-Year Retrospective:, Bull. Sci. Technol. Soc. 25 (2016) 166–169. https://doi.org/10.1177/0270467604274085.

[4] M. Xu, J.M. David, S.H. Kim, The Fourth Industrial Revolution: Opportunities and Challenges, Int. J. Financ. Res. 9 (2018). https://doi.org/10.5430/ijfr.v9n2p90.

[5] C. Böhringer, The Kyoto Protocol: A Review and Perspectives, Oxford Rev. Econ. Policy. 19 (2003) 451–466. https://doi.org/10.1093/OXREP/19.3.451.

[6] R. Falkner, The Paris Agreement and the new logic of international climate politics, Int. Aff. 92 (2016) 1107–1125. https://doi.org/10.1111/1468-2346.12708.

[7] T. Hák, S. Janoušková, B. Moldan, Sustainable Development Goals: A need for relevant indicators, Ecol. Indic. 60 (2016) 565–573. https://doi.org/10.1016/J.ECOLIND.2015.08.003.

[8] M. Elkerbout, C. Egenhofer, J. Núñez Ferrer, M. Catuti, I. Kustova, V. Rizos, The European Green Deal after Corona - Implications for EU climate policy, CEPS Pap. (2020). https://ideas.repec.org/p/eps/cepswp/26869.html (accessed June 25, 2020).

[9] H. Yin, B. Chung, F. Chen, T. Ouchi, J. Zhao, N. Tanaka, D.R. Sadoway, Faradaically selective membrane for liquid metal displacement batteries, Nat. Energy. 3 (2018) 127–131. https://doi.org/10.1038/s41560-017-0072-1.

[10] J. Figgener, P. Stenzel, K.P. Kairies, J. Linßen, D. Haberschusz, O. Wessels, G. Angenendt, M. Robinius, D. Stolten, D.U. Sauer, The development of stationary battery storage systems in Germany – A market review, J. Energy Storage. 29 (2020) 101153–101172. https://doi.org/10.1016/j.est.2019.101153.

[11] C. Blanc, Modeling of a Vanadium Redox Flow Battery Electricity Storage System, EPFL, 2009. https://doi.org/10.5075/EPFL-THESIS-4277.

[12] P.T. Moseley, J. Garche, Electrochemical Energy Storage for Renewable Sources and Grid Balancing, Electrochem. Energy Storage Renew. Sources Grid Balanc. (2014) 1–473. https://doi.org/10.1016/C2012-0-01253-7.

[13] and J.Z. Huamin Zhang, Xianfeng Li, Redox Flow Batteries Fundamentals and Applications, CRC Press Taylor & Francis, London, New York, 2018. https://doi.org/10.1021/acsenergylett.7b00361.

[14] M. Rychcik, M. Skyllas-Kazacos, Characteristics of a new all-vanadium redox flow battery, J. Power Sources. 22 (1988) 59–67. https://doi.org/10.1016/0378-7753(88)80005-3.

[15] A. Paulenova, S.E. Creager, J.D. Navratil, Y. Wei, Redox potentials and kinetics of the Ce3+/Ce4+ redox reaction and solubility of cerium sulfates in sulfuric acid solutions, J. Power Sources. 109 (2002) 431–438. https://doi.org/10.1016/S0378-7753(02)00109-X.

[16] B. Fang, S. Iwasa, Y. Wei, T. Arai, M. Kumagai, A study of the Ce(III)/Ce(IV) redox couple for

redox flow battery application, Electrochim. Acta. 47 (2002) 3971–3976. https://doi.org/10.1016/S0013-4686(02)00370-5.

[17] R. Chen, S. Kim, Z. Chang, Redox Flow Batteries: Fundamentals and Applications, in: Redox - Princ. Adv. Appl., InTech, 2017. https://doi.org/10.5772/intechopen.68752.

[18] C. Choi, S. Kim, R. Kim, Y. Choi, S. Kim, H. young Jung, J.H. Yang, H.T. Kim, A review of vanadium electrolytes for vanadium redox flow batteries, Renew. Sustain. Energy Rev. 69 (2017) 263–274. https://doi.org/10.1016/j.rser.2016.11.188.

[19] Y.K. Zeng, T.S. Zhao, L. An, X.L. Zhou, L. Wei, A comparative study of all-vanadium and iron-chromium redox flow batteries for large-scale energy storage, J. Power Sources. 300 (2015) 438–443. https://doi.org/10.1016/j.jpowsour.2015.09.100.

[20] M. Skyllas-Kazacos, New All-Vanadium Redox Flow Cell, J. Electrochem. Soc. 133 (1986) 1057. https://doi.org/10.1149/1.2108706.

[21] C.M. S. Roe M. Skyllas-Kazacos, A High Energy Density Vanadium Redox Flow Battery with 3 M Vanadium Electrolyte, J. Electrochem. Soc. 163 (2016) A5023–A5028.

[22] Y. Yang, Y. Zhang, L. Tang, T. Liu, S. Peng, X. Yang, Improved energy density and temperature range of vanadium redox flow battery by controlling the state of charge of positive electrolyte, J. Power Sources. 450 (2020) 227675. https://doi.org/10.1016/j.jpowsour.2019.227675.

[23] M. O, N. Pour, Y. Shao-Horn, S. Almheiri, Systematic selection of solvent mixtures for non-aqueous redox flow batteries – vanadium acetylacetonate as a model system, Electrochim. Acta. 223 (2017) 115–123. https://doi.org/10.1016/j.electacta.2016.12.014.

[24] J. Friedl, M. V. Holland-Cunz, F. Cording, F.L. Pfanschilling, C. Wills, W. McFarlane, B. Schricker, R. Fleck, H. Wolfschmidt, U. Stimming, Asymmetric polyoxometalate electrolytes for advanced redox flow batteries, Energy Environ. Sci. 11 (2018) 3010–3018. https://doi.org/10.1039/c8ee00422f.

[25] P. Geysens, Y. Li, I. Vankelecom, J. Fransaer, K. Binnemans, Highly soluble 1,4-diaminoanthraquinone derivative for nonaqueous symmetric redox flow batteries, ACS Sustain. Chem. Eng. 8 (2020) 3832–3843. https://doi.org/10.1021/acssuschemeng.9b07244.

[26] R.M. Darling, K.G. Gallagher, J.A. Kowalski, S. Ha, F.R. Brushett, Pathways to low-cost electrochemical energy storage: A comparison of aqueous and nonaqueous flow batteries, Energy Environ. Sci. 7 (2014) 3459–3477. https://doi.org/10.1039/c4ee02158d.

[27] V.K. Tables, S. Electrode, M. Dekker, N. York, Electrochemical Series, Corros. Mater. (2018) 665–671. https://doi.org/10.31399/asm.hb.v13b.a0006542.

[28] K.T. Y. MATSUDA M. OKADA, Y. TAKASU, M. MORITA, Y. Matsuda, K. Tanaka, M. Okada, Y. Takasu, M. Morita, T. Matsumura-Inoue, A rechargeable redox battery utilizing ruthenium complexes with non-aqueous organic electrolyte, J. Appl. Electrochem. 18 (1988) 909–914. https://doi.org/10.1007/BF01016050.

[29] Y.S. T. Yamamura H. Yamana and H. Moriyama, No Title, Electrochim. Acta. 48 (2002) 43–50.

[30] Q. Liu, A.E.S. Sleightholme, A.A. Shinkle, Y. Li, L.T. Thompson, Non-aqueous vanadium acetylacetonate electrolyte for redox flow batteries, Electrochem. Commun. 11 (2009) 2312–2315. https://doi.org/10.1016/j.elecom.2009.10.006.

[31] A.E.S. Sleightholme, A.A. Shinkle, Q. Liu, Y. Li, C.W. Monroe, L.T. Thompson, Non-aqueous manganese acetylacetonate electrolyte for redox flow batteries, J. Power Sources. 196 (2011) 5742–5745. https://doi.org/10.1016/j.jpowsour.2011.02.020.

[32] Q. Liu, A.A. Shinkle, Y. Li, C.W. Monroe, L.T. Thompson, A.E.S. Sleightholme, Non-aqueous chromium acetylacetonate electrolyte for redox flow batteries, Electrochem. Commun. 12 (2010) 1634–1637. https://doi.org/10.1016/j.elecom.2010.09.013.

[33] J.-H.H.J.-H. Kim, K.J.K.J. Kim, M.-S.S.M.-S. Park, N.J.N.J. Lee, U. Hwang, H. Kim, Y.-J.J.Y.-J. Kim, Development of metal-based electrodes for non-aqueous redox flow batteries, Electrochem. Commun. 13 (2011) 997–1000. https://doi.org/10.1016/j.elecom.2011.06.022.

[34] D. Zhang, H. Lan, Y. Li, The application of a non-aqueous bis(acetylacetone)ethylenediamine cobalt electrolyte in redox flow battery, J. Power Sources. 217 (2012) 199–203. https://doi.org/10.1016/J.JPOWSOUR.2012.06.038.

[35] Carine Yvon, Andrew Macdonell, Saskia Buchwald, A. J. Surman, Noémie Follet, Jennifer Alex, De-Liang Long, Leroy Cronin, A collection of robust methodologies for the preparation of asymmetric hybrid Mn–Anderson polyoxometalates for multifunctional materials, Chem. Sci. 4 (2013) 3810–3817. https://doi.org/10.1039/C3SC51618K.

[36] T. Yamamura, Y. Shiokawa, H. Yamana, H. Moriyama, Electrochemical investigation of uranium β-diketonates for all-uranium redox flow battery, Electrochim. Acta. 48 (2002) 43–50. https://doi.org/10.1016/S0013-4686(02)00546-7.

[37] M.H. Chakrabarti, E.P.L. Roberts, C. Bae, M. Saleem, Ruthenium based redox flow battery for solar energy storage, Energy Convers. Manag. 52 (2011) 2501–2508. https://doi.org/10.1016/j.enconman.2011.01.012.

[38] M.H. Chakrabarti, R.A.W. Dryfe, E.P.L. Roberts, Evaluation of electrolytes for redox flow battery applications, Electrochim. Acta. 52 (2007) 2189–2195. https://doi.org/10.1016/j.electacta.2006.08.052.

[39] J.A.A. Suttil, J.F.F. Kucharyson, I.L.L. Escalante-Garcia, P.J.J. Cabrera, B.R.R. James, R.F.F. Savinell, M.S.S. Sanford, L.T.T. Thompson, Metal acetylacetonate complexes for high energy density non-aqueous redox flow batteries, J. Mater. Chem. A. 3 (2015) 7929–7938. https://doi.org/10.1039/c4ta06622g.

[40] K. Mushtaq, T. Lagarteira, A.A. Zaidi, A. Mendes, In-situ crossover diagnostics to assess membrane efficacy for non-aqueous redox flow battery, J. Energy Storage. 40 (2021) 102713–102722. https://doi.org/10.1016/j.est.2021.102713.

[41] D. Zhang, H. Lan, Y. Li, The application of a non-aqueous bis(acetylacetone)ethylenediamine cobalt electrolyte in redox flow battery, J. Power Sources. 217 (2012) 199–203. https://doi.org/10.1016/j.jpowsour.2012.06.038.

[42] M. Morita, Y. Tanaka, K. Tanaka, Y. Matsuda, T. Matsumura-Inoue, Electrochemical oxidation of ruthenium and iron complexes at rotating disk electrode in acetonitrile solution, Bull. Chem. Soc. Jpn. 61 (1988) 2711–2714. https://doi.org/10.1246/bcsj.61.2711.

[43] J.H. Kim, K.J. Kim, M.S. Park, N.J. Lee, U. Hwang, H. Kim, Y.J. Kim, Development of metal-based electrodes for non-aqueous redox flow batteries, Electrochem. Commun. 13 (2011) 997–

1000. https://doi.org/10.1016/j.elecom.2011.06.022.

[44] X. Xing, D. Zhang, Y. Li, A non-aqueous all-cobalt redox flow battery using 1,10-phenanthrolinecobalt(II) hexafluorophosphate as active species, J. Power Sources. 279 (2015) 205–209. https://doi.org/10.1016/j.jpowsour.2015.01.011.

[45] X. Xing, Y. Zhao, Y. Li, A non-aqueous redox flow battery based on tris(1,10-phenanthroline) complexes of iron(II) and cobalt(II), J. Power Sources. 293 (2015) 778–783. https://doi.org/10.1016/j.jpowsour.2015.06.016.

[46] Q. Xu, T.S. Zhao, L. Wei, C. Zhang, X.L. Zhou, Electrochemical characteristics and transport properties of Fe(II)/Fe(III) redox couple in a non-aqueous reline deep eutectic solvent, Electrochim. Acta. 154 (2015) 462–467. https://doi.org/10.1016/j.electacta.2014.12.061.

[47] D. Lloyd, T. Vainikka, L. Murtomäki, K. Kontturi, E. Ahlberg, The kinetics of the Cu2+/Cu+ redox couple in deep eutectic solvents, Electrochim. Acta. 56 (2011) 4942–4948. https://doi.org/10.1016/j.electacta.2011.03.133.

[48] D. Lloyd, T. Vainikka, K. Kontturi, The development of an all copper hybrid redox flow battery using deep eutectic solvents, Electrochim. Acta. 100 (2013) 18–23. https://doi.org/10.1016/j.electacta.2013.03.130.

[49] M.A. Miller, J.S. Wainright, R.F. Savinell, Communication—Iron Ionic Liquid Electrolytes for Redox Flow Battery Applications, J. Electrochem. Soc. 163 (2016) A578–A579. https://doi.org/10.1149/2.0061605jes.

[50] D. Lloyd, T. Vainikka, M. Ronkainen, K. Kontturi, Characterisation and application of the Fe(II)/Fe(III) redox reaction in an ionic liquid analogue, Electrochim. Acta. 109 (2013) 843–851. https://doi.org/10.1016/j.electacta.2013.08.013.

[51] P. Peljo, D. Lloyd, N. Doan, M. Majaneva, K. Kontturi, Towards a thermally regenerative all-copper redox flow battery, Phys. Chem. Chem. Phys. 16 (2014) 2831–2835. https://doi.org/10.1039/c3cp54585g.

[52] S. Schaltin, Y. Li, N.R. Brooks, J. Sniekers, I.F.J. Vankelecom, K. Binnemans, J. Fransaer, Towards an all-copper redox flow battery based on a copper-containing ionic liquid, Chem. Commun. 52 (2016) 414–417. https://doi.org/10.1039/c5cc06774j.

[53] S.K. Park, J. Shim, J.H. Yang, K.H. Shin, C.S. Jin, B.S. Lee, Y.S. Lee, J.D. Jeon, Electrochemical properties of a non-aqueous redox battery with all-organic redox couples, Electrochem. Commun. 59 (2015) 68–71. https://doi.org/10.1016/j.elecom.2015.07.013.

[54] K. Lin, Q. Chen, M.R. Gerhardt, L. Tong, S.B. Kim, L. Eisenach, A.W. Valle, D. Hardee, R.G. Gordon, M.J. Aziz, M.P. Marshak, Alkaline quinone flow battery, Science (80-.). 349 (2015) 1529–1532. https://doi.org/10.1126/science.aab3033.

[55] H. Alt, H. Binder, A. Köhling, G. Sandstede, Investigation into the use of quinone compounds-for battery cathodes, Electrochim. Acta. 17 (1972) 873–887. https://doi.org/10.1016/0013-4686(72)90010-2.

[56] T. Le Gall, K.H. Reiman, M.C. Grossel, J.R. Owen, Poly(2,5-dihydroxy-1,4-benzoquinone-3,6-methylene): A new organic polymer as positive electrode material for rechargeable lithium batteries, in: J. Power Sources, Elsevier, 2003: pp. 316–320. https://doi.org/10.1016/S0378-

7753(03)00167-8.

[57] Z. Song, H. Zhan, Y. Zhou, Anthraquinone based polymer as high performance cathode material for rechargeable lithium batteries, Chem. Commun. (2009) 448–450. https://doi.org/10.1039/b814515f.

[58] X. Wei, W. Xu, M. Vijayakumar, L. Cosimbescu, T. Liu, V. Sprenkle, W. Wang, TEMPO-based catholyte for high-energy density nonaqueous redox flow batteries, Adv. Mater. 26 (2014) 7649–7653. https://doi.org/10.1002/adma.201403746.

[59] Z. Li, S. Li, S. Liu, K. Huang, D. Fang, F. Wang, S. Peng, Electrochemical properties of an all-organic redox flow battery using 2,2,6,6-tetramethyl-1-piperidinyloxy and N-Methylphthalimide, Electrochem. Solid-State Lett. 14 (2011) A171. https://doi.org/10.1149/2.012112esl.

[60] M.O. Bamgbopa, N. Pour, Y. Shao-Horn, S. Almheiri, Systematic selection of solvent mixtures for non-aqueous redox flow batteries – vanadium acetylacetonate as a model system, Electrochim. Acta. 223 (2017) 115–123. https://doi.org/10.1016/j.electacta.2016.12.014.

[61] M.H. Chakrabarti, F.S. Mjalli, I.M. Alnashef, M.A. Hashim, M.A. Hussain, L. Bahadori, C.T.J. Low, Prospects of applying ionic liquids and deep eutectic solvents for renewable energy storage by means of redox flow batteries, Renew. Sustain. Energy Rev. 30 (2014) 254–270. https://doi.org/10.1016/j.rser.2013.10.004.

[62] L. Bahadori, M.A. Hashim, N.S.A. Manan, F.S. Mjalli, I.M. AlNashef, N.P. Brandon, M.H. Chakrabarti, Investigation of Ammonium- and Phosphonium-Based Deep Eutectic Solvents as Electrolytes for a Non-Aqueous All-Vanadium Redox Cell, J. Electrochem. Soc. 163 (2016) A632–A638. https://doi.org/10.1149/2.0261605jes.

[63] K. Gong, Q. Fang, S. Gu, S. Fong, Y. Li, Y. Yan, Nonaqueous redox-flow batteries: organic solvents, supporting electrolytes, and redox pairs †, Energy Environ. Sci. 8 (2015) 3515. https://doi.org/10.1039/c5ee02341f.

[64] J. Mun, M.-J. Lee, J.-W. Park, D.-J. Oh, D.-Y. Lee, S.-G. Doo, Non-Aqueous Redox Flow Batteries with Nickel and Iron Tris(2,2′-bipyridine) Complex Electrolyte, Electrochem. Solid-State Lett. 15 (2012) A80. https://doi.org/10.1149/2.033206ESL.

[65] W. Duan, R.S. Vemuri, J.D. Milshtein, S. Laramie, R.D. Dmello, J. Huang, L. Zhang, D. Hu, M. Vijayakumar, W. Wang, J. Liu, R.M. Darling, L. Thompson, K. Smith, J.S. Moore, F.R. Brushett, X. Wei, A symmetric organic-based nonaqueous redox flow battery and its state of charge diagnostics by FTIR, J. Mater. Chem. A. 4 (2016) 5448–5456. https://doi.org/10.1039/C6TA01177B.

[66] W. Grzybkowski, M. Pilarczyk, Electrical conductance and apparent molar volumes of Al(ClO4)3, Be(ClO4)2, and Cu(ClO4)2 in N,N-dimethylacetamide solutions at 25°C, Electrochim. Acta. 32 (1987) 1601–1605. https://doi.org/10.1016/0013-4686(87)90012-0.

[67] F. Croce, A. D'Aprano, C. Nanjundiah, V.R. Koch, C.W. Walker, M. Salomon, Conductance of Solutions of Lithium tris(trifluoromethanesulfonyl) Methide in Water, Acetonitrile, Propylene Carbonate, N,N-Dimethylformamide, and Nitromethane at 25°C, J. Electrochem. Soc. 143 (1996) 154–159. https://doi.org/10.1149/1.1836401.

[68] K. Izutsu, Electrochemistry in Nonaqueous Solutions: Second Edition, Electrochem. Nonaqueous

Solut. Second Ed. (2009) 1–415. https://doi.org/10.1002/9783527629152.

[69] M. Galiński, A. Lewandowski, I. Stepniak, Ionic liquids as electrolytes, Electrochim. Acta. 51 (2006) 5567–5580. https://doi.org/10.1016/J.ELECTACTA.2006.03.016.

[70] M. Schmidt, U. Heider, A. Kuehner, R. Oesten, M. Jungnitz, N. Ignat'ev, P. Sartori, Lithium fluoroalkylphosphates: a new class of conducting salts for electrolytes for high energy lithium-ion batteries, J. Power Sources. 97–98 (2001) 557–560. https://doi.org/10.1016/S0378-7753(01)00640-1.

[71] Yu Zhao, Yu Ding, Yutao Li, Lele Peng, H. Ryung Byon, J. B. Goodenough, Guihua Yu, A chemistry and material perspective on lithium redox flow batteries towards high-density electrical energy storage, Chem. Soc. Rev. 44 (2015) 7968–7996. https://doi.org/10.1039/C5CS00289C.

[72] Z. Yang, J. Zhang, M.C.W. Kintner-Meyer, X. Lu, D. Choi, J.P. Lemmon, J. Liu, Electrochemical Energy Storage for Green Grid, Chem. Rev. 111 (2011) 3577–3613. https://doi.org/10.1021/CR100290V.

[73] C. Ponce de León, A. Frías-Ferrer, J. González-García, D.A. Szánto, F.C. Walsh, Redox flow cells for energy conversion, J. Power Sources. 160 (2006) 716–732. https://doi.org/10.1016/J.JPOWSOUR.2006.02.095.

[74] G.J. Hwang, H. Ohya, Crosslinking of anion exchange membrane by accelerated electron radiation as a separator for the all-vanadium redox flow battery, J. Memb. Sci. 132 (1997) 55–61. https://doi.org/10.1016/S0376-7388(97)00040-9.

[75] T. Xu, Ion exchange membranes: State of their development and perspective, J. Memb. Sci. 263 (2005) 1–29. https://doi.org/10.1016/J.MEMSCI.2005.05.002.

[76] S.-H. Shin, S.-H. Yun, S.-H. Moon, A review of current developments in non-aqueous redox flow batteries: characterization of their membranes for design perspective, RSC Adv. 3 (2013) 9095–9116. https://doi.org/10.1039/C3RA00115F.

[77] I.L. Escalante-García, J.S. Wainright, L.T. Thompson, R.F. Savinell, Performance of a Non-Aqueous Vanadium Acetylacetonate Prototype Redox Flow Battery: Examination of Separators and Capacity Decay, J. Electrochem. Soc. 162 (2015) A363–A372. https://doi.org/10.1149/2.0471503JES.

[78] F.R. Brushett, J.T. Vaughey, A.N. Jansen, An All-Organic Non-aqueous Lithium-Ion Redox Flow Battery, Adv. Energy Mater. 2 (2012) 1390–1396. https://doi.org/10.1002/AENM.201200322.

[79] S.H. Shin, Y. Kim, S.H. Yun, S. Maurya, S.H. Moon, Influence of membrane structure on the operating current densities of non-aqueous redox flow batteries: Organic-inorganic composite membranes based on a semi-interpenetrating polymer network, J. Power Sources. 296 (2015) 245–254. https://doi.org/10.1016/J.JPOWSOUR.2015.07.045.

[80] Q. Liu, A.E.S. Sleightholme, A.A. Shinkle, Y. Li, L.T. Thompson, Non-aqueous vanadium acetylacetonate electrolyte for redox flow batteries, Electrochem. Commun. 11 (2009) 2312–2315. https://doi.org/10.1016/J.ELECOM.2009.10.006.

[81] T.M. Anderson, L.J. Small, I.H.D. Pratt, N.S. Hudak, Through-plane conductivities of membranes for nonaqueous redox flow batteries, J. Electrochem. Soc. 162 (2015) A2188–A2194. https://doi.org/10.1149/2.0901510JES.

[82] H.S. Bang, D. Kim, S.S. Hwang, J. Won, Surface-modified porous membranes with electrospun Nafion/PVA fibres for non-aqueous redox flow battery, J. Memb. Sci. 514 (2016) 186–194. https://doi.org/10.1016/J.MEMSCI.2016.04.068.

[83] S.-H. Shin, S.-H. Yun, S.-H. Moon, A review of current developments in non-aqueous redox flow batteries: characterization of their membranes for design perspective, RSC Adv. 3 (2013) 9095–9116. https://doi.org/10.1039/C3RA00115F.

[84] W. Wang, W. Xu, L. Cosimbescu, D. Choi, L. Li, Z. Yang, Anthraquinone with tailored structure for a nonaqueous metal–organic redox flow battery, Chem. Commun. 48 (2012) 6669–6671. https://doi.org/10.1039/C2CC32466K.

[85] X. Wei, W. Xu, M. Vijayakumar, L. Cosimbescu, T. Liu, V. Sprenkle, W. Wang, TEMPO-Based Catholyte for High-Energy Density Nonaqueous Redox Flow Batteries, Adv. Mater. 26 (2014) 7649–7653. https://doi.org/10.1002/ADMA.201403746.

[86] M. Ulaganathan, V. Aravindan, Q. Yan, S. Madhavi, M. Skyllas-Kazacos, T.M. Lim, Recent Advancements in All-Vanadium Redox Flow Batteries, Adv. Mater. Interfaces. 3 (2016) 1500309. https://doi.org/10.1002/ADMI.201500309.

[87] S. Yang, Y. Cheng, X. Xiao, H. Pang, Development and application of carbon fiber in batteries, Chem. Eng. J. 384 (2020) 123294. https://doi.org/10.1016/J.CEJ.2019.123294.

[88] C. Zhang, T.S. Zhao, Q. Xu, L. An, G. Zhao, Effects of operating temperature on the performance of vanadium redox flow batteries, Appl. Energy. 155 (2015) 349–353. https://doi.org/10.1016/J.APENERGY.2015.06.002.

[89] K.J. Kim, M.S. Park, Y.J. Kim, J.H. Kim, S.X. Dou, M. Skyllas-Kazacos, A technology review of electrodes and reaction mechanisms in vanadium redox flow batteries, J. Mater. Chem. A. 3 (2015) 16913–16933. https://doi.org/10.1039/C5TA02613J.

[90] M.H. Chakrabarti, N.P. Brandon, S.A. Hajimolana, F. Tariq, V. Yufit, M.A. Hashim, M.A. Hussain, C.T.J. Low, P. V. Aravind, Application of carbon materials in redox flow batteries, J. Power Sources. 253 (2014) 150–166. https://doi.org/10.1016/J.JPOWSOUR.2013.12.038.

[91] C. Ding, H. Zhang, X. Li, T. Liu, F. Xing, Vanadium flow battery for energy storage: Prospects and challenges, J. Phys. Chem. Lett. 4 (2013) 1281–1294. https://doi.org/10.1021/JZ4001032/ASSET/IMAGES/LARGE/JZ-2013-001032_0013.JPEG.

[92] R. Wang, Y. Li, Carbon electrodes improving electrochemical activity and enhancing mass and charge transports in aqueous flow battery: Status and perspective, Energy Storage Mater. 31 (2020) 230–251. https://doi.org/10.1016/J.ENSM.2020.06.012.

[93] A.G. Osorio, I.C.L. Silveira, V.L. Bueno, C.P. Bergmann, H2SO4/HNO3/HCl—Functionalization and its effect on dispersion of carbon nanotubes in aqueous media, Appl. Surf. Sci. 255 (2008) 2485–2489. https://doi.org/10.1016/J.APSUSC.2008.07.144.

[94] Y. Shao, X. Wang, M. Engelhard, C. Wang, S. Dai, J. Liu, Z. Yang, Y. Lin, Nitrogen-doped mesoporous carbon for energy storage in vanadium redox flow batteries, J. Power Sources. 195 (2010) 4375–4379. https://doi.org/10.1016/J.JPOWSOUR.2010.01.015.

[95] K.J. Kim, Y.J. Kim, J.H. Kim, M.S. Park, The effects of surface modification on carbon felt electrodes for use in vanadium redox flow batteries, Mater. Chem. Phys. 131 (2011) 547–553.

https://doi.org/10.1016/j.matchemphys.2011.10.022.

[96] K.J. Kim, S.-W. Lee, T. Yim, J.-G. Kim, J.W. Choi, J.H. Kim, M.-S. Park, Y.-J. Kim, A new strategy for integrating abundant oxygen functional groups into carbon felt electrode for vanadium redox flow batteries, Sci. Reports 2014 41. 4 (2014) 1–6. https://doi.org/10.1038/srep06906.

[97] K. Mushtaq, S. Delgado, A. Mendes, Thermal Hydrogen Treatment of Electrodes for Performance and Stability Enhancement of Non-Aqueous Redox Flow Batteries, ECS Meet. Abstr. MA2021-01 (2021) 232. https://doi.org/10.1149/MA2021-013232MTGABS.

[98] L. Li, S. Kim, W. Wang, M. Vijayakumar, Z. Nie, B. Chen, J. Zhang, G. Xia, J. Hu, G. Graff, J. Liu, Z. Yang, A Stable Vanadium Redox-Flow Battery with High Energy Density for Large-Scale Energy Storage, Adv. Energy Mater. 1 (2011) 394–400. https://doi.org/10.1002/AENM.201100008.

[99] A. Di Blasi, N. Briguglio, O. Di Blasi, V. Antonucci, Charge–discharge performance of carbon fiber-based electrodes in single cell and short stack for vanadium redox flow battery, Appl. Energy. 125 (2014) 114–122. https://doi.org/10.1016/J.APENERGY.2014.03.043.

[100] Q. Wu, Y. Lv, L. Lin, X. Zhang, Y. Liu, X. Zhou, An improved thin-film electrode for vanadium redox flow batteries enabled by a dual layered structure, J. Power Sources. 410–411 (2019) 152–161. https://doi.org/10.1016/J.JPOWSOUR.2018.11.020.

[101] M.H. Chakrabarti, N.P. Brandon, S.A. Hajimolana, F. Tariq, V. Yufit, M.A. Hashim, M.A. Hussain, C.T.J. Low, P. V. Aravind, Application of carbon materials in redox flow batteries, J. Power Sources. 253 (2014) 150–166. https://doi.org/10.1016/J.JPOWSOUR.2013.12.038.

[102] Z. He, Y. Lv, T. Zhang, Y. Zhu, L. Dai, S. Yao, W. Zhu, L. Wang, Electrode materials for vanadium redox flow batteries: Intrinsic treatment and introducing catalyst, Chem. Eng. J. 427 (2022) 131680. https://doi.org/10.1016/J.CEJ.2021.131680.

[103] K.J. Kim, M.S. Park, Y.J. Kim, J.H. Kim, S.X. Dou, M. Skyllas-Kazacos, A technology review of electrodes and reaction mechanisms in vanadium redox flow batteries, J. Mater. Chem. A. 3 (2015) 16913–16933. https://doi.org/10.1039/C5TA02613J.

[104] K. Mushtaq, S. Delgado, A. Mendes, Nanoparticles Coated Electrodes for Vanadium-Based Non-Aqueous Redox Flow Battery, ECS Meet. Abstr. MA2021-02 (2021) 1924. https://doi.org/10.1149/MA2021-0251924MTGABS.

[105] P. M, R. J, C. J, Nanostructured Electrocatalysts for All-Vanadium Redox Flow Batteries, Chem. Asian J. 10 (2015) 2096–2110. https://doi.org/10.1002/ASIA.201500238.

[106] A. Forner-Cuenca, E.E. Penn, A.M. Oliveira, F.R. Brushett, Exploring the Role of Electrode Microstructure on the Performance of Non-Aqueous Redox Flow Batteries, J. Electrochem. Soc. 166 (2019) A2230–A2241. https://doi.org/10.1149/2.0611910JES/XML.

[107] M.A. Bredig, Mixtures of Metals with Molten Salts, in: Molten Salt Chem., M. Blander, Interscience, New York, 1964: p. 367.

[108] P. Pershin, Y. Khalimullina, P. Arkhipov, Y. Zaikov, The Electrodeposition of Lead in LiCl-KCl-PbCl 2 and LiCl-KCl-PbCl 2 -PbO Melts , J. Electrochem. Soc. 161 (2014) D824–D830. https://doi.org/10.1149/2.0051501jes.

[109] A. Kisza, J. Kazmierczak, B. Børresen, G.M. Haarberg, R. Tunold, Kinetics and Mechanism of the

Magnesium Electrode Reaction in Molten MgCl2 - NaCl Binary Mixtures, J. Electrochem. Soc. 144 (1997) 1646–1651. https://doi.org/10.1149/1.1837654.

[110] B. Bø rresen, G.M. Haarberg, R. Tunold, O. Wallevik, Electrochemical Studies of the Cathode Process in Pure Molten Magnesium Chloride, J. Electrochem. Soc. 140 (1993) L99–L100. https://doi.org/10.1149/1.2221656.

[111] A. Kisza, J. Kaźmierczak, B. Børresen, G.M. Haarberg, R. Tunold, Kinetics and mechanism of the magnesium electrode reaction in molten magnesium chloride, J. Appl. Electrochem. 25 (1995) 940–946. https://doi.org/10.1007/BF00241588.

[112] S. Ghosh, R. Ganesan, R. Sridharan, T. Gnanasekaran, Study of phase equilibria in LiCl-KCl-PrCl3 pseudo-ternary system, Thermochim. Acta. 653 (2017) 16–26. https://doi.org/10.1016/J.TCA.2017.03.024.

[113] W. Zhang, D. Wang, W. Zheng, A semiconductor-electrochemistry model for design of high-rate Li ion battery, J. Energy Chem. 41 (2020) 100–106. https://doi.org/10.1016/j.jechem.2019.04.018.

[114] H. Yin, B. Chung, F. Chen, T. Ouchi, J. Zhao, N. Tanaka, D.R. Sadoway, Faradaically selective membrane for liquid metal displacement batteries, Nat. Energy. 3 (2018) 127–131. https://doi.org/10.1038/s41560-017-0072-1.

[115] M. Hino, M.G. Kelly, J.M. Toguri, Activities of lead chloride in molten PbCl2-KCl-NaCl AND PbCl2-KCl-LiCl ternary systems, Can. Metall. Q. 29 (1990) 177–184. https://doi.org/10.1179/cmq.1990.29.3.177.

[116] B.A. Boukamp, A Linear Kronig-Kramers Transform Test for Immittance Data Validation, J. Electrochem. Soc. 142 (1995) 1885–1894. https://doi.org/10.1149/1.2044210.

[117] M. Urquidi-Macdonald, S. Real, D.D. Macdonald, Applications of Kramers-Kronig transforms in the analysis of electrochemical impedance data-III. Stability and linearity, Electrochim. Acta. 35 (1990) 1559–1566. https://doi.org/10.1016/0013-4686(90)80010-L.

[118] K. Mushtaq, J. Zhao, N. Weber, A. Mendes, D.R. Sadoway, Self-discharge mitigation in a liquid metal displacement battery, J. Energy Chem. 66 (2022) 390–396. https://doi.org/10.1016/J.JECHEM.2021.08.015.

[119] J.A. Kowalski, L. Su, J.D. Milshtein, F.R. Brushett, L.S. Jeffrey A Kowalski Jarrod D Milshtein and Fikile R Brushett, J.A. Kowalski, L. Su, J.D. Milshtein, F.R. Brushett, Recent advances in molecular engineering of redox active organic molecules for nonaqueous flow batteries, Curr. Opin. Chem. Eng. 13 (2016) 45–52. https://doi.org/10.1016/j.coche.2016.08.002.

[120] C.M. S. Roe M. Skyllas-Kazacos, S. Roe, C. Menictas, M. Skyllas-Kazacos, A High Energy Density Vanadium Redox Flow Battery with 3 M Vanadium Electrolyte, J. Electrochem. Soc. 163 (2016) A5023–A5028. https://doi.org/10.1149/2.0041601jes.

[121] L. Su, R.M. Darling, K.G. Gallagher, W. Xie, J.L. Thelen, A.F. Badel, J.L. Barton, K.J. Cheng, N.P. Balsara, J.S. Moore, F.R. Brushett, R.M.D. Liang Su Kevin G. Gallagher, Wei Xie, Jacob L. Thelen, Andres F. Badel, John L. Barton, Kevin J. Cheng, Nitash P. Balsara, Jeffrey S. Moore, and Fikile R. Brushett, L. Su, R.M. Darling, K.G. Gallagher, W. Xie, J.L. Thelen, A.F. Badel, J.L. Barton, K.J. Cheng, N.P. Balsara, J.S. Moore, F.R. Brushett, An Investigation of the Ionic Conductivity and Species Crossover of Lithiated Nafion 117 in Nonaqueous Electrolytes, J.

Electrochem. Soc. 163 (2016) A5253–A5262. https://doi.org/10.1149/2.03211601jes.

[122] K. Lou, T.A. Zawodzinski, Investigation of Non-Aqueous Electrolyte and Crossover of Perfluorsulfonate Ion Exchange Membrane in a Non-Aqueous Flow Battery, (2019) 2017–2018.

[123] Q. Luo, L. Li, Z. Nie, W. Wang, X. Wei, B. Li, B. Chen, Z. Yang, In-situ investigation of vanadium ion transport in redox flow battery, J. Power Sources. 218 (2012) 15–20. https://doi.org/10.1016/j.jpowsour.2012.06.066.

[124] D.C. Sing, J.P. Meyers, Direct Measurement of Vanadium Crossover in an Operating Vanadium Redox Flow Battery, ECS Trans. 50 (2013) 61–72. https://doi.org/10.1149/05045.0061ecst.

[125] S.S. Kocha, J. Deliang Yang, J.S. Yi, Characterization of gas crossover and its implications in PEM fuel cells, AIChE J. 52 (2006) 1916–1925. https://doi.org/10.1002/aic.10780.

[126] R.R. Gagne, C.A. Koval, G.C. Lisensky, Ferrocene as an Internal Standard for Electrochemical Measurements, Inorg. Chem. 19 (1980) 2854–2855. https://doi.org/10.1021/ic50211a080.

[127] H. Wang, Yu. Xiao-Zi, L. HUI, eds., PEM Fuel Cell Diagnostic Tools, Taylor & Francis Group, LLC, 2012.

[128] T. Lagarteira, P. Pacheco, C. Almeida, A. Bentien, R. Monteiro, A. Mendes, In-Situ Measurement of Vanadium Crossover for the Vanadium Redox Flow Battery, J. Electrochem. Soc. 166 (2019) A4067–A4072. https://doi.org/10.1149/2.0331916jes.

[129] E. Agar, K.W. Knehr, D. Chen, M.A. Hickner, E.C. Kumbur, Species transport mechanisms governing capacity loss in vanadium flow batteries: Comparing Nafion® and sulfonated Radel membranes, Electrochim. Acta. 98 (2013) 66–74. https://doi.org/10.1016/j.electacta.2013.03.030.

[130] L. Hao, Y. Wang, Y. He, Modeling of Ion Crossover in an All-Vanadium Redox Flow Battery with the Interfacial Effect at Membrane/Electrode Interfaces, J. Electrochem. Soc. 166 (2019) A1310–A1322. https://doi.org/10.1149/2.1061906jes.

[131] B. Bensmann, R. Hanke-Rauschenbach, K. Sundmacher, In-situ measurement of hydrogen crossover in polymer electrolyte membrane water electrolysis, Int. J. Hydrogen Energy. 39 (2014) 49–53. https://doi.org/10.1016/j.ijhydene.2013.10.085.

[132] X. Cheng, J. Zhang, Y. Tang, C. Song, J. Shen, D. Song, J. Zhang, Hydrogen crossover in high-temperature PEM fuel cells, J. Power Sources. 167 (2007) 25–31. https://doi.org/10.1016/j.jpowsour.2007.02.027.

[133] K. V. Greco, A. Forner-Cuenca, A. Mularczyk, J. Eller, F.R. Brushett, Elucidating the Nuanced Effects of Thermal Pretreatment on Carbon Paper Electrodes for Vanadium Redox Flow Batteries, ACS Appl. Mater. Interfaces. 10 (2018) 44430–44442. https://doi.org/10.1021/acsami.8b15793.

[134] M. Thakurathi, E. Gurung, M.M. Cetin, V.D. Thalangamaarachchige, M.F. Mayer, C. Korzeniewski, E.L. Quitevis, The Stokes-Einstein equation and the diffusion of ferrocene in imidazolium-based ionic liquids studied by cyclic voltammetry: Effects of cation ion symmetry and alkyl chain length, Electrochim. Acta. 259 (2018) 245–252. https://doi.org/10.1016/j.electacta.2017.10.149.

[135] W. Haiss, N.T.K. Thanh, J. Aveyard, D.G. Fernig, Determination of size and concentration of gold nanoparticles from UV-Vis spectra, Anal. Chem. 79 (2007) 4215–4221. https://doi.org/10.1021/ac0702084.

[136] J.S. Shamie, C. Liu, L.L. Shaw, V.L. Sprenkle, New Mechanism for the Reduction of Vanadyl Acetylacetonate to Vanadium Acetylacetonate for Room Temperature Flow Batteries, ChemSusChem. 10 (2017) 533–540. https://doi.org/10.1002/cssc.201601126.

[137] J. Wang, C. Zhao, G. Zhang, Y. Zhang, J. Ni, W. Ma, H. Na, Novel covalent-ionically cross-linked membranes with extremely low water swelling and methanol crossover for direct methanol fuel cell applications, J. Memb. Sci. 363 (2010) 112–119. https://doi.org/10.1016/j.memsci.2010.07.022.

[138] H. Jung, K. Fujii, T. Tamaki, H. Ohashi, T. Ito, T. Yamaguchi, Low fuel crossover anion exchange pore-filling membrane for solid-state alkaline fuel cells, J. Memb. Sci. 373 (2011) 107–111. https://doi.org/10.1016/j.memsci.2011.02.044.

[139] S.-H.S.-H.H. Shin, S.-H.S.-H.H. Yun, S.-H.H.S.-H. Moon, A review of current developments in non-aqueous redox flow batteries: characterization of their membranes for design perspective, RSC Adv. 3 (2013) 9095. https://doi.org/10.1039/c3ra00115f.

[140] W. Xie, J. Cook, H.B. Park, B.D. Freeman, C.H. Lee, J.E. McGrath, Fundamental salt and water transport properties in directly copolymerized disulfonated poly(arylene ether sulfone) random copolymers, Polymer (Guildf). 52 (2011) 2032–2043. https://doi.org/10.1016/j.polymer.2011.02.006.

[141] A. Fick, On liquid diffusion, J. Memb. Sci. 100 (1995) 33–38. https://doi.org/10.1016/0376-7388(94)00230-V.

[142] Y. Zhen, C. Zhang, J. Yuan, Y. Zhao, Y. Li, A high-performance all-iron non-aqueous redox flow battery, J. Power Sources. 445 (2020). https://doi.org/10.1016/j.jpowsour.2019.227331.

[143] A.A. Shinkle, A.E.S. Sleightholme, L.D. Griffith, L.T. Thompson, C.W. Monroe, Degradation mechanisms in the non-aqueous vanadium acetylacetonate redox flow battery, J. Power Sources. 206 (2012) 490–496. https://doi.org/10.1016/j.jpowsour.2010.12.096.

[144] I.L. Escalante-García, J.S. Wainright, L.T. Thompson, R.F. Savinell, Performance of a Non-Aqueous Vanadium Acetylacetonate Prototype Redox Flow Battery: Examination of Separators and Capacity Decay, J. Electrochem. Soc. 162 (2015) A363–A372. https://doi.org/10.1149/2.0471503jes.

[145] L. Su, R.M. Darling, K.G. Gallagher, W. Xie, J.L. Thelen, A.F. Badel, J.L. Barton, K.J. Cheng, N.P. Balsara, J.S. Moore, F.R. Brushett, An Investigation of the Ionic Conductivity and Species Crossover of Lithiated Nafion 117 in Nonaqueous Electrolytes, J. Electrochem. Soc. 163 (2016) A5253–A5262. https://doi.org/10.1149/2.03211601jes.

[146] X.L. Zhou, T.S. Zhao, L. An, Y.K. Zeng, L. Wei, Modeling of ion transport through a porous separator in vanadium redox flow batteries, J. Power Sources. 327 (2016) 67–76. https://doi.org/10.1016/j.jpowsour.2016.07.046.

[147] B. Li, Q. Luo, X. Wei, Z. Nie, E. Thomsen, B. Chen, V. Sprenkle, W. Wang, Capacity Decay Mechanism of Microporous Separator-Based All-Vanadium Redox Flow Batteries and its Recovery, ChemSusChem. 7 (2014) 577–584. https://doi.org/10.1002/cssc.201300706.

[148] S.C. Chieng, M. Kazacos, M. Skyllas-Kazacos, Modification of Daramic, microporous separator, for redox flow battery applications, J. Memb. Sci. 75 (1992) 81–91. https://doi.org/10.1016/0376-7388(92)80008-8.

[149] Fluorinated Ionomers - Walther Grot - Google Books, (n.d.). https://books.google.pt/books?hl=en&lr=&id=E8H1Hwd5GXUC&oi=fnd&pg=PP1&ots=F8aO1TDXks&sig=kghYrdo6aOgJ09CxxntLp9kuWOY&redir_esc=y#v=onepage&q&f=false (accessed November 26, 2020).

[150] N. Elgrishi, K.J. Rountree, B.D. McCarthy, E.S. Rountree, T.T. Eisenhart, J.L. Dempsey, A Practical Beginner's Guide to Cyclic Voltammetry, J. Chem. Educ. 95 (2018) 197–206. https://doi.org/10.1021/acs.jchemed.7b00361.

[151] R.M. Darling, M.L. Perry, Half-Cell, Steady-State Flow-Battery Experiments, ECS Trans. 53 (2013) 31–38. https://doi.org/10.1149/05307.0031ecst.

[152] T. Lagarteira, P. Pacheco, C. Almeida, A. Bentien, R. Monteiro, A. Mendes, In-Situ Measurement of Vanadium Crossover for the Vanadium Redox Flow Battery, J. Electrochem. Soc. 166 (2019) A4067–A4072. https://doi.org/10.1149/2.0331916jes.

[153] R.M.D. Wei Xie and Mike L. Perry, W. Xie, R.M. Darling, M.L. Perry, Processing and Pretreatment Effects on Vanadium Transport in Nafion Membranes, J. Electrochem. Soc. 163 (2016) A5084–A5089. https://doi.org/10.1149/2.0111601jes.

[154] S. on Tung, S.L. Fisher, N.A. Kotov, L.T. Thompson, Nanoporous aramid nanofibre separators for nonaqueous redox flow batteries, Nat. Commun. 9 (2018). https://doi.org/10.1038/s41467-018-05752-x.

[155] H.R. Jiang, J. Sun, L. Wei, M.C. Wu, W. Shyy, T.S. Zhao, A high power density and long cycle life vanadium redox flow battery, Energy Storage Mater. 24 (2020) 529–540. https://doi.org/10.1016/j.ensm.2019.07.005.

[156] K. Mushtaq, R. Monteiro, A.A. Zaidi, N. Delgado, A. Mendes, Current Density Improvement for Vanadium Redox Flow Cell Having Interdigitated Flow-Field, ECS Meet. Abstr. MA2018-02 (2018) 28. https://doi.org/10.1149/ma2018-02/1/28.

[157] R.M. Darling, A.Z. Weber, M.C. Tucker, M.L. Perry, The Influence of Electric Field on Crossover in Redox-Flow Batteries, J. Electrochem. Soc. 163 (2016) A5014–A5022. https://doi.org/10.1149/2.0031601jes.

[158] Forecasted electric vehicle battery demand worldwide 2020 | Statista, (n.d.). https://www.statista.com/statistics/1129463/forecasted-electric-vehicle-battery-demand-worldwide/ (accessed July 28, 2021).

[159] European Commission, The European Green Deal, n.d. https://ec.europa.eu/info/sites/info/files/european-green-deal-communication_en.pdf (accessed January 8, 2021).

[160] K. Mushtaq, T. Lagarteira, A.A. Zaidi, A. Mendes, In-situ crossover diagnostics to assess membrane efficacy for non-aqueous redox flow battery, J. Energy Storage. 40 (2021) 102713. https://doi.org/10.1016/j.est.2021.102713.

[161] I.L. Escalante-García, J.S. Wainright, L.T. Thompson, R.F. Savinell, Performance of a Non-Aqueous Vanadium Acetylacetonate Prototype Redox Flow Battery: Examination of Separators and Capacity Decay, J. Electrochem. Soc. 162 (2015) A363–A372. https://doi.org/10.1149/2.0471503jes.

[162] J. Lu, I. Do, L.T. Drzal, R.M. Worden, I. Lee, Nanometal-decorated exfoliated graphite nanoplatelet based glucose biosensors with high sensitivity and fast response, ACS Nano. 2 (2008) 1825–1832. https://doi.org/10.1021/nn800244k.

[163] N. Elgrishi, K.J. Rountree, B.D. McCarthy, E.S. Rountree, T.T. Eisenhart, J.L. Dempsey, A Practical Beginner's Guide to Cyclic Voltammetry, J. Chem. Educ. 95 (2018) 197–206. https://doi.org/10.1021/acs.jchemed.7b00361.

[164] P. Han, Y. Yue, Z. Liu, W. Xu, L. Zhang, H. Xu, S. Dong, G. Cui, Graphene oxide nanosheets/multi-walled carbon nanotubes hybrid as an excellent electrocatalytic material towards VO 2+ /VO 2+ redox couples for vanadium redox flow batteries, Energy Environ. Sci. 4 (2011) 4710–4717. https://doi.org/10.1039/c1ee01776d.

[165] M. Park, Y. Jung, J. Kim, H. il Lee, J. Cho, Synergistic Effect of Carbon Nanofiber/Nanotube Composite Catalyst on Carbon Felt Electrode for High-Performance All-Vanadium Redox Flow Battery, 13 (2013) 5. https://doi.org/10.1021/nl402566s.

[166] K. V. Greco, A. Forner-Cuenca, A. Mularczyk, J. Eller, F.R. Brushett, Elucidating the Nuanced Effects of Thermal Pretreatment on Carbon Paper Electrodes for Vanadium Redox Flow Batteries, ACS Appl. Mater. Interfaces. 10 (2018) 44430–44442. https://doi.org/10.1021/acsami.8b15793.

[167] B. Manoj, A.M. Raj, G.C. Thomas, Tailoring of low grade coal to fluorescent nanocarbon structures and their potential as a glucose sensor, Sci. Rep. 8 (2018) 13891. https://doi.org/10.1038/s41598-018-32371-9.

[168] X. Huang, N. Hu, R. Gao, Y. Yu, Y. Wang, Z. Yang, E. Siu-Wai Kong, H. Wei, Y. Zhang, Reduced graphene oxide-polyaniline hybrid: Preparation, characterization and its applications for ammonia gas sensing, J. Mater. Chem. 22 (2012) 22488–22495. https://doi.org/10.1039/c2jm34340a.

[169] J. Yang, Y. Wang, J. Wang, M.B. Chan-Park, Reducing graphene oxide with a modified Birch reaction, RSC Adv. 5 (2015) 11124–11127. https://doi.org/10.1039/c4ra13801e.

[170] L. Guglielmero, M.M. Langroudi, M. Al Khatib, M.A.C. de Oliveira, B. Mecheri, M. De Leo, A. Mezzetta, L. Guazzelli, R. Giglioli, A.D. Epifanio, R. Pogni, C. Chiappe, C.S. Pomelli, Electrochemical and spectroscopic study of vanadyl acetylacetonate–ionic liquids interactions, Electrochim. Acta. 373 (2021) 137865. https://doi.org/10.1016/j.electacta.2021.137865.

[171] J.D. Saraidaridis, C.W. Monroe, Nonaqueous vanadium disproportionation flow batteries with porous separators cycle stably and tolerate high current density, J. Power Sources. 412 (2019) 384–390. https://doi.org/10.1016/j.jpowsour.2018.11.058.

[172] O. Schmidt, S. Melchior, A. Hawkes, I. Staffell, Projecting the Future Levelized Cost of Electricity Storage Technologies, Joule. 3 (2019) 81–100. https://doi.org/10.1016/J.JOULE.2018.12.008.

[173] C. Flox, M. Skoumal, J. Rubio-Garcia, T. Andreu, J.R. Morante, Strategies for enhancing electrochemical activity of carbon-based electrodes for all-vanadium redox flow batteries, Appl. Energy. 109 (2013) 344–351. https://doi.org/10.1016/J.APENERGY.2013.02.001.

[174] W. Li, Z. Zhang, Y. Tang, H. Bian, T.W. Ng, W. Zhang, C.S. Lee, Graphene-nanowall-decorated carbon felt with excellent electrochemical activity toward VO2+/VO2+ couple for all vanadium redox flow battery, Adv. Sci. 3 (2016) 1–7. https://doi.org/10.1002/advs.201500276.

[175] P.T. Kissinger, W.R. Heineman, Cyclic voltammetry, J. Chem. Educ. 60 (1983) 702–706.

https://doi.org/10.1021/ED060P702.

[176] A. Ya. Gokhshtein, Ya. P. Gokhshtein, “Kinetic equation of irreversible reactions in oscillographic polarography”, Dokl. Akad. Nauk SSSR, 131:3 (1960), 601–604, (n.d.). http://www.mathnet.ru/php/archive.phtml?wshow=paper&jrnid=dan&paperid=39925&option_lang=eng (accessed October 19, 2021).

[177] T. Soboleva, X. Zhao, K. Malek, Z. Xie, T. Navessin, S. Holdcroft, On the Micro-, Meso-, and Macroporous Structures of Polymer Electrolyte Membrane Fuel Cell Catalyst Layers, ACS Appl. Mater. Interfaces. 2 (2010) 375–384. https://doi.org/10.1021/AM900600Y.

[178] E. Schemberger, Ketjenblack ®, n.d.

[179] W. Li, J. Liu, C. Yan, The electrochemical catalytic activity of single-walled carbon nanotubes towards VO2+/VO2+ and V3+/V2+ redox pairs for an all vanadium redox flow battery, Electrochim. Acta. 79 (2012) 102–108. https://doi.org/10.1016/J.ELECTACTA.2012.06.109.

[180] G. Wei, C. Jia, J. Liu, C. Yan, Carbon felt supported carbon nanotubes catalysts composite electrode for vanadium redox flow battery application, J. Power Sources. 220 (2012) 185–192. https://doi.org/10.1016/J.JPOWSOUR.2012.07.081.

[181] A.M. Chaparro, B. Gallardo, M.A. Folgado, A.J. Martín, L. Daza, PEMFC electrode preparation by electrospray: Optimization of catalyst load and ionomer content, Catal. Today. 143 (2009) 237–241. https://doi.org/10.1016/J.CATTOD.2008.12.003.

[182] M.S. Wilson, S. Gottesfeld, Thin-film catalyst layers for polymer electrolyte fuel cell electrodes, J. Appl. Electrochem. 1992 221. 22 (1992) 1–7. https://doi.org/10.1007/BF01093004.

[183] G. Sasikumar, J.W. Ihm, H. Ryu, Optimum Nafion content in PEM fuel cell electrodes, Electrochim. Acta. 50 (2004) 601–605. https://doi.org/10.1016/J.ELECTACTA.2004.01.126.

[184] A.A. Shinkle, A.E.S. Sleightholme, L.D. Griffith, L.T. Thompson, C.W. Monroe, Degradation mechanisms in the non-aqueous vanadium acetylacetonate redox flow battery, in: J. Power Sources, Elsevier, 2012: pp. 490–496. https://doi.org/10.1016/j.jpowsour.2010.12.096.

[185] K. Mushtaq, S. Delgado, A. Mendes, Thermal Hydrogen Treatment of Electrodes for Performance and Stability Enhancement of Non-Aqueous Redox Flow Batteries, (2021). https://ecs.confex.com/ecs/239/meetingapp.cgi/Paper/148209 (accessed June 18, 2021).

[186] K.A.M. and, R.B. Moore*, State of Understanding of Nafion, Chem. Rev. 104 (2004) 4535–4585. https://doi.org/10.1021/CR0207123.

[187] Raw Materials Information System, (n.d.). https://rmis.jrc.ec.europa.eu/?page=crm-list-2020-e294f6 (accessed December 5, 2021).

[188] T. Leisegang, F. Meutzner, M. Zschornak, W. Münchgesang, R. Schmid, T. Nestler, R.A. Eremin, A.A. Kabanov, V.A. Blatov, D.C. Meyer, The aluminum-ion battery: A sustainable and seminal concept?, Front. Chem. 7 (2019). https://doi.org/10.3389/fchem.2019.00268.

[189] H. Pan, Y.-S. Hu, L. Chen, Room-temperature stationary sodium-ion batteries for large-scale electric energy storage, Energy Environ. Sci. 6 (2013) 2338–2360. https://doi.org/10.1039/C3EE40847G.

[190] D. Ye, B. Luo, G. Max Lu, L. Wang, Will new aluminum-ion battery be a game changer?, Sci. Bull. 60 (2015) 1042–1044. https://doi.org/10.1007/S11434-015-0808-X.

[191] M. Chen, L. Chen, Z. Hu, Q. Liu, B. Zhang, Y. Hu, Q. Gu, J.-L. Wang, L.-Z. Wang, X. Guo, S.-L. Chou, S.-X. Dou, Carbon-Coated Na3.32Fe2.34(P2O7)2 Cathode Material for High-Rate and Long-Life Sodium-Ion Batteries, Adv. Mater. 29 (2017) 1605535. https://doi.org/10.1002/ADMA.201605535.

[192] E. Faegh, B. Ng, D. Hayman, W.E. Mustain, Practical assessment of the performance of aluminium battery technologies, Nat. Energy. 6 (2021) 21–29. https://doi.org/10.1038/S41560-020-00728-Y.

[193] G.W. Heise, E.A. Schumacher, N.C. Cahoon, A Heavy Duty Chlorine-Depolarized Cell, J. Electrochem. Soc. 94 (1948) 99. https://doi.org/10.1149/1.2773830.

[194] P.R. Gifford, J.B. Palmisano, An Aluminum/Chlorine Rechargeable Cell Employing a Room Temperature Molten Salt Electrolyte, J. Electrochem. Soc. 135 (1988) 650. https://doi.org/10.1149/1.2095685.

[195] N. Jayaprakash, S.K. Das, L.A. Archer, The rechargeable aluminum-ion battery, Chem. Commun. 47 (2011) 12610–12612. https://doi.org/10.1039/c1cc15779e.

[196] G. Steinberg-Yfrach, J.L. Rigaud, E.N. Durantini, A.L. Moore, D. Gust, T.A. Moore, Light-driven production of ATP catalysed by F0F1-ATP synthase in an artificial photosynthetic membrane, Nature. 392 (1998) 479–482. https://doi.org/10.1038/33116.

[197] H. Kurreck, M. Huber, Model Reactions for Photosynthesis—Photoinduced Charge and Energy Transfer between Covalently Linked Porphyrin and Quinone Units, Angew. Chemie Int. Ed. English. 34 (1995) 849–866. https://doi.org/10.1002/ANIE.199508491.

[198] D.T. Scott, D.M. Mcknight, E.L. Blunt-Harris, S.E. Kolesar, D.R. Lovley, Quinone moieties act as electron acceptors in the reduction of humic substances by humics-reducing microorganisms, Environ. Sci. Technol. 32 (1998) 2984–2989. https://doi.org/10.1021/ES980272Q.

[199] Y. Ding, Y. Li, G. Yu, Y. Ding, Y. Li, G. Yu, Exploring Bio-inspired Quinone-Based Organic Redox Flow Batteries : A Combined Experimental and Computational Study Exploring Bio-inspired Quinone-Based Organic Redox Flow Batteries : A Combined Experimental and Computational Study, CHEMPR. 1 (n.d.) 790–801. https://doi.org/10.1016/j.chempr.2016.09.004.

[200] M.S.S. Santos, L. Peixoto, K. Mushtaq, C. Dias-Ferreira, A. Mendes, M.M. Alves, Bioelectrochemical energy storage in a Microbial Redox Flow Cell, J. Energy Storage. 39 (2021) 102610. https://doi.org/10.1016/J.EST.2021.102610.

[201] R. Checker, R.S. Patwardhan, D. Sharma, S.K. Sandur, Effects of Plumbagin : Novel Mechanism (s) via Modulation of Cellular Redox, 1st ed., Elsevier Inc., n.d. https://doi.org/10.1016/B978-0-12-812373-7.00016-4.

[202] S.K. Sandur, H. Ichikawa, G. Sethi, S.A. Kwang, B.B. Aggarwal, Plumbagin (5-Hydroxy-2-methyl-1,4-naphthoquinone) Suppresses NF-κB Activation and NF-κB-regulated Gene Products Through Modulation of p65 and IκBα Kinase Activation, Leading to Potentiation of Apoptosis Induced by Cytokine and Chemotherapeutic Agents, J. Biol. Chem. 281 (2006) 17023–17033. https://doi.org/10.1074/JBC.M601595200.

[203] S.R. De Paiva, M.R. Figueiredo, T.V. Aragão, M.A. Coelho Kaplan, Antimicrobial Activity in Vitro of Plumbagin Isolated from Plumbago Species, Mem. Inst. Oswaldo Cruz. 98 (2003) 959–961. https://doi.org/10.1590/S0074-02762003000700017.

[204] P. Komaraiah, S. V. Ramakrishna, P. Reddanna, P.B. Kavi Kishor, Enhanced production of plumbagin in immobilized cells of Plumbago rosea by elicitation and in situ adsorption, J. Biotechnol. 101 (2003) 181–187. https://doi.org/10.1016/S0168-1656(02)00338-3.

[205] A.E.S. Sleightholme, A.A. Shinkle, Q. Liu, Y. Li, C.W. Monroe, L.T. Thompson, Non-aqueous manganese acetylacetonate electrolyte for redox flow batteries, J. Power Sources. 196 (2011) 5742–5745. https://doi.org/10.1016/J.JPOWSOUR.2011.02.020.

[206] D. Aaron, Z. Tang, A.B. Papandrew, T.A. Zawodzinski, Polarization curve analysis of all-vanadium redox flow batteries, J Appl Electrochem. 41 (2011) 1175–1182. https://doi.org/10.1007/s10800-011-0335-7.

[207] A.S. Basin, A.B. Kaplun, A.B. Meshalkin, N.F. Uvarov, The LiCl-KCl binary system, Russ. J. Inorg. Chem. 53 (2008) 1509–1511. https://doi.org/10.1134/S003602360809026X.

[208] D. Aaron, Z. Tang, A.B. Papandrew, T.A. Zawodzinski, Polarization curve analysis of all-vanadium redox flow batteries, J. Appl. Electrochem. 41 (2011) 1175–1182. https://doi.org/10.1007/s10800-011-0335-7.

ANNEXURE - A

11. Supplementary Information

11.1 Supplementary Information for Chapter 2

Self-discharge current density for LDB

A formulation based on Faraday's law and by applying the Nernst-Planck equation leads to a relationship highlighting the direct proportionality of self-discharge current and diffusion. The detailed derivation is given below. Faraday's law relates the amount of an active substance to the current as

$$n = \frac{It}{zF}, \qquad (1)$$

where n is the amount of substance, I is an electrical current, t is the total time of the applied constant current, z is the electrons transferred per ion and F is the Faraday constant. Considering the rate of reaction

$$\dot{n} = \frac{I}{zF} \qquad (2)$$

and normalizing it by the surface area (A), becomes

$$N_i = \frac{\partial \dot{n}}{\partial A} = \frac{J}{zF}, \qquad (3)$$

where J is the current density, subscript i refers to the active species (Pb in this case) and N_i denotes the net flux of Pb^{2+} without Cl^-. This leads to

$$J = F \sum_i z_i N_i. \qquad (4)$$

According to the assumptions of negligible migration or convection, the transport equation for the active species reads

$$N = -D\nabla c_{\mathrm{Pb}}. \qquad (5)$$

Thus, the self-discharge current density is simply defined as

$$J = -zFD\nabla c_{\mathrm{Pb}}, \qquad (6)$$

where c_{Pb} denotes the molar concentration of Pb^{2+}.

Battery Testing of LDB

A graphite crucible containing 7.7 g of Pb was used as positive electrode, and 26.9 g lead contained in the TiN membrane fitted graphite crucible were used as negative electrode. A MgO cylinder was used as insulation between both crucibles. The electrolyte was prepared using anhydrous Lithium chloride (LiCl) and Potassium chloride (KCl). The eutectic composition (for Li/K = 0.592:0.408 [207]) allowed to decrease the melting

point of the electrolyte mixture and the temperature of the cell was maintained at 410 ºC measured by an ASTM type-K thermocouple. The distance between the TiN membrane and bottom of the positive graphite crucible was 2 cm.

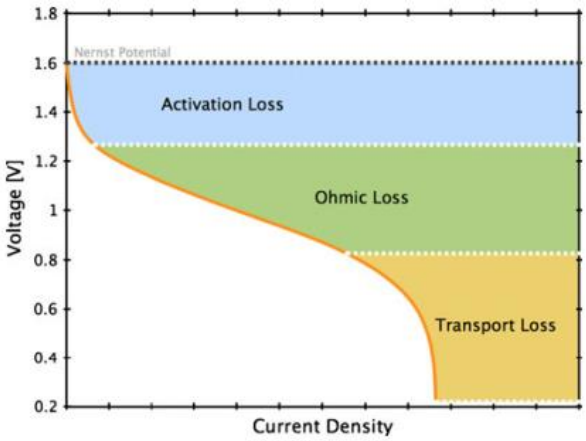


Figure S 11.1 Generalized polarization curve for a battery indicating the dominant source of the overpotentials in each region (adapted from [208]*).*

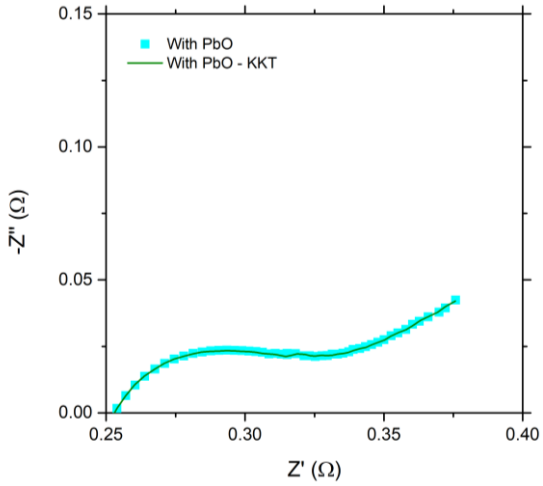


Figure S 11.2: Kramers-Kronig Transforms for the cell having the addition of PbO.

11.2 Supplementary Information for Chapter 3

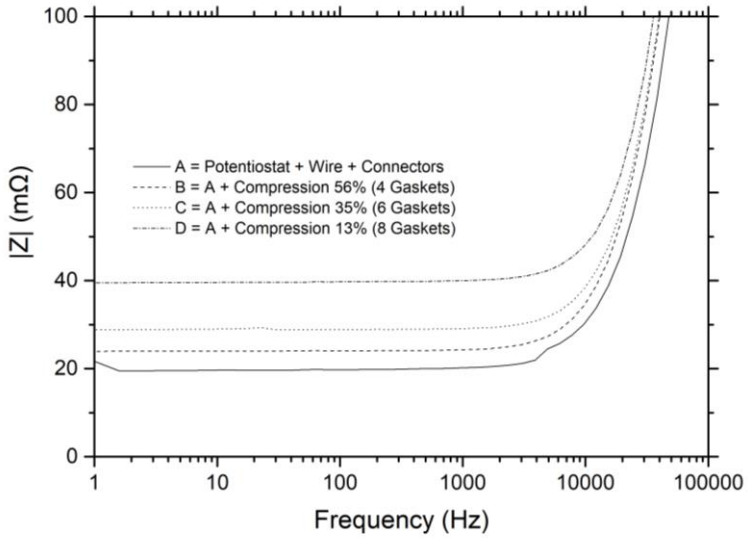


Figure S 11.3 Bode plots of the cell having different compression ratios.

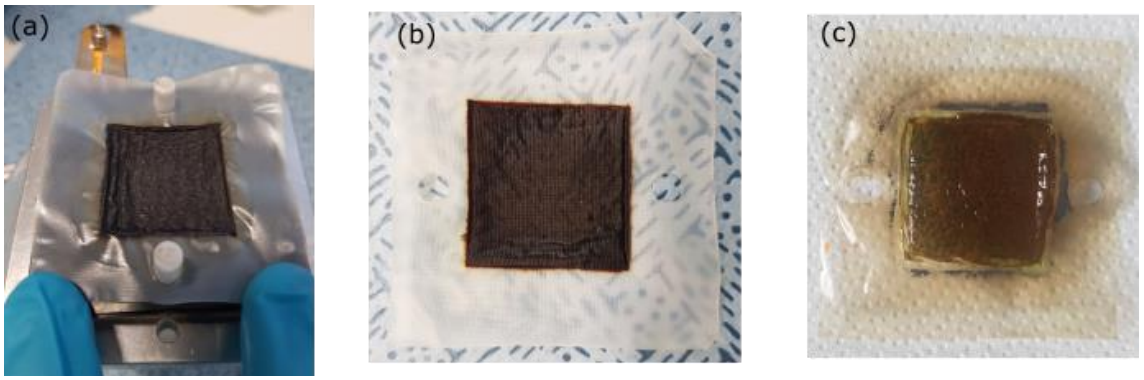


Figure S 11.4 NAqRFB-cell having (a) and (b) FAPQ-375-PP and (c) FAP-330-PE as anion exchange membrane. Charge-discharge cycling was not possible because of vanadium deposition on the layer of the membrane during cycling.

11.3 Supplementary Information for Chapter 4

EIS using A1 electrolyte at the following conditions:

a) The resistance of the cell having an only current-collector and bipolar plates = 6.382 mΩ
b) The resistance of the cell having two dry electrodes at 35 % compression but without membrane = 51.38 mΩ
c) The resistance of the cell (R1) having two wet electrodes (0.05 M Vacac + 0.1 M $TEABF_4$) at 35 % compression but without membrane = 48.46 mΩ
d) The resistance of the cell having two wet electrodes after removing the electrolyte (0.05 M Vacac + 0.1 M $TEABF_4$) from the point (c) = 48.5 mΩ
e) The resistance of the cell (R_2) having two wet electrodes at 35 % compression with each membrane

Table S 11.1 Membrane conductivity for charge carriers through each membrane using electrolyte A1

Membranes	A (cm^2)	L (μm)	R_1 (Ω)	R_2 with membrane (Ω)	K_m ($mS \cdot cm^{-1}$)
N115	7.29	127	0.0485	1.4268	1.264
C4560	7.29	110	0.0485	0.6805	2.387
C2500	7.29	25	0.0485	0.315	1.287
Nafion HP	7.29	20.3	0.0485	0.371	0.863
C45|HP|C45	7.29	240.3	0.0485	1.35	2.533
C25|HP|C25	7.29	70.3	0.0485	0.719	1.438
C4560|C4560	7.29	220	0.0485	1.282	2.446
C2500|C2500	7.29	50	0.0485	0.5	1.519

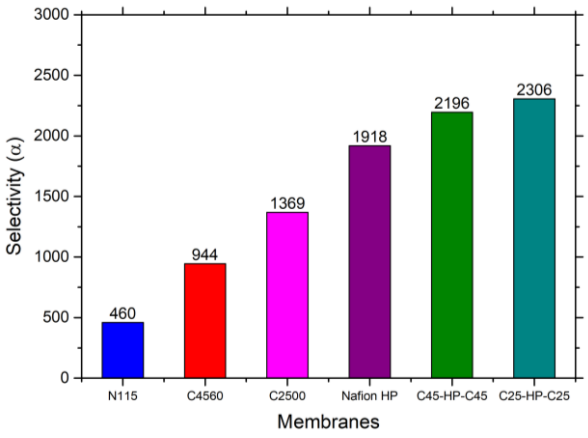


Figure S 11.5 Selectivity of the mentioned membranes

11.4 Supplementary Information for Chapter 5

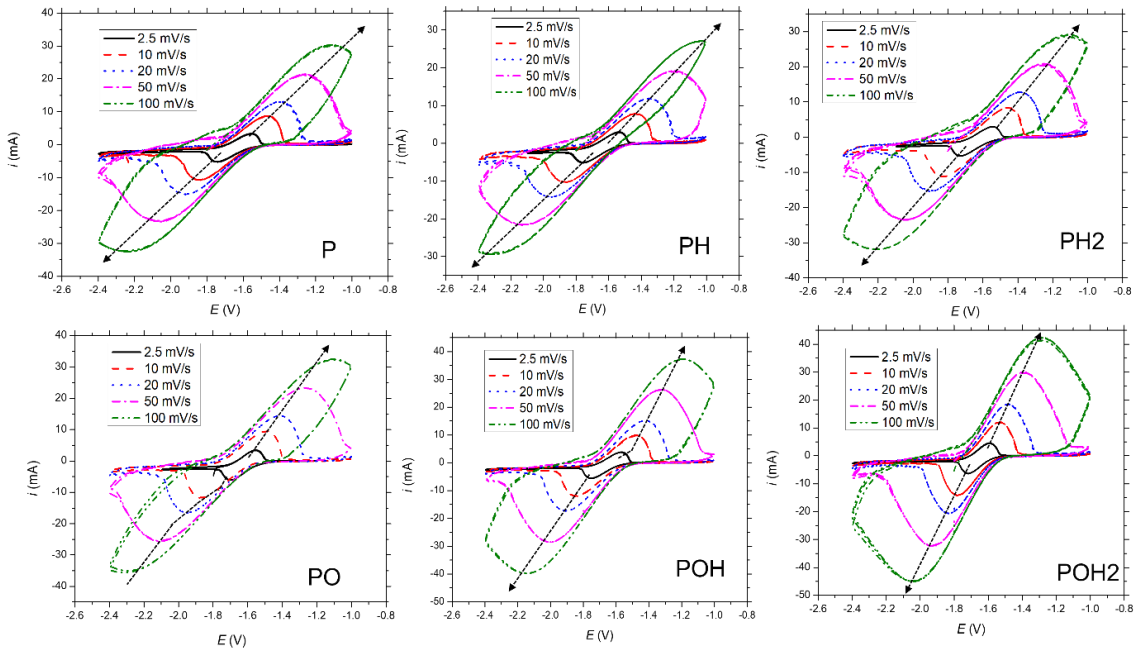


Figure S 11.6 Cyclic voltammograms of Pristine, PH, PH2, PO, POH, and POH2 in 0.1 M $TEABF_4$ + 0.02 M $V(acac)_3$ + Acetonitrile electrolyte at several scan rates.

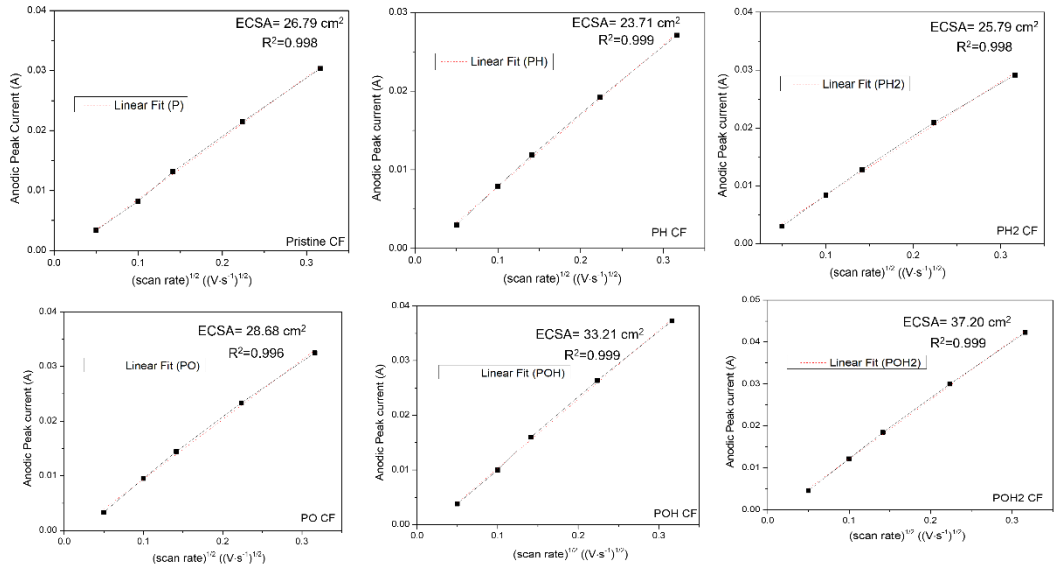


Figure S 11.7 Randles-Sevcik plots for a) P, b) PH, c) PH2, d) PO, e) POH, and d) POH2 to calculate their respective ECSAs.

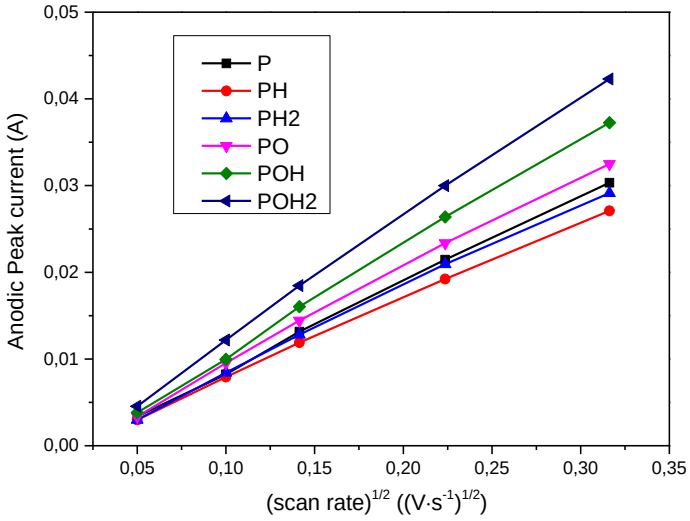


Figure S 11.8 Comparison of all slopes from Randles-Sevcik plots to understand mass transport-related phenomena.

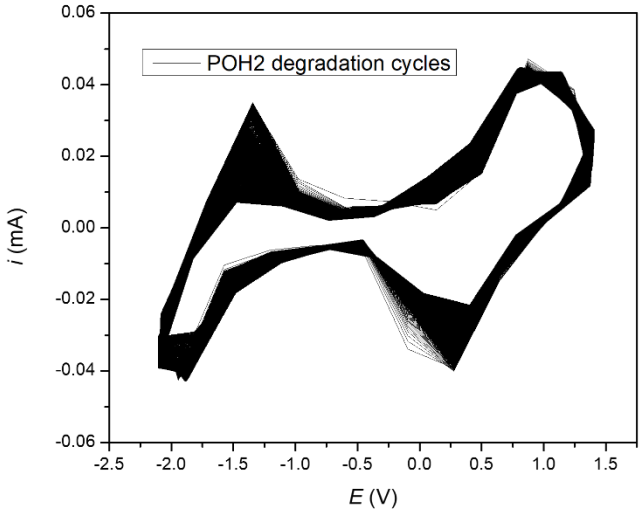


Figure S 11.9 Accelerated stress test applied to POH2 electrode – 700 potential cycles at 100 mV·s^{-1} from -2.1 V to 1.4 V in N_2 purged electrolyte.

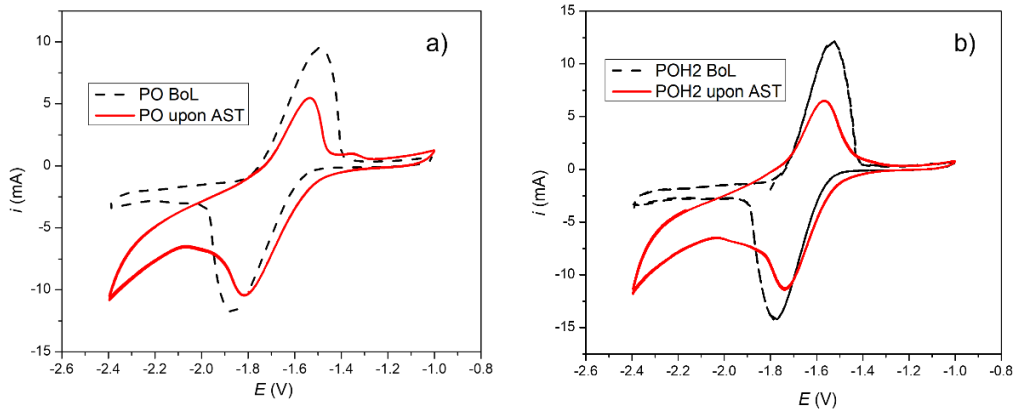


Figure S 11.10 Cyclic voltammograms before and after the accelerated stress test (AST) for both (a) PO and (b) POH2 electrodes, in N_2 purged electrolyte.

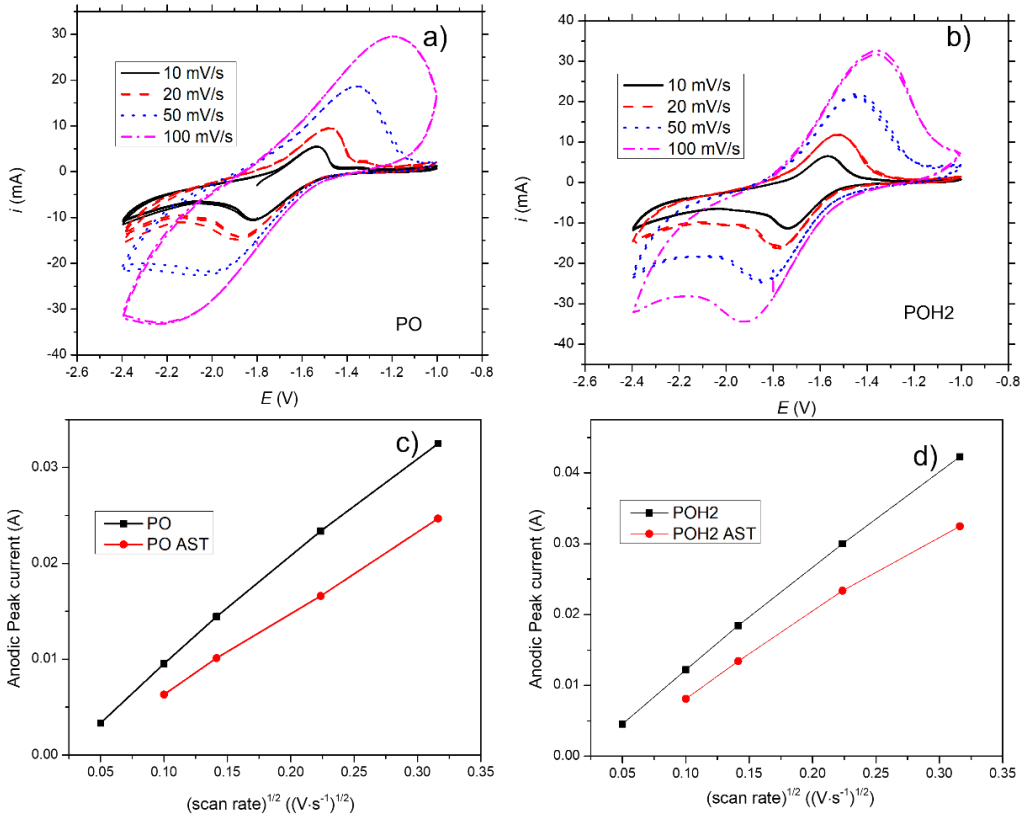


Figure S 11.11 Cyclic voltammograms of (a) PO and (b) POH2 and corresponding Randles Sevcik plots (c-d) in 0.1 M $TEABF_4$ + 0.02 M $V(acac)_3$ + Acetonitrile electrolyte at various scan rates upon the AST/stability test.

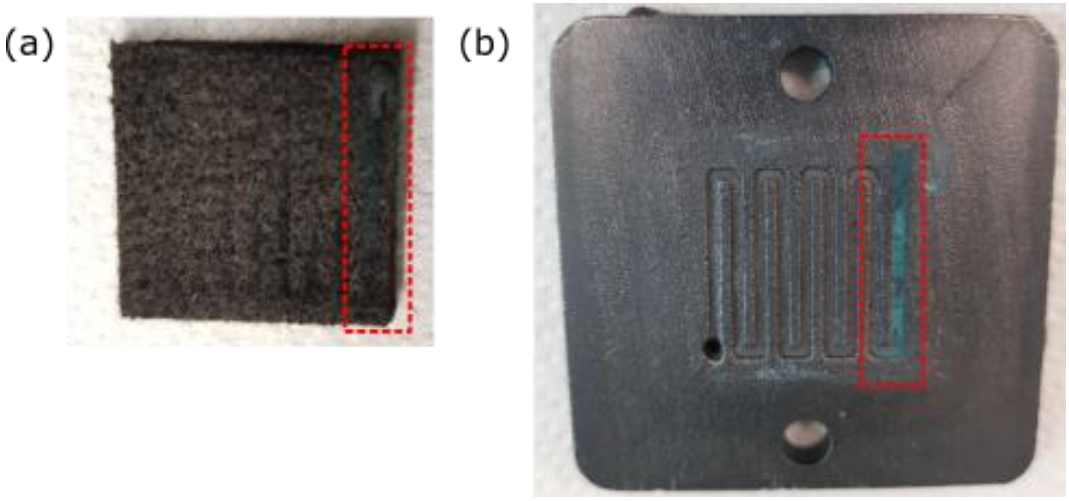


Figure S 11.12 Greenish precipitates of $VO(acac)_2$ (a) PO Carbon felt electrode after charge-discharge cycling (b) Bipolar plate after disassembly of the cell and the precipitates deposited in the channels of the flowfield.

Table S 11.2 Ohmic resistances of the carbon felt electrodes measured before and after charge/discharge cycling (CDC)

	Ohmic Resistances (Ω)		
Electrodes	Before CDC	After CDC	Percent Change
P	0.367	0.963	162.4 %
PH	0.381	0.948	148.8 %
PH2	0.559	1.15	105.7 %
PO	0.359	0.8	122.8 %
POH	0.355	0.68	91.5 %
POH2	0.43	0.616	43.2 %

11.5 Supplementary Information for Chapter 6

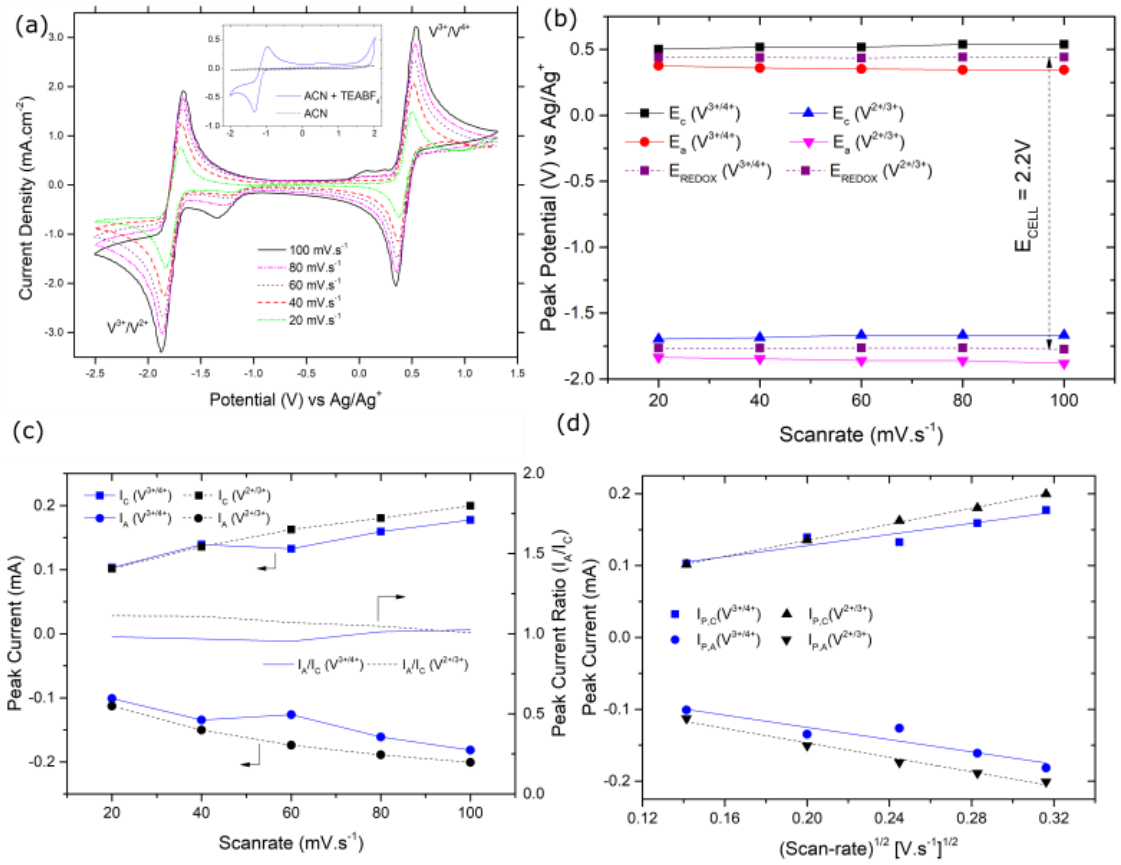


Figure S 11.13 (a) Cyclic voltammogram as a function of scan-rate in the range of 20 mV·s^{-1} to 100 mV·s^{-1} of V^{3+}/V^{2+} & V^{4+}/V^{3+} (b) Peak potentials and redox potential for the V^{3+}/V^{2+} & V^{4+}/V^{3+} redox couple. (c) Peak currents and their current ratios (I_C/I_A). (d) Randles-Sevcik analysis for $V(acac)_3$ oxidation and reduction. Adapted from our previous work [40].

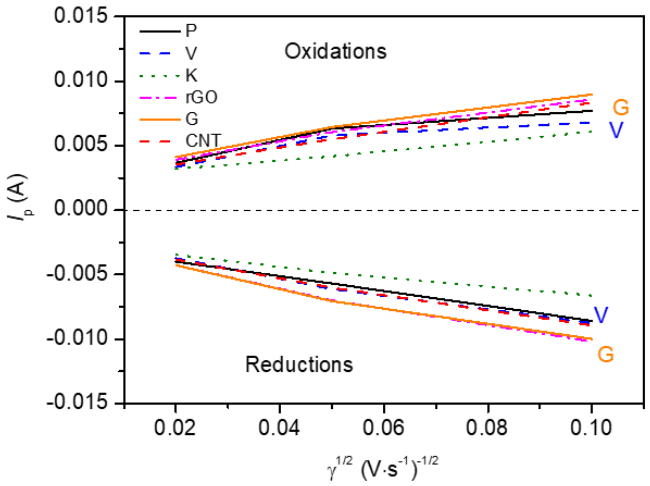


Figure S 11.14 The linear fit of the points taken from each of the voltammograms for all sample prepared electrodes having different nanoparticle coatings.

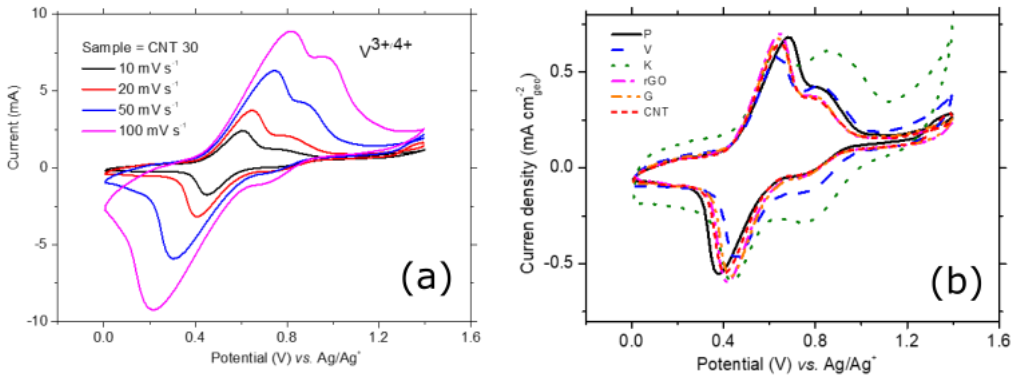


Figure S 11.15 Cyclic voltammogram in a 3-electrode configuration cell using platinum wire as a counter electrode, and Ag^{+}/Ag as a reference electrode. The electrolyte was composed of 0.1 M $TEABF_4$ + 0.02 M $V(acac)_3$ + Acetonitrile for V^{4+}/V^{3+} reaction i.e. for negolyte. (a) Measurements at various scan rates for the same sample of CNT 30 (b) Measurements at 20 $mV{\cdot}s^{-1}$ for each sample.

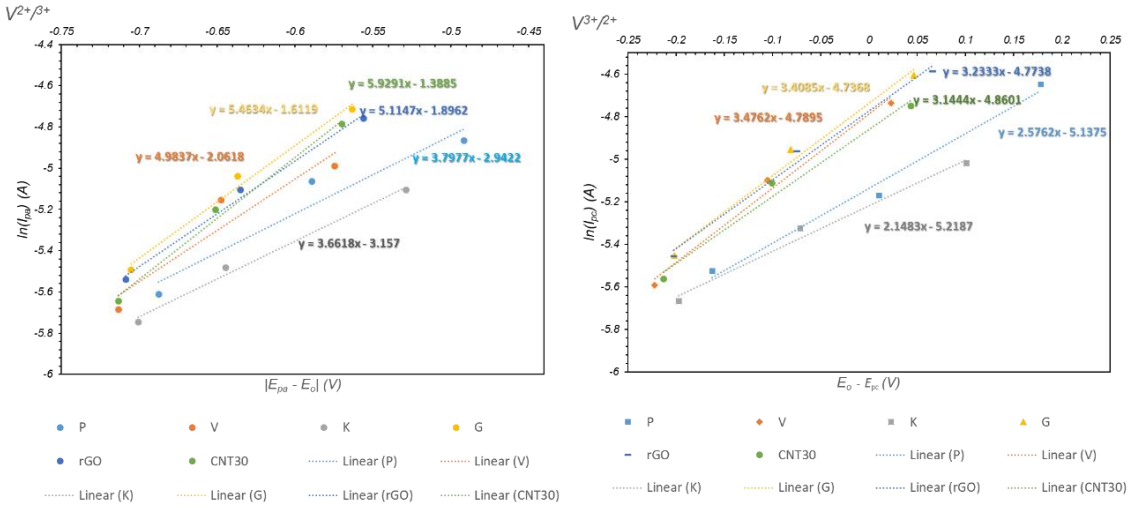


Figure S 11.16 The plot of $ln|I_P|$ $vs.|(E_P - E_O)|$ determined at different scan rates for V^{3+}/V^{2+} has a slope of $-\alpha f$ and an intercept proportional to K^O.

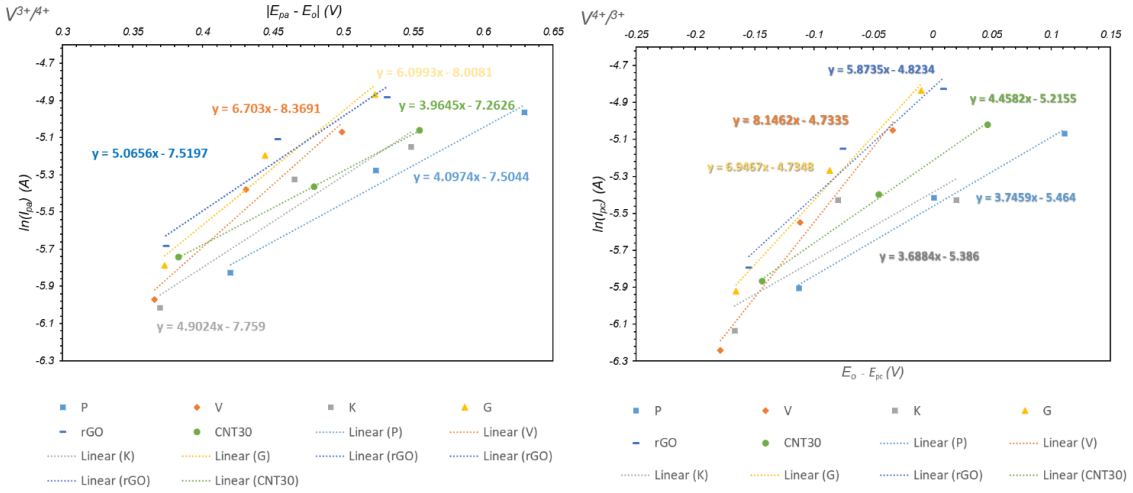


Figure S 11.17 The plot of $ln|I_P|$ $vs.|(E_P - E_O)|$ determined at different scan rates for V^{3+}/V^{2+} has a slope of $-\alpha f$ and an intercept proportional to K^O.

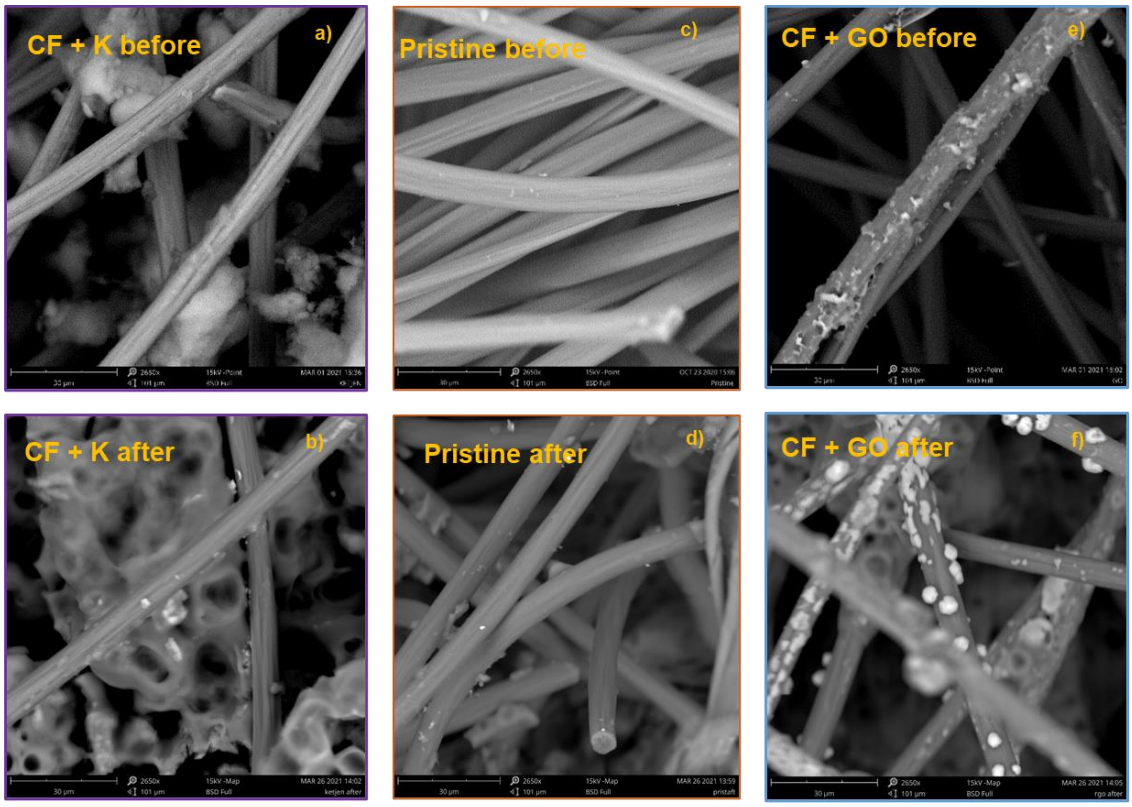


Figure S 11.18 SEM images for surface morphology of carbon fibers with ketjen, none (pristine), and rGO nanoparticles from left to right, before (upper row), and after CDC (underneath row) at 6400 X magnification.

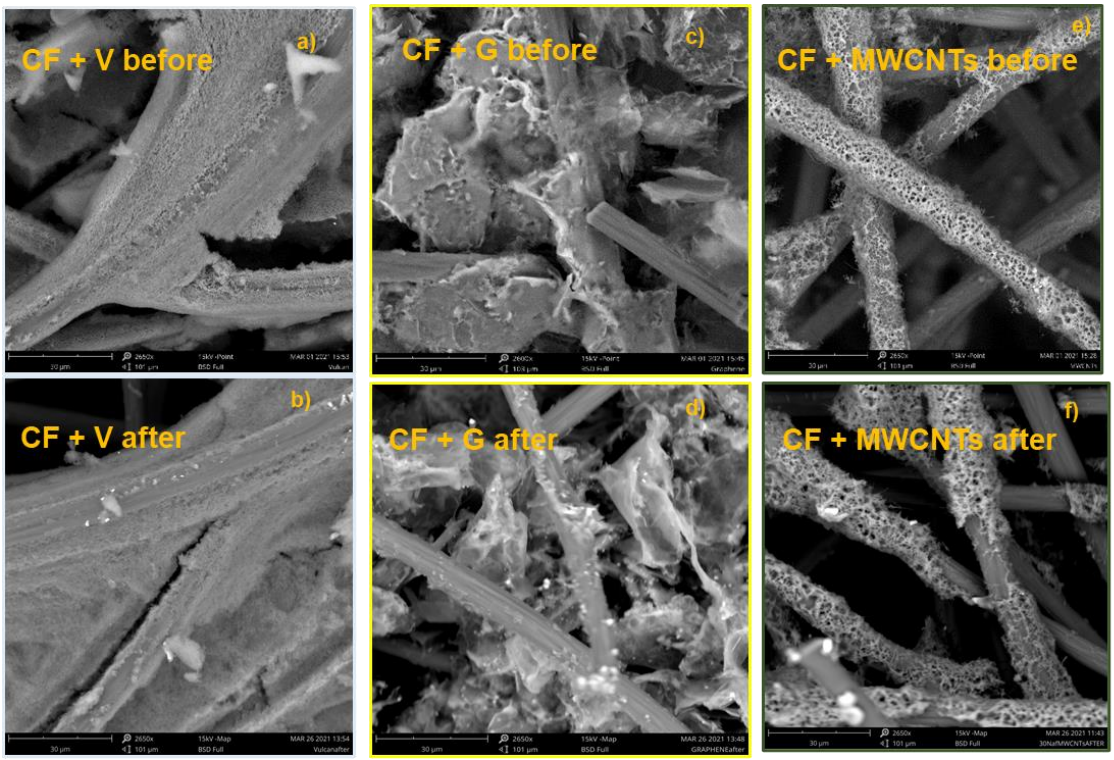


Figure S 11.19 SEM images for surface morphology of carbon fibers coated with nanoparticles of Vulcan, graphene, and MWCNTs from left to right, before (upper row), and after CDC (underneath row) at 6400 X magnification.

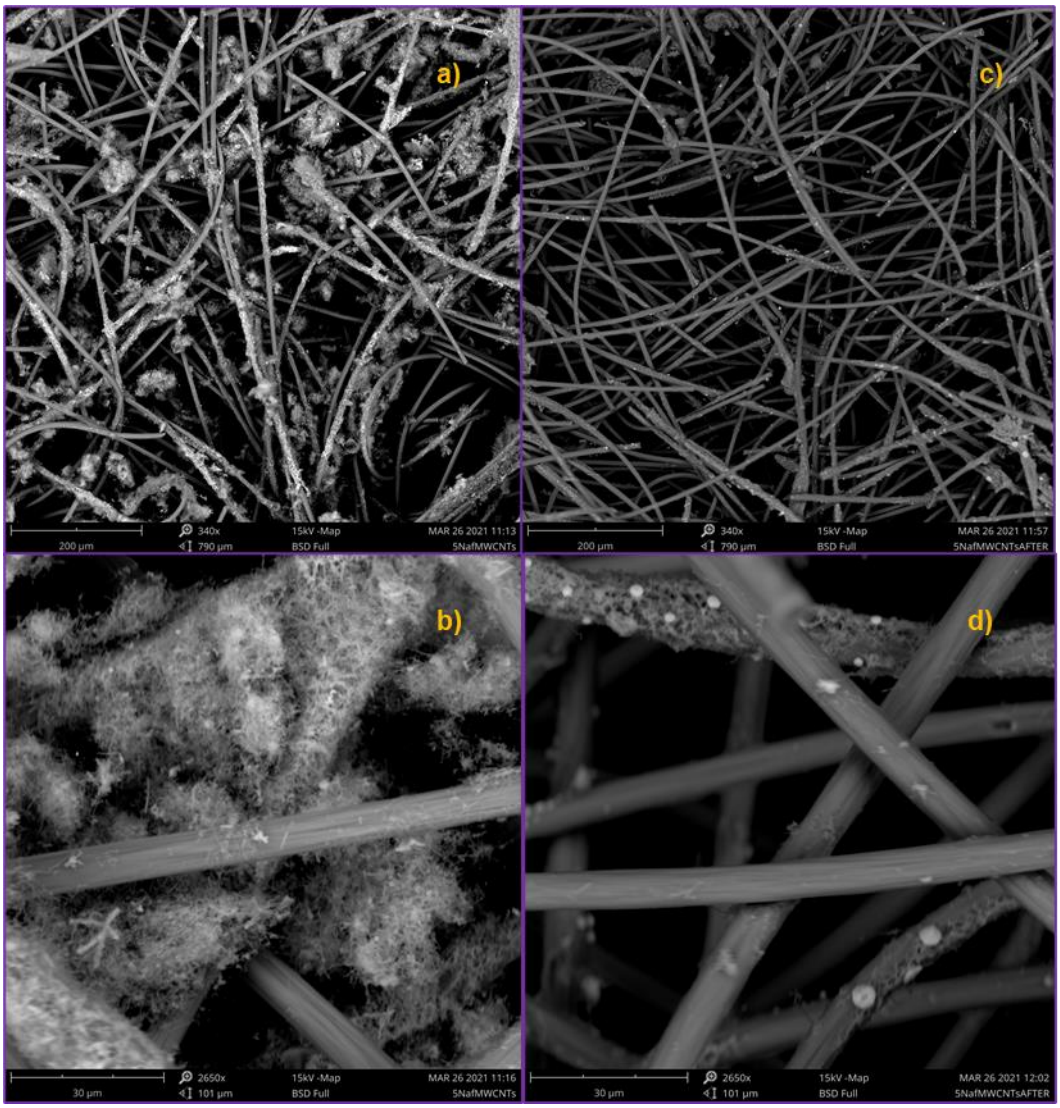


Figure S 11.20 SEM images for surface morphology of carbon fibers with MWCNTs using Nafion ionomer in a ratio of 0.05 for I/C, before (left column a and b) and after CDC (right columns c and d) at 340 X and 6400 X magnifications.

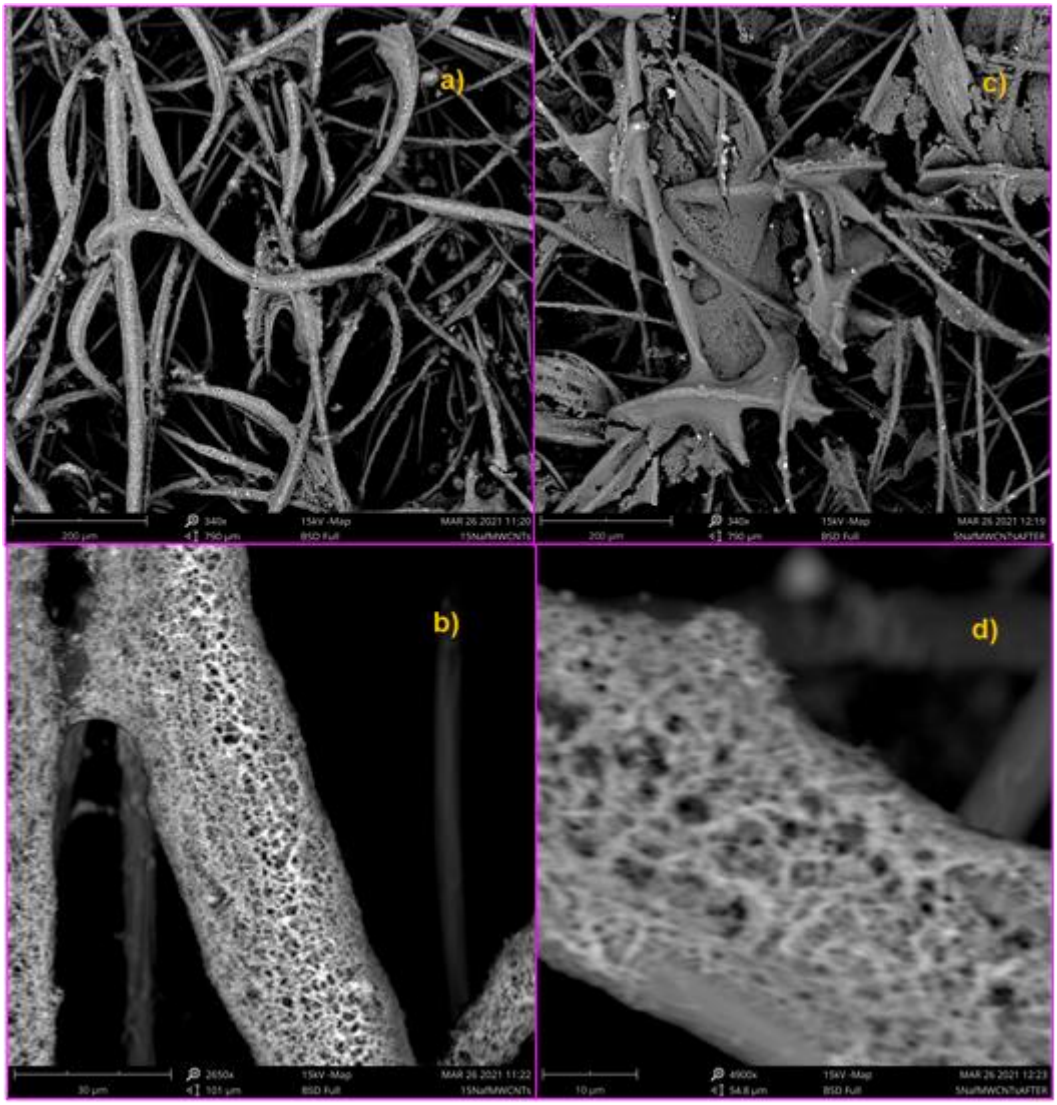


Figure S 11.21 SEM images for surface morphology of carbon fibers with MWCNTs using nafion ionomer in a ratio of 0.15 for I/C , before (left column a and b) and after CDC (right column c and d) at 340 X and 6400 X magnifications.

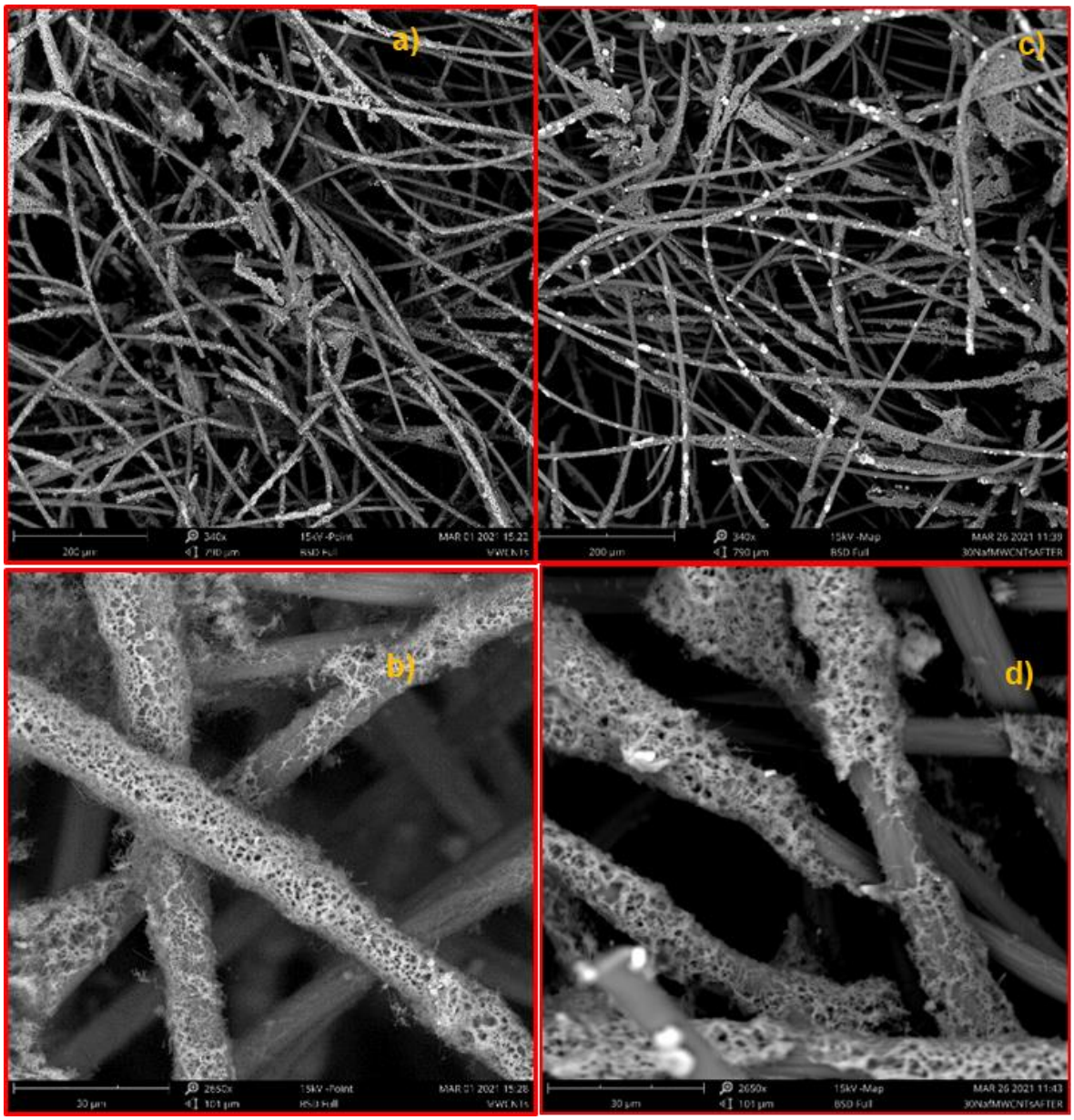


Figure S 11.22 SEM images for surface morphology of carbon fibers with MWCNTs using nafion ionomer in a ratio of 0.30 for I/C, before (left column a and b) and after CDC (right column c and d) at 340 X and 6400 X magnifications.

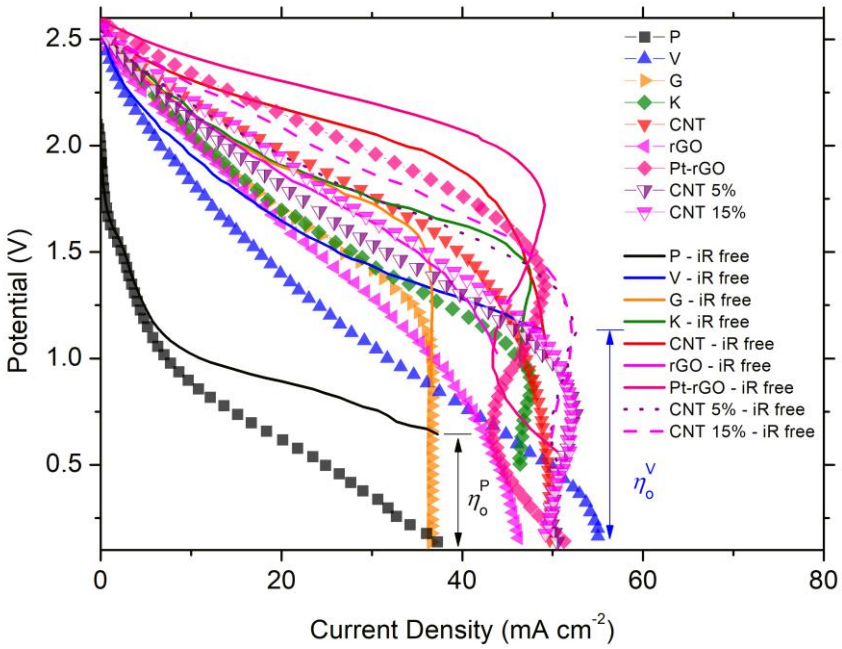


Figure S 11.23 iR-free Polarization curve for each electrode, where the contribution of R is taken from results of EIS.

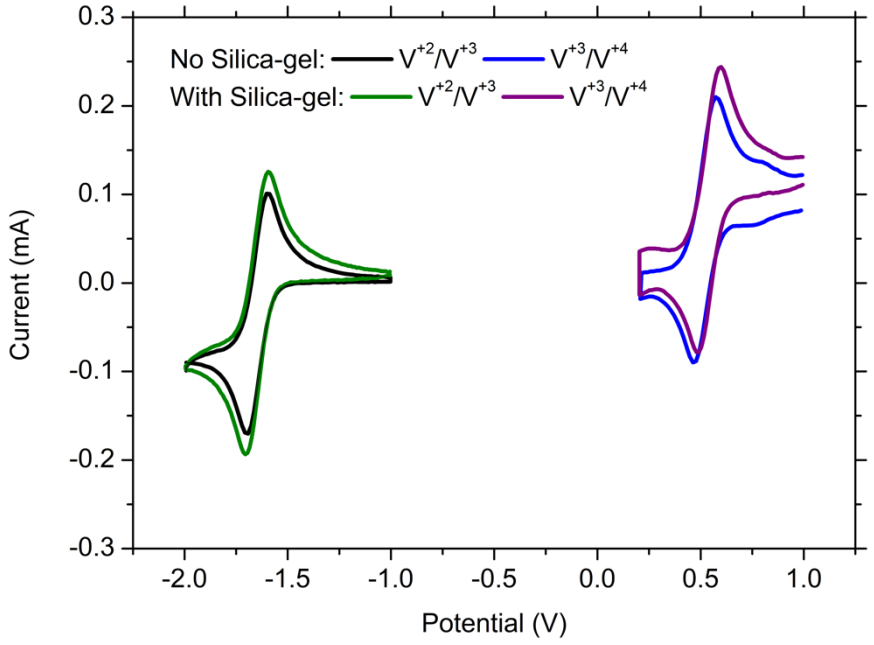


Figure S 11.24 Cyclic voltammogram of electrolyte with and without silica gel, which was added to capture the moisture in the electrolyte. It has a positive effect on peak currents and also there are no side reactions.

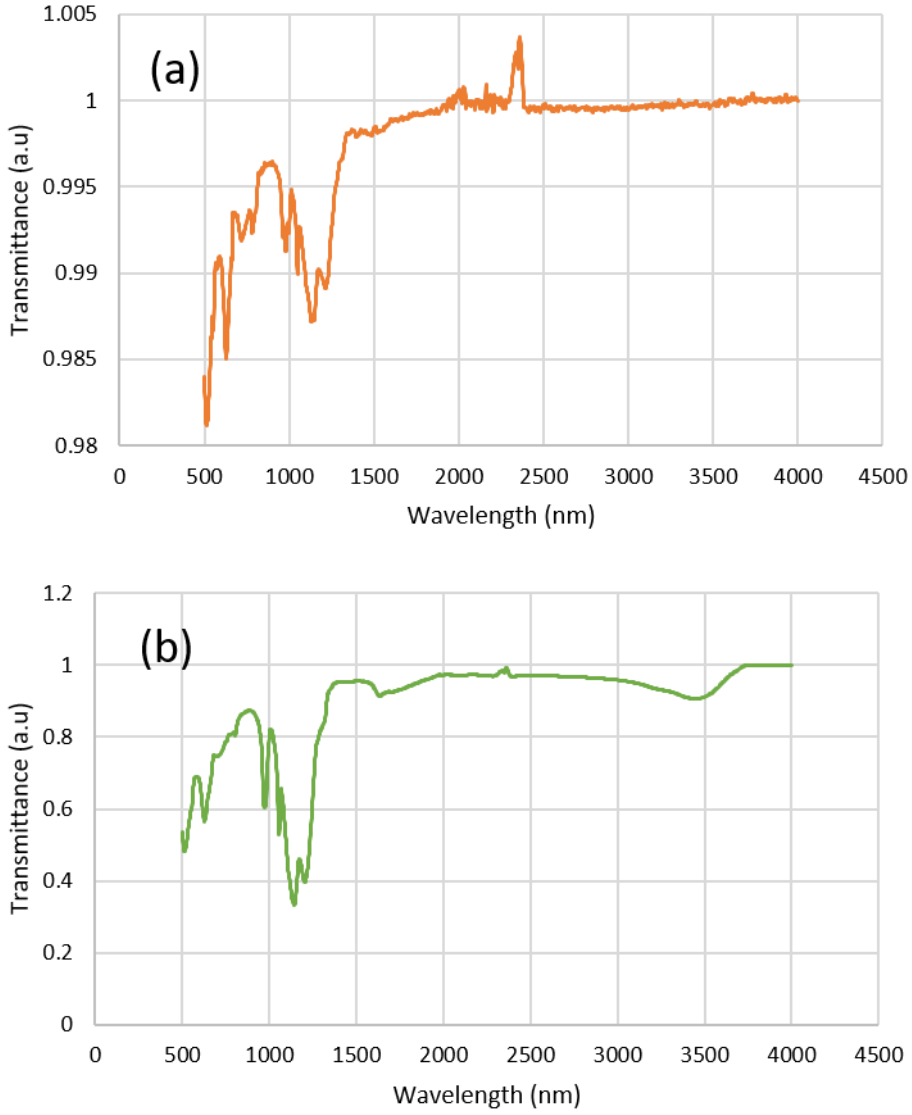


Figure S 11.25 FTIR spectra of the membrane (a) pristine before CDC (b) after CDC.

11.6 Supplementary Information for Chapter 7

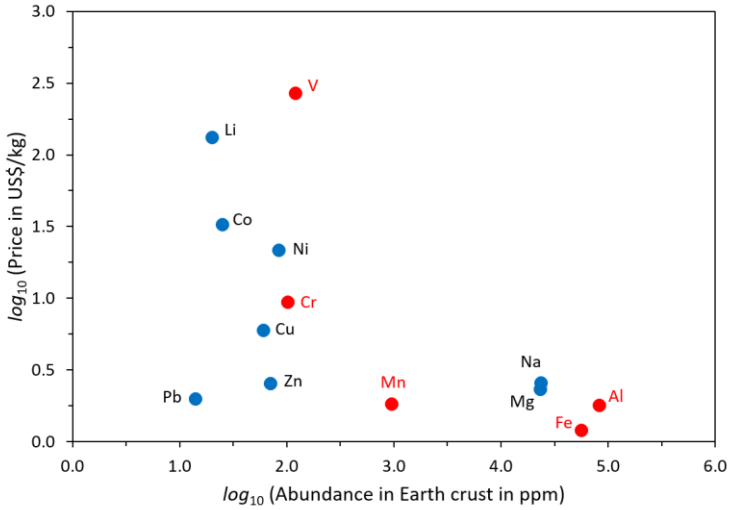


Figure S 11.26 Metals used for electrochemical energy storage systems. Price of metals in USD per kg vs. abundance of the metal in the Earth crust in ppm. The elements used in this study are highlighted in RED color.

Sources = www.metal.com & https://en.wikipedia.org/wiki/Prices_of_chemical_elements

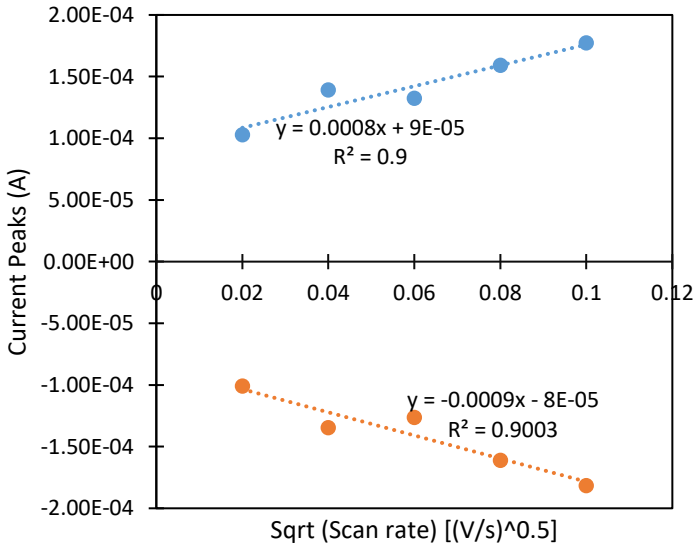


Figure S 11.27 Randles Sevcik plot for V^{4+}/V^{3+}. The linear relationship highlights the reversibility of the redox reaction.

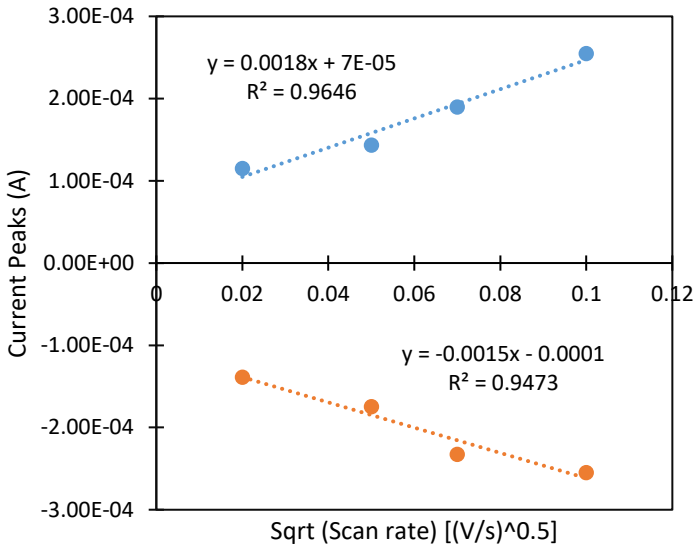


Figure S 11.28 Randles Sevcik plot for Mn^{4+}/Mn^{3+}. The linear relationship highlights the reversibility of the redox reaction.

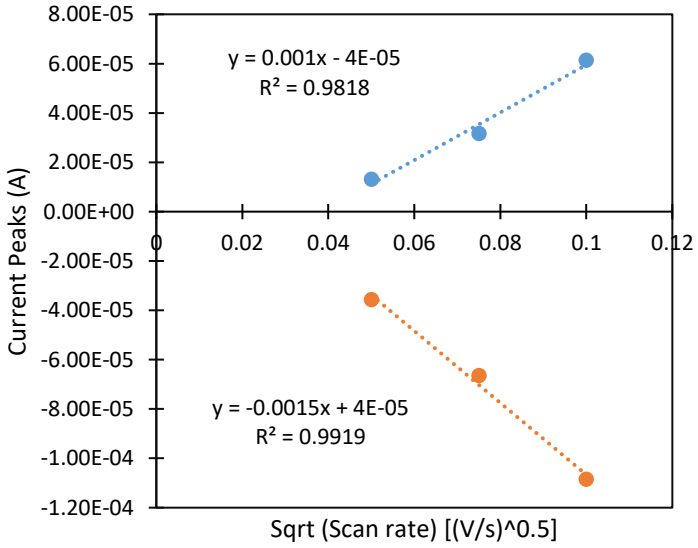


Figure S 11.29 Randles Sevcik plot for Fe^{3+}/Fe^{2+}. The linear relationship highlights the reversibility of the redox reaction.

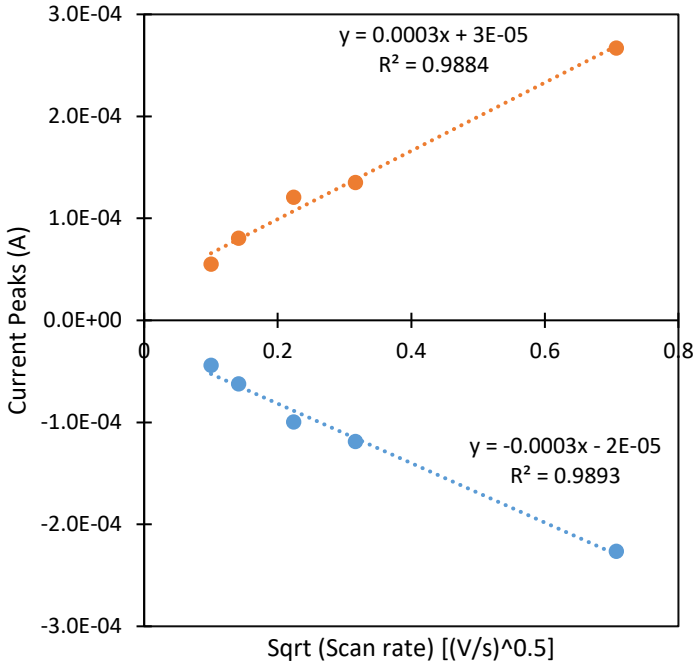


Figure S 11.30 Randles Sevcik plot for Fc^{+}/Fc. The linear relationship highlights the reversibility of the redox reaction.

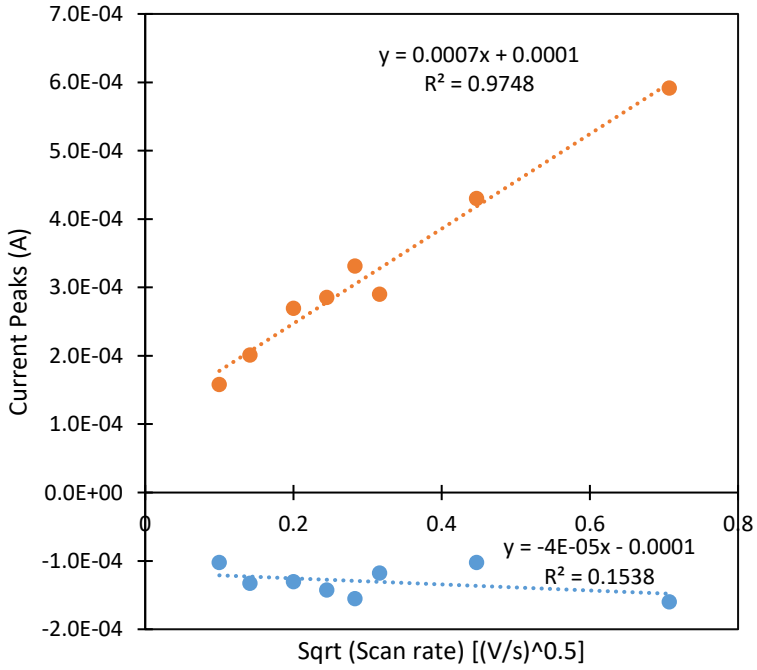


Figure S 11.31 Randles Sevcik plot for Cr^{4+}/Cr^{3+}. An unsymmetrical relationship highlights that the redox reaction is quasi-reversible.

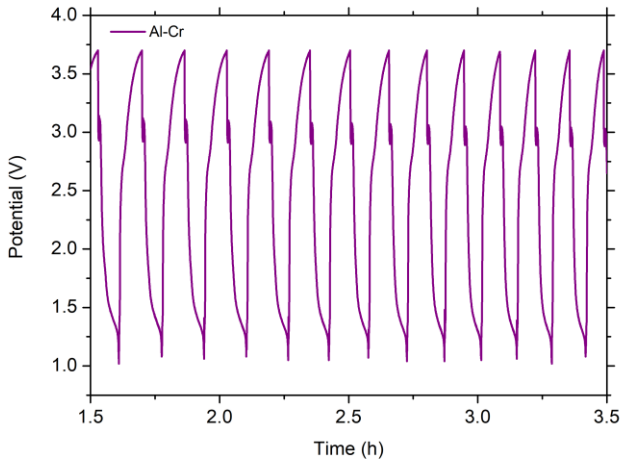


Figure S 11.32 Two hours extract of charge/discharge cycles of Al || Cr battery.

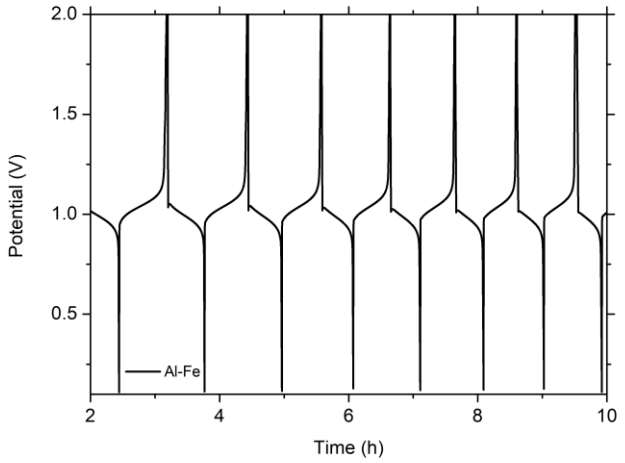


Figure S 11.33 Eight hours extract of charge/discharge cycles of Al || Fe battery.

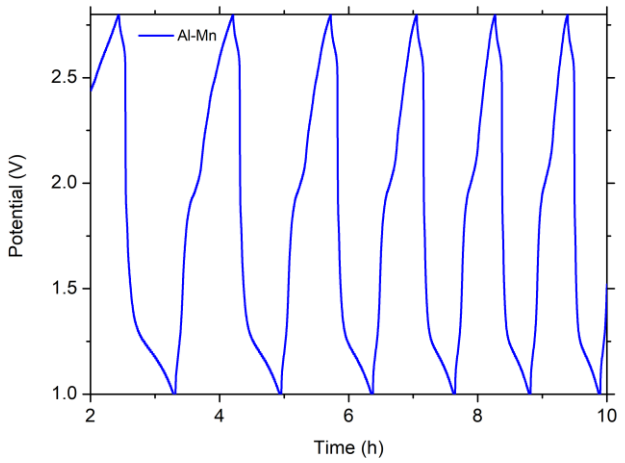


Figure S 11.34 Eight hours extract of charge/discharge cycles of Al || Mn battery.

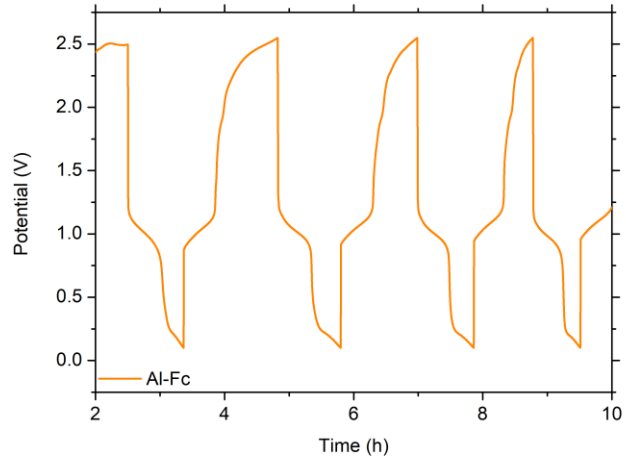


Figure S 11.35 Eight hours extract of charge/discharge cycles of Al || Fc battery.

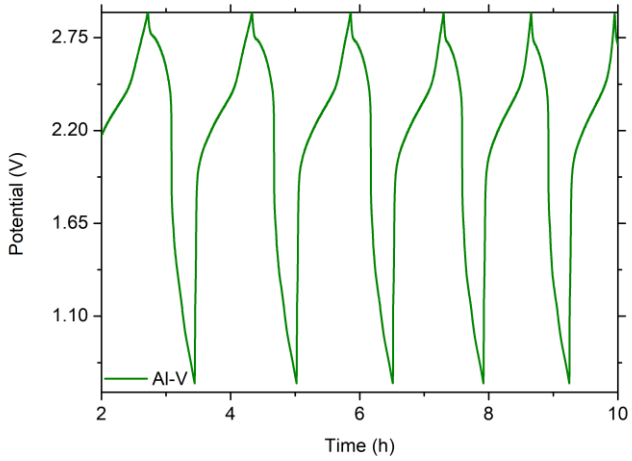


Figure S 11.36 Eight hours extract of charge/discharge cycles of Al || V battery.

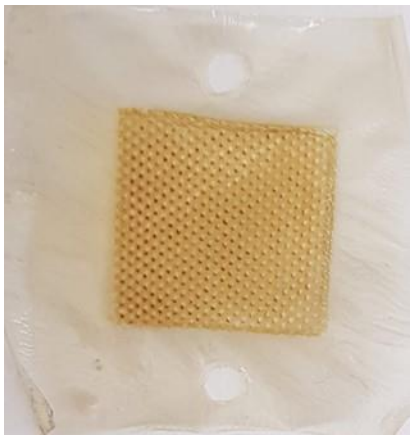


Figure S 11.37 Post-mortem picture of the Nafion HP layer of composite membrane used for Al || Fc NAqRFB-cell. It shows a significant change in the appearance from transparent to

brownish which indicates the deposition of redox species on the surface and results in higher ohmic resistance.

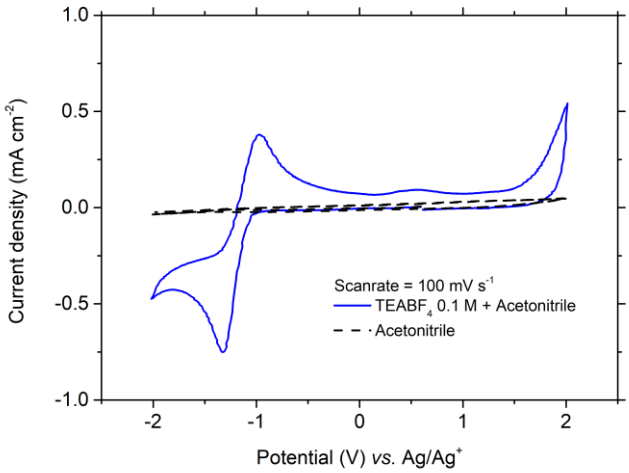


Figure S 11.38 Cyclic voltammogram of blank electrolyte i.e. without any redox species. The composition of the electrolyte is $TEABF_4$ 0.1 M and acetonitrile.

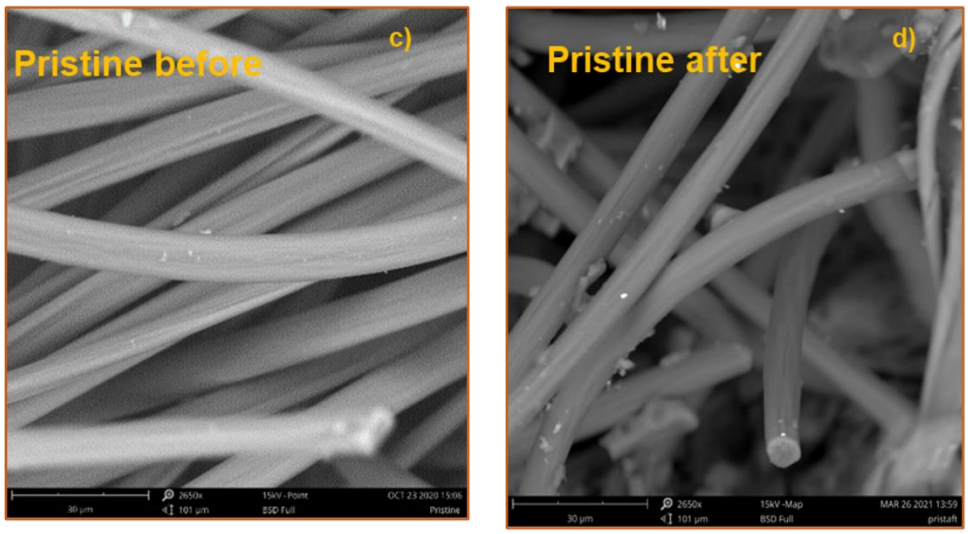


Figure S 11.39 The pristine carbon felt electrode used for all types of NAqRFB-cells (a) before and (b) after charge-discharge cycling. It shows that carbon felt is stable and there is no significant difference.

11.7 Supplementary Information for Chapter 8

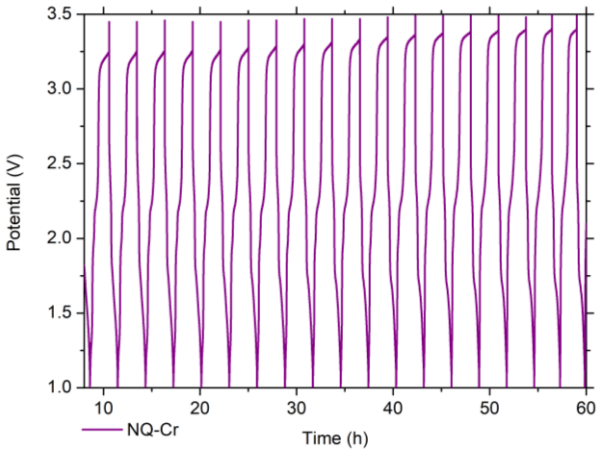


Figure S 11.40 The fifty hours extract of charge/discharge cycles for NQ || Cr battery.

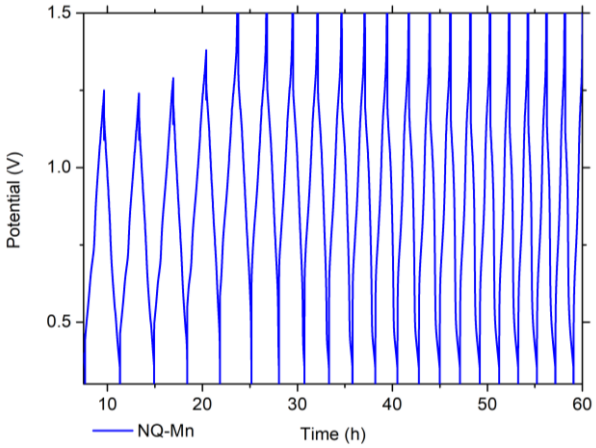


Figure S 11.41 The fifty hours extract of charge/discharge cycles for NQ || Mn battery.

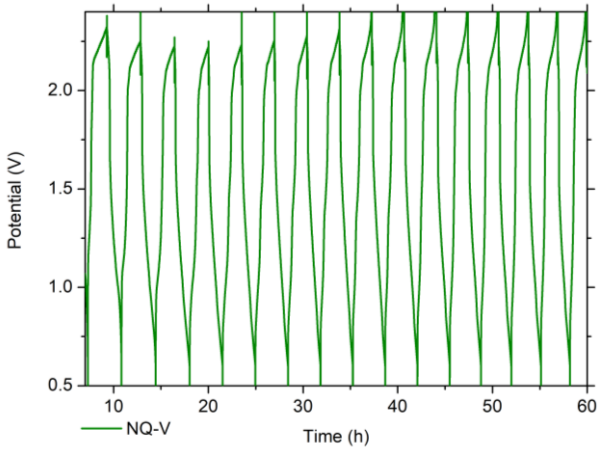


Figure S 11.42 The fifty hours extract of charge/discharge cycles for NQ || V battery.

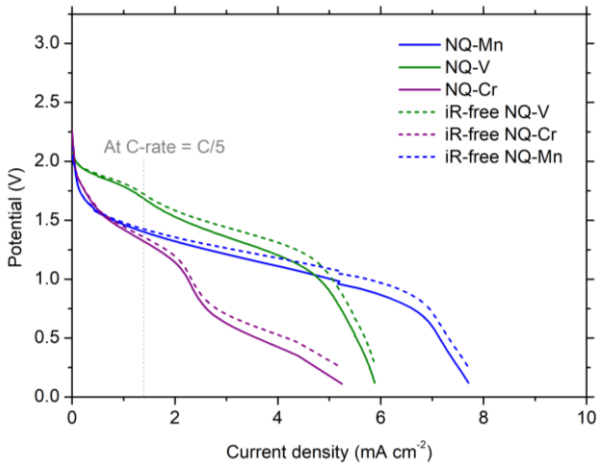


Figure S 11.43 iR-free curves for each cell indicating current density at the flow-limiting condition and ohmic overpotential at C-rate = C/5 i.e. 1.4 mA·cm^{-2}.

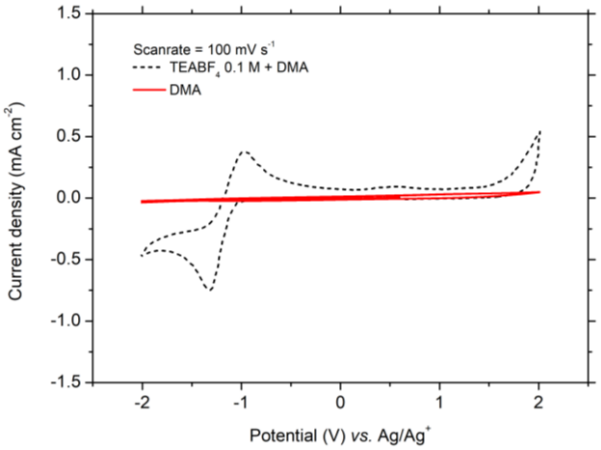


Figure S 11.44 Cyclic voltammogram of blank electrolyte i.e. without any redox species. The composition of the electrolyte is TEABF$_4$ 0.1 M and DMA.

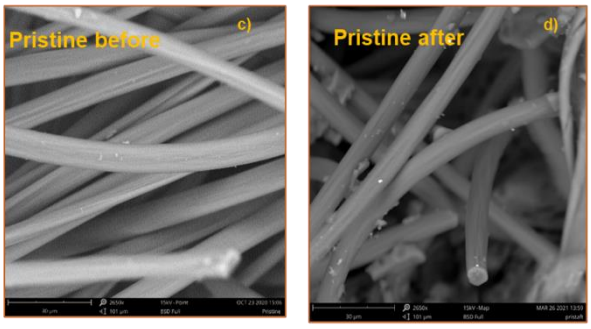


Figure S 11.45 The pristine carbon felt electrode used for all types of NAqRFB-cells (a) before and (b) after charge-discharge cycling.

Thanks for reaching this page.